THE CATHOLIC UNIVERSITY OF AMERICA

The Search for Missing Resonances in $\gamma p \rightarrow K^+ + \Lambda$ and $K^+ + \Sigma^0$ Using Circularly Polarized Photons on a Transversely Polarized Frozen Spin Target

A DISSERTATION

Submitted to the Faculty of the

Department of Physics

School of Arts and Sciences

Of The Catholic University of America

In Partial Fulfillment of the Requirements

For the Degree

Doctor of Philosophy

By

Natalie Kathleen Walford

Washington, D.C.

2014

The Search for Missing Resonances in $\gamma p \rightarrow K^+ + \Lambda$ and $K^+ + \Sigma^0$ Using Circularly Polarized Photons on a Transversely Polarized Frozen Spin Target

Natalie Kathleen Walford, Ph.D.

Director: Franz J. Klein, Ph.D.

The search for undiscovered excited states of the nucleon continues to be a focus of experiments at the Thomas Jefferson National Accelerator Facility (JLab). A large effort has been launched using the CEBAF Large Acceptance Spectrometer (CLAS) detector to provide the database, which will allow nearly model-independent partial wave analyses (PWA) to be carried out in the search for such states. Polarization observables play a crucial role in the effort, as they are essential in disentangling the contributing resonant and non-resonant amplitudes. Recent coupled-channel analyses have found strong sensitivity of the K^++Λ channel to several higher mass nucleon resonances. In 2010, double-polarization data were taken at JLab using circularly and linearly polarized tagged photons incident on a transversely polarized frozen spin butanol target (FROST), operated at the temperature of 30 mK. The reaction products were detected in CLAS. This work is based on the analysis of FROST data and the extraction of the T, F, T_x, and T_z asymmetries of the $K^+\Lambda$ and $K^+\Sigma^0$ final states and their comparison to predictions of recent multipole analyses. There are very few published measurements of the T asymmetry and none for the F, T_x, and T_z asymmetries for the $K^+\Lambda$ final state. The $K^+\Sigma^0$ final state has no published measurements for these asymmetries. This work is the first of its kind and will significantly broaden the world database for these reactions.

To Robert Joseph Walford, Sr., who left too soon to see this work completed.

"I keep thinking about this river somewhere, with the water moving really fast. And these two people in the water, trying to hold onto each other, holding on as hard as they can, but in the end it's too much. The current's too strong. They've got to let go, drift apart. It's a shame because we've loved each other all our lives. But in the end, we can't stay together forever."

-Kazuo Ishigiro

Never Let Me Go

Contents

List of Figures

List of Tables

Acknowledgement

There are so many people to thank for helping me through this arduous and difficult time called being a graduate student. It's hard to even know where to begin.

The first person I would like to thank is my best friend, Allyson Trail. We have known each other a long time and met that fateful day at the patent office and without her funny stories, daily phone calls and wonderful children, Ebin Rivers, Cameron Bennett, and Caleb Morgan and husband Eric, I wouldn't be the person I am today. They have always been there for me, to cheer me up, a constant support and to let me crash multiple vacations and holidays. Never has one had so much fun at Disney World at our ages. I have become a member of the Trail and Sanders family and almost like the fourth child, the daughter Allyson never had. Thank you for being my best friend Allyson. And I would be remissed not to mention Bookclub, which is the best Bookclub in the whole world. Little reading, lots of drinking and talking, Vegas trips, and yearly trips to Lake Anna, which all made me able to survive doing a PhD.

I would next like to thank everyone in the FROST group, whom, without our weekly meetings, this analysis wouldn't be what it is today. Constant input from Mike Dugger, Steffen Strauch, Eugene Pasyuk, and Volker Crede have made me realize the physicist I want to be. My first real comrade of g9b was Ross Tucker and without our many self-deprecating talks, I would have never finished. *HUGS* to you. Priya Roy was an amazing addition and made Ross and me work harder. Mike always answered every email and never thought a question was too stupid. Volker gave me plenty to think about as an American physicist and how I should present myself to others, especially in Europe. I am eternally grateful for the email he sent about a postdoc job, which will no doubt forever change my life. I would also like to thank Volker Burkert who allowed me to come to JLab and finish many of the little projects that just couldn't be finished in DC and wrote amazing reference letters. Thanks to Taya Mineeva and Francois Xavier-Girod, very good friends who really like guns and American flags. To the Glasgow guys, Ken Livingston, Bryan McKinnon, David Hamilton and Dave Ireland, my dinner companions EVERY time they came over to the good 'ole US of A. Those were some good dinners together! To my committee, Dan Sober, Hall Crannell, Tanja Horn, and Dan Carman, thank you for being understanding with the time constraints and reading this document in a timely manner multiple times! To Dr. Steve Landy, the best physics teacher ever who made high school physics fun. Who wouldn't love listening to Queen while doing their weekly quiz wearing their Maxwell equations t-shirt? Also thanks to Dr. Lorenzo Resca, who supported me and believed in me when no one else did. And finally, thanks to Dr. Liam Casey, an amazing friend who can truly understand the CUA physics experience, which is certainly, one of a kind.

I would also like to thank my advisor, Dr. Franz Klein. My life changed for the better in 2009 when I went to Jefferson Lab for the first time to look around. He taught me more about physics than I ever thought possible. I wasn't always the best student, but with his patience and understanding, he shaped who I am today as a physicist and as a person. And even though I am a product of a generation that wants the answers yesterday, he helped me realize I don't always need the answer immediately. Patience truly is a virtue and I thank him for his help in learning physics. I truly am grateful for his guidance throughout this process.

My parents are without a doubt the result of who I am today and cannot be forgotten either. My mom did everything she ever could do to make me the successful woman I am today. She helped me get to college and I am eternally grateful. My dad has always been proud of me regardless of what I did and I am lucky to have him as my dad as it turn's out, I really am daddy's little girl. All I ever wanted was to never let anyone down and I hope I didn't. I hope I was a constant good example for my brother Colin, to show him that anyone can succeed, regardless of where we start. I know Uncle Ed and Aunt Barbara are proud of my accomplishment and see me for the Walford I am. Ed showed me that anyone

could succeed if they put their mind to it. And a big thanks to Uncle Dennis, who allowed me to go to college as I would not be in graduate school today without his signature for undergraduate school. And my Grandma, the classiest, nicest Grandma to ever exist. Even though she didn't always understand what I was doing, she always told me how proud of me she was and how much she loved me. I only wish my Grandpa was still alive to see his granddaughter now.

And of course, to Deuce and Forscher, who are a constant reminder of how to show true love, as dogs should be. And now...off to a new life!

This work was supported in part by NSF grants PHY-0969434 and PHY-1306418.

Chapter 1

Introduction

Quantum Chromodynamics (QCD) is the theory that describes the strong interaction, the dynamics of the fundamental constituents of most matter, as the interaction between quarks and gluons [1]. Quarks exist in six flavors (up, down, charm, strange, top, and bottom). A gluon is a subatomic particle that binds quarks together. QCD also dictates the binding of quarks into composite particles, hadrons, which include baryons and mesons.

At higher energies, the strong interaction is weaker and easier to describe. There, the quarks are seen as 'asymptotically' close together, where they behave as if they were non-interacting. This asymptotic freedom gives way to simplifications in the math of the theory. One can use perturbative techniques to produce solutions to QCD in high energy reactions.

At lower to medium energies, that is a few GeV, the strong interaction remains as an interesting, puzzling force. At these energies, the QCD equations cannot be simplified due to the meson and baryon degrees of freedom that dominate the physics. Lattice QCD has made profess towards finding direct solutions of QCD, but these calculations are still intensive computationally and not yet close enough to current experimental data [2]. In particular, the lattice spacing is still rather wide, corresponding to pion masses of 300–400 MeV instead of the correct value of 140 MeV. Currently, there is no simple analytic solution to QCD at medium energies.

In this chapter, the motivation for our study of kaon photoproduction will be discussed. Theoretical efforts such as the Constituent Quark Model and past analyses in experiments and theory will also be discussed, and it will be demonstrated how this analysis will contribute significantly to the field of nuclear physics.

1.1 QCD and Quarks

QCD has the capability to give a wealth of information regarding the strong interaction. Quantum Electrodynamics (QED), the more familiar theory, describes the electromagnetic interaction between particles that have electric charge. A photon, a massless gauge particle, mediates the interaction. In QED, a charged particle can either emit or absorb a photon at a vertex, and any electromagnetic phenomenon can be realized by constructing various ways the processes can occur. The electromagnetic coupling, α_{em}, or the strength with which a charged particle emits or absorbs the photon at a vertex, is small, $\frac{1}{137}$.

In QCD, quarks are the fundamental point-like particles along with gluons, that make up composite subatomic particles, hadrons, from particles such as protons and neutrons and a variety of less familiar, shorter lived particle states. Quarks can combine in two fundamental ways to make two types of hadrons, baryons and mesons. Baryons consist of three valence quarks, or main quarks, and mesons consist of a valence quark and an antiquark. The gluon acts as the mediator in QCD, just as the photon acts as the mediator in QED. However, the gluon gives rises to interesting features that the photon does not, which distinguishes the two theories. While photons carry no electric charge, gluons carry a color charge (red, green or blue), the charge of QCD. Gluonic interactions occur in QCD when there is a color charge, which leads to nonlinear equations that cannot be solved analytically, meaning that the equations of QCD cannot be solved exactly.

In high energy physics, an easier method for calculations can be used, perturbative QCD. The strong interaction becomes weaker with increasing energy, and quarks in the nucleon begin to behave essentially as free non-interacting particles at high energy, or asymptotic freedom. This asymptotic freedom for QCD calculations corresponds to the QCD coupling constant, α_s, being sufficiently small at high energies. α_s has a strong energy dependence at lower energies and decreases at higher energies as shown in Fig. 1.1. In contrast, α_{em} is constant over accessible energies.

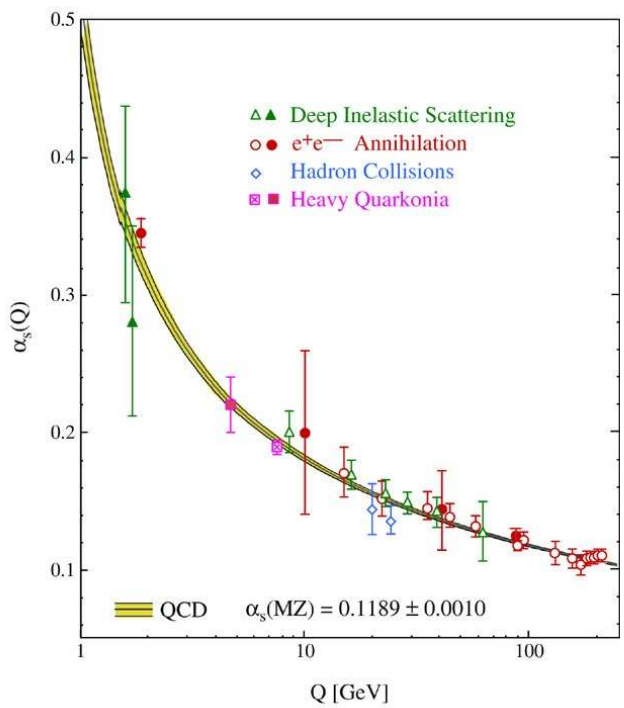

Figure 1.1: The coupling constant of the strong interaction, α_s, as function of energy. α_s shows a strong energy dependence. Its value is most precisely known from e^+e^- scattering near the mass of the Z^0 boson (91.187 GeV/c^2). Figure taken from [3].

At medium energies, the coupling constant approaches unity. This phenomenon governs the non-perturbative regime of QCD, which describes both the interaction of quarks inside of a nucleon and the excited baryon spectrum. Complicated higher-order terms make large contributions to the overall reaction strength and can no longer be neglected.

1.2 The QCD Spectrum and Spectroscopy

Since QCD cannot be directly used for calculations at intermediate energies, certain calculation tools and models have been developed. These approximations to QCD allow for detailed predictions of the spectrum of excited states of the nucleon. Direct comparisons of experimental data to the calculations can then allow for tuning and testing of these tools and models. The baryon spectroscopy program at Jefferson Lab (JLab) and many other facilities has been designed to provide the necessary experimental data for these comparisons. The baryon spectrum has many resonances, or excited states, which are closely spaced in energy and overlap. These states are identified by their quantum numbers and masses. Baryon spectroscopy is the detailed program of mapping out the nucleon resonant states that are excited in a given reaction. These states can then decay into quasi-stable baryons and mesons, which can be detected experimentally, allowing for their masses and quantum numbers (e.g. spin, parity) to be determined.

Baryon spectroscopy can be compared to earlier studies of atomic spectroscopy. Around the 1900s, it was realized that the description of the atomic spectra would need to be re-analyzed using a new theoretical framework. Atomic spectroscopy is the process of detecting and mapping out the spectra of photons emitted from atoms. First, electrons in atoms are brought to excited states and in turn, return to their ground state by emitting photons. With a diffraction grating and a photon detector, one can see the emitted radiation at different wavelengths corresponding to the energy difference between the excited and stable atomic states. These wavelengths correspond to atomic spectral lines that can be quite narrow, but not necessarily sharp. Their width is inversely proportional to their lifetime by an uncertainty relation:

$$\Delta E = \Gamma \approx \frac{\hbar}{\tau} \ , \tag{1.1}$$

where ΔE is the width of the spectral line, $\hbar = \frac{h}{2\pi}$ is the Planck constant, and τ is the mean lifetime of the excited state. The width is usually negligible since the lifetime of excited atomic states is usually on the order of 10^{-8} seconds, which gives a width $\Delta E \approx 10^{-7}$ eV. Atomic spectroscopy is concerned with electromagnetic interactions, whereas baryon spectroscopy is more complicated due to the strong force and occasionally the weak nuclear interaction.

Experimentally, it was observed that light was emitted by atoms due to electronic de-excitation, or the transition from a higher energy state to a lower energy state, and came at specific wavelengths, or energies, depending on which element was studied. Classical theory could not explain this observation because it predicted that a continuous spectrum of energy states corresponds to a continuous photon energy spectrum. Naturally, many theories were postulated, but in the end, a suggestion which led to the accepted theory of the atom was given by Niels Bohr with his introduction of the Bohr Model in 1913 [4]. The Bohr Model suggested that only discrete values of orbital angular momentum of the atomic system, or atomic energy states, were allowed. This model described the hydrogen spectrum well, which then led to theories to describe the quantized nature of physics at the microscopic scale.

Knowing this information about atomic spectroscopy, a similar approach may be taken with QCD in the non-perturbative regime. Using the laws of Quantum Mechanics, excited baryon states, referred to as N^* states, will exist at discrete intervals.

The baryon spectrum can be probed in experiments involving the scattering of π mesons from the proton. Intermediate N^* states are produced and then decay into detectable hadrons, mainly a nucleon and one or more pions. The total πp cross section is shown in Fig. 1.2. It shows the existence of many broad and overlapping resonances, making it clear that a complete identification of these resonant states based on energy alone is not possible.

It is also possible to produce excited baryon states via the electromagnetic interaction. In the electromagnetic interaction, as depicted in Fig. 1.3, the interaction of a real or virtual photon with hadrons is calculated using QED, whereas in πN scattering, complicated

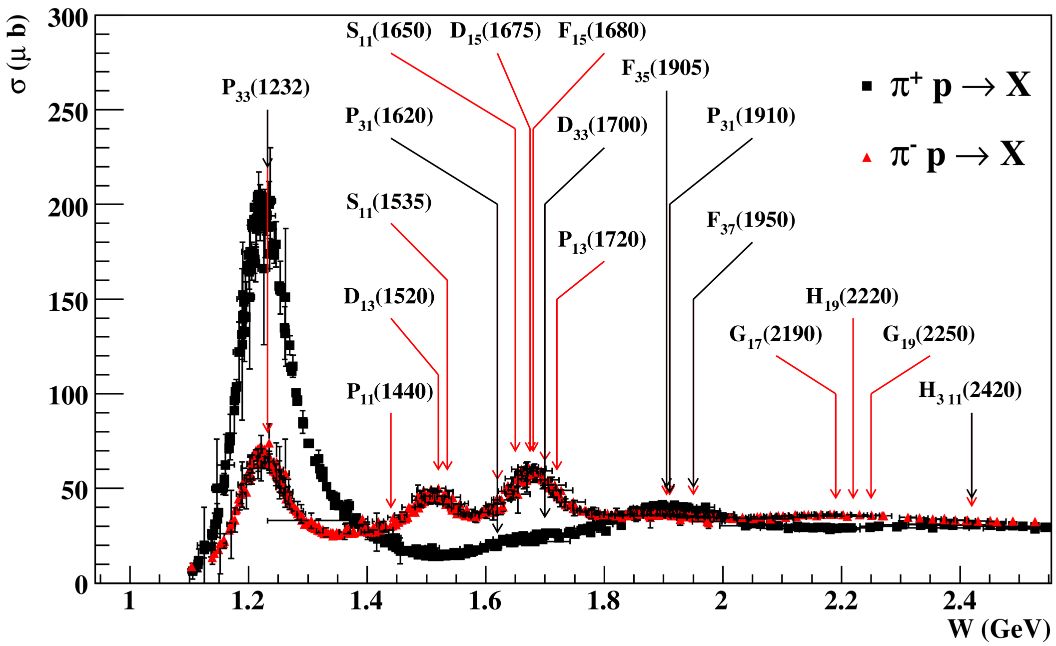

Figure 1.2: Total cross section for πp scattering. Only resonances with a **** rating from the PDG [5] are indicated. Only the Δ resonance, $P_{33}(1232)$, can be clearly isolated. Figure taken from [6].

initial state interactions occur because the π is a quark anti-quark pair and interacts by exchanging gluons. Photoproduction is somewhat complementary to electroproduction in the sense that the initial photon in photoproduction is on its "mass shell" ($Q^2 = 0$) whereas in electroproduction the photon has a virtual mass ($Q^2 > 0$), where Q^2 is the momentum transfer squared.

Baryon spectroscopy is based on the observation and identification of the excited nucleon states in order to map out the entire baryon spectrum. These states are categorized using a notation of the form $L_{2I2J}(M)$, where L is the orbital angular momentum for the resonance πN decay with the standard s, p, d, and f notation, I is the isospin of the state, J is its total spin, and M is its mass. The quantum numbers of the states share different bands of energy levels with increasing masses for progressive bands.

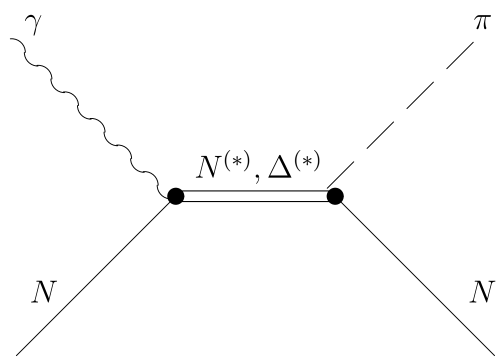

Figure 1.3: A diagram of a photon–proton interaction producing an N^* or Δ^*, which decays into a pion and a nucleon.

The biggest complication in baryon spectroscopy comes from the width of the nucleon resonances. Most of these excited states have a lifetime of the order of 10^{-23} s, which corresponds to energy widths on the order of ≈ 100 MeV, resulting in significant overlap of the states as shown in Fig. 1.2. Careful analysis of the experimental data is required to isolate the individual N^* states in the energy spectrum and detailed analysis of the angular distributions of the decay products of the resonant state is then required to determine the quantum numbers of the state. Partial wave analysis (PWA), i.e. the decomposition of the scattering amplitude in angular momentum dependent partial waves, is the method used to extract resonances by analyzing the angular distributions of the final state particles [7].

1.3 The Constituent Quark Model and the Missing Resonance Problem

The Constituent Quark Model (CQM) describes the hadron spectrum by means of valence quarks and correlations of gluons and sea-quarks (virtual quarks), which contribute to effective, or 'constituent' quark masses of the valence quarks. For baryons, three constituent quarks are considered. Resonances can then be described from the radial or angular momentum excitations of these valence quarks in a harmonic oscillator potential. The composition of up, down, and strange quarks for SU(3) together with quark spin and orbital angular momentum leads to multiple predicted resonances that are calculated from the SU(6)×O(3) symmetry of the CQM. In Tables 1.1 and 1.2, one can see the N^* and Δ^* states that are predicted and observed experimentally by the CQM according to the calculations of Simon Capstick and Winston Roberts [8–10]. One can clearly see that a discrepancy exists between the number of states that have been predicted and those states that have actually been observed, indicated by the lack of stars. This discrepancy is known as 'the missing resonance problem'. More stars, such as four, are associated with resonance states whose properties have been well explored in various experiments. Fewer stars means that the existence of the resonance states has less experimental evidence, which means that many predicted states have not yet been explored in detail. No stars means that the existence of the state has no experimental evidence and has yet to be seen or is 'missing'. It should be noted that in these tables and throughout the text, the convention is used to give masses and momenta the units of energy, in different words, the speed of light is set to $c = 1$.

Table 1.1: Predicted N^* states from the CQM of Capstick–Roberts compared to the observed states. The model states are denoted by $N^p_J(\text{mass})[L_{2I2J}]_n$, where n is the n$^{\text{th}}$ resonance in that partial wave. The amplitudes for γp, $K\Lambda$ and $K\Sigma$ couplings are in units of 10^{-3} GeV$^{-\frac{1}{2}}$. Table based on [8–10]. The "star" rating of the observed resonances is from [5]. For some $N\pi$ states a "(?)" indicates that the assignment to model states is ambiguous.

Model state	$N\pi$ state	$A_{\frac{1}{2}}$	$A_{\frac{3}{2}}$	$A_{K\Lambda}$	$A_{K\Sigma}$
$N^{-}_{\frac{1}{2}}(1460)[S_{11}]_1$	N(1535)****	76			
$N^{-}_{\frac{3}{2}}(1495)[D_{13}]_1$	N(1520)****	-15	134	$0.0^{+0.0}_{-0.9}$	$2.1^{+1.3}_{-1.4}$
$N^{-}_{\frac{1}{2}}(1535)[S_{11}]_2$	N(1650)****	54		$-5.2^{+1.4}_{-0.5}$	
$N^{+}_{\frac{1}{2}}(1540)[P_{11}]_2$	N(1440)****	4		2.3 ± 2.7	
$N^{-}_{\frac{3}{2}}(1625)[D_{13}]_2$	N(1700)***	-33	-3	-0.4 ± 0.2	$0.0^{+0.0}_{-0.3}$
$N^{-}_{\frac{5}{2}}(1630)[D_{15}]_1$	N(1675)****	2	3	0.0 ± 0.0	
$N^{+}_{\frac{5}{2}}(1770)[F_{15}]_1$	N(1680)****	-38	56	-0.1 ± 0.0	$2.1^{+1.3}_{-1.4}$
$N^{+}_{\frac{1}{2}}(1770)[P_{11}]_3$	N(1710)***	13		-2.8 ± 0.6	$1.1^{+0.9}_{-1.1}$
$N^{+}_{\frac{3}{2}}(1795)[P_{13}]_1$	N(1720)****	-11	-31	$-4.3^{+0.8}_{-0.7}$	0.3 ± 0.3
$N^{+}_{\frac{3}{2}}(1870)[P_{13}]_2$	N(1900)***(?)	-2	-15	$-0.9^{+0.4}_{-0.1}$	$-7.0^{+4.9}_{-2.5}$
$N^{+}_{\frac{1}{2}}(1880)[P_{11}]_4$	N(1880)**	0		-0.1 ± 0.1	$-3.7^{+2.4}_{-1.2}$
$N^{+}_{\frac{3}{2}}(1910)[P_{13}]_3$	N(1900)***(?)	-21	-27	0.0 ± 0.0	1.0 ± 0.1
$N^{-}_{\frac{1}{2}}(1945)[S_{11}]_3$	N(1895)**	12		2.3 ± 2.7	$-2.1^{+1.4}_{-1.3}$
$N^{+}_{\frac{3}{2}}(1950)[P_{13}]_4$	N(2040)*(?)	-5	2	$-1.9^{+0.5}_{-02}$	$-1.4^{+0.6}_{-0.3}$
$N^{-}_{\frac{3}{2}}(1960)[D_{13}]_3$	N(1875)***	36	-43	$-5.6^{+1.7}_{-1.3}$	0.7 ± 0.3
$N^{+}_{\frac{1}{2}}(1975)[P_{11}]_5$		-12		$-1.1^{+0.3}_{-0.2}$	-0.6 ± 0.1
$N^{+}_{\frac{7}{2}}(1980)[F_{17}]_1$	N(1990)****	-1	-2	0.0 ± 0.0	$-1.1^{+0.5}_{-0.7}$
$N^{+}_{\frac{5}{2}}(1980)[F_{15}]_2$	N(1860)**	-11	-6	0.0 ± 0.0	-0.4 ± 0.3
$N^{+}_{\frac{5}{2}}(1995)[F_{15}]_3$	N(2000)**	-18	1	-0.5 ± 0.3	$0.6^{+0.6}_{-0.4}$
$N^{-}_{\frac{1}{2}}(2030)[S_{11}]_4$		20		0.3 ± 0.5	$4.5^{+2.4}_{-2.8}$
$N^{+}_{\frac{3}{2}}(2030)[P_{13}]_5$	N(2040)*(?)	-9	15	-0.9 ± 0.2	0.0 ± 0.0
$N^{-}_{\frac{3}{2}}(2055)[D_{13}]_4$	N(2150)**	16	0	$-2.7^{+0.9}_{-0.8}$	$-1.8^{+0.8}_{-0.7}$
$N^{+}_{\frac{1}{2}}(2065)[P_{11}]_6$	N(2100)*			-0.1 ± 0.1	-0.3 ± 0.3
$N^{-}_{\frac{1}{2}}(2070)[S_{11}]_5$		1		2.7 ± 1.3	1.5 ± 0.6
$N^{-}_{\frac{5}{2}}(2080)[D_{15}]_2$	N(2060)**	-3	-14	$-2.9^{+0.8}_{-0.4}$	$2.4^{+0.5}_{-0.9}$
$N^{-}_{\frac{7}{2}}(2090)[G_{17}]_1$	N(2190)****	-34	28	$-1.3^{+0.4}_{-0.6}$	0.2 ± 0.1
$N^{-}_{\frac{5}{2}}(2095)[D_{15}]_3$		-2	-6	$-1.7^{+0.5}_{-0.4}$	$-2.5^{+0.9}_{-0.6}$
$N^{-}_{\frac{3}{2}}(2095)[D_{13}]_5$		-9	-14	-0.1 ± 0.1	-0.4 ± 0.1
$N^{-}_{\frac{9}{2}}(2215)[G_{19}]_1$	N(2250)****	0	1	0.0 ± 0.0	-1.1 ± 0.4
$N^{-}_{\frac{7}{2}}(2305)[G_{17}]_2$		-16	4	-0.5 ± 0.2	-0.4 ± 0.2
$N^{+}_{\frac{9}{2}}(2345)[H_{19}]_1$	N(2220)****	-29	13	-0.4 ± 0.1	1.1 ± 0.3
$N^{+}_{\frac{7}{2}}(2390)[F_{17}]_2$		-14	-11	-1.7 ± 0.4	-0.1 ± 0.1
$N^{+}_{\frac{7}{2}}(2410)[F_{17}]_3$		1	-1	0.1 ± 0.1	$-1.7^{+0.4}_{-0.3}$

Table 1.2: Predicted Δ^* states from the CQM of Capstick–Roberts compared to the observed states. Notation is the same as in Table 1.1. Amplitudes are in units of 10^{-3} GeV $^{-\frac{1}{2}}$. Table based on [8–10]. The "star" rating of the observed resonances is from [5]. The $A_{K\Lambda}$ column is empty because $K\Lambda$ does not couple to Δ^* states.

Model state	Nπ state	$A_{\frac{1}{2}}$	$A_{\frac{3}{2}}$	$A_{K\Lambda}$	$A_{K\Sigma}$
$\Delta^-_{\frac{1}{2}}(1720)[S_{31}]_1$	$\Delta(1620)^{****}$	81	68		
$\Delta^-_{\frac{3}{2}}(1700)[D_{33}]_1$	$\Delta(1700)^{****}$	82	68		0.2±0.1
$\Delta^+_{\frac{3}{2}}(1795)[P_{33}]_2$	$\Delta(1600)^{***}$	30	51		$0.0^{+0.0}_{-1.1}$
$\Delta^+_{\frac{1}{2}}(1835)[P_{31}]_1$	$\Delta(1750)^{*}$	-31			$-2.9^{+2.9}_{-1.4}$
$\Delta^+_{\frac{1}{2}}(1875)[P_{31}]_2$	$\Delta(1910)^{****}$	-8			$-6.9^{+0.7}_{-0.6}$
$\Delta^+_{\frac{5}{2}}(1910)[F_{35}]_1$	$\Delta(1905)^{****}$	26	-1		-0.4±0.1
$\Delta^+_{\frac{3}{2}}(1915)[P_{33}]_3$	$\Delta(1920)^{***}$	13	14		-3.3±0.3
$\Delta^+_{\frac{7}{2}}(1940)[F_{37}]_1$	$\Delta(1950)^{****}$	-33	-42		-1.2±0.1
$\Delta^+_{\frac{3}{2}}(1985)[P_{33}]_4$		6	3		$-3.2^{+0.9}_{0.3}$
$\Delta^-_{\frac{5}{2}}(1990)[F_{35}]_2$	$\Delta(2000)^{**}$	-10	-28		$-0.2^{+0.2}_{-0.3}$
$\Delta^-_{\frac{1}{2}}(2035)[S_{31}]_2$	$\Delta(1900)^{**}$	20			1.9±0.3
$\Delta^-_{\frac{3}{2}}(2080)[D_{33}]_2$	$\Delta(1940)^{*}$	-20	-6		-1.1±0.7
$\Delta^-_{\frac{1}{2}}(2140)[S_{31}]_3$	$\Delta(2150)^{*}$	4			4.1±2.4
$\Delta^-_{\frac{3}{2}}(2145)[D_{33}]_3$		0	10		$-1.9^{+0.6}_{-0.5}$
$\Delta^-_{\frac{5}{2}}(2155)[D_{35}]_1$	$\Delta(1930)^{***}$	11	19		-2.1±0.4
$\Delta^-_{\frac{5}{2}}(2165)[D_{35}]_2$					-1.0±0.3
$\Delta^-_{\frac{7}{2}}(2230)[G_{37}]_1$	$\Delta(2200)^{*}$	14	-4		$-0.4^{+0.2}_{-0.3}$
$\Delta^-_{\frac{5}{2}}(2265)[D_{35}]_3$	$\Delta(2350)^{*}$				-2.5±0.1
$\Delta^-_{\frac{9}{2}}(2295)[G_{39}]_1$	$\Delta(2400)^{**}$	-4	-7		$-1.4^{+0.8}_{-1.0}$
$\Delta^+_{\frac{7}{2}}(2370)[F_{37}]_2$	$\Delta(2390)^{*}$	-33	-42		$-1.9^{+0.5}_{-0.4}$
$\Delta^+_{\frac{9}{2}}(2420)[H_{39}]_1$	$\Delta(2300)^{**}$	-14	-17		0.2±0.1
$\Delta^+_{\frac{11}{2}}(2450)[H_{3,11}]_1$	$\Delta(2420)^{****}$	-13	-16		-0.5±0.3
$\Delta^+_{\frac{7}{2}}(2460)[F_{37}]_3$		24	30		-0.5±0.1

There are some theories as to why these resonances are missing [11]. The two most rational explanations are either that not all of the predicted resonances actually exist or that they do exist, but have thwarted detection in experiments. If the predicted resonances do NOT exist, this means that the CQM creates too many baryon states. If this statement is correct, then that implies that the model fails to predict the interaction of the valence quarks correctly. An alternative to the SU(6) symmetric CQM is the diquark model [12–15]. Instead of describing the nucleon as a system of three symmetric constituent quarks, it pairs up two of the quarks into a tightly coupled diquark. Describing the nucleon as a diquark plus quark system greatly reduces the degrees of freedom in the system, which results in significantly fewer resonant states being predicted. If the states DO exist, but have not been seen in experiments, this means that experiments were inadequate up until now and that it is likely that the missing resonances couple weakly or do not couple at all to the reaction channels, such as πN, which have been predominantly studied to date.

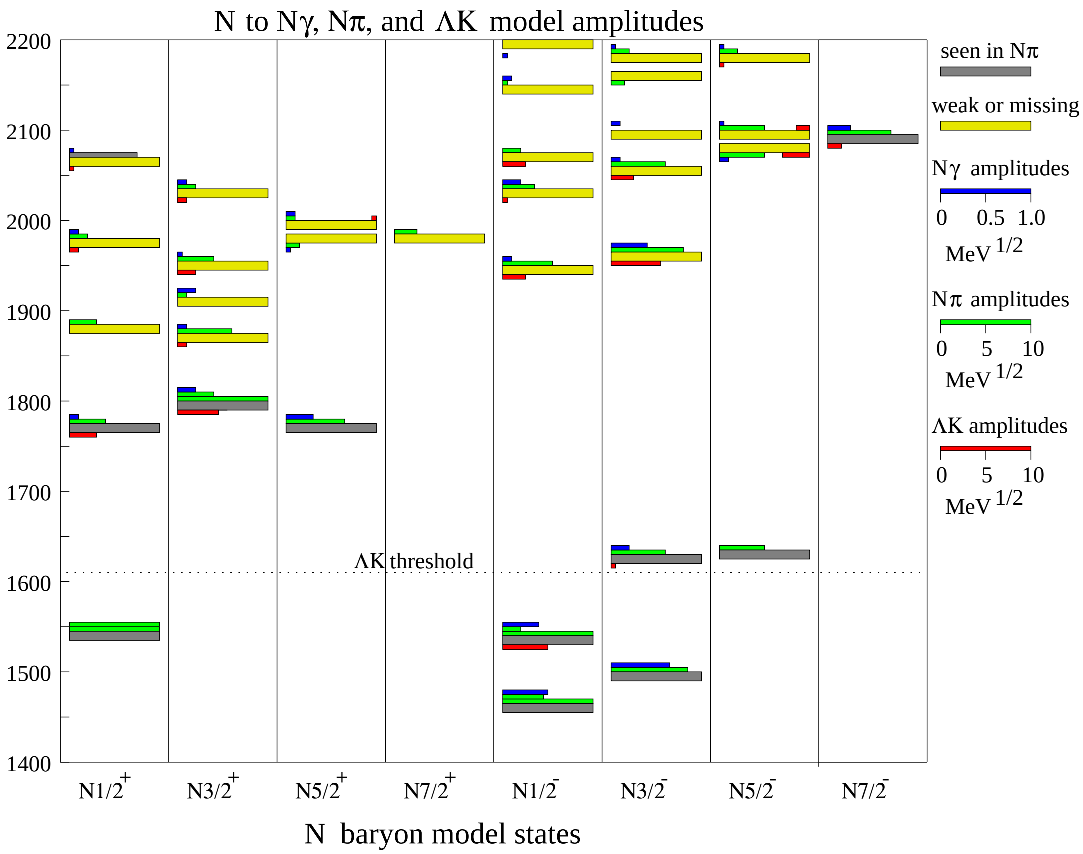

Figure 1.4: Capstick–Roberts predicted amplitudes for N^* resonances. For most states with masses above ≈ 1850 MeV there is poor or no experimental evidence. Figure taken from [10].

Pion production with πN final states have been the focus of experimental data until

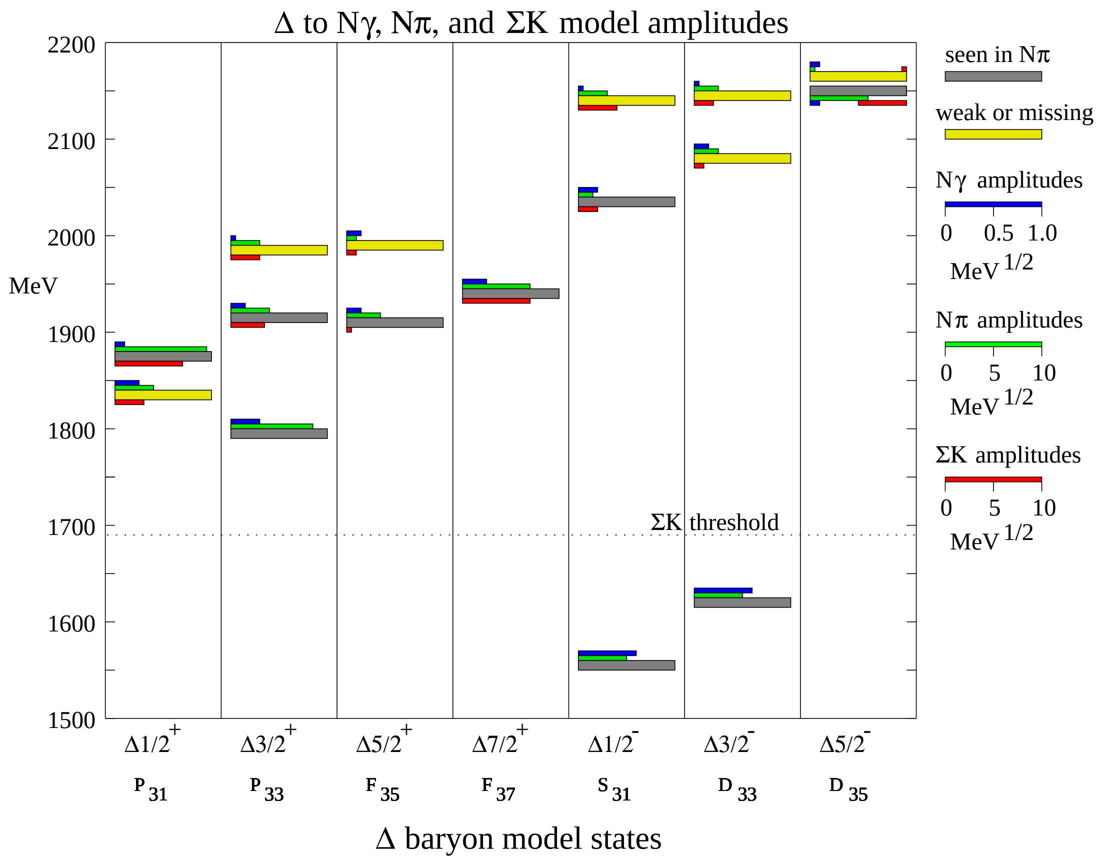

Figure 1.5: Capstick–Roberts predicted amplitudes for Δ^* resonances. Several states with masses above $\approx$ 2000 MeV have not been observed experimentally. Figure taken from [10].

recently. Many N^* and Δ^* resonances have been found but higher mass states (above $\approx$ 1900 MeV) were difficult to disentangle since πN couples to N^* ($I{=}\frac{1}{2}$) and Δ^* ($I{=}\frac{3}{2}$) states. One must also look at all photoproduction channels available (e.g. $K^+\Lambda$ or $K^+\Sigma^0$), and they must be probed sufficiently to study the validity of the CQM. It has been theorized by Capstick and Roberts in their quark model calculations that some missing resonances couple strongly to hyperon final state channels in photoproduction reactions [8–10]. Their model further predicts that a number of negative-parity resonant states from the $N = 3$, 4, and 5 bands will appear clearly in the final state reaction of $K^+\Lambda$, which is one of the main focuses of the present analysis. Fig. 1.4 shows the Capstick and Roberts predictions for the coupling of nucleon resonances up to 2200 MeV to $K^+\Lambda$ for N^* resonances. Fig. 1.5 shows the Capstick and Roberts predictions for the coupling of nucleon resonances up to 2200 MeV to $K^+\Sigma$ for Δ^* resonances. The figures show that most predicted states with masses above $\approx$ 1850 MeV have not been observed experimentally.

1.4 Kaons and Hyperons

The main concern of this analysis is studying the spectrum of excited states of the proton using a high-energy beam of photons. Even though the use of kaon photoproduction has been done to excite discrete hyperon states in the past, there is still much information that can be gathered and learned. In order to do so, one must examine certain final-state kaon reactions, and two were chosen for this analysis because of their similarity in experimental identification, $\gamma p \to K^+\Lambda$ and $K^+\Sigma^0$. These two reaction have almost the same final state particles due to the fact that Σ^0 decays into $\Lambda\gamma$. These final states can be identified using the CLAS detector at JLab, which will be described in full detail in Chapter 2. The Λ and Σ^0 hyperons both carry a strangeness equal to -1, have the same valence quark structure (uds), have a spin of 1/2, and come from the same baryon octet as the proton and neutron. Λ is an isoscalar (isospin equal to zero) and has a mass of 1115.7 MeV [5]. Σ^0 is an isovector component and has a mass of 1192.6 MeV [5]. The Λ decays into $p\pi^-$ with a branching ratio of 63.9%, and also to $n\pi^0$ with a branching ratio of 35.8%. This analysis does not consider $\Lambda \to n\pi^0$ decays as the CLAS spectrometer was not an optimized neutral particle detector. More properties of the Λ and Σ^0 can be seen in Table 1.3.

The decay $\Lambda \to p\pi^-$ occurs in p and s waves, which causes an interference between the parity-violating s-wave and parity-conserving p-wave, so that the decay distribution behaves like:

$$\frac{d\ N}{d\cos\theta_{y'}} = \frac{1}{2}(1 + \alpha_\Lambda P \cos\theta_{y'}), \tag{1.2}$$

where $\cos\theta_{y'}$ is the direction cosine of the normal to the production plane, P is the recoil polarization, and α_Λ is the weak decay parameter of Λ. The Λ is said to be a self-analyzing particle in that its angular decay distribution allows for its polarization to be determined. If the Λ was not self-analyzing, then to find out information about the spin orientation of the Λ, one would have to measure the spin orientation of the recoiling proton from the decay using a polarimeter system. The Σ^0 has one major decay into $\Lambda\gamma$ with a branching ratio of 99.9%, upon which this analysis will also focus. As previously mentioned, due to the non-perturbative nature of QCD in the regime of nucleon resonance excitation and decay, the interpretation of the results that will be presented cannot be compared directly to QCD or CQM, but are compared to the currently available models such as KAON-MAID [16], the Bonn-Gatchina coupled-channel approach [17], and the Ghent Regge–Plus-Resonance model [18, 19]. Each of these calculations might be considered as an approximation to or a representation of QCD.

Table 1.3: Properties of the particles detected in this analysis. Compiled from [5].

	K^+	Λ	Σ^0
mass (MeV)	493.677	1115.683	1192.642
isospin	$\frac{1}{2}$	0	1
quark composition	$u\bar{s}$	uds	uds
spin	0	$\frac{1}{2}$	$\frac{1}{2}$
mean life τ (s)	1.238×10^{-8}	2.632×10^{-10}	7.4×10^{-20}
main decay channels	$\mu^+\nu_\mu$ (63.4%)	$p\pi^-$ (63.9%)	$\Lambda\gamma$ (99.9%)
	$\pi^+\pi^0$ (21.1%)	$n\pi^0$ (35.8%)	

1.5 Polarization Observables

For many years now, it has been understood that differential cross section data is not sufficient to carry out a full partial wave analysis of $\gamma p \to K^+\Lambda$ and $K^+\Sigma^0$ [20, 21]. In order to do a complete PWA, polarization observables are also required. Hyperon photoproduction is described by four complex amplitudes, which in turn define a total of sixteen experimental observables [21–24]. The sum of the squared amplitudes is used to calculate the differential cross section thus interferences between these amplitudes cannot be employed in pure cross-section measurements. The differential cross section is given by:

$$\frac{d\sigma}{d\Omega_{CM}} = \frac{(E_p + M_p)(E_\Lambda + M_\Lambda)}{128\pi^2} \; \frac{|\vec{q}|}{|\vec{k}|} \; Tr(\mathcal{F}\mathcal{F}^\dagger) \; , \tag{1.3}$$

where $\vec{k}$ is the momentum of the incoming photon, $\vec{q}$ is the momentum of the kaon in the center-of-mass frame, E_p, M_p, E_Λ, and M_Λ are the center-of-mass energy or mass of the proton and the Λ hyperon, respectively, and $\mathcal{F}$ is given by the CGLN [25] amplitudes $\mathcal{F}_1$ to $\mathcal{F}_4$, which relate to different couplings to spin matrices ($\vec{\sigma}$) and photon polarization vector ($\vec{\epsilon}$):

$$\mathcal{F} = i\vec{\sigma}\cdot\vec{\epsilon}\;\mathcal{F}_1 + \vec{\sigma}\cdot\hat{q}\;\vec{\sigma}\cdot(\hat{k}\times\vec{\epsilon})\;\mathcal{F}_2 + i\vec{\sigma}\cdot\hat{k}\;\vec{\epsilon}\cdot\hat{q}\;\mathcal{F}_3 + i\vec{\sigma}\cdot\hat{q}\;\vec{\epsilon}\cdot\hat{q}\;\mathcal{F}_4 \; . \tag{1.4}$$

The CGLN amplitudes $\mathcal{F}_i$ are related to the transversity amplitudes b_i in Table 1.4 by the following expressions:

$$\begin{aligned} b_1 &= -\frac{i}{\sqrt{2}}(\mathcal{F}_1 - \mathcal{F}_2 e^{-i\theta_{cm}})e^{i\theta_{cm}/2} \; ; \qquad & b_3 &= -b_1 - \frac{\sin\theta_{cm}}{\sqrt{2}}(\mathcal{F}_3 + \mathcal{F}_4 e^{-i\theta_{cm}})e^{i\theta_{cm}/2} \; ; \\ b_2 &= \frac{i}{\sqrt{2}}(\mathcal{F}_1 - \mathcal{F}_2 e^{i\theta_{cm}})e^{-i\theta_{cm}/2} \; ; \qquad & b_4 &= -b_2 - \frac{\sin\theta_{cm}}{\sqrt{2}}(\mathcal{F}_3 + \mathcal{F}_4 e^{i\theta_{cm}})e^{-i\theta_{cm}/2} \; . \end{aligned}$$

The 16 observables in kaon (or pseudoscalar) photoproduction can be seen in Table 1.4 and are divided into groups based on what is polarized in the reaction, such as the beam, target, or recoil hyperon. The first group comprises the unpolarized differential cross section $(d\sigma/d\Omega)_u$, hyperon recoil polarization P, linearly polarized photon beam asymmetry Σ, and the transversely polarized target asymmetry T, referred to as single polarization observables and labeled S in Table 1.4. The next groups consists of double–polarization observables, where two of the reaction participants are polarized, such as beam and target, beam and hyperon, or target and hyperon. The specific analysis presented in this work has measured the observables that are accessible with circularly polarized beam and transversely polarized target, T, T_x, T_z, and F for the final states of $\gamma p \to K^+\Lambda$ and $\gamma p \to K^+\Sigma^0$ since these observables have never been measured before.

Table 1.4: The 16 spin observables for $\gamma p \to K^+\Lambda$ and $\gamma p \to K^+\Sigma^0$ expressed in the transversity representation. The set label $\mathcal{S}$ refers to single polarization observables, $\mathcal{BT}$ refers to beam-target observables, $\mathcal{BR}$ refers to beam-recoil observables, and $\mathcal{TR}$ refers to target-recoil observables. Polarization of the photon beam is denoted as l for a linearly polarized beam and c for a circularly polarized beam. The coordinate frames for the polarization directions of the target proton and the recoil hyperon are explained in Sec. 5.1. This table is compiled from Refs. [23, 24].

Spin Observable	Polarization Beam	Target	Recoil	Transversity Representation	Set
$\left(\frac{d\sigma}{d\Omega}\right)_u$	-	-	-	$\frac{1}{2}(\lvert b_1\rvert^2 + \lvert b_2\rvert^2 + \lvert b_3\rvert^2 + \lvert b_4\rvert^2)$	
Σ	l	-	-	$\frac{1}{2}(\lvert b_1\rvert^2 + \lvert b_2\rvert^2 - \lvert b_3\rvert^2 - \lvert b_4\rvert^2)$	$\mathcal{S}$
T	-	y	-	$\frac{1}{2}(\lvert b_1\rvert^2 - \lvert b_2\rvert^2 - \lvert b_3\rvert^2 + \lvert b_4\rvert^2)$	
P	-	-	y'	$\frac{1}{2}(\lvert b_2\rvert^2 + \lvert b_4\rvert^2 - \lvert b_1\rvert^2 - \lvert b_3\rvert^2)$	
E	c	z	-	$\mathrm{Re}(b_1 b_3^* + b_2 b_4^*)$	
F	c	x	-	$\mathrm{Im}(b_1 b_3^* - b_2 b_4^*)$	$\mathcal{BT}$
G	l	z	-	$\mathrm{Im}(-b_1 b_3^* - b_2 b_4^*)$	
H	l	x	-	$\mathrm{Re}(b_1 b_3^* - b_2 b_4^*)$	
O_x	l	-	x'	$\mathrm{Re}(-b_1 b_4^* + b_2 b_3^*)$	
O_z	l	-	z'	$\mathrm{Im}(b_1 b_4^* + b_2 b_3^*)$	$\mathcal{BR}$
C_x	c	-	x'	$\mathrm{Im}(b_2 b_3^* - b_1 b_4^*)$	
C_z	c	-	z'	$\mathrm{Re}(-b_1 b_4^* - b_2 b_3^*)$	
T_x	-	x	z'	$\mathrm{Re}(b_1 b_2^* - b_3 b_4^*)$	
T_z	-	x	z'	$\mathrm{Im}(b_3 b_4^* - b_1 b_2^*)$	$\mathcal{TR}$
L_x	-	z	x'	$\mathrm{Im}(-b_1 b_2^* - b_3 b_4^*)$	
L_z	-	z	z'	$\mathrm{Re}(-b_1 b_2^* - b_3 b_4^*)$	

T, the target asymmetry, is a single polarization observable requiring a transversely polarized target. F is a double polarization observable that is based on beam-target polarization, meaning it must have a circularly polarized beam and a transversely polarized target to be extracted. For this setting of beam and target polarization and when summed over all outgoing hyperon spin states, T and F are related as [23]:

$$\frac{d\sigma}{d\Omega} = \left(\frac{d\sigma}{d\Omega}\right)_u \left(1 + P_{xy}^{\mathrm{tg}} P_c^{\gamma} \mathbf{F} \cos(\phi - \varphi_0) + P_{xy}^{\mathrm{tg}} \mathbf{T} \sin(\phi - \varphi_0)\right), \tag{1.5}$$

where P_{xy}^{tg} is the degree of target polarization, P_c^{γ} is circular beam polarization, ϕ is the kaon azimuthal scattering angle, and φ_0 is the angle of the target polarization relative to the horizontal lab plane.

T_x and T_z are both double polarization observables based on target-recoil polarization, meaning they are associated with measurements involving a transversely polarized target where the hyperon recoil polarization is measured. They too can be described in reference to the differential cross section together with other polarization observables as shown in the following equation [23]:

$$\begin{aligned} \frac{d\sigma}{d\Omega} &= \left(\frac{d\sigma}{d\Omega}\right)_u \left(1 + P_{xy}^{\mathrm{tg}} \sin(\phi - \varphi_0)\ \mathbf{T} + P_c^{\gamma} P_{xy}^{\mathrm{tg}} \cos(\phi - \varphi_0)\ \mathbf{F}\right. \\ &+ \alpha_Y c_{x'}\ (P_c^{\gamma}\ \mathbf{C_x} + P_{xy}^{\mathrm{tg}} \cos(\phi - \varphi_0)\ \mathbf{T_x} - P_c^{\gamma} P_{xy}^{\mathrm{tg}} \sin(\phi - \varphi_0)\ \mathbf{O_z}) \\ &+ \alpha_Y c_{y'}\ (\mathbf{P} + P_{xy}^{\mathrm{tg}} \sin(\phi - \varphi_0)\ \mathbf{\Sigma} + P_c^{\gamma} P_{xy}^{\mathrm{tg}} \cos(\phi - \varphi_0)\ \mathbf{G}) \\ &+ \left.\alpha_Y c_{z'}\ (P_c^{\gamma} \mathbf{C_z} + P_{xy}^{\mathrm{tg}} \cos(\phi - \varphi_0)\ \mathbf{T_z} + P_c^{\gamma} P_{xy}^{\mathrm{tg}} \sin(\phi - \varphi_0)\ \mathbf{O_x})\right) . \end{aligned} \tag{1.6}$$

The actual extraction methods for the observables of interest, T, T_x, T_z, and F, are described in more detail in Chapter 5.

1.6 Previous Results on Kaon Photoproduction

Kaon photoproduction has been studied in multiple experiments over the past several decades, but the database is still relatively small. Even just 10 years ago, data on kaon photoproduction reactions in the resonance region were particularly sparse with low precision, mainly due to the small cross sections and the difficulty of separating kaons from pions and protons in the experiments, which resulted in insufficient data on resonance couplings to $K^+\Lambda$ and $K^+\Sigma^0$. However, with new precision data available from present accelerator facilities with their complex detectors, there is a common endeavor to have a complete meson photoproduction database. With the new experimental data, theoretical analyses have also been updated which tend to suggest that new resonances should be incorporated in the nucleon spectrum and other resonances omitted. The available experimental results for kaon photoproduction will now be discussed in reference to the cross-section data first and then to polarization observable data.

1.6.1 Early Experiments

The first measurements of $\gamma p \to K^+\Lambda$ and $\gamma p \to K^+\Sigma^0$ were experiments from the 1960s, 1970s, and 1980s and relate to differential cross-section data. Before the modern technology of large acceptance spectrometers, small acceptance magnetic spectrometers were used. These experiments could detect a kaon, K^+, and would then identify hyperons using the well-known missing mass technique. Photon tagging was not available during these experiments, so other less precise techniques were used to determine the initial photon beam energy. These detectors were best used to measure the cross-section of kaon photoproduction, and multiple experiments were performed at DESY, Cornell, CalTech, MIT, SLAC, and elsewhere [26]. One experiment at DESY was carried out using a hydrogen bubble chamber developed by the Aachen-Berlin-Bonn-Hamburg-Heidelberg-Muenchen (ABBHHM) Collaboration [27]. The hydrogen bubble chamber could detect the K^+ and all charged particles of the hyperon decay, but could only operate at a very low rate. These early measurements together make up a total of 144 data points for the $K^+\Lambda$ differential cross-section in $\cos\theta$ and center-of-mass energy E_{CM} [28]. These data points, along with model calculations, can be seen in Fig. 1.6. The overall coverage of the data in energy and angle is meager, has low statistics, and large error bars, which makes the data not so useful for constraining model parameters.

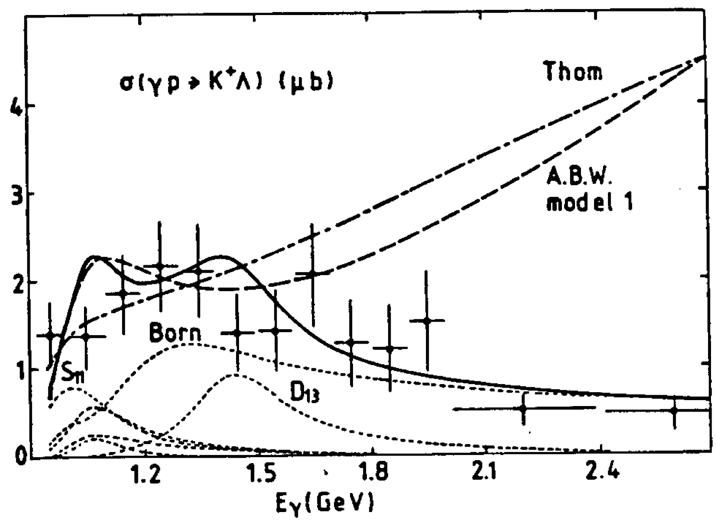

Figure 1.6: Data are from [27], and the curves are from models from that time [29]. Figure taken from [30].

1.6.2 Large Acceptance Spectrometers-SAPHIR Results

The first modern large acceptance spectrometer used in kaon photoproduction was the SAPHIR detector [31], which could collect data for photoproduction reactions on multiple final states including $K^+ + \Lambda$ and $K^+ + \Sigma^0$ over a wide range in angle and center-of-mass energy. SAPHIR was located at the Electron Stretcher Accelerator facility (ELSA) at the University of Bonn, Germany. SAPHIR had a photon tagging system that tagged photon energies from 53% to 90% of the incident electron beam endpoint energy. Particles were tracked by drift chambers surrounding the target, and had full angular coverage at both forward and backward angles. The drift chambers were then surrounded by scintillator hodoscopes that were capable of measuring time-of-flight. In the forward direction, an electromagnetic shower calorimeter could detect photons and a beam veto counter was included to prevent false triggers from photons not interacting with the target. The SAPHIR Collaboration published three sets of results for the $K^+\Lambda$ differential cross-sections and details may be found in [32–34]. The results of [34] were taken from the final run of SAPHIR in 1997-1998 and are plotted in Fig. 1.7. The results from SAPHIR provide a wealth of information, including trends of the differential cross-section in angle and center-of-mass energies. These results help for partial wave analyses of kaon reactions.

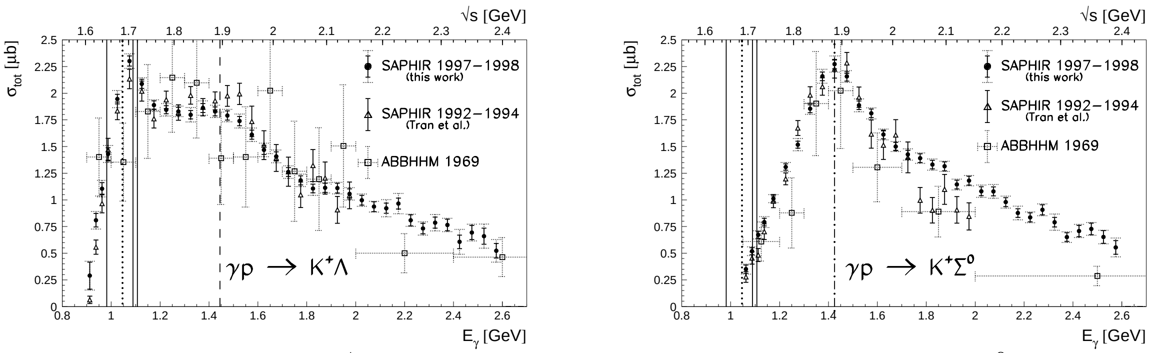

(a) for $\gamma p \to K^+\Lambda$ (b) for $\gamma p \to K^+\Sigma^0$

Figure 1.7: SAPHIR total cross section data from the data runs in 1992-1994 and 1997-1998 together with ABBHHM data [27]. The vertical *dotted* line indicates the $K^+\Sigma^0$ threshold energy, the *solid* lines the masses of known resonances $S_{11}(1650)$, $P_{11}(1710)$, and $P_{13}(1720)$, and the *dashed* line in plot (a) the position of the hypothetical $D_{13}(1895)$. Figure taken from [34].

This SAPHIR dataset has proven to be quite intriguing as their data showed a prominent structure in the $K^+\Lambda$ cross section data that was initially attributed to the $D_{13}(1895)$ resonance [35]. The necessity for a D_{13} resonance around 1900 MeV was disputed by B. Saghai [36], who argued that the bump in the cross section could be accounted for by off-shell contributions from excited hyperon exchanges. Subsequent theoretical models provided alternative explanations for this structure [19, 37–39], as discussed further in Section 1.6.3.

1.6.3 Large Acceptance Spectrometers-CLAS Results

After SAPHIR, the next large acceptance spectrometer to do high-precision, high-statistics measurements of multiple final states, including K^++Λ and K^++Σ^0, was the CEBAF Large Acceptance Spectrometer (CLAS) located at the Thomas Jefferson National Accelerator Facility (JLab) in Newport News, VA, USA. This detector system will be discussed in more detail in Chapter 2. In 2005, the CLAS Collaboration published differential cross-section results [40], which came from two Ph.D. analyses, [41] and [42].

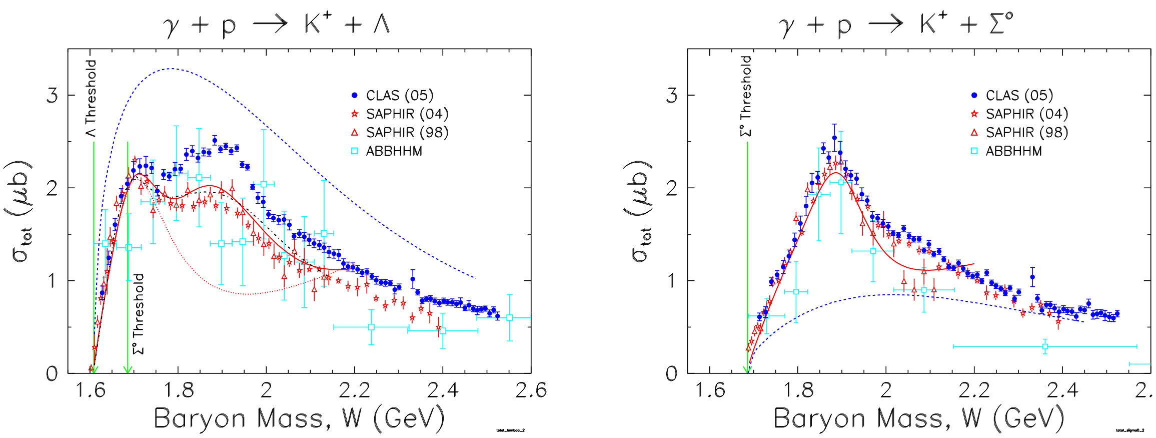

(a) for $\gamma p \to K^+\Lambda$ (b) for $\gamma p \to K^+\Sigma^0$

Figure 1.8: CLAS total cross section data from the CLAS-g1c run together with previous data from SAPHIR [33, 34] and ABBHHM [27]. Figure taken from [42].

These results were from the CLAS g1c experiment collected in late 1999 with a circularly polarized photon beam incident on an unpolarized liquid-hydrogen target. CLAS collected higher statistics than the SAPHIR experiment and could go higher in energy, from threshold up to 2.53 GeV. Despite CLAS having more statistics and finer binning than SAPHIR, the two datasets of the total and differential cross section can be compared. The $K^+\Sigma^0$ cross section data of SAPHIR and CLAS are in good agreement and can be seen in Fig. 1.8(b). However, the $K^+\Lambda$ cross section in Fig. 1.8(a) shows that the data from CLAS and SAPHIR do not agree and the CLAS results have an apparent bump in the cross section of $K^+\Lambda$ at $E_{cm} \approx 1.9$ GeV that is more noticeable than the bump of the SAPHIR data.

However, at energies near the threshold, there is an agreement of measured data between the $K^+\Lambda$ datasets. Furthermore, in 2010, more CLAS cross-section results were published [43]. Here, the bump or enhancement between 1.8 and 1.95 GeV can be seen again in the CLAS data in Fig. 1.9. This enhancement is important to understand and investigate further through measurements of polarization observables as this type of feature is suggestive of resonance production. This discrepancy between the CLAS and SAPHIR data sets is then problematic for partial wave analysis, as they are dependent upon this published data. Currently, there is still no resolution of this discrepancy between the SAPHIR and CLAS data.

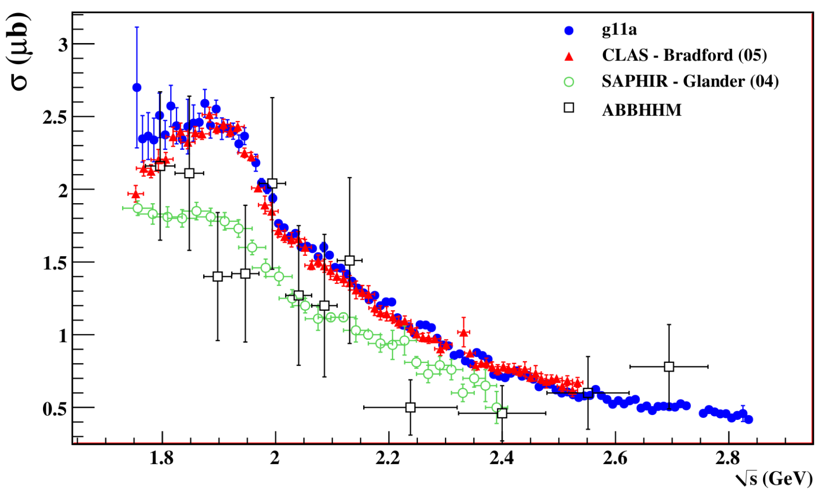

Figure 1.9: CLAS total cross section data for $\gamma p \rightarrow K^+\Lambda$ from CLAS-g11 data together with previous data from CLAS [40]. Figure taken from [6].

Comparison between CLAS and SAPHIR measurements of the differential cross section for $K^+\Lambda$ shows that the SAPHIR data is consistently lower than the CLAS data but no other systematic discrepancy Several structures that were apparent in previous measurements are confirmed by these results and can be seen in Fig. 1.10.

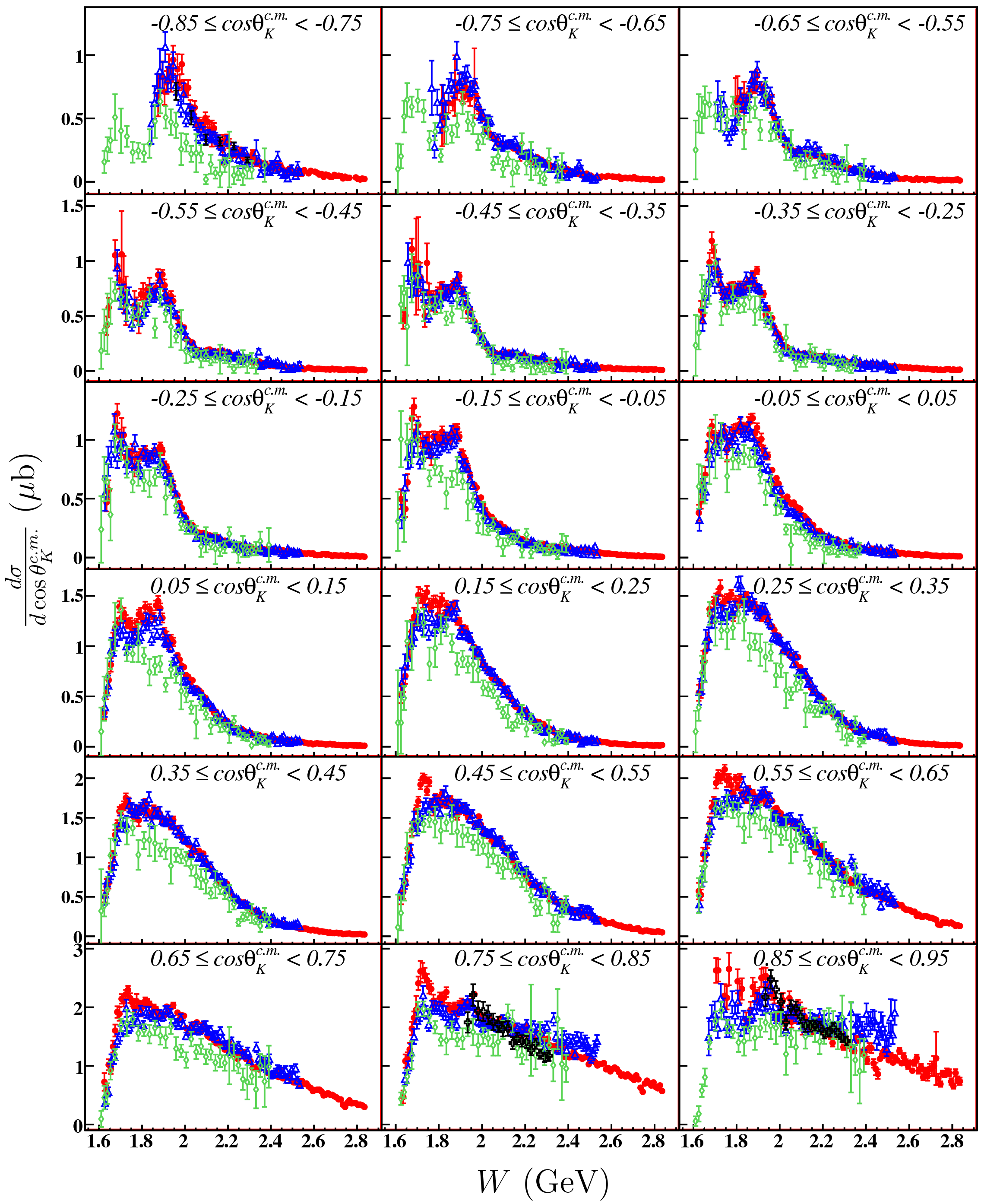

Figure 1.10: The differential cross-section for $\gamma p \to K^+\Lambda$ versus W in bins of cosθ is shown. CLAS-g11 data is the closed red circles, CLAS-g1c results are open blue triangles, SAPHIR results are open green diamonds, and LEPS results are open black crosses. Figure taken from [43].

1.6.4 LEPS Results

Another important effort studying $K^+\Lambda$ and $K^+\Sigma^0$ photoproduction is the LEPS experiment at the SPring-8 facility in Hyogo, Japan [44]. They measured differential cross-section data for $K^+ + \Lambda$ at both forward [45] and backward [46] K^+ angles. Although this data are not nearly as extensive as the CLAS or SAPHIR data, nonetheless, they can provide information that large acceptance detectors cannot provide, for example in the extreme angles that CLAS cannot measure as well. In Fig. 1.11(a), the forward angular bins of LEPS

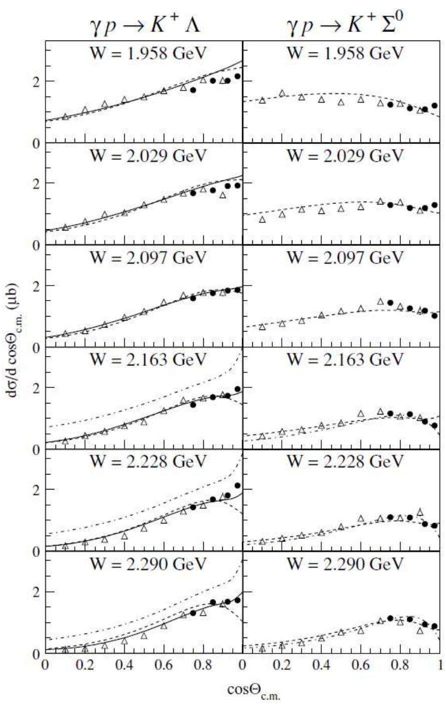

(a) Forward cross section

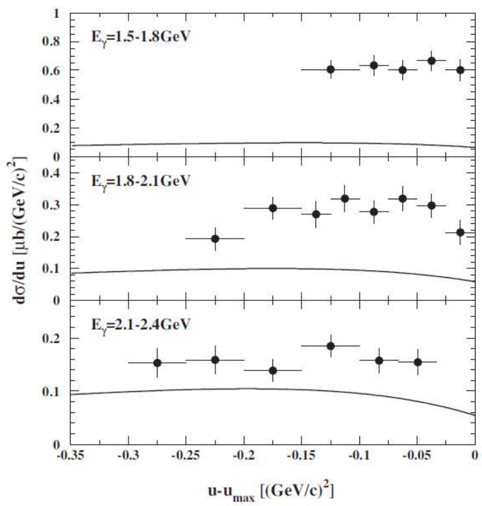

(b) Backward cross section for $K^+\Lambda$

Figure 1.11: Differential cross section for $\gamma p \to K^+\Lambda$ and $K^+\Sigma^0$ from LEPS. The closed circles are the LEPS results, open squares are SAPHIR, and open triangles from CLAS. (a) shows the forward cross section results and (b) shows the backward cross section results. Figures taken from [45, 46].

nicely overlap with the CLAS $K^+\Lambda$ and $K^+\Sigma^0$ results and confirm the CLAS measurements. However, in the backward angle the LEPS data agrees with the CLAS $K^+\Lambda$ data only up to 1.95 GeV and has a steeper decrease at higher energies, as shown in Fig. 1.11(b).

1.6.5 MAMI Results

Although several experiments have published kaon differential cross-section results, one should not consider the subject matter closed, especially as the CLAS/SAPHIR discrepancy has not been resolved. The results of a new experiment for $K^+\Lambda$ and $K^+\Sigma^0$ performed using the Crystal Ball calorimeter at MAMI-C in Mainz, Germany, were published in 2014 by Jude et al. [47].

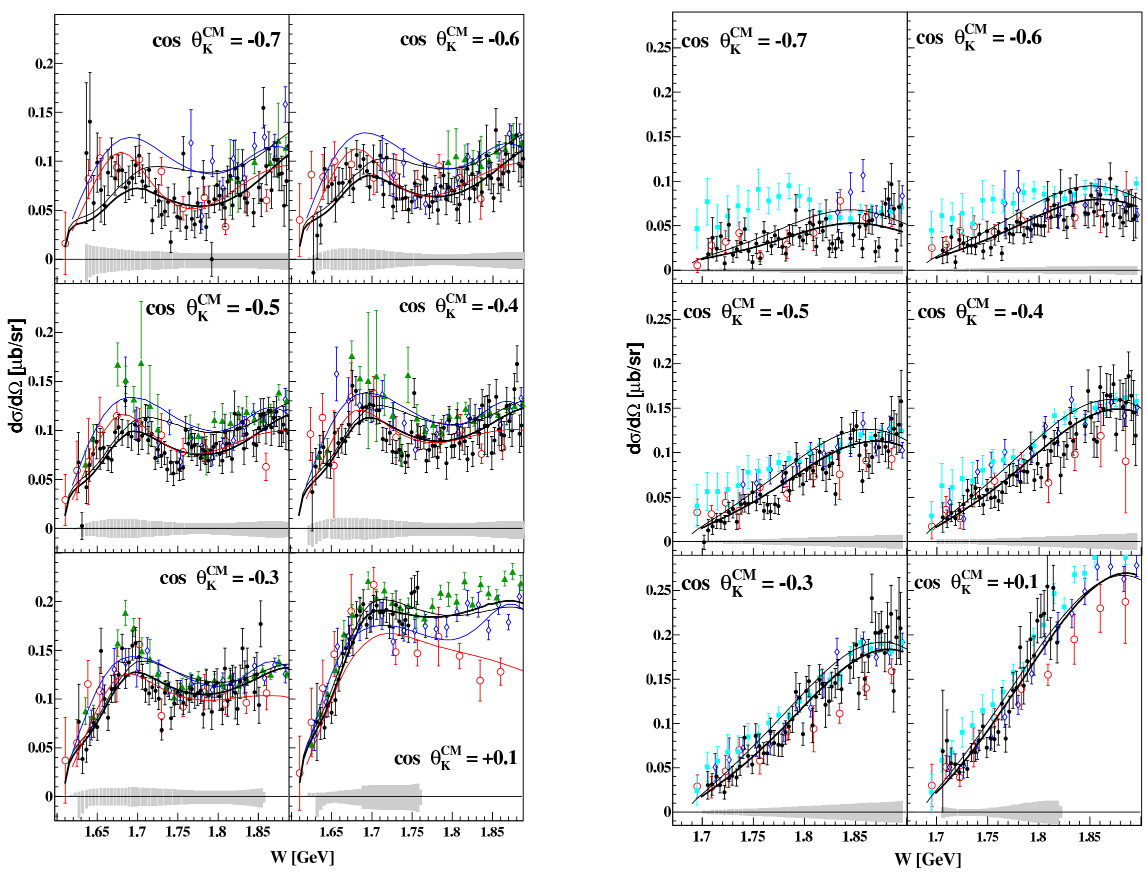

Figure 1.12: The differential cross-section for $\gamma p \to K^+\Lambda$ (left) and $\gamma p \to K^+\Sigma^0$ (right) versus W are shown. Black filled circles are MAMI data, red open circles are SAPHIR data, blue open diamonds are CLAS-Bradford data, green filled triangles are CLAS-McCracken data, and cyan solids squares are CLAS-Dey data. The thin black line is the BOGA 2011 model, the thick black line is BOGA 2012 model including these data, and the thin red and blue lines are fits from the KAON-MAID model to SAPHIR and CLAS data, respectively. Figure taken from [47].

The differential cross-section data presented by MAMI can be seen in Fig. 1.12, together with the results of several theoretical models, which are further discussed in Section 1.7. The data of MAMI show general agreement with the previously published data of $K^+ + \Lambda$ at backward angles and confirm the existence of the broad structure around 1670 MeV in the backward direction of the kaon production angle. With regards to $K^+ + \Sigma^0$, the MAMI differential cross-section data is consistent with the world data over most of the angular range, but the most backward direction shows a discrepancy between previous measurements. However, the MAMI data does have good agreement with the SAPHIR data as seen in Fig. 1.12. The results of Jude [47] provide valuable information about the existence and width of the $P_{11}(1710)$ resonance. Because of its fine binning in W these new data allow for further constraints on the existence of narrow structures in the cross-section that might arise from coupled-channels effects.

Now that previous differential cross-section experimental results have been discussed, it is important to review the previously measured polarization observables, as they are vital to discuss in comparison to the present work.

1.6.6 CLAS Results-Bradford

The polarization transfer observables C_x and C_z were measured by Bradford et al. [48] using the CLAS g1c data and were the first time any polarization observable of $K^+\Lambda$ has been measured with such precision. These observables are double polarization observables that trace the transfer of polarization from the incident circularly polarized photon to the recoiling hyperon. These observables were measured with respect to the x and z axes that lie in the production plane (as shown in Fig. 5.1). C_z measures the polarization transfer along the photon momentum direction and C_x measures the polarization transfer along the orthogonal direction. For the reaction $\gamma p \rightarrow K^+\Lambda$, the results of Bradford et al. show that for the Λ, the polarization transfer coefficient C_z along the photon momentum axis was measured to be near unity for a wide range of energy and kaon production angles as shown in Fig. 1.13.

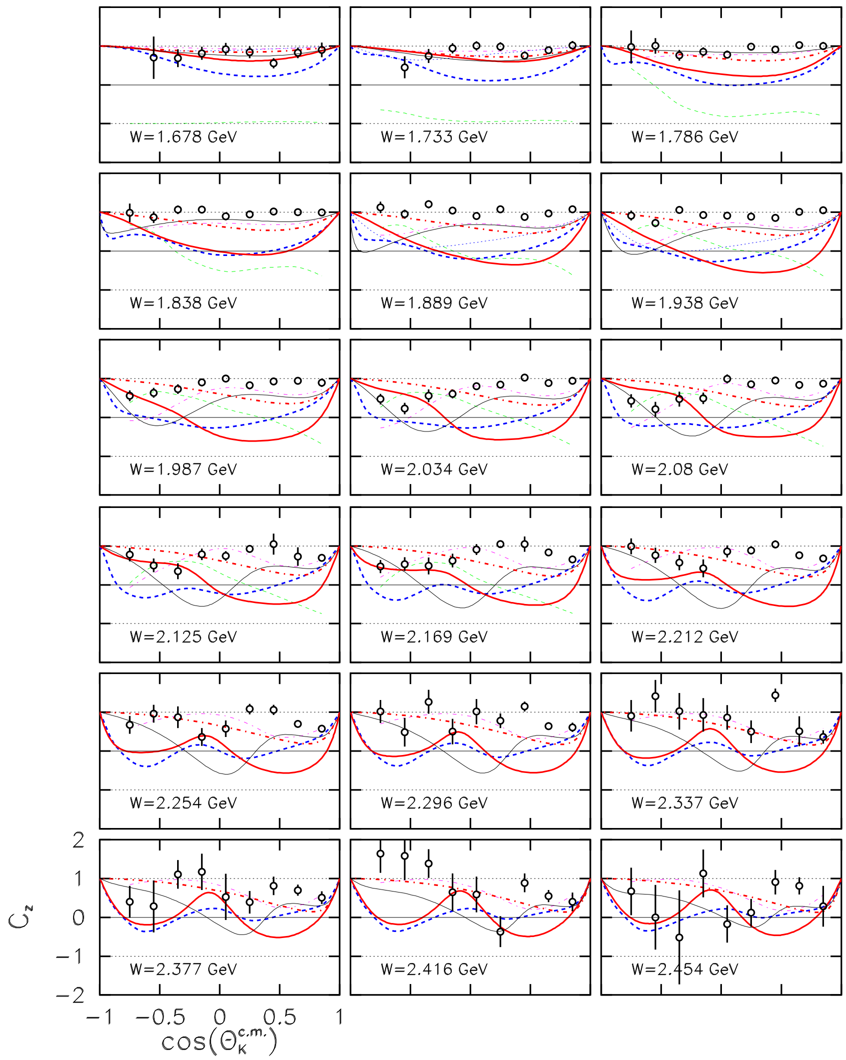

Figure 1.13: The observable C_z for $\gamma p \rightarrow K^+\Lambda$ plotted as a function of the kaon angle. The circles are Bradford results, the thin dashed green curves are KAON-MAID, the thick solid red curves are SAP, the thick dashed blue curves are BOGA, the thin solid black curves are RPR, and the thick dot-dashed magenta curves are Ghent. Figure taken from [48].

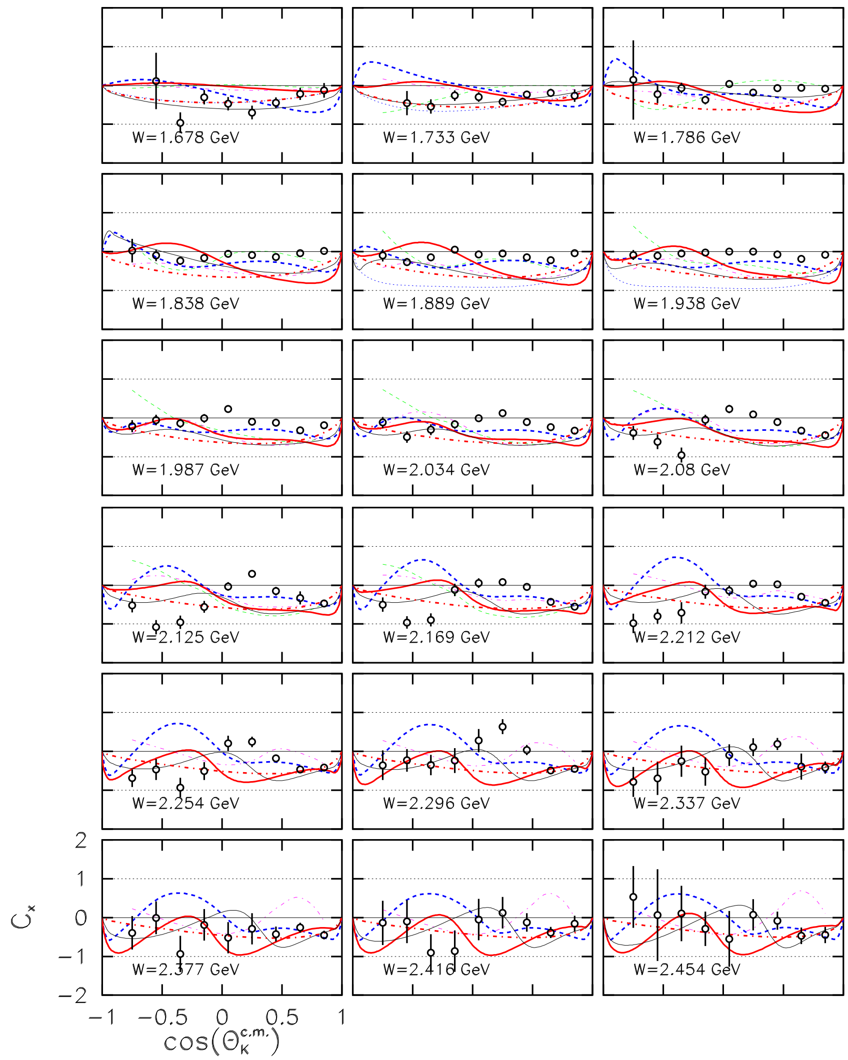

Figure 1.14: The observable C_x for $\gamma p \rightarrow K^+\Lambda$ plotted as a function of the kaon angle. The circles are Bradford results, the thin dashed green curves are KAON-MAID, the thick solid red curves are SAP, the thick dashed blue curves are BOGA, the thin solid black curves are RPR, and the thick dot-dashed magenta curves are Ghent. Figure taken from [48].

It is clearly shown in these results that the photon polarization is directly transferred to the Λ hyperon, along the spin direction of the photon, $\pm z$. C_z is roughly one from threshold up to 1.9 GeV regardless of the production angle of the kaon, which means that the Λ hyperon has almost all of the full polarization of the photon beam transferred to it along the beam direction. At higher values of W, C_z deviates from near unity as a function of the kaon center-of-mass production angle.

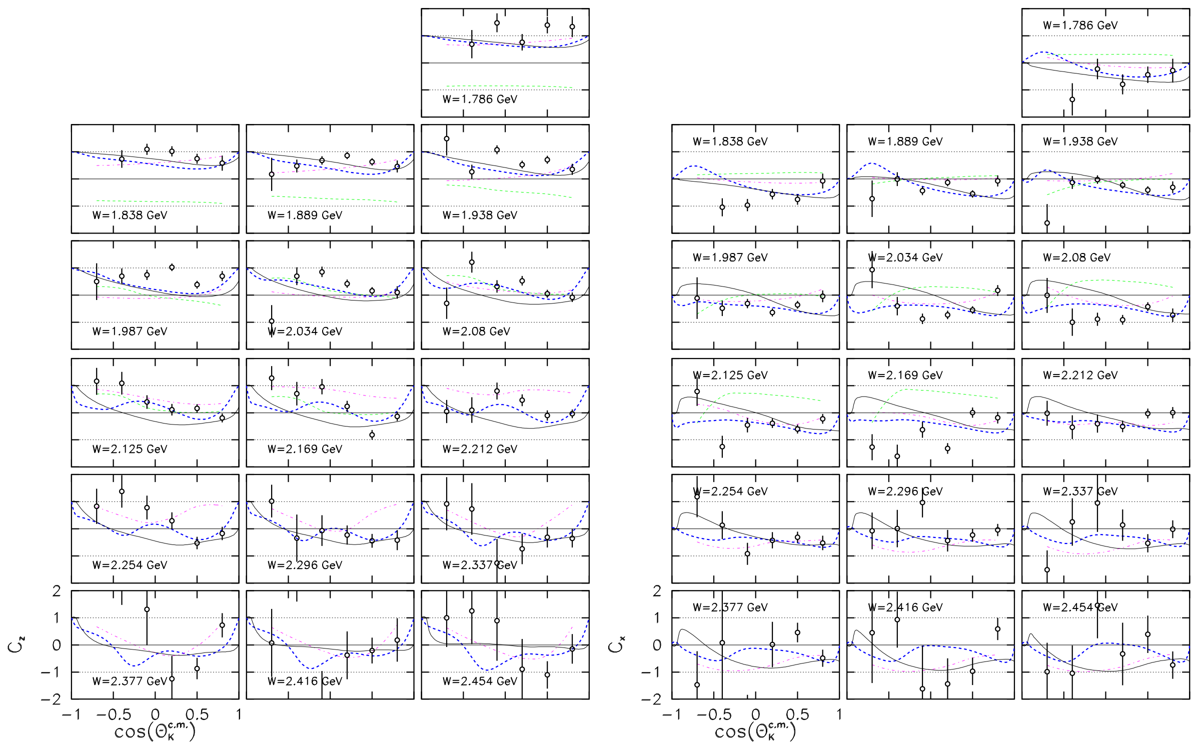

Figure 1.15: Results for $\gamma p \to K^+\Sigma^0$ for C_z (*left*) and C_x (*right*) plotted as a function of kaon angle. W is in bins of 50 MeV. Circles are CLAS-Bradford, thin-dashed green curve from KAON-MAID, thick-dashed blue curve BOGA, thin-solid back curves from RPR, and thick-dashed magenta dot curves are from Ghent. Figure taken from [48].

The associated transverse polarization coefficient C_x, shown in Fig. 1.14, has values close to zero, with negative values normally corresponding to high energies and both backward and forward kaon production angles [48]. The biggest conclusion drawn from these results was that the KY models [19, 37–39] had to include several resonances around 1900 MeV:

$P_{13}(1900)$, $P_{11}(1900)$ and/or $D_{13}(1900)$, where both P_{11} and D_{13} are 'missing' resonances and not included in diquark models [13–15]. The Ghent group [19] and Bonn-Gatchina group [38] obtained better results when including $P_{13}(1900)$, whereas the EBAC dynamical coupled-channels model [39] and the Giessen model [37] confirmed the $D_{13}(1960)$, which was postulated by T. Mart and C. Bennhold [35] with a mass of 1895 MeV to describe the SAPHIR cross section data.

Bradford also measured C_x and C_z for $\gamma p \rightarrow K^+\Sigma^0$ [48], but these data do not have the same precision as for $\gamma p \rightarrow K^+\Lambda$. Although Bradford used coarser binning for the Σ^0 reaction, the statistical precision of C_x and C_z, seen in Fig. 1.15, are still good.

1.6.7 CLAS Results-McCracken

The recoil Λ polarization for $\gamma p \rightarrow K^+\Lambda$ was measured at CLAS by McCracken et al. [43]. McCracken's results cover a wide center-of-mass energy range and kaon production angle range and are shown in Fig. 1.16. The Λ recoil polarization P_Λ, induced from an unpolarized photon beam is only allowed to be non-zero from parity conservation along the y-axis, which is perpendicular to the reaction plane. The angular resolution of the McCracken results is unparalleled by any other measurement.

In the forward direction, the reaction is known to be dominated by t-channel K^+ and K^{*+} exchanges, but the results of the recoil polarization is featureless with respect to center-of-mass energies. However, in the backward angles, a large positive Λ polarization is clear at center-of-mass energies around 2.0 GeV. At intermediate angles, the feature remains, but its magnitude is decreased.

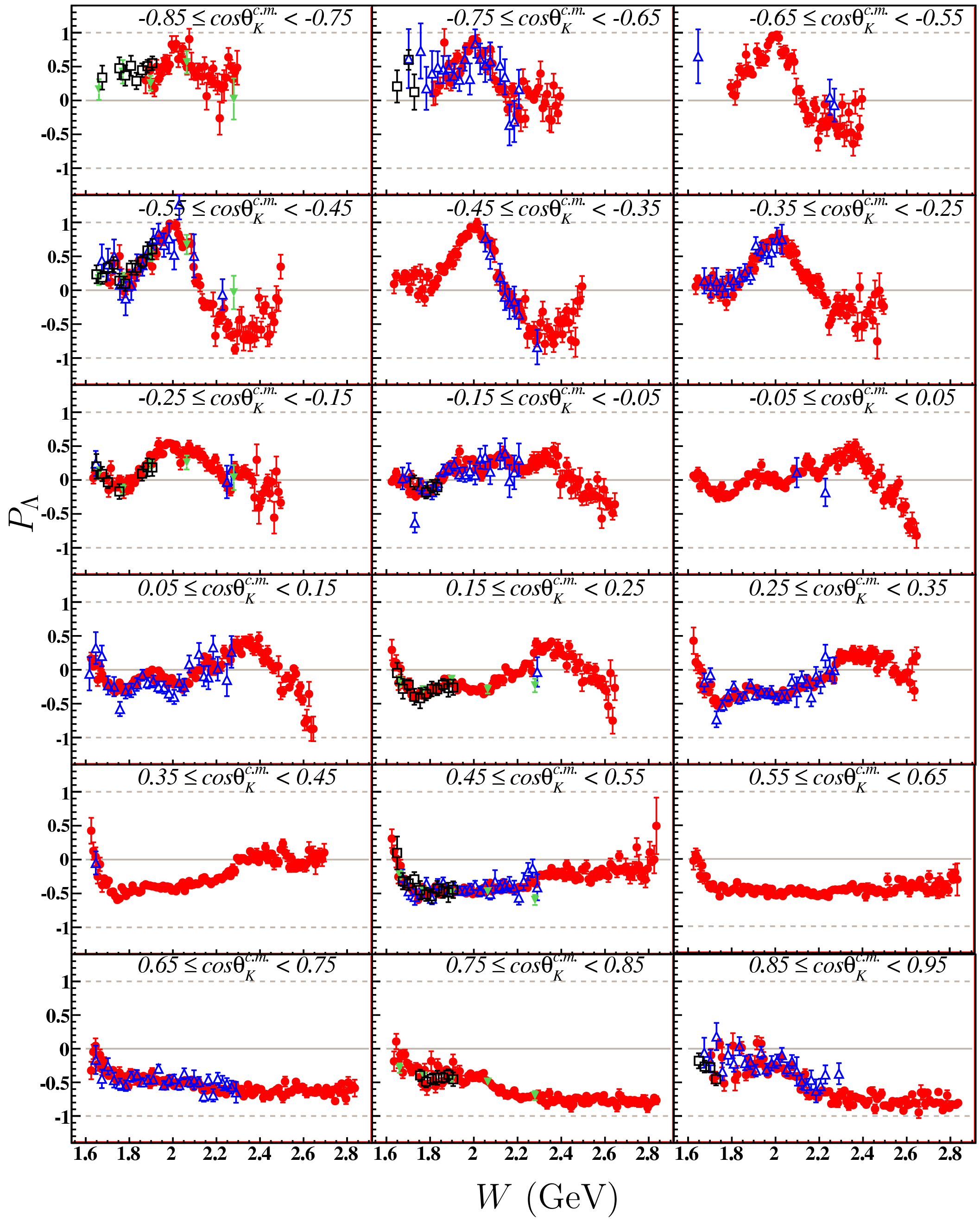

Figure 1.16: Recoil polarization P_Λ versus W in bins of $\cos\theta$. CLAS-McCracken results are red circles, CLAS-McNabb are blue triangles, SAPHIR are green triangles, and GRAAL are black squares. Figure taken from [43].

1.6.8 GRAAL Results

Several experiments measuring $\gamma p \to K^+\Lambda$ and $\gamma p \to K^+\Sigma^0$ have been performed at the GRAAL facility in Grenoble, France at the European Synchrotron Radiation Facility (ESRF) [49]. The publication by Lleres et al. [50] focused on measurements of polarized beam asymmetries and hyperon recoil polarizations for $\gamma p \to K^+\Lambda$ at several photon beam energies from threshold up to 1500 MeV with almost full angular coverage. The previously published results by LEPS only show the forward angles [45, 51], but one can see the overlap in Fig. 1.17.

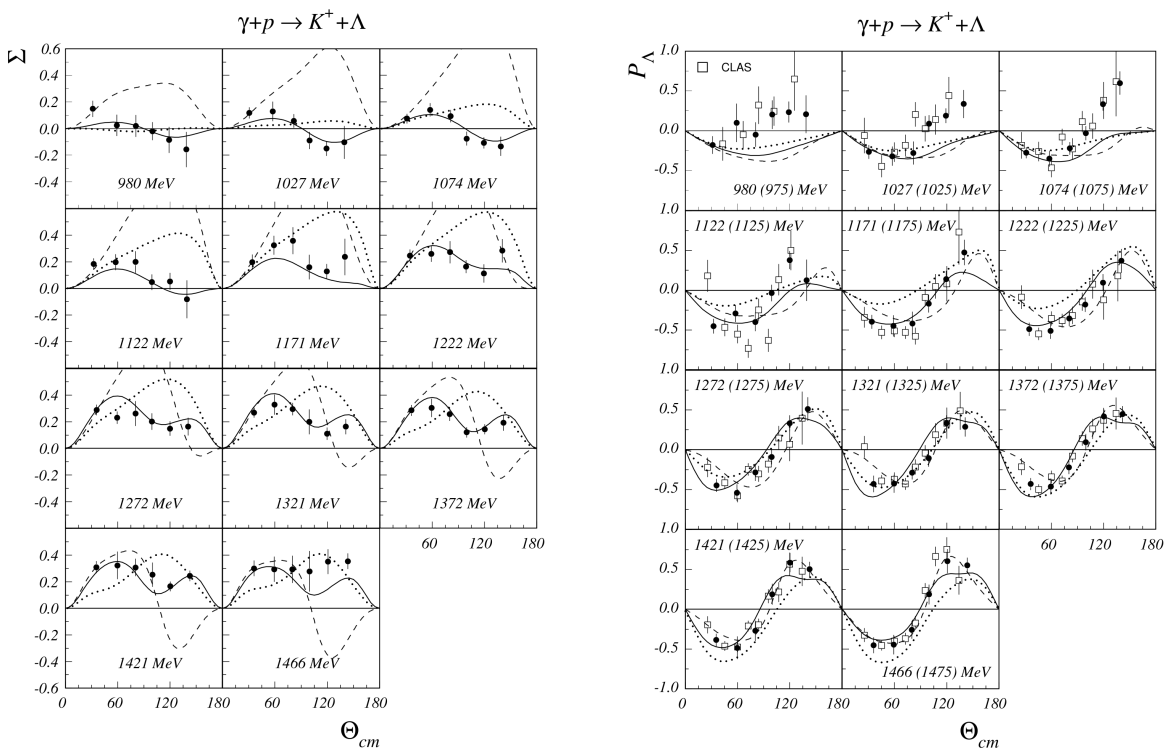

Figure 1.17: Angular dependence of the beam asymmetries Σ for $\gamma p \to K^+\Lambda$ (*left*) and P_Λ (*right*). GRAAL data are closed circles, CLAS data are open squares, BOGA model is the solid line, EBAC model [39] is the dashed line, and Giessen model [37] is dotted line. Figure taken from [50].

For the recoil polarization measurement, P, the data cover a similar range as the SAPHIR [34] and CLAS [43] data, with reasonable argument, as seen in Fig. 1.17. GRAAL also published results for the measurements of the beam-recoil observables O_x and O_z and the target asymmetry T for $\gamma p \rightarrow K^+\Lambda$ [52]. The conclusion by the Ghent [53] and BOGA [54] groups, drawn from the GRAAL results, was such that the resonances added to explain the Bradford results are more firmer and that both $P_{11}(1900)$ and D_131900 had to be added to describe the recent $K^+\Lambda$ and $K^+\Sigma^0$ data.

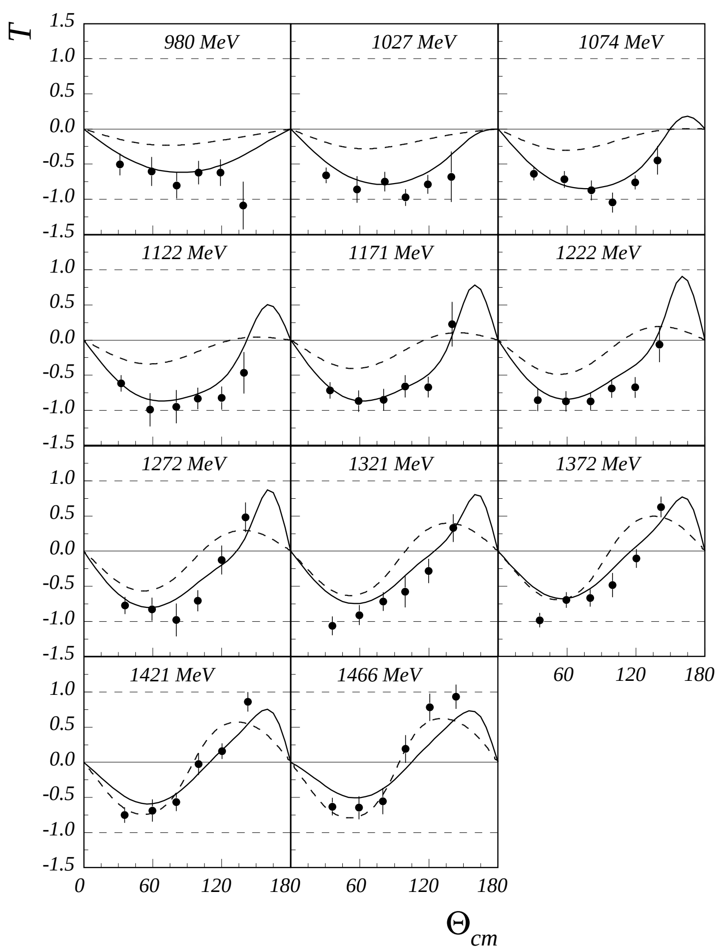

Figure 1.18: Angular dependence of the target asymmetry T for various photon energies. Data from GRAAL are compared to the BOGA model (solid line) and the RPR model (dashed line). Figure taken from [52].

The target asymmetry for GRAAL is particularly of interest here as it is one of the measurements upon which this analysis is focused. The biggest difference between GRAAL's measurement of the T asymmetry and this current analysis, is the way T is obtained. This current analysis is directly measuring the target asymmetry, while GRAAL extracted their measurements from double polarization data, and the relationship between O_x and O_z:

$$\begin{aligned} \rho_f \frac{d\sigma}{d\Omega} &= \frac{1}{2}\left(\frac{d\sigma}{d\Omega}\right)_u [1 - P_\gamma \Sigma \cos(2\phi_\gamma) + \sigma_{x'} P_\gamma O_x \sin(2\phi_\gamma) \\ &\quad + \sigma_{y'}(P - P_\gamma T \cos(2\phi_\gamma)) + \sigma_{z'} P_\gamma O_z \sin(2\phi_\gamma)] \ , \end{aligned} \tag{1.7}$$

where ρ_f is the density matrix for the Λ final state, P_γ is the polarization of the photon beam, and ϕ_γ refers to the azimuthal angle of the kaon relative to the beam polarization direction. The GRAAL T measurement covered the production threshold region and a large angular range and were compared to two separate models as can be see in Fig. 1.18.

1.6.9 Bonn Results

The first target asymmetry measurement for hyperon photoproduction was performed by Althoff et al. [55] at the University of Bonn, Germany, at the Bonn 2.5 GeV synchroton using a large aperture magnetic spectrometer. Data were taken at a fixed kaon center-of-mass production angle of 90° and at photon energies between 1.1 and 1.3 GeV. The Bonn measurement is crucial to the analysis that will be discussed here as the experimental setup in Bonn and in CLAS were quite similar. Both used a frozen-spin polarized target of the same material, butanol, and a magnetic spectrometer to measure the final state products. Despite publishing only three data points as seen in Fig. 1.19, these data points were measured directly like CLAS, whereas the results from GRAAL [49] were calculated using double-polarization data.

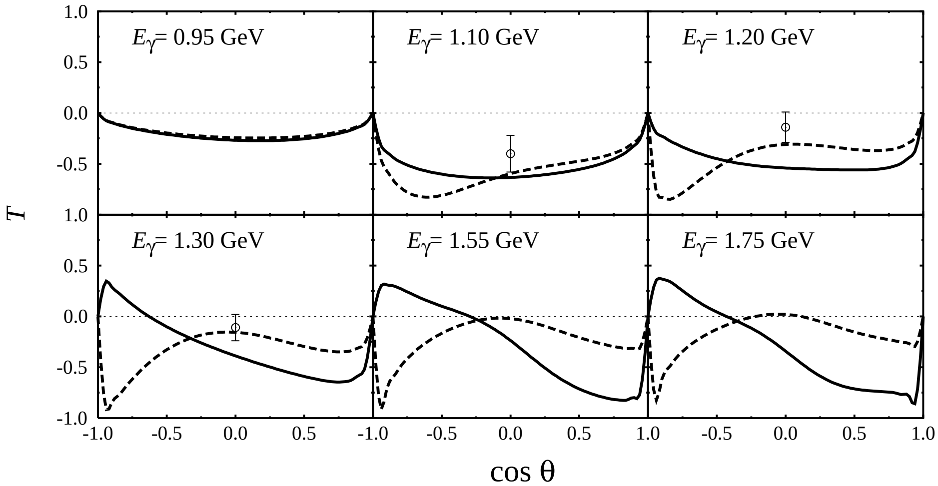

Figure 1.19: Target asymmetry T result for $\gamma p \rightarrow K^+\Lambda$ from Althoff with KAONMAID (Mart-Bennhold) calculations, *dashed* line is without $D_{13}(1900)$, *solid* curve with $D_{13}(1900)$. Figure taken from [35].

1.7 Theoretical Models

Since baryons and their excited states cannot be fully calculated within QCD, models are used to describe the phenomena observed in the data and to predict transition amplitudes and observables in kinematic regions that have not been measured yet. Such descriptions use effective hadronic degrees of freedom instead of the fundamental quark and gluon degrees of freedom. There are numerous models readily available, but those that serve the greatest interest to this analysis are the KAON-MAID model [16], the Bonn-Gatchina model [17], and the Ghent model [18, 19].

Some models follow a field-theoretical approach using effective interaction Lagrangians that reflect symmetry properties and conservation laws. Form factors are introduced to account for the finite size of hadrons. In addition, the reaction dynamics must be restricted as complicated higher-order terms might contribute significantly to the transition amplitudes (i.e. the $\mathcal{F}_i$ or b_i in eqn. 1.4 and Table 1.4). The isobar approach used by the KAON-MAID group and the Ghent group restricts the dynamics to tree-level amplitudes, consisting of two interaction vertices and one propagator, which reflects the class of exchanged particles.

For kaon production, the propagator can describe the exchange of a non-strange baryon $(N, N^\star, \Delta, \Delta^\star)$ in the s-channel, or the exchange of a hyperon $(Y, Y^\star)$ in the u-channel, or the exchange of a meson $(K, K^\star, K_1)$ in the t-channel. s, u, and t refer to the invariant Mandelstam variables $s = (P_\gamma + P_p)^2$, $t = (P_\gamma - P_K)^2$, and $u = (P_p - P_K)^2$, where P_γ, P_p, P_K are the four-vectors of the beam photon, target proton, and kaon, respectively.

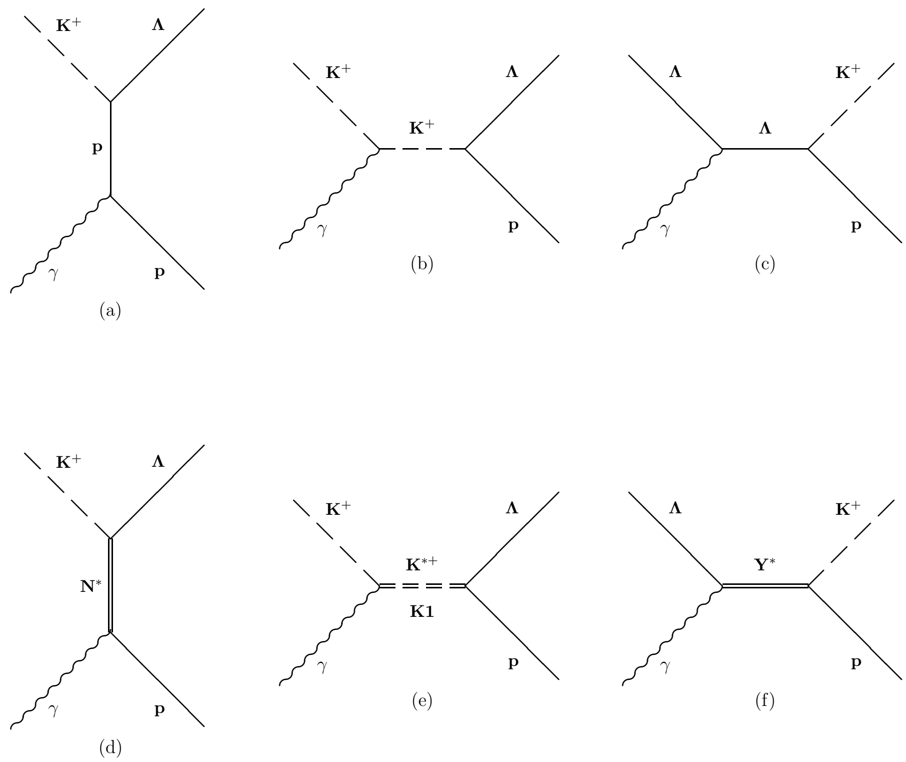

Figure 1.20: Feynman graphs for contributing processes to $\gamma p \to K^+\Lambda$ in lowest order: Born contributions to s–exchange (a), t–exchange (b), and u–exchange (c), and resonance terms for s– (d), t– (e), and u– (f) exchange as used in Isobar models. The corresponding diagrams are similar for $\gamma p \to K^+\Sigma^0$ where both N^* and Δ^* terms contribute in the s–channel.

Figure 1.20 depicts the tree-level Feynman diagrams used in isobar models. The top row shows the so-called Born term diagrams, meaning the exchange of (virtual) ground-state hadrons (p, K, Λ, Σ). The bottom row shows diagrams for the exchange of excited states in the s, t, and u channel, respectively. The kinematics of photoproduction allows the intermediate state in the $N^\star$ and $\Delta^\star$ exchange to be on the mass shell, which means that the propagator goes through a pole and produces a resonant structure. The propagators in the other diagrams in Fig. 1.20 cannot reach their resonant poles in photoproduction. Most coupling constants in the isobar approach are not fixed by fundamental relations but must be determined from fitting to existing data. Such a phenomenological analysis has the disadvantage that resonant and background contributions are correlated since the parameters are fitted simultaneously or kept fixed based on theoretical constraints.

A weakness of the isobar approach is its restriction to a specific reaction channel, where requirements from unitarity and gauge invariance arise as complications to consider [56]. On the other hand, a coupled-channels approach like the Bonn-Gatchina model takes into consideration all possible meson–baryon channels; in practice however, existing data are restricted to a few pion- and photoproduction channels, making it complicated to constrain the model parameters. This is particularly true for strangeness production where the world database of measured observables is still rather limited.

1.7.1 KAON-MAID

KAON-MAID is a theoretical calculative model that is maintained by the Institut für Kernphysik at the University of Mainz, Germany [16]. Although severely outdated as it has not been updated since 2000 [57], the model is still worth mentioning as it was one of the first isobar models that described the forward peaking and simultaneous decrease of the cross section above 2 GeV. Older models, like those shown in Fig. 1.6, show an exponential increase of the cross section at higher energies.

The KAON-MAID group has presented a tree-level model of kaon photoproduction that includes hadronic form factors at the vertices with gauge invariance using SU(3) values for the Born couplings, non-resonant propagators, and a set of resonances that are consistent with previous analyses, such as $S_{11}(1650)$, $P_{11}(1710)$, $P_{13}(1720)$, $D_{13}(1900)$. It has detailed model predictions, not only for the differential cross-section for $\gamma p \rightarrow K^+\Lambda$ and $K^+\Sigma^0$, but also for all polarization observables. KAON-MAID is an isobar model with final-state interactions. The group extended the model to reactions on light nuclei [58,59] and studied the sensitivity of the observables to the hyperon-nucleus final state interaction. Those observables that are insensitive to distortion effects make them excellent tools to search for modifications of the basic amplitude. One of the goals of KAON-MAID is to find the kinematic range of the distortion effects, which also allows one to establish the sensitivity of polarization observables to the elementary amplitude, but are not affected by relativistic effects or particular nuclear targets. Their results can be seen in Fig. 1.19, but as previously mentioned, the model has not been updated in almost 15 years. However, the author has discussed the results with Terry Mart, a member of the KAON-MAID group, and he expects that the model will be updated in due course once these current results are published in their entirety [60].

1.7.2 Bonn-Gatchina

The Bonn-Gatchina group (BOGA) is a theoretical group similar to KAON-MAID, but has been actively developing their model over the past several years to establish more accurate constraints based on recently published data [38, 54, 61]. Maintained by both the Helmholtz-Institut für Strahlen und Kernphysik at the University of Bonn, Germany, and the Petersburg Nuclear Physics Institute in Gatchina, Russia, they updated their solutions in 2010, 2011, and 2012, the latter being the most current. The main difference in the last two models is that they differ in the number and properties of some positive-parity nucleon resonances at masses above 1.9 GeV. Table 1.5 shows the data from around the world for kaon photoproduction that BOGA has utilized. Instead of using an isobar model like KAON-MAID, BOGA employs the partial wave analysis method in a coupled-channels approach. Resonances are introduced as Breit-Wigner functions. For resonances with strong coupling to several channels the K-matrix formalism is used. Using a PWA is difficult due to the fact that many partial waves can contribute in certain regions and overlap, which makes the waves more difficult to disentangle, but with more world data forthcoming, in the end PWA will be accurate. The newest version (2011-02) of the models finds significant coupling to $K^+\Lambda$ from the following resonances: $S_{11}(1650)$, $P_{11}(1710)$, $P_{13}(1720)$, $D_{13}(1875)$, $P_{11}(1880)$, $S_{11}(1895)$, $P_{13}(1900)$, $F_{15}(2000)$, $D_{13}(2150)$, and $G_{17}(2190)$, and the following resonances couple to $K^+\Sigma^0$: $S_{11}(1650)$, $P_{11}(1710)$, $P_{13}(1720)$, $D_{13}(1875)$, $P_{13}(1900)$, $S_{31}(1900)$, $F_{35}(1905)$, $P_{31}(1910)$, $P_{33}(1920)$, $F_{37}(1950)$, and $D_{15}(2060)$ [61].

Table 1.5: Hyperon photoproduction observables fitted in the coupled-channel analysis and χ^2 contributions for the solution BG2011-02 [54].

$\gamma p \to K^+\Lambda$	Observ.	N_{data}	χ^2_i/N_{data}
[43] CLAS	$d\sigma/d\Omega$	1320	0.69
[51] LEPS	Σ	45	2.11
[50] GRAAL	Σ	66	2.95
[43] CLAS	P	1270	1.82
[50] GRAAL	P	66	0.59
[52] GRAAL	T	66	1.62
[40] CLAS	C_x	160	1.52
[40] CLAS	C_z	160	1.58
[52] GRAAL	$O_{x'}$	66	1.95
[52] GRAAL	$O_{z'}$	66	1.66

$\gamma p \to K^+\Sigma^0$	Observ.	N_{data}	χ^2_i/N_{data}
[62] CLAS	$d\sigma/d\Omega$	1590	1.44
[51] LEPS	Σ	45	1.23
[52] GRAAL	Σ	42	1.99
[62] CLAS	P	344	2.69
[40] CLAS	C_x	94	1.95
[40] CLAS	C_z	94	1.66
$\gamma p \to K^0\Sigma^+$	Obsv.	N_{data}	χ^2_i/N_{data}
[63] CLAS	$d\sigma/d\Omega$	48	3.84
[64] SAPHIR	$d\sigma/d\Omega$	160	1.91
[65] CBT	$d\sigma/d\Omega$	72	0.76
[66] CBT	$d\sigma/d\Omega$	72	0.62
[65] CBT	P	72	0.90
[66] CBT	P	24	0.94
[66] CBT	Σ	15	1.73

1.7.3 Ghent Regge-Plus-Resonance Model

The characteristic dominance of non-resonant t-channel contributions at higher energies is well described using t-channel propagators that exchange a family of particles with the same quantum numbers but different masses, i.e. a series of excited states of a meson. The framework that has been successfully employed in high-energy physics to describe the data for many reaction channels is called Regge theory [67]. It fulfills the theoretical requirements of analyticity, crossing symmetry and unitarity, and requires only a few free parameters to be fitted to the data.

The RPR (Regge–Plus–Resonance) model of the University of Ghent, Belgium group [18,19,68] uses an extrapolation of the Regge approach to lower energies for the $K(0^-)$ and $K^\star(1^-)$ families. This can reliably account for the background processes in kaon photoproduction. Mixed with an isobar model to account for s-channel processes, this model shows a good description of the low-energy data and of the transition to the high-energy regime using only a small number of $N^\star$ and $\Delta^\star$ resonances in the s-channel. The following N^* resonances are included in the newest version, RPR-2011: $S_{11}(1535)$, $S_{11}(1650)$, $F_{15}(1680)$, $P_{11}(1710)$, $P_{13}(1720)$, $D_{13}(1900)$, $P_{11}(1900)$, and $F_{15}(2000)$ [53]. The group also studies the most probable set of resonances to be included, given the currently available $K^+\Lambda$ data, and introduced a penalty term for a model's parameter space dimensionality. In this case, the optimal set of resonances coupling to $\gamma p \to K^+\Lambda$ is: $S_{11}(1535)$, $S_{11}(1650)$, $P_{11}(1710)$, $P_{13}(1720)$, and $D_{13}(1900)$.

1.8 Summary

This chapter has described the need for a more detailed exploration of the Constituent Quark Model. It has also described the results from various experiments around the world and the theoretical models that have been developed. The data from these experiments has added greatly to the knowledge of $\gamma p \to K^+ + \Lambda$ and $K^+ + \Sigma^0$, but it is still not enough. To some extend, the presentation focused on the $K\Lambda$ channel and did not discuss the recent precision data from CLAS [62] for $\gamma p \to K^+\Sigma^0$. However, the discussion on 'missing resonances' does not relate to the $K^+\Sigma^0$ since the spectrum has been well described by excitation of known resonances. It was pointed out that the picture of the nucleon spectrum is incomplete, and this analysis will be another piece necessary to complete the puzzle. The following chapters will discuss more in detail about the polarization observables extracted in this analysis and how they are obtained, the high-precision results, and what can be gained from these new data.

Chapter 2

Experimental Setup

In this chapter, the facility and experimental setup that was used to collect the data for this analysis will be described. The data were taken in Hall B during the g9b running period from March of 2010 through August of 2010 at JLab, in Newport News, Virginia. The experimental Hall B housed the CEBAF (Continuous Electron Beam Accelerator Facility) Large Acceptance Spectrometer (CLAS) and the frozen spin target (FROST). This analysis was part of experiment E-02-112, "Search for Missing Nucleon Resonances in the Photoproduction of Hyperons using a Polarized Photon Beam and a Polarized Target" [69]. Data were taken using a photon beam with both circularly and linearly polarized photons. More details will be described in the following sections.

2.1 CEBAF

The CEBAF accelerator at JLab delivers continuous electron beams to the three different experimental end stations: Halls A, B, and C. After construction was completed in 1996, CEBAF was the first continuous electron accelerator in the medium-energy regime (> 500 MeV). An aerial view of JLab can be seen in Fig. 2.1. CEBAF provides high-luminosity electron beams up to an energy of 6 GeV in a racetrack configuration, 7/8 of a mile in circumference, with multiple liquid helium cooled niobium cavities that form an anti-parallel pair of superconducting radio-frequency linear accelerators, or linacs, maintaining a full-energy beam current of up to 200 μA. The two linacs are along each straight section of the facility and the two re-circulation arcs that guide the electrons between the linacs are along the curved sections of the facility [70].

Figure 2.1: An aerial view of CEBAF is shown with the race-track configuration of the accelerator. Hall B is seen at the bottom of the figure, in the middle of the three mounds (circular grass-covered hills), between Halls A and C. Figure taken from [71].

Each linac has 169 accelerating cavities immersed in liquid-helium to keep them cooled to a temperature of 2 K, which makes them superconducting [70]. Two cavities are sealed hermetically to each other and installed in the linac as a cyro unit, where four of the units make up an 8.25 m, eight-cavity cyromodule. Each cyromodule, as seen in Fig. 2.2, is connected to the next via a beam vacuum pipe, vacuum pumps and valves, quadrupoles, and steering dipoles [72].

Figure 2.2: A cryomodule cavity shown before installation. Figure taken from [71].

The electrons are produced in bunches in the 45 MeV injector. Three lasers, pulsed at 499 MHz and 120° out of phase, are incident on a gallium arsenide (GaAs) photocathode. The knocked electrons are accelerated at first by an anode. The pulsing of the laser results in the bunching of the electrons into beam 'buckets', spaced at 2.004 ns for each hall. Once the electrons are accelerated through two of the cavities, they are sent through the linacs as seen in the schematic view of the lab in Fig. 2.3. [72]

Each linac has a maximum of 600 MeV of acceleration capability. The recirculation arcs on either ends of the linacs allow the electron beam to make up to five passes through the linacs for a maximum final electron beam energy of approximately 6 GeV. The recirculation arcs have a series of dipole magnets that produce a field, that bends the electron beam from linac to linac. The beam is divided into five sub-beams by energy such that electrons of different energies can pass through a different set of dipole magnets as it makes passes

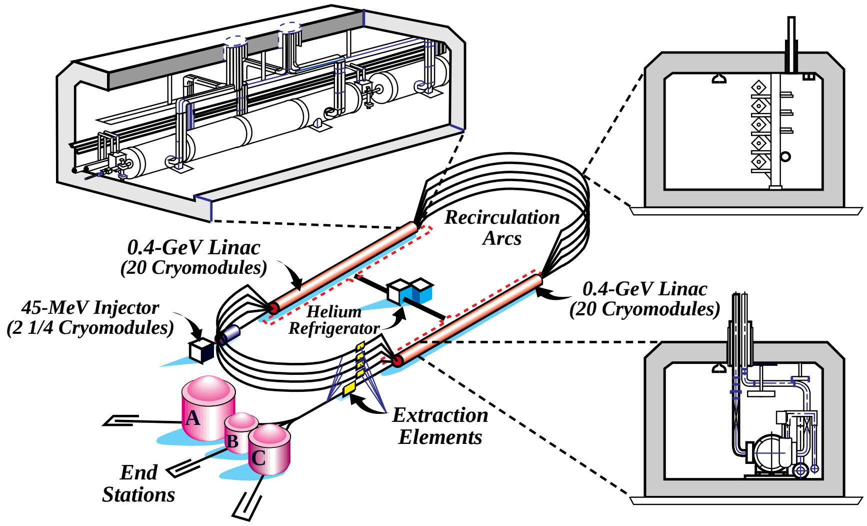

Figure 2.3: A schematic view of CEBAF. Figure taken from [71].

through the accelerator. These sub-beams are combined again as they reenter the linacs. Once the beam has passed through the accelerator the desired number of times, it can be sent to one of the three experimental halls via RF separator cavities that use 120° phase separations to direct specific beam 'buckets' to the beamline that are directed into the different experimental halls. All three halls can take beam at the maximum energy, but due to the extraction system design, two halls cannot receive beam on the same pass for lower energies. [72]

2.2 Hall B

Hall B, as seen in Fig. 2.4, is the smallest of the three end stations at JLab and until 2012 housed the CLAS detector, which could be used to study photo- and electro-induced nuclear and hadronic reactions. A new detector, CLAS12, is under construction as a part of JLab's upgrade to a 12 GeV electron beam. A schematic view of Hall B can be seen in Fig. 2.5. Also within Hall B is a photon tagging beamline, which along with CLAS makes real photon experiments possible. The detector and beamline are described in the following subsections.

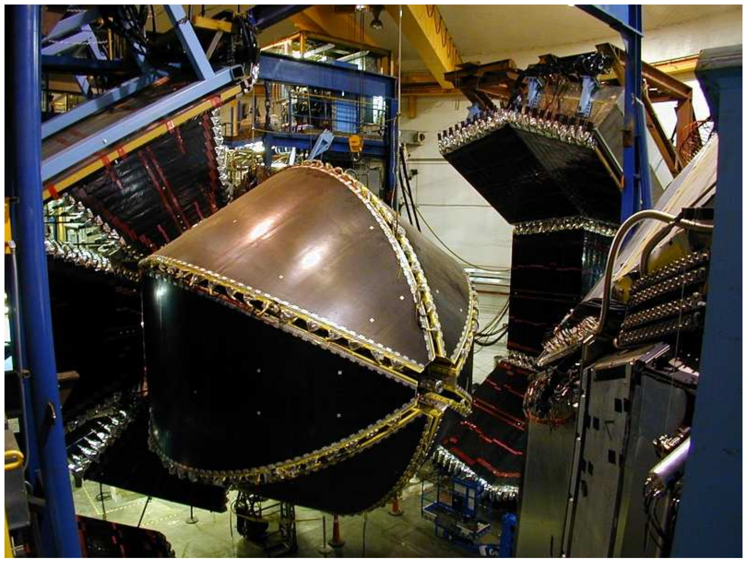

Figure 2.4: The inside of Hall B with CLAS spread open for servicing. The round item in the middle is the outer face of the Region 3 drift chamber. The TOF detectors surround the chambers during physics running. Figure taken from [71].

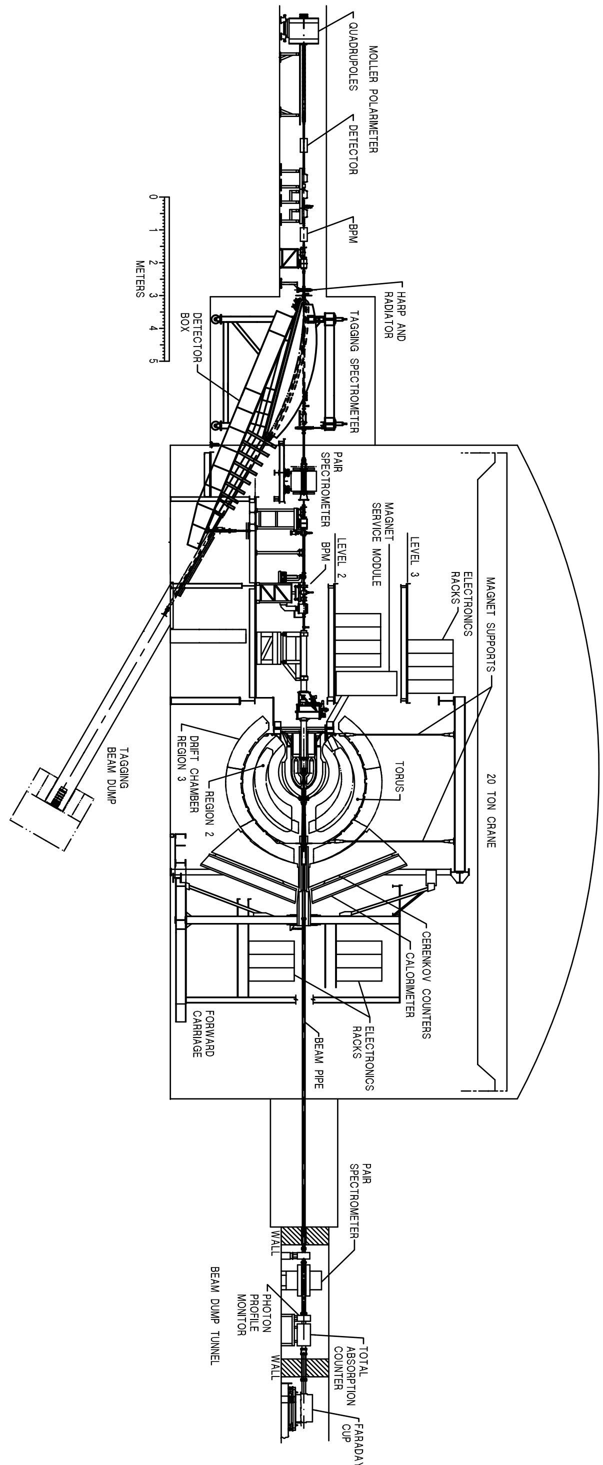

Figure 2.5: The schematic diagram of Hall B is shown. Figure taken from [71].

2.3 Photon Tagger

The electron beam is split between the three end stations. As the electron beam enters Hall B through the extraction beamline, it passes through the desired radiator (depending on the specific photon beam desired, such as circularly or linearly polarized photon beam), and enters the tagger magnetic spectrometer, which deflects the full-energy electron beam to the dump. These elements of the Hall B photon tagging system result in the production of the photon beam and allow for measurement of the photon energy [73], which is necessary for later analysis. The radiators are used to produce the photon beam and the tagger magnetic spectrometer allows for bending the electron beam away from the beamline into a beam dump. The tagger magnetic spectrometer is a dipole producing a maximum magnetic field of 1.75 T. The tagger magnet maximum field is the field value required to transport a 6 GeV beam along the full-energy orbit to the beam dump. Once the electron has radiated a bremsstrahlung photon and lost energy, the tagging hodoscope allows for measurement of the electron timing and energy, which then allows to calculate the associated photon energy. The tagging spectrometer measures the energy of the bremsstrahlung recoil electrons, thus providing the photon energy according to:

$$E_\gamma = E_0 - E_e, \tag{2.1}$$

where E_γ is the energy of the photon, E_0 is the energy of the electron from the accelerator, and E_e is the energy of the scattered electron after bremsstrahlung. A schematic view of the tagger is shown in Fig. 2.6.

In addition, these measurements allow for the determination of the event start time or the time of the interaction of the photon at the FROST target located within the CLAS detector. It should be noted that for electron runs, the tagging system is not used as photons are not being produced.

The electrons interact with the radiator and, as bremsstrahlung photons are produced,

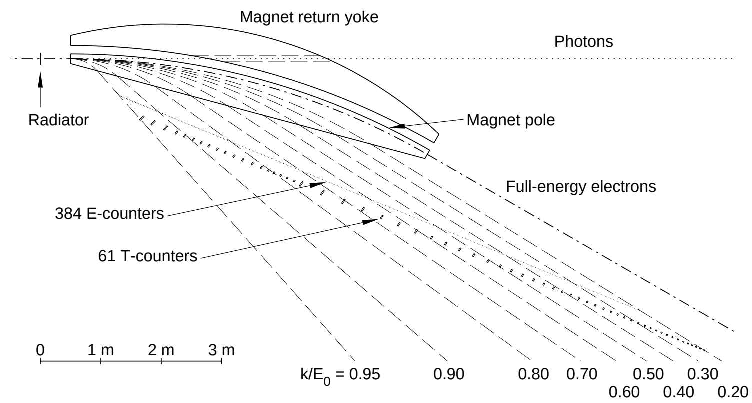

Figure 2.6: Schematic view of the tagger is shown here. Figure taken from [71].

the electrons travel along as well. Then, the electrons are bent away towards the tagger hodoscope by the tagger magnetic spectrometer, allowing the photons to continue to the collimators and the target, which is inside the CLAS detector. Those electrons that did interact with the radiator have less than their initial energy, E_0. Electrons with energy between 5% to 80% of E_0 are detected in two hodoscope planes. The upper hodoscope, designated the E-plane, has 384 scintillator paddles that are 20 cm in length, 4 mm thick, and varying widths between 6 and 18 mm. Each scintillator paddle, referred to as an E-counter, is readout via a photomultiplier tube (PMT) and is connected to a multi-hit TDC. The E-counters are arranged to be overlapping to give 767 bins, each having an energy width of 10^{-3} of E_0.

The lower tagger hodoscope plane, referred to as the T-plane, gives a good timing resolution. The T-plane has 61 scintillator paddles overlapped slightly to provide for 121 bins. Each paddle, or T-counter, employs double-sided PMT readout with each PMT connected to a discriminator and a pipeline TDC. The T-counter widths were chosen to define two photon effective regions: 75-95% of E_0 (T-counters numbered T1-T19) and 20-75% of E_0 (T-counters numbered T20-T61). The counters in the beginning range allow for higher rates near the bremsstrahlung endpoint where lower photon energies are not of interest. The T-counter paddles are 2 cm thick and have a timing resolution of $\approx$ 110 ps. This allows for successfully identifying the correct beam bucket with which to associate every photon so that the RF time for that bucket may be correlated with a particle detected in CLAS to calculate the event vertex time. Further details about the tagger system may be found in Ref. [73].

2.3.1 Circularly Polarized Photon Beam

The circularly polarized photon beam of the g9b running period was produced when a longitudinally polarized electron beam was incident on a thin gold foil radiator of thickness 10^{-4} radiation lengths. Gold has a high atomic number, which reduces the background from electron-electron scattering in production of photons via bremsstrahlung radiation [5]. The produced photons will have circular polarization proportional to the longitudinal polarization of the electron beam [74], see equation 2.2. Further details about the beam polarization are in Section 2.5.3. The helicity of the electron beam was reversed at a rate of 30 Hz so that both helicities appear in the same data run, as will be discussed more in Section 5.2. The photon bremsstrahlung energy spectrum for the experiment can be seen in Fig. 2.7.

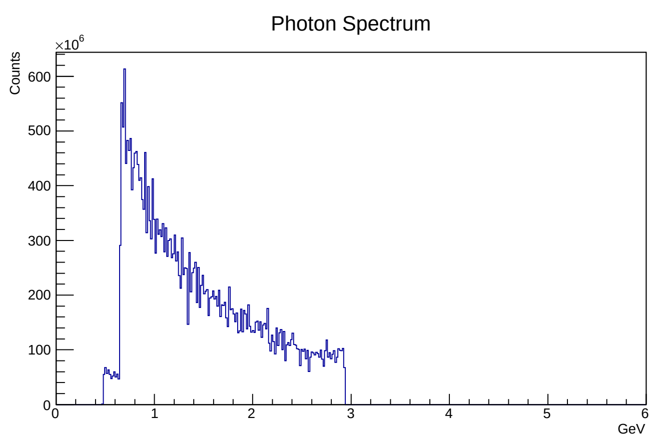

Figure 2.7: The tagged photon spectrum for the circularly polarized photon beam at $E_0 = 3.09$ GeV.

2.3.2 Linearly Polarized Photon Beam

The linearly polarized photon beam of the g9b running period was produced when the electron beam was incident on a diamond radiator of thickness 50 microns. A diamond radiator is used to produce a linearly polarized photon beam due to the fact that it has a small lattice constant and a high Debye temperature, which results in small thermal motion of the atoms in the lattice and a lattice structure that suffers minimal thermal effects [75]. When the diamond lattice is aligned relative to the electron beam direction, the bremsstrahlung photons will have discrete fractional energies, corresponding to specific momentum transfers from the electrons to the crystal lattice, and the energy spectrum can then exhibit a coherent peak structure (a sharp, highly polarized peak at an energy that corresponds to the crystal lattice orientation). Once the orientation of the diamond is chosen, the photons produced can have a high degree of linear polarization in the coherent peak region [76].

In order to produce highly polarized photons in coherent bremsstrahlung, the diamond crystal lattice must have precise alignment relative to the incident photon beam, so that highly linearly polarized photons are produced. In order to control the diamond radiator alignment, the diamond was mounted in a goniometer, a device which can move the diamond in the horizontal and vertical direction and rotate it around all three axes with high precision. The precision of the goniometer allows for the coherent peak to be dialed into a specific photon energy with accuracy of within 1 MeV. The goniometer used in Hall B can be seen in Fig. 2.8. The goniometer was placed upstream of the tagger magnetic spectrometer and was under vacuum. The design allowed for several diamond radiators and an amorphous carbon foil, to be held on a ‘ladder’ that could be moved in and out of the beamline when necessary. [77]

Figure 2.8: The Hall-B goniometer. The target ladder, which holds the various radiators, is in the center of the device. Figure taken from [71].

2.3.3 Collimators

Two collimators were placed downstream of the tagger magnet to allow for removal of the photon beam halo. Sweeping magnets between the collimators removed any charged particles created by photons interacting with the first collimator. The collimator also helped to increase the degree of linear polarization in the linear running period by tightly collimating the photon beam. The 2.0-mm collimator used for the coherent bremsstrahlung beams was made from nickel (Ni) diskettes with a small hole in the center of each. They were stacked in a cylindrical sheath of stainless steel with four 4-mm-diameter cubic scintillators in between the first two diskettes to measure the rate of off-centered photons hitting the front face of the collimator. During data taking with circularly polarized beam, a single

4.6 mm collimator was used to reduce the beam halo.

2.4 CLAS Detector

The main physics detector in Hall B was the CLAS detector. The CLAS detector was a multi-layered and segmented arrangement of different kinds of particle detectors, almost 10 m in diameter. The CLAS detector inside of Hall B can be seen in Fig. 2.4. The different detectors within CLAS are described below. Further details about CLAS may be found in Ref. [78].

2.4.1 Torus Magnet

The CLAS torus was based on six kidney-shaped superconducting coils arranged around the beamline and separated at 60° angles in the azimuthal direction. The toroidal arrangement allowed for a field-free region around its center where the FROST target was located. The position of the coils designates the geometry for CLAS, most importantly the six sectors that make up CLAS. However, the width of the coils and cryostats unfortunately reduced the acceptance of CLAS to about 80% of the 4π solid angle. The torus field was primarily in the azimuthal direction with deviations at areas close to the coils. In its standard operating configuration, the field direction was such that positively charged particles bent away from the beamline and negatively charged particles bent toward the beamline. Due to the bending of particles, low-momentum particles with a negative charge could not be reconstructed in CLAS. For the g9b running period, the torus was operated at a current of 1920 A. This allowed for a maximum field of 1.75 T in an anti-clockwise direction around the beamline (when viewed from upstream).

The magnet was almost 5 m in diameter and 5 m in length and can be seen in Fig. 2.9. The torus magnet allowed for the determination of the momentum of charged particles that passed through its volume via measurement of their curvature in the known field.

Figure 2.9: The CLAS torus coils in Hall B prior to detector installation. Figure taken from [71].

As there was no iron present in the magnet, the torus magnetic field could be calculated precisely by knowing the current in the coils. The coils had four layers of 54 turns of an aluminum-stabilized niobium-titanium/copper (NbTi/Cu) conductor and were cooled to a superconducting temperature of 4.5 K by helium running through cooling tubes at the edge of the windings. The magnet was capable of generating a maximum field strength of 3.5 T when operated at a current of 3860 A. Further details about the torus may be found in Ref. [79].

2.4.2 Start Counter

The start counter is an essential component of CLAS for running photon beams, as it provides the raw initial timing information of charged particles as they emerge from the target. It allows for a coincidence measurement of charged particles in the final state, a function that it shares with the time-of-flight system (see Section 2.4.4). The start counter is the first detector to detect charged particles traveling from the target region, as seen in

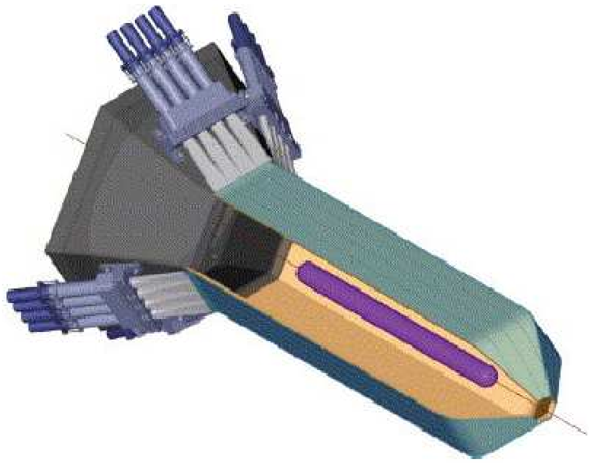

Figure 2.10: Schematic view of the start counter with one sector removed to show the target inside.

Fig. 2.10. This start time is later used in the calculation of a particle's flight time. The start counter consists of 24 scintillator paddles, each coupled to an acrylic light guide and divided equally into the six sectors of CLAS. The setup allows for a coverage of the full acceptance of CLAS, from $7^\circ < \theta < 145^\circ$ and $-29^\circ < \phi < 29^\circ$ for each sector. Each scintillator has a 502-mm-long straight section, known as the leg, and a tapered end, known as the nose. The scintillators are 2 mm thick to ensure that multiple scattering is minimized, so that particles do not have to travel through too much material before entering the drift chamber. The timing resolution of the start counter is roughly 400 ps. Further details about the start counter may be found in Ref. [80].

2.4.3 Drift Chambers

The drift chambers of CLAS are necessary to determine the position of charged particles. The position of the particle is determined before, during, and after their passage through the magnetic field of the torus. The drift chamber system consists of 18 separate drift chamber assemblies, such that three radial regions (referred to as Regions 1, 2, or 3) occupy each sector of CLAS. Each region has two superlayers comprised of six layers of hexagonal drift cells. In Regions 2 and 3, the first superlayer is oriented such that it is axial to the field direction. The second superlayer is tilted at a 6° stereo angle with respect to the first superlayer, which allows azimuthal information to be obtained. A Region 3 drift chamber may be seen in Fig. 2.11. In the inner drift chamber (Region 1), the first superlayer is tilted and the second is axial to the field direction.

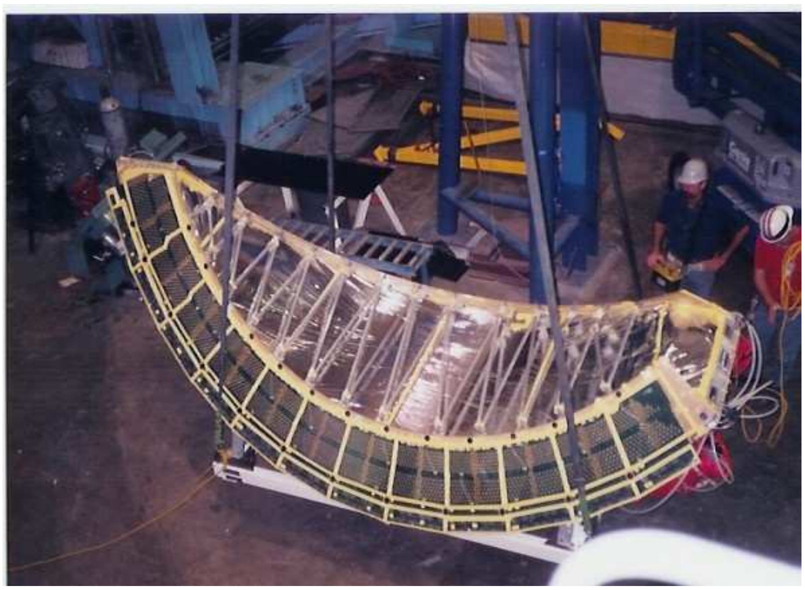

Figure 2.11: A Region 3 drift chamber is shown before installation inside of CLAS. Figure taken from [71].

The Region 1 drift chambers are located inside the torus in an area of weak field, which allows the region to provide information on the initial trajectory of charged particles before they are bent by the torus magnetic field. The Region 2 drift chambers are located between the torus coils, where the torus magnetic field is the strongest. This allows for determination of the particle momentum using the curvature of the tracks within the region. The Region 3 drift chambers are located outside the magnet coils, which is another area of weak field. This region gives the final trajectory of charged particles before they reach the time-of-flight system. The drift chamber system provides a coverage of 8° to 142° in the polar angle and 80% of the azimuthal angle.

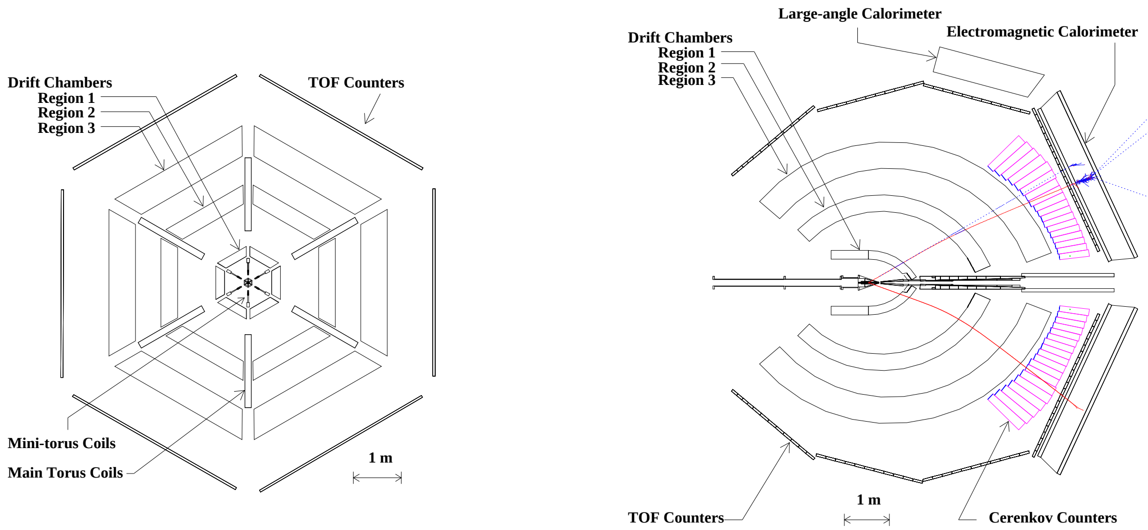

Figure 2.12: Cross section through CLAS showing the 6 sectors in a front view perpendicular to the beamline (*left*) and a side view (*right*) with a typical hit pattern from 2 charged tracks. Figure taken from [71].

Within each drift chamber, drift cells consist of a 20 micron diameter gold-plated tungsten sense wire in the center of a hexagonal arrangement of six 140 micron gold-plated aluminum alloy field wires. The field wires have a negative potential and the sense wires a positive potential. The drift chambers contain a gas mixture of 90% argon and 10% CO_2, which ionizes as charged particles move through the gas. This gas mixture improves the operating lifetime of the drift chambers, minimizes multiple scattering and random backgrounds, is non-flammable, and is inexpensive. Electrons that become freed in the ionization process also ionize the gas as they are attracted towards the sense wires, providing additional electrons. These electrons then register an electric pulse on the wire. An example of a hit pattern in the superlayers that has registered the electric pulses may be seen in Fig. 2.12. Further details about the drift chamber system may be found in Ref. [81].

2.4.4 Time-of-Flight System

The Time-of-Flight (TOF) system provides precise timing information for charged tracks as they exit the CLAS magnet. The TOF system is a six-fold segmented array of scintillator bars that are located about 4 m from the target and oriented perpendicularly to the beam. Each sector of the TOF system is made up of 57 scintillator bars fabricated from Bicron BC-408 material. Most of the produced tracks travel through the forward region of CLAS, at angles less than 45° from the beamline, and here the scintillator bars are 15 cm wide. At angles greater than 45°, the scintillator bars are wider at 22 cm. The lengths vary as well from 32 to 445 cm based on the shape of the sector. All scintillators are 5.08 cm thick, which allows for a robust signal for minimum ionizing tracks.

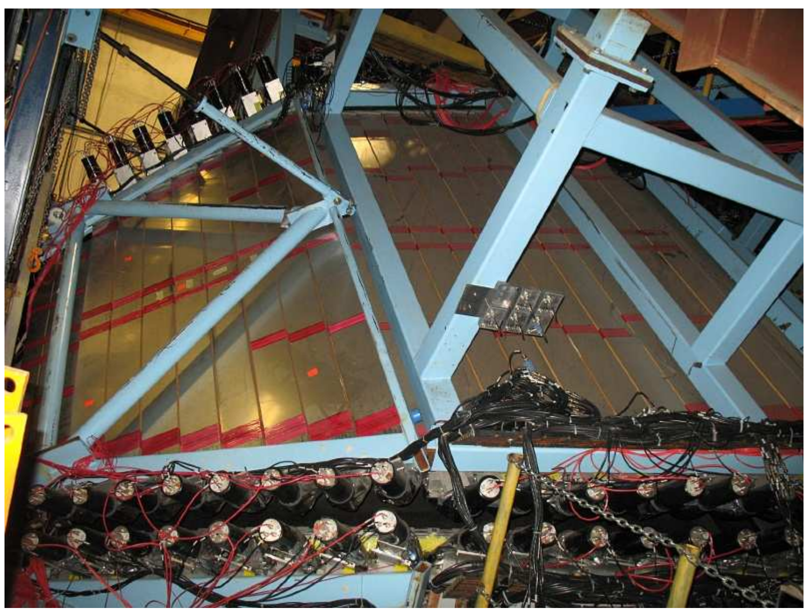

Figure 2.13: The outer portion of the TOF system paddles are shown here with PMTs attached to either end of the paddle.

Each scintillator is read out by two PMTs, one on either end via a Lucite light-guide. The outer portion of the TOF system can be seen in Fig. 2.13. The time in each PMT provides information about the azimuthal hit position, and provides a precise measurement of the hit time. The timing resolution of each scintillator is between 80 and 160 ps, depending on the length of the paddle. This information can be used to calculate the particle velocity knowing the path length from the target, which was then used to identify charged particles by computing their mass. The system allowed for excellent π/p separation for track momenta up to 2.0 GeV. Due to its excellent timing resolution and acceptance for charged tracks, the TOF system was an integral part of the trigger that was setup for g9b. Further details about the TOF system may be found in [82].

2.5 Beamline Devices

Many devices were included in the upstream and downstream beamlines when operating the FROST experiment. The upstream devices were used to monitor beam quality and included beam position monitors, harps, a pair spectrometer, and a Møller Polarimeter. In the downstream beamline, a total absorption shower counter was included. These devices are described in the following subsections.

2.5.1 Beam Position Monitors

Beam Position Monitors (BPMs) allowed for the beam position to be monitored and controlled during data taking. The monitors operate using currents induced by the beam. The electron beam will induce a current in wires that are proportional to the distance of the beam from the wires. The BPMs current is used to calculate the x and y positions of the beam. During data taking, an orbit lock corrects the beam position if the beam drifts outside of set parameters for an extended period of time [83].

2.5.2 Harp Scanners

The profile of the beam can be measured during dedicated runs with harp scanners, which are tungsten and iron wires pulled through the electron beam in the two directions perpendicular to the beamline. Electrons that were scattered by the wires were detected by PMT arrays arranged around the beam pipe upstream from CLAS. The beam profile was then created using the detected count rate as a function of the wire position as seen in Fig. 2.14. A similar scanner is used to produce the photon beam profile downstream of the tagger magnet [83].

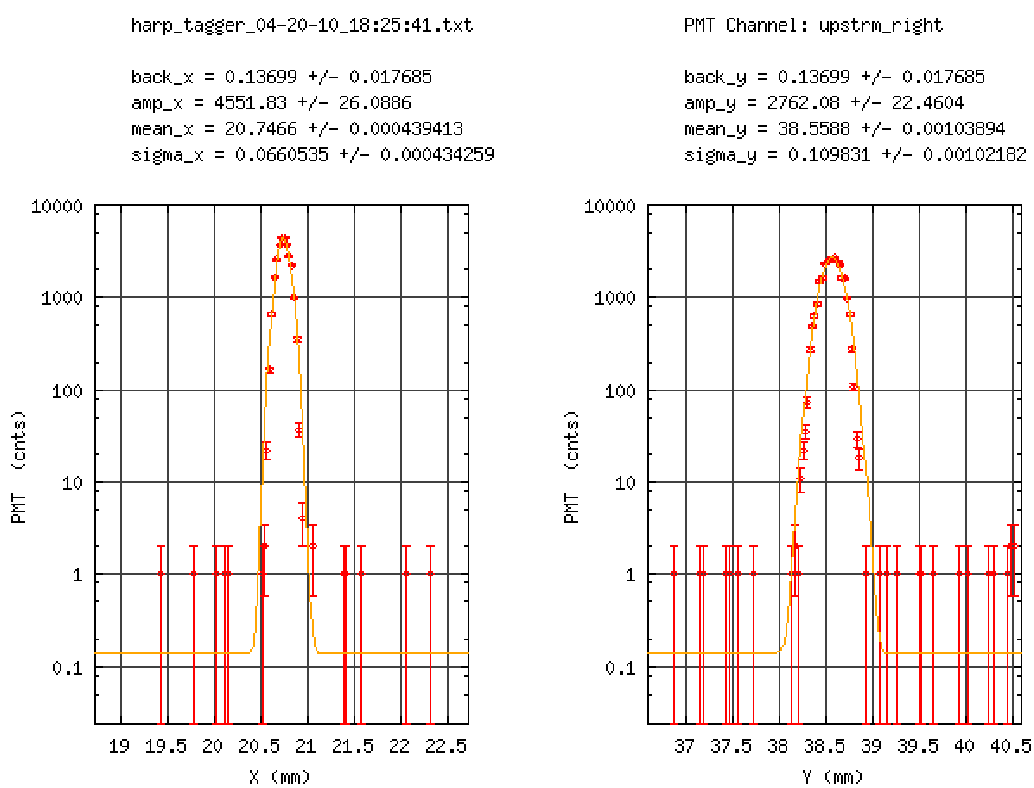

Figure 2.14: A typical harp scan to measure the electron beam profile taken during the FROST experiment. The peak is fit by a Gaussian and the count rate is shown on a logarithmic scale. The size of the beam is on the order of 100 μm.

2.5.3 Møller Polarimeter

For experiments with circularly polarized photons, it is necessary to know the polarization of the electron beam. This is measured by the Møller Polarimeter, a magnetic spectrometer for detecting electrons, consisting of a 25 micron thick Permedur foil target, two quadrupole magnets, and scintillators with PMTs. Since the photon beam polarization cannot be measured directly, the Møller polarimeter allows for measuring the electron beam polarization, which can then be used to calculate the circular photon polarization using equation [74]:

$$P_c = P_{el} \frac{4x - x^2}{4 - 4x + 3x^2}, \tag{2.2}$$

where x is the ratio of photon energy, E_γ, to electron beam energy, E_0, and P_{el} is the longitudinal electron beam polarization which is measured using:

$$P_{el} = \frac{A}{A_z} P_T, \tag{2.3}$$

where A is the asymmetry measured by the Møller detectors, A_z is the analyzing power of the target, and P_T is the target foil polarization. Typical measured values of P_{el} were between 80 - 85 % during this experiment. Using the Møller Polarimeter requires a special data acquisition setting, so the polarimeter is used in special runs performed in between production runs [78].

2.5.4 Pair Spectrometer

The Hall B Pair Spectrometer (PS) is located roughly 10 m downstream of the photon beam radiator just upstream of CLAS and consists of a dipole magnet and two planes of scintillation counters, positioned symmetrically to the left and right of the beam axis in the horizontal plane and downstream of the magnet. The PS was constructed to measure the relative tagged photon flux over a range of intensities and operates continuously throughout the experiment. During the linear running period it was useful for monitoring the flux stability of the tightly collimated photon flux [78].

2.5.5 Total Absorption Shower Counter

The Total Absorption Shower Counter (TASC) was located downstream of CLAS and was an almost 100% efficient photon detector used during special normalization runs, for measuring the tagging ratio for the tagger hodoscope T-counters. The TASC had four lead-glass blocks coupled to a PMT. The special runs used a 100 pA electron beam and a thinner radiator to produce fewer photons than used during production runs. The ratio of photons detected in the TASC to 'good' electrons, where 'good' was considered to be with hits in the left and right TDC matching in time and a corresponding hit in an E-counter, gave the tagging ratio. The tagging ratio was used to calculate the photon flux for the experiment [84].

2.6 Data Acquisition System

The FROST experiment was designed to investigate many different final states. In order to collect data for these different measurements simultaneously with minimal bias, the condition to record data from the readout electronics (known as a 'trigger') had to be properly defined such that the event rate could be maximized. During the FROST experiment, the trigger required a sector-based timing coincidence between the start counter and the time-of-flight system. In addition, the drift chamber had to record hit segments belonging to a charged particle track in the same sector. For the most part, analog signals for each detector channel are split into two types, one connected to an Analog-to-Digital Converter (ADC) and the other to a discriminator and a Time-to-Digital Converter (TDC). The data acquisition system reads out all ADC and TDC channels when a trigger occurs. The CLAS data acquisition system was comprised $\approx$ 21,000 TDC channels and $\approx$ 2000 ADC channels. The system was highly parallelized to allow for a trigger rate of up to 10 kHz. More information about the DAQ system can be found in Section 3.1.

2.7 FROST Target

Polarized targets have long been used in experiments to align the spins of the target nuclei in a particular direction by some external means. The degree of polarization is proportional to the fraction of target nuclei that become aligned. After being exposed to high magnetic field, the spins of the target nuclei align and the polarization can be measured using Nuclear Magnetic Resonance (NMR) [85].

The FROzen Spin Target (FROST) used in this experiment was designed by the JLab Target Group [86] and a picture of the target may be seen in Fig. 2.15. This nuclear spin polarized target was made from butanol (C_4H_9OH) and placed in the center of CLAS, allowing for the extraction of single and double-polarization observables, and is critical to this analysis. In contrast to a dynamically polarized target, a 'frozen-spin' target requires only a modest (a few hundred Gauss) holding field, so that the angular acceptance of the detector is not reduced by the presence of a massive polarizing magnet. Using an extremely low temperature of the polarized target, less than 50 mK, only a small holding field was required to maintain the polarization for a long period of time. The following subsections describe the construction of the target, and how it was cooled, polarized, and maintained throughout the experiment. For a full discussion of the target, more details may be found in Ref. [86].

2.7.1 Dynamic Nuclear Polarization

Dynamic Nuclear Polarization (DNP) is the process by which protons in FROST (and other similar experimental targets) are initially polarized. It is possible to polarize nuclei directly through the use of a magnet, but this takes very long and requires a very strong

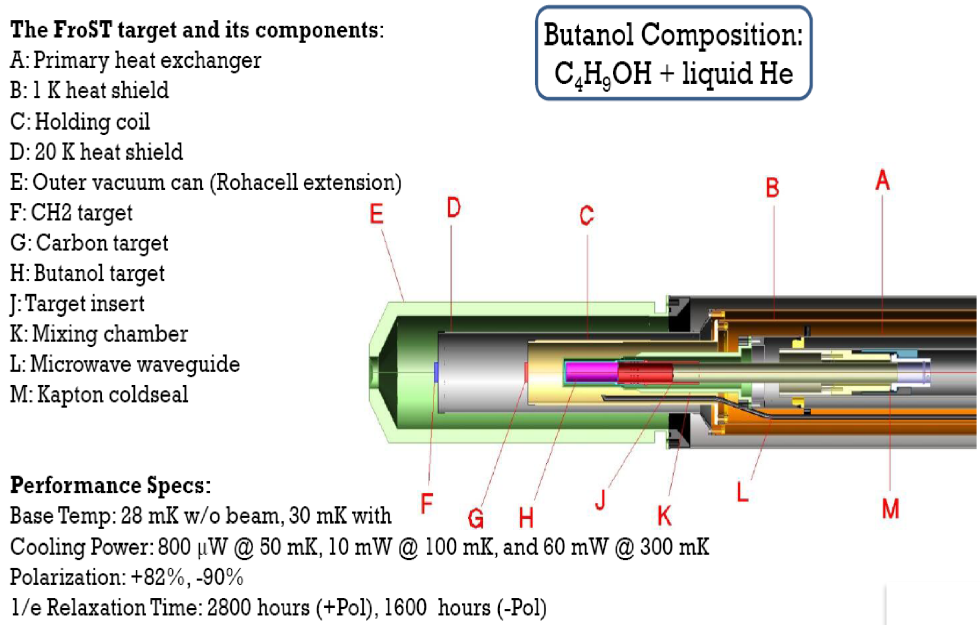

Figure 2.15: The FROST target apparatus is shown here. Figure taken from [71].

magnetic field. The DNP process uses a polarizing magnet (here, a 5 T solenoid) to polarize the electrons in the target material and then transfers the electron polarization to the nuclei by saturating the target with microwaves near the Electron Spin Resonance (ESR) frequency of paramagnetic radicals dissolved in the butanol [85]. The nuclear spins can be polarized either parallel or anti-parallel to the direction of the field by adjusting the microwave frequency to be either above or below the ESR frequency.

The 5 T solenoid polarizing magnet was only used to provide the initial polarization of FROST, which was done while there was no data taking and no beam in Hall B. Once the experiment was running, a small holding field of 0.56 T helped to maintain the FROST target polarization. This field was generated by a superconducting holding magnet coil and the materials in the coils was minimal such that they had only a negligible effect on the CLAS acceptance.

The process of polarizing FROST began with the target cryostat being inserted into the horizontal bore of the polarizing magnet and energizing the microwave generator. The target was then polarized via DNP at a temperature of around 0.3 K for a few hours. Once polarization was complete, the microwave generator was turned off and the dilution refrigerator then took around 30-45 minutes to cool the target below 50 mK. After the target reached this temperature, known as the 'Frozen Spin Mode', the polarizing magnet was ramped down and the holding magnet coil was energized. The polarizing magnet was removed and the target cryostat was inserted into the center of CLAS. The polarizing magnet can be seen in Fig. 2.16.

Figure 2.16: The FROST 5 T polarizing magnet is shown here. Figure taken from [71].

The remaining temperature of ≤ 50 mK also has a depolarizing effect. Since the beam has a heating effect on the target and raised the temperature of the target by approximately 2 mK while running, the target polarization decreased by roughly 1-1.5% per day, which required the target to be regularly re-polarized. This would happen, on average, once per week during the course of the experiment. This also means that the target polarization had some small variations over the data set and this variation must be taken into account when calculating certain polarization observables. The degree of target polarization during the course of the g9b experiment is shown in Fig. 2.17 and also listed in Appendix A.

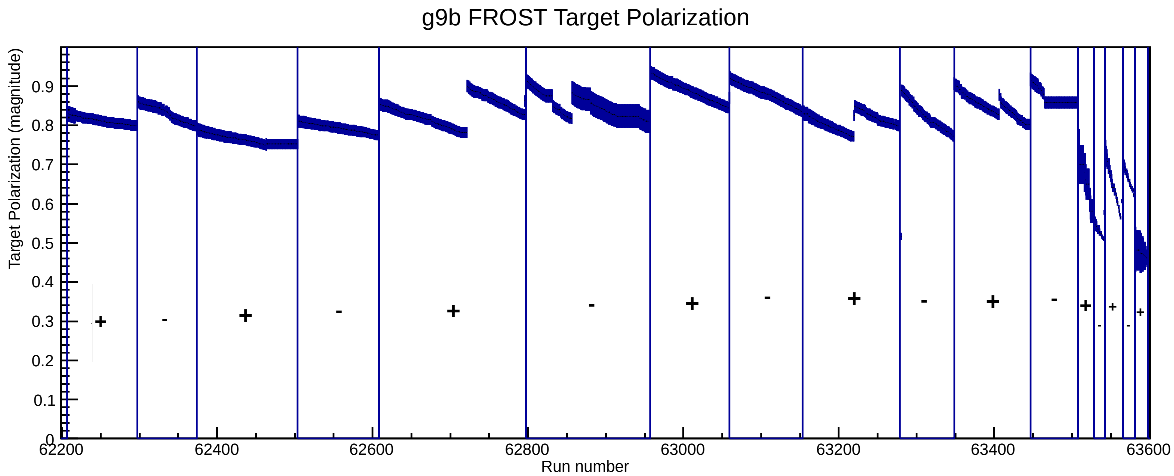

Figure 2.17: Degree of target polarization during the g9b run period. The run number versus degree of polarization is shown. A vertical line indicates the first run number after the target polarization was changed, the direction of the polarization direction is indicated by "+" and "-" signs.

2.7.2 Dilution Refrigerator

The cooling of the target was achieved by a ^{3}He-^{4}He dilution refrigeration and a ^{4}He evaporation refrigerator (called the precooler), and both may be seen in Fig. 2.18. Both units were constructed around a separate, thin-walled stainless steel tube, which was 50 mm in diameter for the precooler and 40 mm in diameter for the dilution refrigerator and the two tubes were connected together to form a single tube. This combined tube then served as the beam pipe for the photon beam and as the insertion point for the target sample into a mixing chamber. At one end, the tube was sealed with a 0.13 mm thick polyimide beam-entrance window. The other end was sealed by a 0.13 mm thick aluminum window.

The precooler cooled and condensed the ^{4}He before it circulated throughout the dilution refrigerator. It had two counterflow gas-gas heat exchangers and two pots with liquid helium at 4 K and 1 K. A dilution refrigerator was also present, which was a unit consisting of a still, a heat exchanger, and a mixing chamber. Both the dilution and precooler refrigerators were housed inside a custom-built stainless steel vacuum chamber. The downstream end of the chamber was made of a closed-cell foam to reduce the energy loss of particles that were scattered from the polarized butanol target.

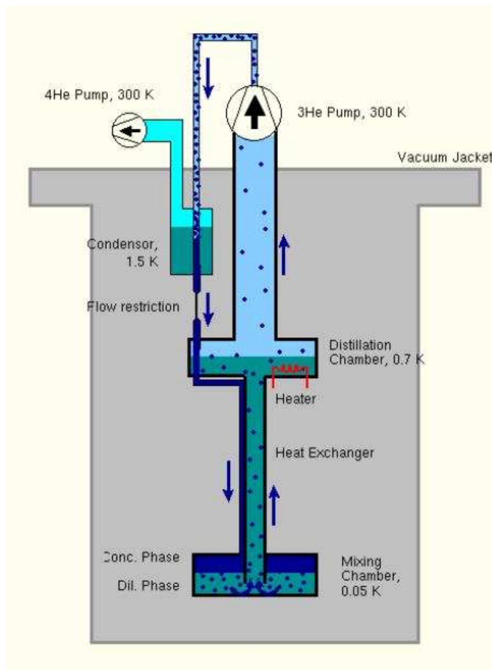

Figure 2.18: Diagram of a dilution refrigeration cooling process. Figure taken from [87].

2.7.3 FROST Target Cell

Frozen beads of butanol (C_4H_9OH) doped with the nitroxyl radical TEMPO were used as the target material, with a small addition of water to avoid a crystalline solid before freezing. The 'beads' were formed by dripping the solution through a hypodermic needle into a bath of liquid nitrogen to form beads of diameter 1-2 mm. Afterwards, roughly 5 g of beads were loaded into a 15 mm diameter, 50 mm long PCTFE target cup, which was attached to the end of a 25 cm stainless steel tube and can be seen in Fig. 2.19. This gave a total target length of 5 cm of butanol. On one end, the tube was sealed by a 0.13 mm thick aluminum vacuum window, which served as a locking mechanism for the PCTFE cup. The other end contained a vacuum seal.

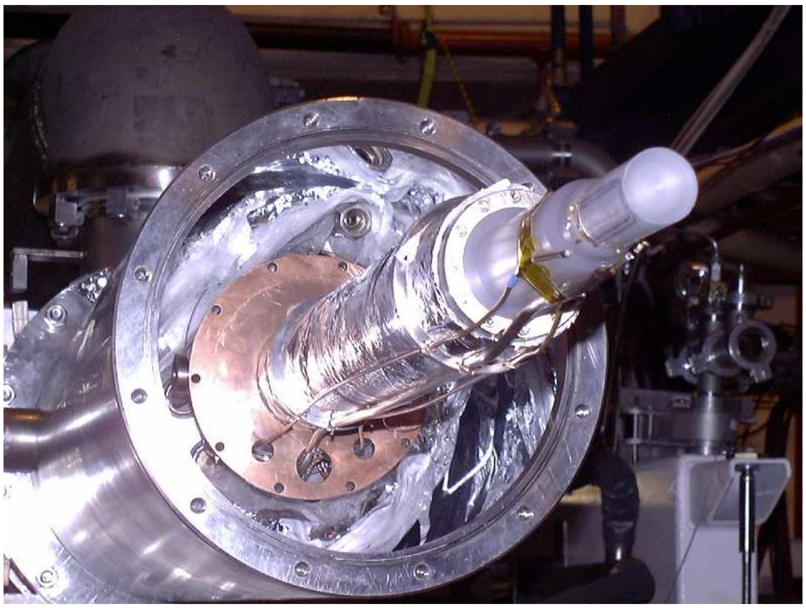

Figure 2.19: The FROST target cell attached to the dilution refrigerator before being inserted into CLAS. Figure taken from [87].

In the butanol sample, not all of the nuclei were polarized. Only covalently bonded protons were polarized during the DNP process, but hadronic events may be produced from a photon interaction with any nucleon in the butanol, including those inside the unpolarized carbon and oxygen nuclei [85]. To measure the background produced on the unpolarized nucleons, the target system included additional targets that were used for background and dilution studies. A 1.5 mm thick carbon disk and a 3.5 mm thick CH_2 disk were mounted on the heat shields, roughly 6 and 16 cm, respectively, downstream from the butanol. These targets were added for the purpose of allowing the background from bound nucleons in the butanol to be normalized. Their further use will be described later in Section 4.12.

2.7.4 Holding Coil

Figure 2.20: The holding coils used in the FROST experiment. (a) The holding coil for the longitudinally polarized target and (b) the holding coil for the transversely polarized target. Figures taken from [87].

Holding coils were specifically designed by the JLab target group for this experiment in order to maintain polarization once the target was placed in the beam. The FROST experiment was divided into two parts, referred to as g9a (longitudinally polarized target) and g9b (transversely polarized target), each part requiring its own holding coil. g9a utilized a 110 mm long solenoid to maintain the longitudinal polarization (along the beam line, z-axis) and consisted of three layers of 0.14 mm copper-clad, multifilament NbTi wire wound on a 50 mm diameter, 1 mm thick aluminum former. The g9a holding coil produced a 0.56 T central field at 22 A. For g9b, a four layer, saddle-shaped dipole holding coil was used to maintain the transverse polarization (transverse in the $x - y$ plane to the beam line). The g9b holding coil produced a maximum field of 0.54 T, but was operated at 0.50 T and a current of 35.5 A. The holding coils used for the two parts of the experiment may be seen in Fig. 2.20. The analysis presented in this dissertation pertains to the g9b running period, using the transversely polarized butanol target.

2.7.5 Target Quench

During data taking of the experiment on July 2, 2010, the target magnet unfortunately quenched from a power surge due to a power outage in Hall C. The turbo pumps of the refrigeration system stopped working and the target warmed up rapidly, which caused a loss of the target. It took three weeks to get the system working again, meaning three weeks of data taking were lost. The resulting fix was to use a smaller diameter stainless steel stick (a beam pipe, to which the target was connected) that was originally used in g9a. Despite the knowledge that this beam pipe caused large upstream background in g9a, it was the quickest fix in order to resume data taking. The effects of the quench were studied and can be found in Section 6.2.3.

2.8 Summary

This chapter has described the equipment used in the experiment allowing for the measurement of various polarization observables. The production of the incident electron beam, resulting photon beam, the target, and the detection of multi-particle final states have been discussed. At the conclusion of g9b, 14 billion events were collected. The final state $\gamma p \rightarrow K^+\Lambda$ and $K^+\Sigma^0$ events represent a very small subset of the recorded data ($\approx 0.02\%$). The following chapter will discuss the detailed process of calibration and event selection used to extract the polarization observables.

Chapter 3

Calibration of Data and Cooking

The g9b data set was taken from March 18 to August 12 of 2010 by the CLAS Collaboration and contains roughly 14 billion triggers and about 36 terabyte of raw data. Before one can actually analyze the data, the raw data must be *cooked*, meaning that the raw electrical signals must be transformed into physical 4-momentum vectors for each charged track recorded for each event. In order to obtain the 4-momentum of the track, each detector system of CLAS must be calibrated individually with calibration constants uploaded to a database. Many iterations of calibrations were required in order to fully calibrate the detectors in each sector of CLAS. Once the calibration and cooking was complete, data analysis could commence. In a data set of this size, not only one or two final state reactions can be studied, but many. The $\gamma p \to K^+\Lambda$ and $K^+\Sigma^0$ reactions make up a small portion of the data set due to their small cross-sections. The recorded data were dominated by more highly probable reactions, such as single or double pion production. Therefore, the desired events had to be carefully extracted to keep the number of background events low while keeping the events of interest.

Due to the instability of electronic components and deterioration of CLAS over time, the response of each detector system varied throughout the different experiments including g9b, which is why a run-by-run calibration of the detector components was required. Calibration of such a large detector system as CLAS cannot be done by one person alone, so it was divided up among different groups who were members of the CLAS Collaboration. The contribution from the CUA group, carried out by the author, was the tagger and time-of-flight calibration and cooking of the g9b data. Charles Taylor and Olga Cortes, Ph.D. students at Idaho State University performed the start counter calibration. Sungkyun Park, a Ph.D. student at Florida State University carried out the drift chamber calibration. Another piece of the calibration process specific to the FROST experiment, was the target polarization calibration, done by Yuqing Mao at the University of South Carolina, as will also be described later and the target offset calibration, completed by multiple people. For the most part, the calibration of the detectors should be completed in a certain order due to the fact that one detector system depends on measurements of another system. Due to the nature of the calibrations, many iterations occur until all detector systems calibrations reach a satisfactory level. This chapter will carefully outline the procedure of the calibrations for certain detector components relevant to this thesis.

3.1 Trigger and Data Acquisition System

Event triggering determined which types of events in CLAS were recorded. Events taken during the g9b running period were recorded at a rate of 2-3 kHz with a dead time of $\approx 15-20\%$, which is the percentage of the time when the data acquisition (DAQ) system is busy recording a physics event and cannot record any other during that time. CLAS could have two types of triggers based on the desired events of the experiment. A Level-1 trigger recorded prompt signals from the detector systems of CLAS and was used to set the relative timing of the gate signals for the analog-to-digital converters (ADCs) and the reference signal for the time-to-digital converters (TDCs). A Level-2 trigger recorded events based on a pattern recognition of hits from the drift chambers and sent a fail signal if an insufficient number of track segments was found in the same sector that reported a Level-1 trigger. In g9b, the Level-1 trigger was defined by a sector-based coincidence time between start counter paddles and TOF paddles, and for the later part of the run included the Tagger MasterOR. The Tagger MasterOR included the sum over all tagger counters with hits within a 20 ns coincidence interval with the start counter. The Level-1 trigger logic for g9b was realized by a Field Programmable Gate Array (FPGA). Level-2 triggering was used for the g9b experiment to minimize triggers from accidental start counter and TOF coincidences while maximizing the DAQ rate for charged particle events. The data were recorded in the form of a Bank Object System (BOS) file [88]. This raw BOS file contained information about each detector system such as ADC and TDC channels and detector status. These raw files were kept on the JLab data storage silo. A group of raw files that correspond to about 20 million triggers makes up a *run*. Every time a new run was started, all DAQ components were quickly checked, pedestals (or offsets) were downloaded into the ADC modules, and the trigger electronics were reloaded to ensure that all components of the DAQ worked properly during data taking. During the g9b experiment, 967 runs were recorded.

3.2 Cooking of Data

The raw data taken during the experiment was kept on the JLab data storage silo. To convert the raw data into usable information, calibration parameters were used along with a track fitting package and particle identification packages within the reconstruction code used for cooking [89]. The particle identification routines, such as the simple event builder (SEB) package, found groups of geometrically matched drift chamber tracks and TOF system hits and then reconstructed the trigger particle and trigger time, which then determined the particle ID (e.g. pion, kaon, or proton). To reconstruct particle tracks from hits in the detector, adjacent hits in every superlayer of the drift chamber were grouped into clusters or track segments. The track segments were then grouped across the three drift chamber regions to produce a full hit-based track, which is based on the positions of the drift cells that form the tracks. The sign and magnitude of the curvature of the track as it traveled through the Region 2 drift chambers then determined the sign of the charge $\pm e$ and the momentum. It is worth noting that this first approximation of the hit-based tracks were not always tracks, meaning sometimes the hits were actually clusters of spurious noise hits not associated with an actual track. These 'fake' tracks could easily be discarded by extrapolating the hit-based track to the TOF system to see if a matching hit in the TOF counter was present. Once the TOF counter hit was located, the time measurement was used to determine the flight time from the track's assumed origin close to the beamline to the hit drift chamber cell. The recorded time from the drift chamber TDC for this cell was corrected for the flight time to the the cell and a drift-time-to-distance relation was used to find the distance of closest approach of the track to the sense wire position. By using the time information for each hit cell on the track's path accidental hits could successfully be identified and discarded. The final fit determined the momentum with an uncertainty of about 0.5%. The track 'vertex' was obtained by calculating the smallest distance of the extrapolated track to the beamline. The calibration of the drift chamber system is described in more detail later in Section 3.5. [81, 90]

During event reconstruction, data banks were created that contained information about the reconstructed events such as momentum, particle ID, and corresponding timing information, and were used in the physics analysis. For this specific analysis, the GPID bank was mainly used, which gets its particle information from the start counter and the TOF [91]. The GPID method used the CLAS measured three momentum of the particle and calculated theoretical values of β ($=\frac{v}{c}$) for various particle types (pion, kaon, or proton) and compared it to the measured value of β. The particle could then be identified based on the closest expected value of β to the empirically measured value of β. These banks were added to the data stream during data cooking. Although the data started out in the format of a BOS file, it was converted to a ROOT file, which was the type of file used for this analysis.

ROOT is an object-oriented framework used in large-scale data analysis, such as this one, and was developed at CERN. It allows for the utilization of standard libraries for data analysis procedures, which include but are not limited to fitting routines and histogramming of results [92].

3.2.1 Charge and Momentum of a Particle

The charge of a particle can be determined from the direction of curvature of the reconstructed track in CLAS in the field produced by the torus magnet. The track reconstruction determines the particle's curvature and three momentum, which was taken from information obtained from the drift chamber. The magnetic force on the particle is given by the Lorentz force law:

$$\vec{F} = q\vec{v} \times \vec{B} \ , \tag{3.1}$$

where $\vec{F}$ is a force, q is the charge of the particle, $\vec{v}$ is the velocity of the particle, and $\vec{B}$ is the magnetic field. The particle's track has a curvature of radius r, and one can use the magnetic field map of CLAS to find the momentum of the particle by numerically integrating eq. (3.1) for the inhomogeneous magnetic field of the CLAS torus. The main magnetic field component of the torus is roughly perpendicular to the direction of particles emerging from the target, which can maximize the momentum sensitivity with small changes in the radius of the curvature.

3.2.2 Velocity and Mass of a Particle

The velocity of the particle, β, is reconstructed by using its time of flight, t_f, and its path length, d_f, from the vertex position to the TOF paddle that was hit. The particle's time of flight is the time between the event start time, at the event vertex, and the time of the TOF hit. The event start time can be obtained by using the reconstruction software and comparing the hit times in the start counter to the RF electron beam bunch times to select the closest bunch. The velocity of the particle can be expressed as:

$$\beta_{meas} = \frac{d_f}{ct_f}, \tag{3.2}$$

where c is the speed of light. The rest mass, m_0, of the detected particle can be computed from the reconstructed momentum and velocity using:

$$E = \gamma m_0 c^2 = \frac{pc}{\beta} \;\Rightarrow\; m_0 = \frac{p}{c\beta\gamma} = \frac{p}{c}\sqrt{\frac{1}{\beta^2} - 1}\;. \tag{3.3}$$

The particle ID that was extracted during cooking was dependent upon the value of the reconstructed mass. The information was based upon a comparison of the reconstructed velocity, β_{meas}, as described in Eqn. (3.2) and the velocity based on reconstructed momentum and a presumption about the particle's mass or β_{calc}:

$$\beta_{calc} = \frac{pc}{\sqrt{m_i^2 c^4 + p^2 c^2}}\;, \tag{3.4}$$

where m_i is the nominal mass of the particle and p the reconstructed momentum.

Once the nominal mass was obtained, the particle ID was determined in the reconstruction code. The following mass ranges can be used to determine the different particles in first approximation: pion if $m_0 < 0.3$ GeV, kaon if $0.35 < m_0 < 0.65$ GeV, proton if $0.8 < m_0 < 1.2$ GeV. Particle masses that fall outside these cuts were considered not known and the reason they fall in between the cuts was mostly because a failure in timing has occurred. A variety of different failures can be responsible for the unknown particle ID such as when a photon from the event is not properly recorded by the tagger and a different photon is chosen instead, or a single start counter or TOF paddle has two consecutive hits with different timing. The particle ID was stored in the banks that were previously described, so that the information can be used in the analysis.

3.3 Tagger Calibration

The photon tagger has already been described in detail in Section 2.3, but here the process in which the timing calibrations of the tagger were performed is described. The tagger calibration of a photoproduction experiment is one of the most crucial as the timing of the interacting beam photon is obtained from the tagger information. An error of one RF bunch would result in a 2.004 ns offset of the tagger time, which would in turn result in variations in the timing of the event's start time of this same amount. The tagger calibration provided for assigning tagger hits to the correct accelerator RF bucket, which allowed for the most precise timing information of the detector. The accelerator sent beam in ≈ 2 ps long packets, every 2.004 ns. There were a variety of constants that had to be determined in order to have the most correct tagger calibration including RF adjustment, TDC slopes, base peak position, and a global timing offset with respect to CLAS. These constants are described in the following sections.

3.3.1 RF Offset Adjustment

The first set of constants to be described will be with respect to the RF adjustment. The easiest way to select the RF bucket associated with the event is to adjust a set of constants that will replace the tagger time with the RF time on an event by event basis. The RF offset is a simple offset to set the average tagger and TOF time to roughly the center of a 2.004 ns beam bucket period. The RF time, which varies from event to event, can be understood by using:

$$t_{RF} = t_{pho} + k_{event} \times 2.004 \text{ ns} , \tag{3.5}$$

where t_{RF} is the RF time, t_{pho} is the time of the produced photon propagated to the target relative to the trigger time and k_{event} is an offset that corresponds to an integer number of beam buckets. k_{event} is obtained through a set of constants called C_i, which were updated almost per run and is the offset of each T-counter (numbered 1-121) relative to an already adjusted T-counter left-right time offset. C_i can be obtained using:

$$C_i = C_i^{RF} + k_i \times 2.004 \text{ ns} , \tag{3.6}$$

where C_i^{RF} is an overall time offset for each T-counter i relative to the RF signal and k_i is an integer of the number of beam buckets of the specific tagger channel. Before each phase difference correction, the correct peak position of the T-counter hit must be identified. In order to do so, one must balance the left and right TDC times for each T-counter and must also calibrate the TDC slopes such that a dependence on hit position is circumvented. In the end, 122 constants, or one for every TDC, of the slopes and peak positions must be checked. Also, for the phase correction, 121 C_i constants must be determined, one for every T-counter, 61 in total, and 60 for the overlap of the T-Counters that are associated with hits in adjacent T-counters, giving the total. [93] Once all of the C_i constants are determined, each T-Counter should show a good alignment between the tagger time and the RF time. The time difference between the specific tagger channel and the RF time can be found using:

$$\begin{aligned} t_i - t_{RF} &= t_i - t_{pho} - k_{event} \times 2.004 \text{ ns} && (3.7) \\ &= C_i - k_{event} \times 2.004 \text{ ns} && (3.8) \\ &= C_i^{RF} + (k_i - k_{event}) \times 2.004 \text{ ns} . && (3.9) \end{aligned}$$

The 121 C_i^{RF} offsets were obtained using Gaussian fits to the distributions $(t_i - t_{RF})$ mod 2.004 ns. The peak of the time shift $(t_i - t_{RF})$ as a function of tagger channel should be centered at zero and an example of two calibrated runs from g9b can be seen in Figs. 3.1 and 3.2.

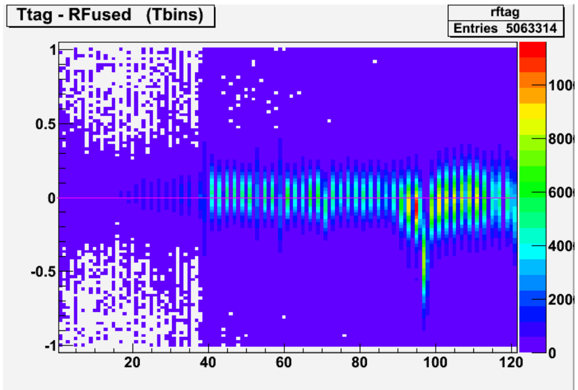

(a) Before Tagger Calibration

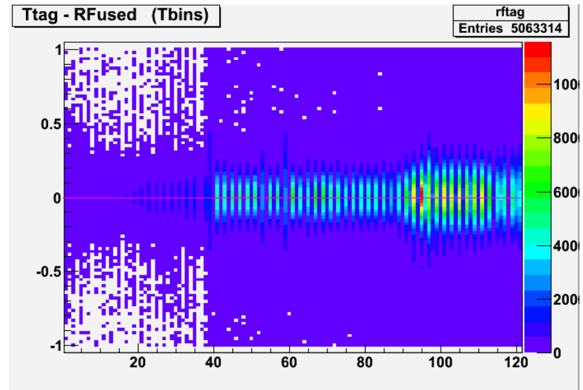

(b) After Tagger Calibration

Figure 3.1: Tagger calibration for run 62220, tagging time and RF time difference versus T-counter bin is shown. Before (a) shows a timing offset in T-counter 48. After (b) shows the result after the correction is applied. The vertical axes are in ns.

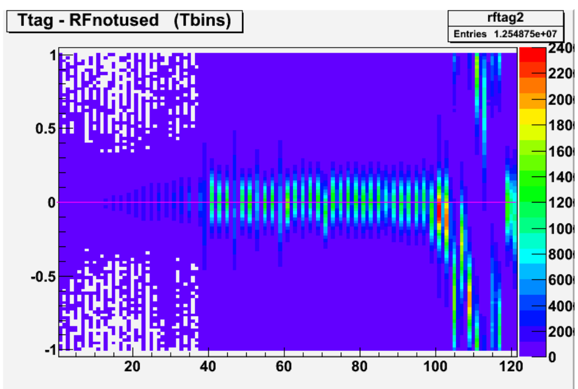

(a) Before Tagger Calibration

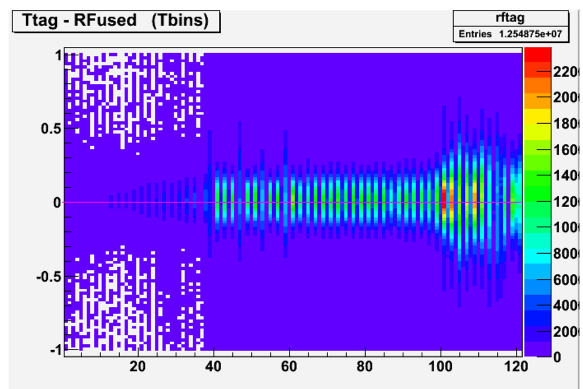

(b) After Tagger Calibration

Figure 3.2: Tagger calibration for run 62707, tagging time and RF time difference versus T-counter bin is shown. Before (a) shows a large timing offset in multiple T-counters. After (b) shows the result after the correction is applied. The vertical axes are in ns.

Since the calibration of the tagger used the start counter as a reference, the time difference between the two should be zero. It is vital to use the start counter as a reference detector because the start counter is closely related to the start time of a particle created at the target. The time difference between the tagger and start counter as a function of T-counter bin can be seen in Fig. 3.3.

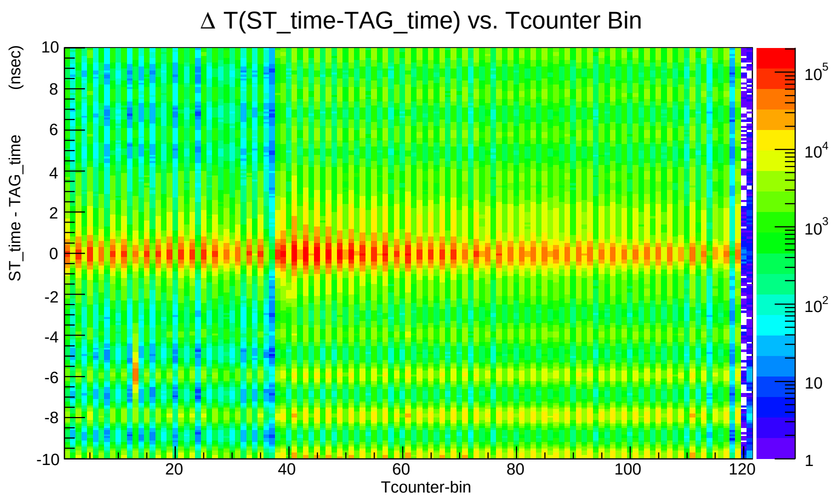

Figure 3.3: Difference in tagger and start counter time versus T-counter bin after the calibration of the tagger was performed. Here, T-counter 7 was still unstable after calibration.

3.3.2 TDC slopes

TDC slopes represent the conversion factor from TDC channel to time using the following equation:

$$t = c_0 + c_1 T, \tag{3.10}$$

where t is the converted time in ns, c_0 and c_1 are polynomial coefficients corresponding to each time-of-flight TDC that was used for the channel to time conversion, and T is the raw time in units of TDC channels. This TDC calibration information was obtained during special runs in which the pulser system was used. CLAS had a pulser system for each detector element and pulsed logic signals in sets of 50 ns were delivered simultaneously to all TDC channels during the run that spanned the full TDC dynamic range. For g9b, pulser data was taken 86 times. The E-counter TDC slopes were fixed at 500 ps/channel and the T-counter TDC slopes were roughly 25 ps/channel. The T-counter TDC slope could vary from channel to channel, so the slopes were determined for both the left and right T-counter TDCs. The TDC slope balance between the left and right PMTs of a given counter could be understood by looking at the raw T-counter TDC time difference $t^i_{left} - t^i_{right}$ and sum $t^i_{left} + t^i_{right}$, which should come out correctly when the slopes and base offsets are correct. A non-optimal calibration of the TDC slope balance between the left and the right TDC could, for a given T-counter, affect the measured timing resolution. [93]

3.3.3 Base Peak Position

The base peak position is the centroid of the peak in the TDC spectra for every TDC. The raw timing spectrum of every TDC channel had a sharp peak over a continuum where the sharp peak corresponds to self-triggered hits, or hits in the T-counter that produced the trigger, and the continuum corresponds to hits when other T-counters produced the trigger. The time of the sharp peak was subtracted from the TDC value in the calculation of the tagger time such that the absolute value of the tagger time was zero relative to the trigger time. This same technique used for the T-counter was also used for the E-counter, which allowed the correct identification of the reconstructed electron, based on the timing coincidence. The base peak position for a specific counter can be seen in Fig. 3.4. [93]

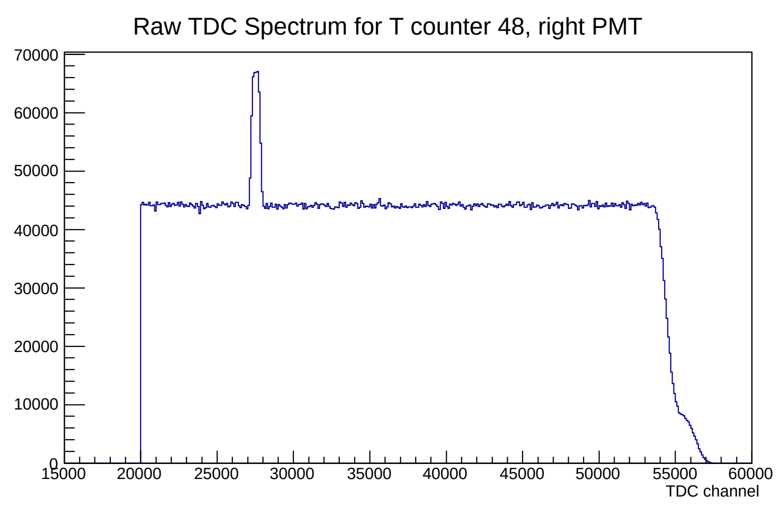

Figure 3.4: The raw TDC spectrum for T-counter 48, right PMT. A prompt peak is clearly shown over a large background of out of time hits.

3.3.4 Global Offset with Respect to CLAS

The final stage of the tagger calibration was to determine the global time offset between the tagger time and the time determined by the other detector subsystems such as the TOF and start counter. With this correction, the time reported from the tagger reconstruction corresponds to the arrival time of the bremsstrahlung photon at the center of the FROST target.

3.4 Start Counter Calibration

The calibration of the start counter was related to the reconstructed event start time in CLAS and was correlated to the event in CLAS and the tagged photon that produced that specific event. Since the start counter consisted of 24 scintillator paddles, the timing of each of the paddles had to be aligned to the others. Using the pulser data mentioned in Section 3.3.2, the channel to time TDC conversion was completed. The raw paddle TDC spectra was fitted using:

$$t_{ST} = C_T T, \tag{3.11}$$

where t_{ST} corresponds to the start counter paddle time in ns, T is the specific TDC channel, and C_T is the channel to time calibration constant that was determined from the fit. After the TDC calibration, the hit time occurring in the start counter was aligned to the RF adjusted tagger time described in Section 3.3.1. Several quantities were adjusted, such as the paddle time delays, the time difference between the RF time and the start counter for every paddle, the time for light to travel through the scintillator paddle to the PMT, time-walk corrections, which are correlations between timing and pulse heights associated with the use of leading-edge discriminators, and a correction of the position of the hit, which was based on the non-linear geometry of every paddle. The non-linear geometry of the paddles gave rise to a non-linear relationship between the hit position in the scintillator and the light propagation time. The correction for the time it takes light to travel from the scintillator paddle hit position to the PMT can be written as:

$$\Delta t = \frac{z_0}{v_{eff}} + k_0 z_1 + k_1 z_1^2 + K_{RF}, \tag{3.12}$$

where k_0 and k_1 are calibration constants, v_{eff} is the effective velocity for light propagation in the scintillator material, z_0 is the distance of the hit position from the PMT along the straight section of the paddle, z_1 is the distance of the hit position along the bent section of the paddle, and K_{RF} is a constant. [94] To determine K_{RF} for each start counter paddle, the start counter timing relative to the RF timing was fitted with a Gaussian and the centroid of this fit yielded K_{RF}.

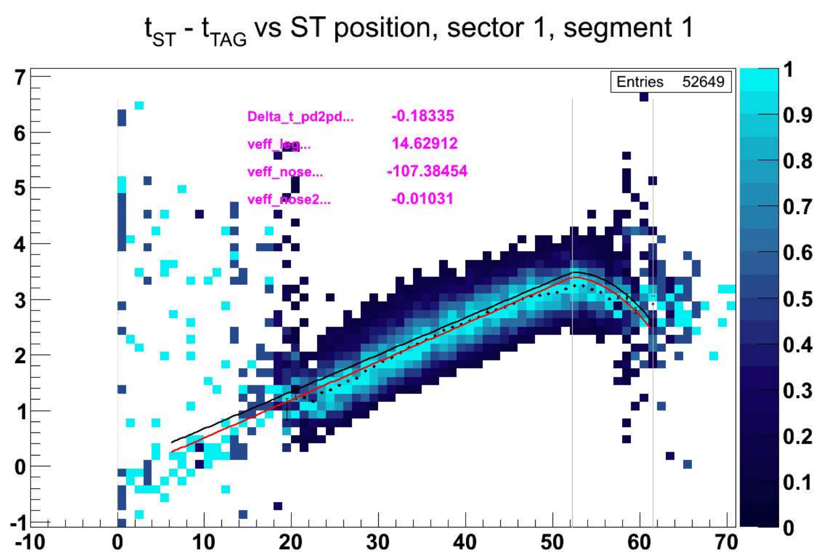

Figure 3.5: Timing difference of the start counter and tagger versus the start counter position for sector 1, segment 1. The black curve represents the old calibration result and the red curve represents the new calibration result using Eq. 3.12. Figure taken from O. Cortes. [95]

Another alignment necessary for the start counter is the start counter timing relative to the RF timing. Here, the propagation time corrected time difference, Δt^c, between the start counter event vertex time and the RF event vertex time for each start counter paddle was used. The time difference is fitted with a Gaussian to obtain K_{RF} as the mean value. The width of the Gaussian gives a start counter time resolution of about 300 ps. The calibration of the start counter propagation velocity can be seen in Fig. 3.5.

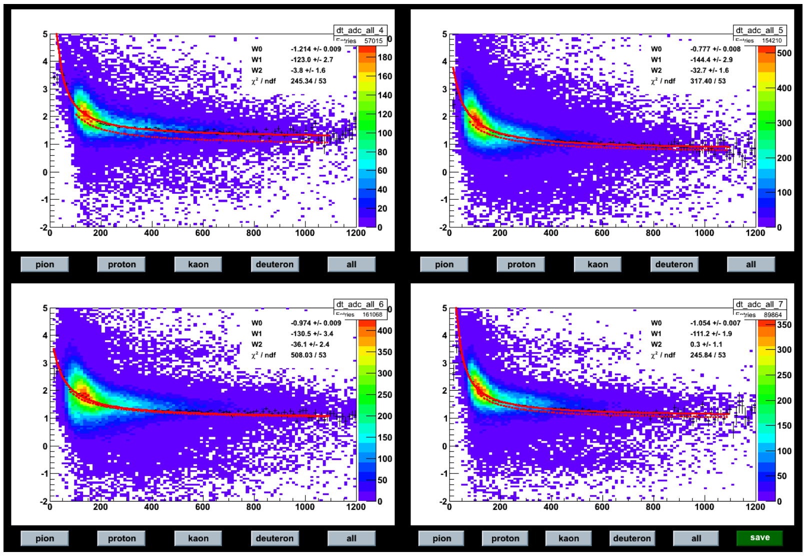

Figure 3.6: An example of the start counter timewalk correction for sector 2, all four paddles. Each panel shows the time difference between the start counter and tagger (in ns) versus the energy deposit (in ADC channels) for a different paddle. The red curves are the fits applied. Figure taken from O. Cortes. [95]

The start counter has a time-walk correction which was determined by studying the time walk as a function of the pulse height. A time-walk correction refers to a correction for a timing shift that was introduced by leading-edge discriminators. The mean values of the time-walk corrections were extracted for each ADC channel for the different paddles by a fit described by the equation:

$$\Delta t^w = W_0 + \frac{W_1}{A - W_2} \ , \tag{3.13}$$

where Δt^w is the time difference of pulses with different amplitudes that will cross a predetermined threshold at different times for the leading-edge discriminators (LED) fed into the TDCs of CLAS [94], A is the ADC channel, and W_0, W_1, and W_2 are time-walk calibration constants that were determined by the fits. An example of the start counter time-walk calibration can be seen in Fig. 3.6.

3.5 Drift Chamber Calibration

The calibration of the drift chambers allowed for correctly reconstructing the particle track through the six superlayers in each sector. The track reconstruction started with hit wire pattern recognition or segment finding within each superlayer, then the linking of these segments within a sector. Track candidates were then fit to the hit positions on the wires, a procedure known as "hit-based" tracking. The particle momentum was reconstructed with a resolution $\frac{\sigma_p}{p} \approx 2\%$ using hit-based tracking, the precision largely due to the small size of the drift cells and the large number of wire layers in the drift chambers. [96]

Once other detector systems of CLAS had gone through some iterations of their calibrations, a more complete calibration of the drift chambers was then carried out. The timing information from the other detectors in combination with the drift chamber wire hit times was used to obtain the electron drift times from the location of the distance of closest approach of the track to the sense wire, which allowed for more precise reconstruction of the track position within each layer. The hit positions in every drift cell were fit in a procedure known as "time-based" tracking, which gave the final charged track three momentum with a resolution of $\frac{\sigma_p}{p} \approx 0.5\%$. [96]

The drift chamber calibration also included a time-walk correction, magnetic-field corrections associated with the Lorentz angle of tracks passing through the high field region of the Region 2 drift chambers, and a time correction for the flight time of the particle from the event vertex to the hit position in every layer [96]. The time-to-distance relation was determined by fitting an empirical function [96]. The quality of the calibration was studied by requiring the residual (time difference between the position determined by the track fit and the distance from the timing information and time-to-distance function)) to have a

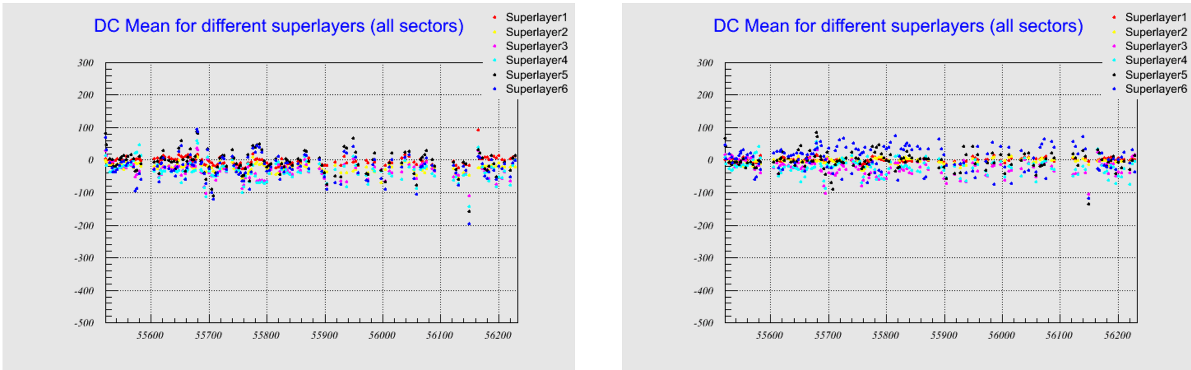

(a) Before DC Calibration (b) After DC Calibration

Figure 3.7: Mean value of the residuals for superlayers 1 to 6 versus run number. For most runs all residuals are close to zero after the DC calibration. Figure taken from S. Park [97].

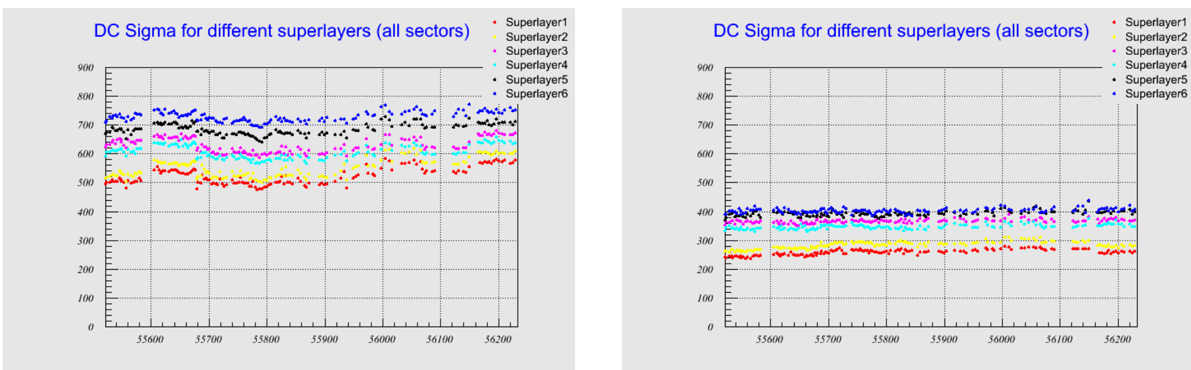

(a) Before DC calibration (b) After DC Calibration

Figure 3.8: Sigma of the residuals for superlayers 1 to 6 versus run number after the DC calibration. Figure taken from S. Park [97].

small width, σ, and to be centered at zero, as shown in Figs. 3.7 and 3.8. The calibration constants used for time-based track reconstruction were extracted by fitting a distribution of the residuals as a function of drift time with a predetermined function. [96]

3.6 Time of Flight Calibration

The TOF detector was previously described in Section 2.4.4. The TOF system was calibrated to ensure that the time of the particle's arrival at a paddle and the energy deposited in the same paddle were reconstructed to a high accuracy. The calibration began with the energy calibration of the TOF. This required a determination of the pedestals for each ADC channel, which corresponded to the baseline response of the ADC with no track hit present. The pedestal information was determined multiple times during the running of the experiment to account for any baseline shifts with time. The pedestal data was loaded into the TOF ADCs, and the ADCs were operated in a pedestal-subtracted mode. The conversion of the TOF ADC values to energy in MeV can be written as:

$$E = \frac{10(A - P)}{A_{NMIP}}, \tag{3.14}$$

where A is the ADC value of the hit in channels, P is the pedestal, and A_{NMIP} is the pedestal-subtracted ADC value that corresponds to a normally incident minimum ionizing particle (NMIP) in MeV, which deposits $\approx$ 10 MeV in the 5 cm thick TOF scintillator material.

A pulser calibration run was carried out to calibrate the TDC channel-to-time conversion. Pulsed logic signals were delivered simultaneously to all of the TDC channels over their full dynamic range. This allowed for a fit to be performed to fix the TDC channel to time conversion for every channel. Once this calibration was completed, the time-walk corrections, the left-right balance between the TDC times from each end of the scintillator, and the alignment of the paddle hit times to the common overall CLAS trigger time were carried out. [98]

The time-walk and the TDC left-right balance calibrations were found by using laser calibration runs where a light pulse was injected at the central part of the scintillator paddle and at a reference PMT. The pulse height measured by the ADC varied over its full dynamic range, due to the use of a neutral density filter. The time-walk calibration was then carried out by fitting the measured TDC time as a function of the ADC value. The fit is described by the following equation:

$$\Delta t^w = f^w\left(\frac{600}{V_T}\right) - f^w\left(\frac{A-P}{V_T}\right) \ , \tag{3.15}$$

with

$$\begin{aligned} f^w(x) &= \frac{w_2}{x_3^w} \ \text{ if } \ x < w_0 & (3.16) \\ &= \frac{w_2}{w_0^{w_3}}(1+w_3) - \frac{w_2 w_3}{w_0^{w_3}} + 1 \ \text{ if } \ x > w_0, & (3.17) \end{aligned}$$

where A is the ADC channel, V_T is the discriminator threshold in ADC channels, P is the pedestal value, and the w_i are the time-walk calibration constants [98]. The data used for the time-walk can also be used to correct the left-right balance of the paddle, meaning that the time offsets of the PMTs on either side of the scintillator paddle were adjusted such that they gave the same timing for tracks passing through the center of the paddle.

The attenuation length λ of each counter also had to be calibrated, meaning that the energy deposited in the paddle had to be corrected for the light loss during propagation through the paddle from the track hit point to the PMT. The attenuation is described by the equation:

$$E^{l,r} = E_0^{l,r} e^{\frac{x}{-\lambda}}, \tag{3.18}$$

where λ is the attenuation length, x is the hit coordinate along the paddle, and $E^{l,r}$ refers to the energy measured by the left and right PMT, respectively. The attenuation length of each counter was obtained in practice using the pulse heights in the left and right PMTs using:

$$\ln\left(\frac{ADC^l}{ADC^r}\right) = ln\left(\frac{E^l}{E^r}\right) = C + \frac{2x}{\lambda} \ . \tag{3.19}$$

Distributions of $\ln(ADC^l/ADC^r)$ versus x are shown in Fig. 3.9 for all of the 57 working paddles for Sector 1.

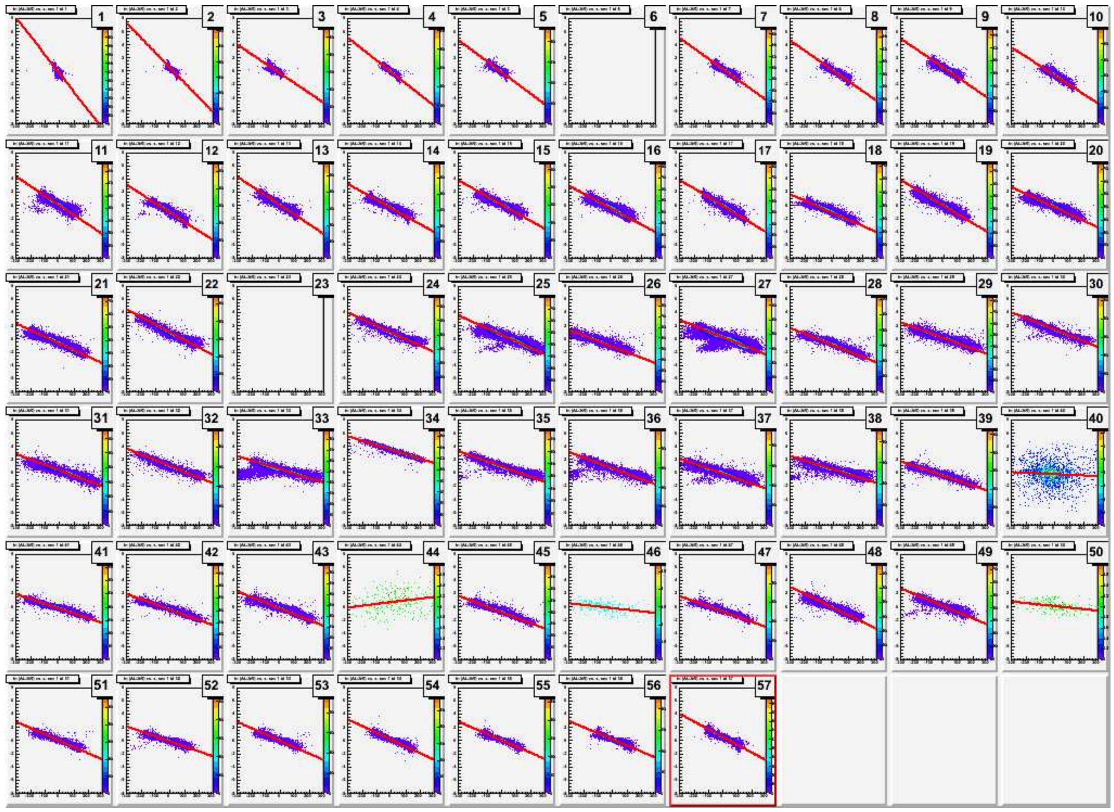

Figure 3.9: The attenuation calibration of the TOF is shown here for sector 1 and all 57 paddles of the sector are shown for run 63060. The logarithmic energy deposit measured by the left and right PMTs versus the counter position are plotted and fit with Eq. 3.19.

The effective light propagation velocity of light propagation in the scintillators was calculated by using the dependence of the hit distance of the extrapolated tracks relative to the edge of the paddle, which was found by using the drift chamber tracking of the time measured in the left and right TDCs. The position of the hit along the scintillator is given by:

$$x = \frac{1}{2v_{eff}}(\mathrm{TDC}^l - \mathrm{TDC}^r) \; , \tag{3.20}$$

where v_{eff} is the effective velocity of light propagation in the scintillator and $\mathrm{TDC}^{l,r}$ are the TOF TDC hit times. Using x determined from extrapolating the drift chamber track to the TOF counter, v_{eff} can then be determined. The effective velocity calibration is shown in Fig. 3.10. Lastly, the times of the paddles were corrected so that they were aligned to each other. The alignment was carried out by fitting Gaussians to event distributions of the difference of the measured time-of-flight and the calculated time-of-flight for every paddle, and the mean values of the Gaussians were then the calibration constants.

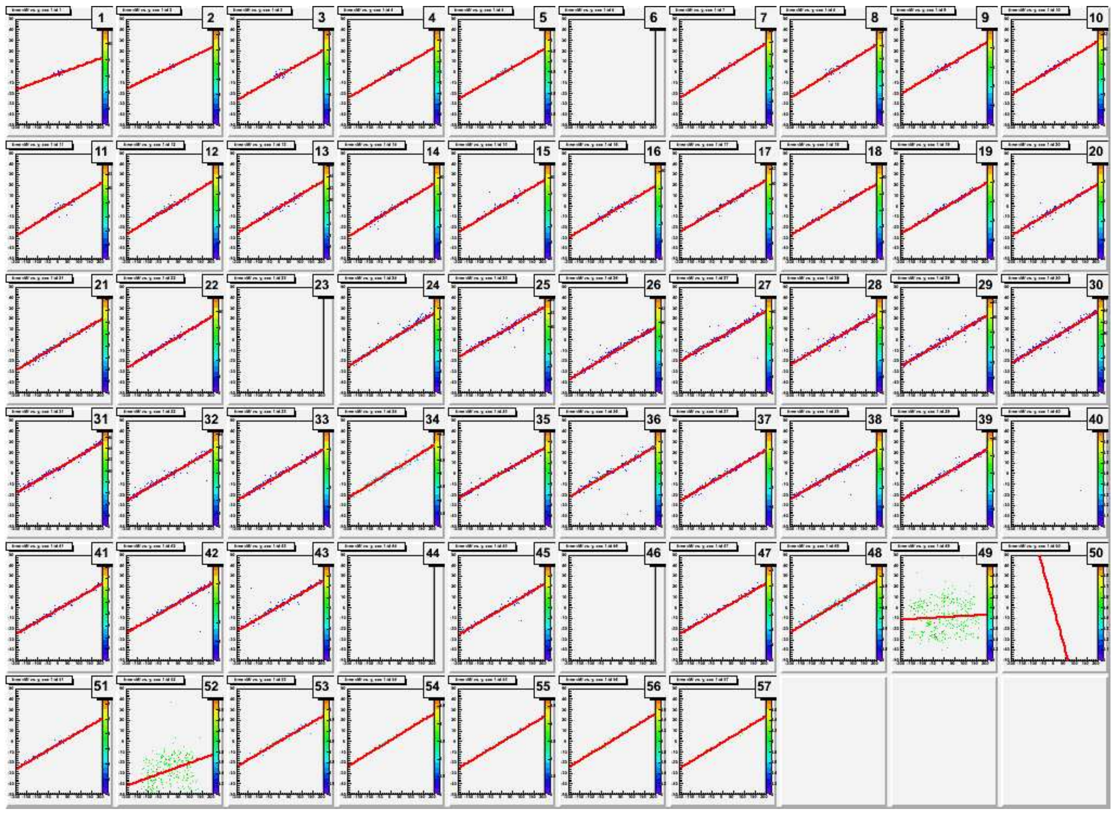

Figure 3.10: The effective propagation velocity calibration of the TOF is shown here for sector 1 with all 57 paddles of the sector shown for run 623557. The time difference of the left and right PMTs versus the counter position x are plotted and fit with Eq. 3.20. For the paddles where a fit didn't work, the fit was corrected by averaging neighboring counters.

3.7 Target Polarization Calibration

Due to the use of a polarized target, the polarization of the target must be calibrated since it is changing through out the course of the experiment. The direction of the proton polarization for this analysis was transverse to the incoming photon beam. The polarization of the target was measured with the nuclear magnetic resonance (NMR) method [85], where nuclei in a magnetic field absorb and re-emit electromagnetic (EM) energy. This energy corresponds to specific resonance frequencies, which depend on the strength of the magnetic field. During the g9b experiment, the scan over a certain frequency produced an NMR signal. The integral of the NMR signal was proportional to the polarization degree. For more details of the calibration process of the target, see Ref. [99].

Overall, the average target polarization was found to be 81% and varied in a range from 45 to 94% throughout the experiment, with the typical uncertainty being $\pm$ 1.7%. For exact numbers, see Appendix A and also Fig. 2.17.

3.8 Target Polarization Angle Offset Calibration

In addition to the careful determination of the degree of target polarization, the target polarization offset angle, ϕ_0, must also be determined. The target used in the g9b experiment was a transversely polarized butanol target. If the transverse B-field were in a vertical direction, e^+e^- pairs produced in the target would be deflected into sectors 1 and 4 of the drift chambers. Instead, the B-field was oriented at $\approx 60°$ to the horizontal, so that e^+e^- pairs were deflected into the torus coils and did not appear in the chambers. Therefore, when extracting the polarization observables, ϕ_0, which is defined in Fig. 3.11, must be known. The transverse holding coils were attached to the target cryostat and their position could not be surveyed when the target was in place. Thus, the angle ϕ_0 was determined by measuring the well-known azimuthal dependence of the polarization asymmetry for the high-rate reaction $\gamma p \rightarrow \pi^+ n$. A look into the $K^+\Lambda$ and $K^+\Sigma^0$ channel of the present analysis would prove to be fruitless, due to the low statistics of kaons. The study of ϕ_0 was done by the author, along with Michael Dugger and Ross Tucker at Arizona State University. More information can be found in Ref. [100].

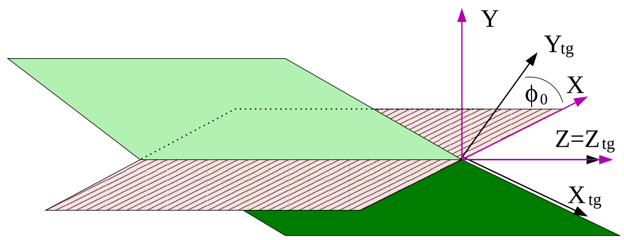

Figure 3.11: Orientation of the target plane (in green) relative to the Lab frame (in red). The target defined the target plane and is polarized along the Y_{tg} direction.

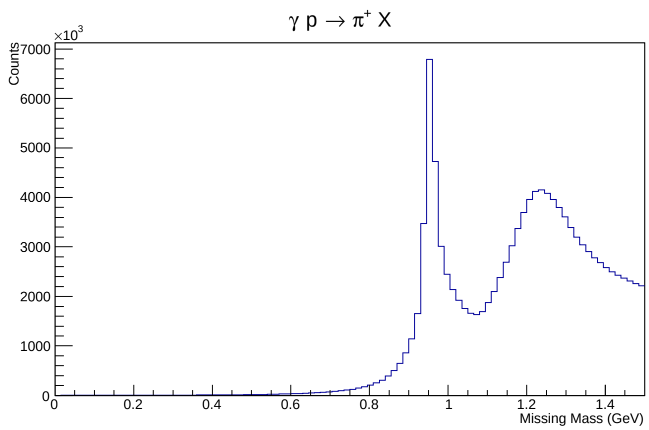

Figure 3.12: Reaction $\gamma p \rightarrow \pi^+ X$ used to calculate target polarization angle offset calibration.

The offset ϕ_0 can be measured in multiple ways and the author's approach will be presented here. A π^+ is required to be detected and in order to reconstruct the neutron, a cut on the $\gamma p \rightarrow \pi^+ X$ missing mass was made:

$$|M_{\mathrm{X}} - M_{\mathrm{Neutron}}| < 0.06 \text{ GeV}, \tag{3.21}$$

where M_X is the reconstructed missing mass and $M_{Neutron}$ is 938.565 MeV. The missing mass spectrum may be seen in Fig. 3.12. The raw target polarization asymmetry is calculated as:

$$T_{raw} = \frac{T_{pos} - T_{neg}}{T_{pos} + T_{neg}}, \tag{3.22}$$

where T_{pos} is the number of counts above the target polarization plane and T_{neg} is the number of counts below the target polarization plane. With the raw asymmetry T_{raw} calculated, it can be fit to extract the target offset, $p[0] * \sin((x - p[1]) * \pi/180) + p[2]$, where $p[0]$ is the amplitude, $p[1]$ is the phase offset or ϕ_0, and $p[2]$ is a constant offset. Figs. 3.13(a) and 3.13(b) shows examples of the raw asymmetry with the fit for different photon beam energies.

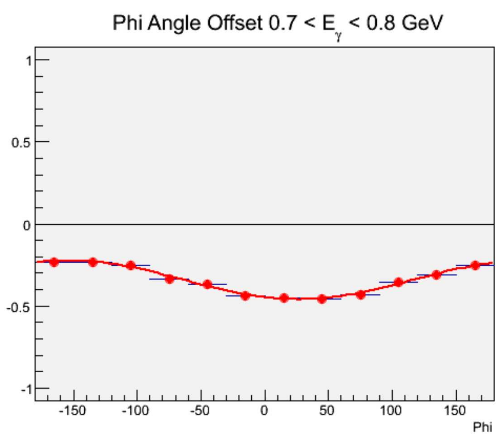

(a) ϕ_0 Study for $E_\gamma = 750$ MeV

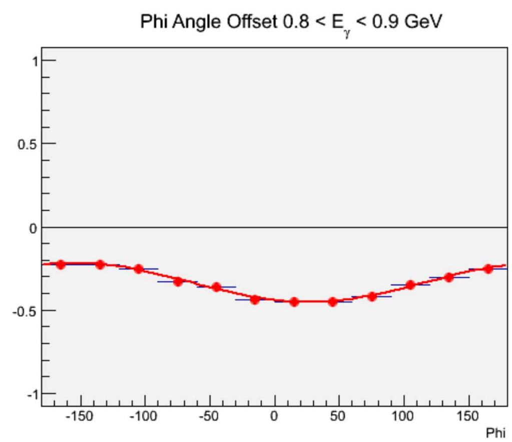

(b) ϕ_0 Study for $E_\gamma = 850$ MeV

Figure 3.13: Target offset study for two different E_γ bins. T_{raw} is shown with the data fit with the function described in Section 3.8. Offset of (a) was found to be $63.5° \pm 0.4°$ and of (b) was $64.23° \pm 0.6°$.

The final result from the author of $63.5° \pm 0.4°$ is consistent with both R. Tucker and M. Dugger's calculations. It has been determined that ϕ_0 is $63.9° \pm 0.4°$ for the g9b experiment [100].

3.9 Summary

This chapter has described how the data in CLAS was obtained and provided information about the data acquisition. Information about the processes for calibrating the CLAS detector systems was also presented. Both calibrations and data acquisition are crucial to understand how the particle identification of this current analaysis was performed, and is described in the next chapter.

Chapter 4

Event Selection

Now that the cooking and calibration of data has been described, the process for extracting the $K^+\Lambda$ and $K^+\Sigma^0$ events will be discussed. These events are necessary to measure the polarization observables. Details on the specific cuts and corrections that were made to the data set are described. The background from other contaminating reaction channels, which must be properly subtracted without eliminating too many of the events of interest will also be discussed.

4.1 Run Selection

Approximately 14 billion events were collected during the running of the g9b experiment. Both linearly ($\approx$ 7 billion events) and circularly ($\approx$ 7 billion events) polarized photons were used, but for this present analysis, only the circularly polarized runs are relevant. Circularly polarized beam data were taken at the beginning and at the end of the run period with electron beam energies of 3081.73 MeV and 2265.99 MeV, respectively, using a $10^{-4}X_o$ radiator to create the bremsstrahlung photons. The torus current was set to 1920 A and the typical electron beam current used was in the range of 8-14 nA. The nominal photon flux on the FROST target of $\approx 5 \times 10^7$ photons/s spanned the energy range from 20% to

95% E_0. Beam commissioning was done at the beginning of the experiment (runs 62187-62197) and the associated commissioning runs were excluded from the analysis since these runs were taken for testing and set-up of the target and CLAS. Other runs excluded are those where whole detector components failed, the data acquisition system failed, or where the beam was too unstable to collect events. In Appendix A, the runs used in the analysis are listed. In Table 4.1, a more detailed list of the experimental conditions pertinent to this analysis with circularly polarized photons is given. [101]

Table 4.1: Data set of the g9b experiment detailed according to various running conditions. The target polarization has two signs associated with it, the first is the NMR sign and the second is the holding magnet sign. (+ +) and (- -) means an overall positive sign and (+ -) and (- +) means an overall negative sign.

Run Range	Date Range	Events	Beam Energy	Beam Current	Live Time %	Target Pol.
62187-62197	3/18-3/19	95 M	3081.73 MeV	14 nA	0.8	(+ +)
62207-62289	3/19-3/23	723.1 M	3081.73 MeV	11.9 nA	0.82	(+ +)
62298-62372	3/24-3/30	894.9 M	3081.73 MeV	13.4 nA	0.83	(- +)
62374-62464	3/30-4/05	1129.7 M	3081.73 MeV	13.4 nA	0.78	(+ +)
62504-62604	4/07-4/13	1307.1 M	3081.73 MeV	13.6 nA	0.83	(+ -)
62609-62704	4/13-4/19	972.6 M	3081.73 MeV	13.5 nA	0.83	(- -)
63508-63525	7/28-7/30	138.2 M	2265.99 MeV	10.7 nA	0.74	(+ +)
63529-63542	7/31-8/02	166.8 M	2265.99 MeV	8.3 nA	0.74	(+ -)
63543-63564	8/02-8/05	321.7 M	2265.99 MeV	13.3 nA	0.70	(+ +)
63566-63581	8/06-8/08	249.6 M	2265.99 MeV	13.2 nA	0.72	(+ -)
63582-63598	8/10-8/12	242.3 M	2265.99 MeV	13.3 nA	0.69	(+ +)

4.1.1 Beam Trips

One problem taken into consideration throughout the duration of the experiment were the frequent beam trips. A beam trip can happen due to beam steering migration, which resulted in the electron beam being off for a few seconds or more typically up to 20 seconds. Even longer beam trips were often due a cryogenic magnet trip or a vacuum leak. Another cause of the trips was from arcing or discharge in the linac RF cavities. Beam trips affect cross-section measurements more than polarization observable measurements because the cross section depends on absolute photon flux normalization, but nevertheless should be discussed. Some analyses may remove the runs that have too frequent beam trips, however, for this current analysis, none were removed due to the low kaon statistics in CLAS. Every event was taken into consideration. An example of unacceptable beam quality can be seen in Fig. 4.1 and acceptable beam quality can be seen in Fig. 4.2.

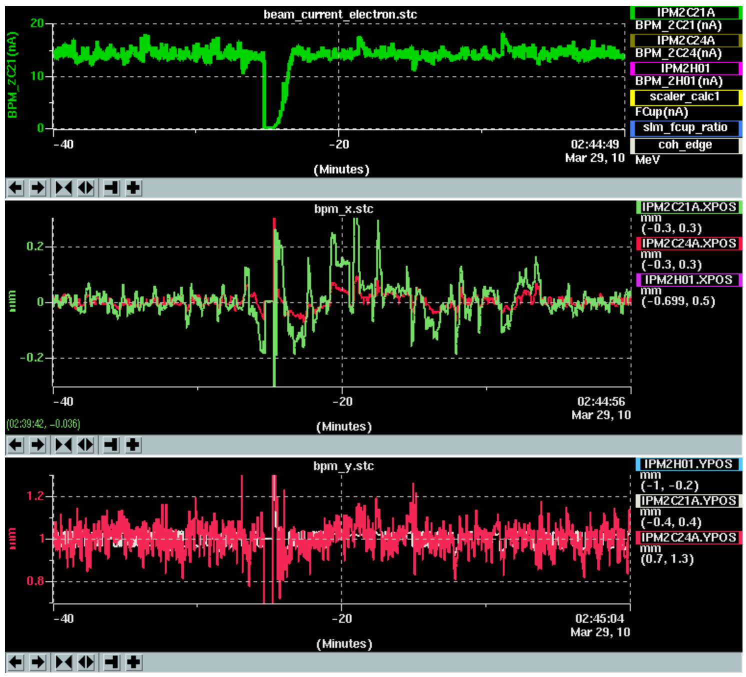

Figure 4.1: A typical stripchart of unacceptable beam quality for the FROST experiment due to the rapid fluctuations of the x-position of the beam over a short period of time. The top panel shows the beam current (nA), the middle panel shows the x-position (mm) of the beam, and the bottom panel shows the y-position (mm) of the beam.

4.1.2 Electron Beam Polarization

As previously mentioned in Section 2.5.3, the Møller Polarimeter was used to measure the electron beam polarization, which allowed for calculating the photon polarization. In order to do so, Møller runs were performed, using a different procedure than production runs. Møller runs were done every time when there was a change in beam energy or after a Hall-C spin dance (when the effect of the electron spin orientation was studied in the

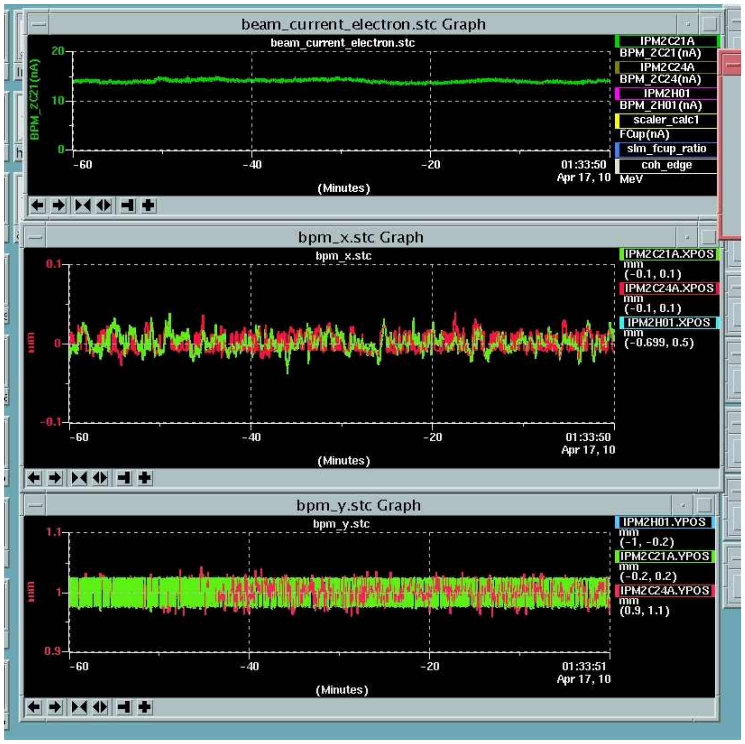

Figure 4.2: A typical stripchart of acceptable beam quality for the FROST experiment due to the stability of the beam over time. The top panel shows the beam current (nA), the middle panel shows the x-position (mm) of the beam, and the bottom panel shows the y-position (mm) of the beam.

injector). They were done with two opposite polarization settings of the Møller target, the iron foil. The measured polarization was corrected for beam charge asymmetry and shows only the statistical uncertainty, the systematic uncertainty being about 3%. The Møller runs performed during the g9b experiment are presented in Table 4.2. Typically during the whole experiment, the electron beam polarization was $\approx$ 86-88% and the beam charge asymmetry, which measured the relative difference in the number of electrons with positive or negative helicity, was $< 0.01\%$ [102].

Table 4.2: Møller measurements taken over the course of the g9b experiment. "left, negative" means the left Møller target and polarization opposite to the beam direction. "left, positive" means the left Møller target and polarization in the beam direction.

Date	Previous Run	Measured Pol.	Beam Charge Asym.	Møller Setting
2010-04-08	62530	88.1 ± 1.5%	0.008 ± 0.002%	left, negative
2010-04-08	62530	-86.5 ± 1.4%	0.008 ± 0.002%	left, positive
2010-04-19	62704	86.8 ± 1.4%	0.011 ± 0.002%	left, negative
2010-04-19	62704	-86.9 ± 1.3%	0.011 ± 0.002%	left, positive
2010-07-30	63525	-88.6 ± 1.5%	-0.039 ± 0.002%	left, negative
2010-08-11	63594	87.1 ± 1.5%	0.004 ± 0.001%	left, negative

4.2 Skimming of Data

Once the calibration and cooking were completed to satisfaction, an initial filter to select the events of interest was applied to the data, which is referred to as *skimming*. Skimming the data resulted in a reduction in the file size, which made the analysis easier to handle and quicker to process in computing time. In the cooking, the SEB package was used for particle identification. However, the SEB package does not necessarily have to be used for particle identification in the analysis since other banks contain similar information, obtained in a slightly different way. There are various skims that were applied to the g9b data set. One skimmed data set had a filter over kaon events based on the SEB particle identification [89]. Another skimmed data set had a filter over the GPID bank [91], which is based on a particle identification scheme using momentum dependent mass cuts. In Fig. 4.3, one can see the difference between the GPID skim, kaon skim, and an unskimmed file, referred to as DST, which contains a larger set of banks for all events. The author chose to use the GPID skimmed data set as it appeared that the kaon skimmed data set was losing more events due to tight cuts being applied and the DST files were too large for a reasonable computing time. The GPID skims have no cuts on event topology, only less bank information such that cuts were applied at the author's discretion.

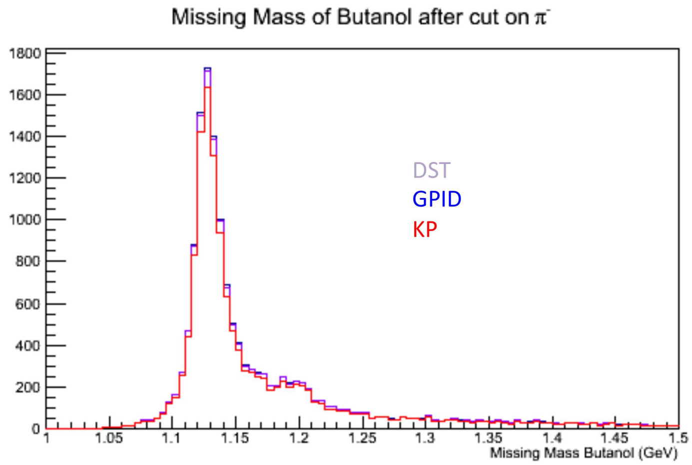

Figure 4.3: The difference of skimmed files for the $\gamma p \to K^+\Lambda$ reaction is shown. The gray line refers to the DST skimmed data set, the blue line to the GPID skimmed data set, and the red line to the kaon skimmed data set. Ultimately, the GPID skimmed data set was used in this analysis.

4.3 Photon Selection

One must carefully select the proper photon to be used in the analysis of each event. The same photon should be used for every particle track in the event and should have a coincidence time of ± 1 ns between the photon arrival time at the interaction point and the vertex time of the reconstructed tracks. This coincidence requirement allowed for reducing background and random electron hits that were not associated with the bremsstrahlung photon interacting in CLAS. The T-counter time information can help determine the beam bucket associated with a given photon. Occasionally, more than one electron in a given beam bucket interacted with the radiator, such that more than one bremsstrahlung photon was created. This happened with a frequency of < 1 %, which is deduced in Fig. 4.4.

The RF time associated with the beam bucket arriving at the tagger was then used to calculate the resulting time of the photon that arrived at the FROST target. This time, the 'tagger vertex time' t_γ, included a small correction for the propogation time of the photon from the center of the target to the interaction point, which was the start position of the

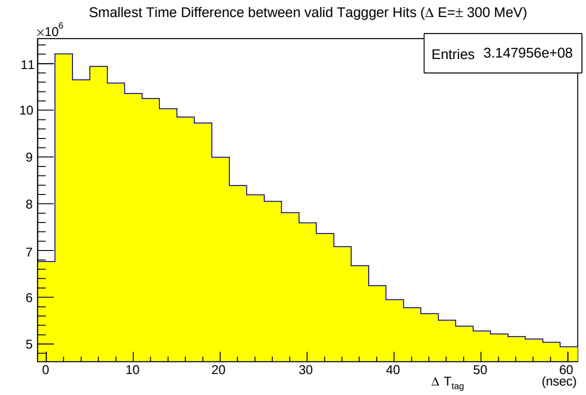

Figure 4.4: The smallest time difference between valid tagger hits is shown here. More than one electron would occasionally interact with the radiator and created more than one bremsstrahlung photon, but less than 1% of events had more than one photon during the g9b experiment.

reconstructed event vertex. t_γ gave the most exact timing of the event start time, since the correct photon has been correlated to the event. The event vertex time, t_ν, of the reaction is given by:

$$t_\nu = t_{ST} - \frac{d}{c\beta_{calc}} \ , \tag{4.1}$$

where t_{ST} is the time measured by the scintillators of the start counter with respect to the global start time, d is the length of the track from the particle vertex to the start counter paddle obtained from tracking and β_{calc} was described in Section 3.2.2. To further attempt to calculate the coincidence time, the calculated arrival time of the photon at the event vertex, t_γ, was calculated using:

$$t_\gamma = t_T + \frac{Z}{c}, \tag{4.2}$$

where t_T is the photon arrival time at the center of the FROST target and Z is the distance of the event vertex along the beam axis (determined from the extrapolated track to the beamline) relative to the center of the FROST target. Because the photon beam spot size was small (on the order of 1 cm), the x and y offsets of the event vertex were neglected.

Finally, the coincidence time, ΔT, may be calculated by

$$\Delta T = t_\nu - t_\gamma \ . \tag{4.3}$$

To see that the correct photon and coincidence time was chosen, one can plot the time difference, ΔT, as seen in Fig. 4.5. The fact that ΔT is centered around zero gives proof that the track is associated with the beam photon. The small peaks on either side of zero occur every 2.004 ns, originating from electrons that were in different beam buckets. One should note that the trigger records events over a 20 ns time window, which is why the other beam buckets can be seen. If the coincidence time is outside of the 2.004 ns range, then the event was removed from the analysis.

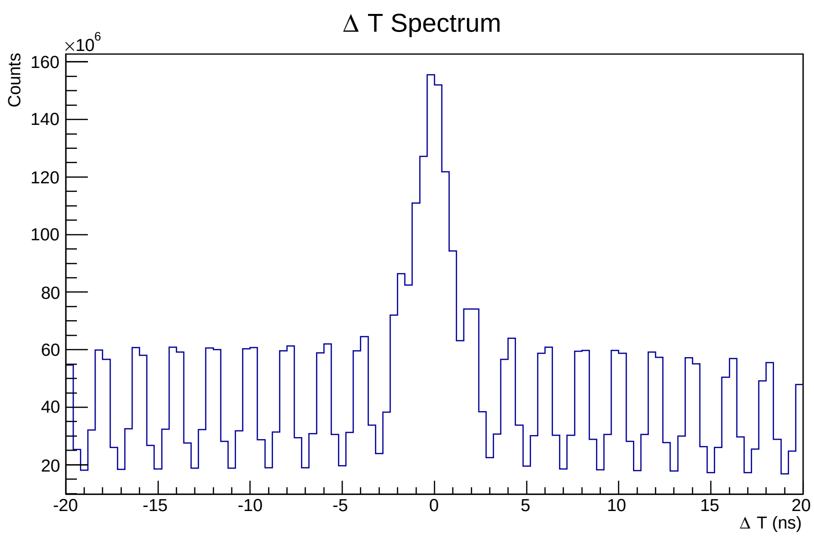

Figure 4.5: The timing difference, ΔT, between the reconstructed vertex time and the photon time measured by the tagger. The characteristic 2 ns beam 'bucket' structure can also be seen.

4.3.1 Accidental Events

It could also happen that events were present in the data sample where two beam photons within a time coincidence of ± 1 ns. Multiple electrons in a given beam bucket might create bremsstrahlung photons in the radiator, which then leads to multiple photons within the same 2.004 ns interval. In addition, background hits in the T-counters might also happen in the same time window. These events have been discarded from the analysis since it is very difficult to distinguish which photon actually caused the interaction given the 300 ps resolution of the start counter. If the wrong photon is selected, the reaction will not be properly reconstructed.

4.3.2 Tagger Sag

The initial energy calibration for the tagger E-counters neglected the fact that the three pairs of aluminum rails holding the detectors were not perfectly rigid, but sagged slightly (up to a few mm) under the weight of the detectors. The physical distortion has been referred to as the 'tagger sag'. The sag moved the narrow E-counters from their nominal location, which caused them to detect electrons at slightly different energies from their design values. This was found in previous CLAS experiments and discussed in Ref. [103]. Previous experiments dealt with the sag in their individual analyses, however now the sag is accounted for and corrected in the reconstruction code.

4.4 TOF Corrections

Further time-of-flight corrections for specific TOF paddles for the charged tracks were found to be necessary due to incomplete timewalk corrections that were determined during the laser calibration of the detector, discussed in Section 3.6. Due to the fact that ≈ 20 % of the fibers from the lasers to the TOF scintillators were broken, time-walk corrections could not be determined directly for the affected counters. Aneta Netz from USC did a study of the ΔTOF in ns for every paddle in every sector. ΔTOF is the difference between calculated and measured flight time, $\Delta\mathrm{TOF} = \frac{d}{\beta_{calc}} - \frac{d}{\beta_{meas}}$, where d is the path length of the track from identified p, π^+, and π^- events from the event vertex to the TOF paddle and β_{calc} and β_{meas} were given earlier.

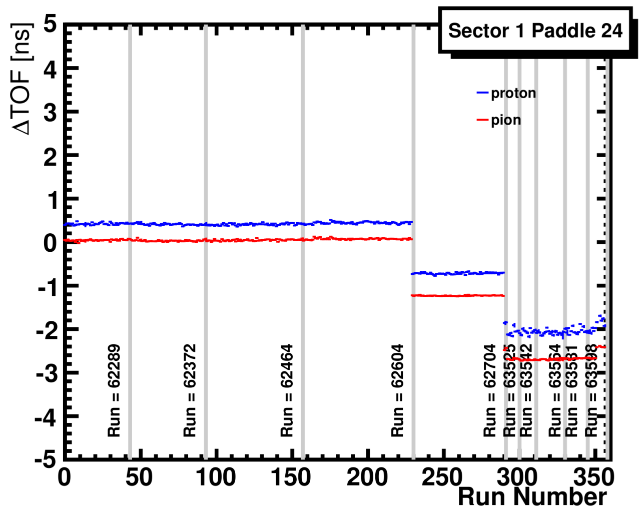

Figure 4.6: ΔTOF (ns) versus the run number is shown over the course of the g9b experiment for sector 1, TOF paddle 24. A clear discrepancy is seen between the protons (blue line) and pions (red line) and also an overall offset. Figure taken from A. Netz [104].

In Figs. 4.6, 4.7, and 4.8, some of her results are shown, which make the use for a time-offset correction obvious.

Also, in Fig. 4.9, one can clearly see the problem of a specific TOF paddle for β versus momentum. Therefore, a time-offset correction function that was based on energy loss in the poorly calibrated TOF paddle was employed. This correction code was developed by Franz Klein from the CUA group and was used in the present analysis [105]. Due to the low statistics of kaons, it is preferable to use a final state reaction with sufficient statistics, such as $\gamma p \rightarrow p\pi^+\pi^-$ to determine the correction. By looking at this reaction, it is possible to cut out backgrounds associated with electron and positron tracks, using a cut on $\beta \approx 1$ and low momenta. In addition, a cut on the difference between the vertex positions of the three particles, p, π^+, and π^- and also on the missing 4-momentum, was used to identify the reaction. The identification was not always unambiguous because if both positive tracks have low momentum, usually either can be assigned to a proton or pion. In this case, the event was discarded.

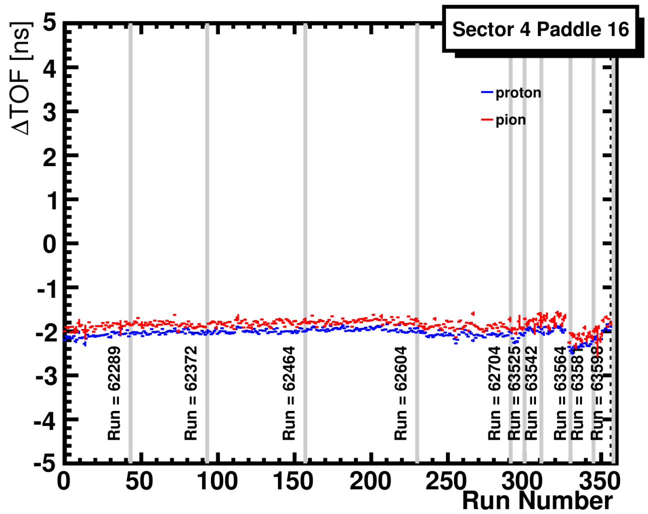

Figure 4.7: ΔTOF (ns) versus the run number is shown over the course of the g9b experiment for sector 4, TOF paddle 16. A clear offset of 2 ns is shown here. Figure taken from A. Netz [104].

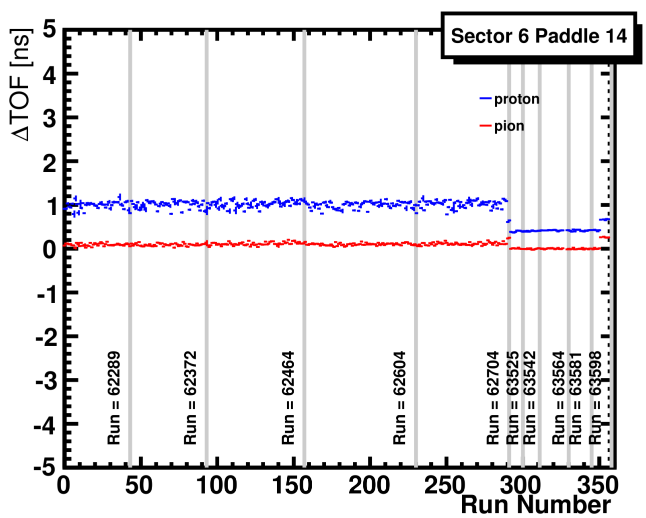

Figure 4.8: ΔTOF (ns) versus run number is shown over the course of the g9b experiment for sector 6, TOF paddle 14. A clear discrepancy is seen between the protons (blue line) and pions (red line). Figure taken from A. Netz [104].

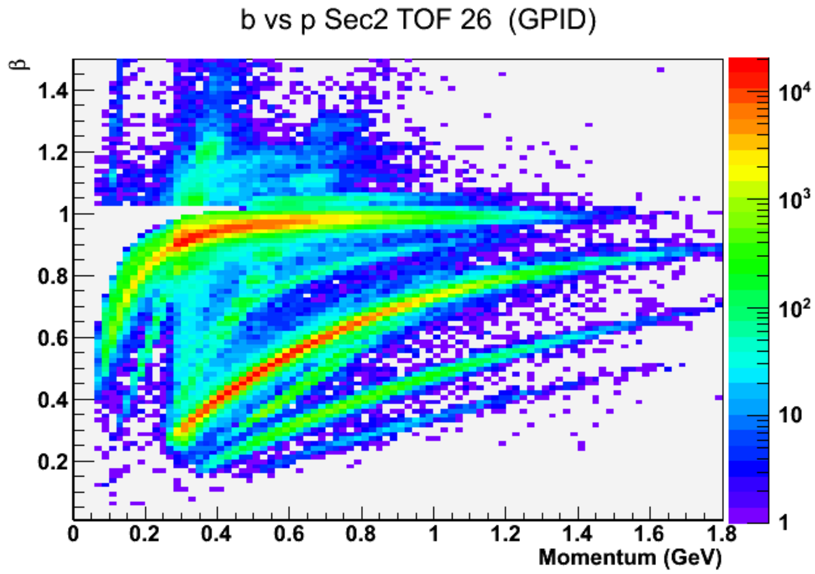

Figure 4.9: β versus momentum for sector 2, TOF paddle 26 can be seen with background, a broad pion band, and a shadow bands (out of time hits). The hole around β=1 at low momenta is due to electrons being cut out of the spectrum. Figure taken from F. Klein [106].

In the actual procedure, time shift corrections (time offsets) are determined and the time shift was used to recalculate a new measured β. Then a momentum dependent fit can be applied to the energy loss in the time-of-flight paddles for protons and pions. The same can be done for the start counter paddles and the energy loss of those paddles compared to the momentum spectrum. That is to say, if the energy deposited in the TOF paddle is out of range (where the range is the expected range of the energy deposited as a function of momentum), the range was corrected by using the corresponding bands of energy deposited in the start counter instead. Using the time difference, ΔT, between the newly recalculated measured time and expected flight time for the particle for each TOF paddle, one can fit ΔT in order to get an empirical time-walk correction function, as described in Eqn. (3.17). An example of the corrections applied can be in seen in Fig. 4.10. [105]

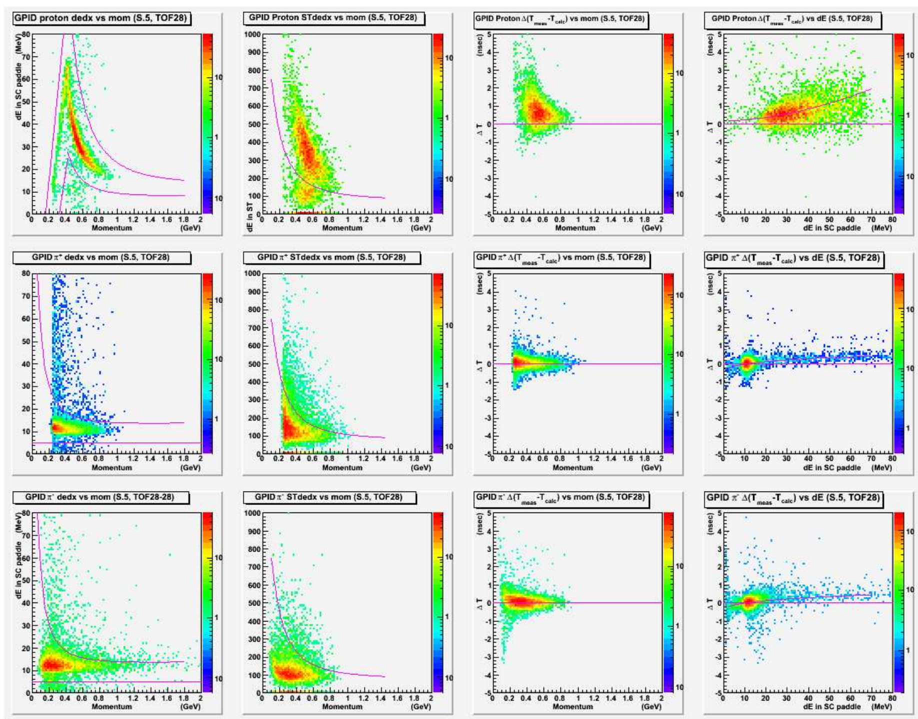

Figure 4.10: An example of the corrections applied can be seen for sector 5, TOF paddle 28. The first row is for protons, the middle row is for π^+, and the bottom row is for π^-. The first column shows plots of the energy deposit versus momentum for TOF. The second column shows plots of the energy deposit versus momentum for the start counter. The third columns shows plots of the measured and calculated difference in the TOF versus momentum. The fourth columns shows plots of the measured and calculated difference in the TOF versus energy deposit in the TOF. The magenta lines in the figures are the ranges assigned for pions or protons (first two columns) and for the time difference to be at zero (last two columns). Figure taken from F. Klein [106].

Another time-of-flight issue was the poor performance of various counters associated with dead, noisy, or low gain PMTs. These problematic counters were identified by studying the reconstructed hadron mass versus counter number for all six sectors as shown in Fig. 4.11. One can also look at the missing mass of Λ and Σ^0 for both detected kaons and protons per paddle to identify poorly performing TOF counters. Table 4.3 shows the list of TOF paddles removed from the analysis due to identified problems.

Sector 1	no paddle cuts
Sector 2	24, 44, 45, 49, 51
Sector 3	22, 38
Sector 4	15, 48, 49, 53
Sector 5	22, 50-55
Sector 6	12, 13, 49, 53, 56

Table 4.3: List of the poorly performing TOF paddles for each sector that were cut from this g9b analysis.

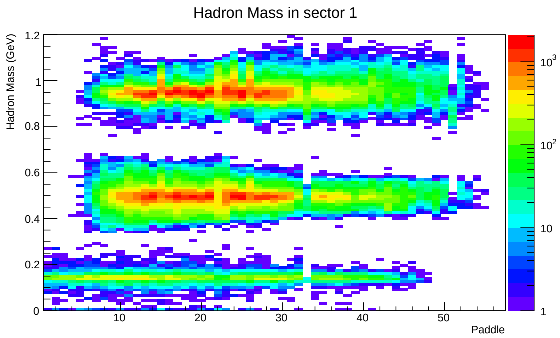

(a) Sector 1

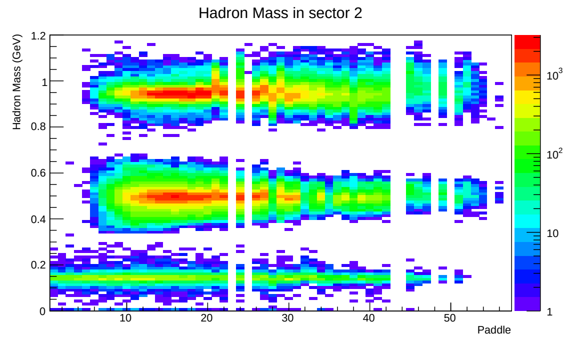

(b) Sector 2

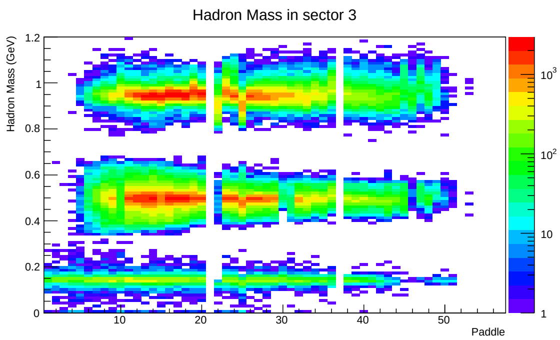

(c) Sector 3

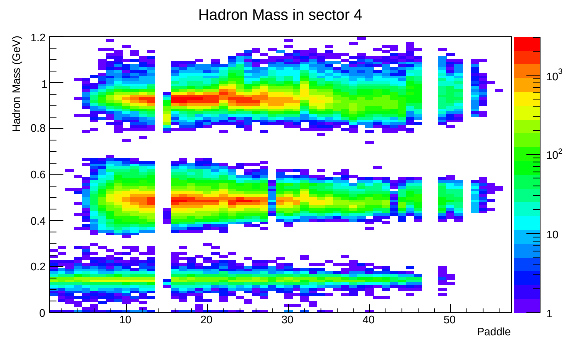

(d) Sector 4

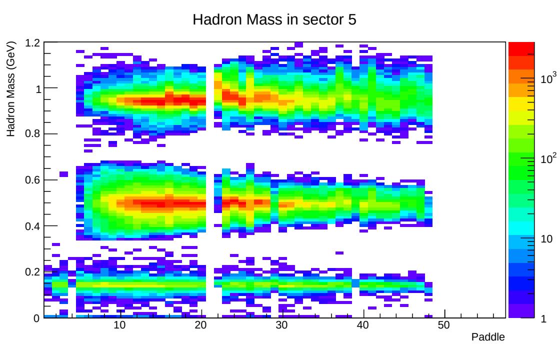

(e) Sector 5

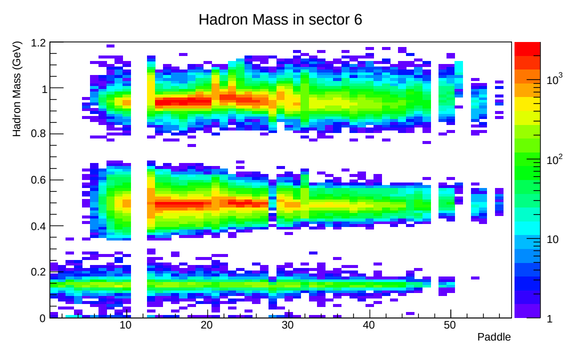

(f) Sector 6

Figure 4.11: The hadron mass distributions versus TOF paddles for each sector before any corrections were applied. A white vertical stripe designates a malfunctioning paddle that were cut from this analysis.

4.5 β cuts

In most analyses, one uses the timing information from the various detectors to clearly identify the reconstructed charged hadrons as pions, protons, or kaons. The CLAS detectors give timing and tracking information, which then allows the mass for each charged track to be calculated. The track velocity β can be calculated using:

$$\beta = \frac{v}{c} = \frac{d}{ct}, \tag{4.4}$$

where d is the path length of the track from its vertex to the TOF, and t is its associated flight time. With the track velocity calculated, the mass, m_c, of the particle can be calculated using the relativistic momentum equation:

$$|\vec{p}| = \gamma m_c \beta c = \frac{1}{\sqrt{1-\beta^2}} m_c \beta c, \tag{4.5}$$

which can easily be written in the form:

$$m_c = \sqrt{p^2 \frac{1-\beta^2}{\beta^2 c^2}}. \tag{4.6}$$

Unfortunately, due to the finite momentum and timing resolution of CLAS, and hence a finite mass resolution, backgrounds were present where the K^+ candidates were actually misidentified protons or pions. To reduce the fraction of misidentified particles, distributions of the measured β versus the measured momentum of the particles can be studied, as shown in Fig. 4.12(a). By looking at the plot, one can see clear bands related to certain particles, specifically for protons, kaons, and pions. Cuts around the bands can be made to improve the sample purity by using the following requirements:

$$\begin{aligned} & \beta_{min} < \beta_{meas} < \beta_{max} \\ \text{with} \qquad & \beta_{min} = \frac{p}{\sqrt{p^2 + m_{min}^2}} - c_{min} \\ \text{and} \qquad & \beta_{max} = \frac{p}{\sqrt{p^2 + m_{max}^2}} + c_{max} \ . \end{aligned} \tag{4.7}$$

where c_{min} and c_{max} are offsets of β in order to widen the range at larger momenta and m_{min} and m_{max} define mass ranges, which depend on the considered particle type. The above equation allows for cuts based on momentum dependent mass ranges and offsets. The mass ranges are between 0.11-0.2 MeV for pions, 0.44-0.55 MeV for kaons, and 0.85-1.05 MeV for protons. After the time-of-flight corrections were applied, as discussed in Section 4.4, the kaon momentum was examined and a loose cut was applied to have a minimum momentum of 0.1 GeV applied to the kaon only.

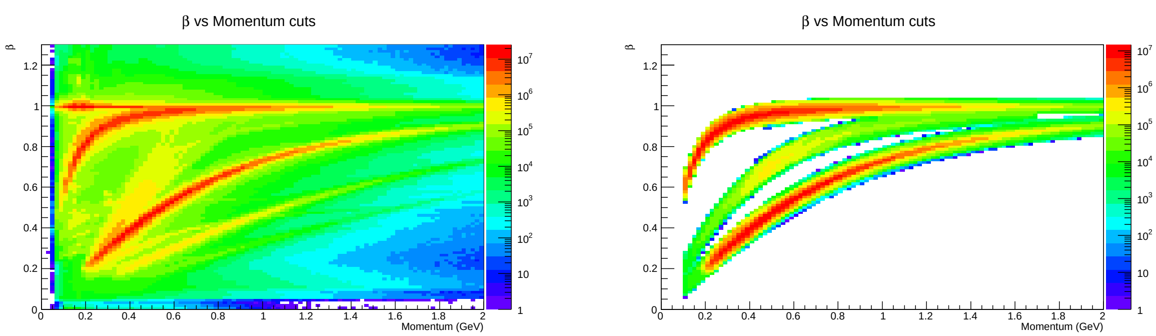

(a) Before (b) After

Figure 4.12: β versus momentum plots before any cuts or corrections were applied (a) and after mass range cuts on pions, kaons, and protons (b) were applied. The band in the top corresponds to pions, the middle band corresponds to kaons, and the bottom band corresponds to protons.

The improvement in particle identification is obvious by looking at the β versus momentum plot after the $\Delta\beta$ cut. The $\Delta\beta$ cut refers to taking the difference in the calculated β and the measured β, which should be zero ideally. A one dimensional plot of the $\Delta\beta$ cut can be seen in Fig. 4.13 and a two dimensional plot of $\Delta\beta$ versus momentum can be seen in Fig. 4.14. The $\Delta\beta$ cut seemed to clear up the particle identification. This cut can be done for all particles, but more specifically for kaons and protons, the main particles of this analysis. After the kaon $\Delta\beta$ cut, we can see a clear improvement in the K^+ identification as seen in Fig. 4.15(a), but the horizontal band around 0.1 GeV is still present, which is why a minimum momentum cut was applied to kaons.

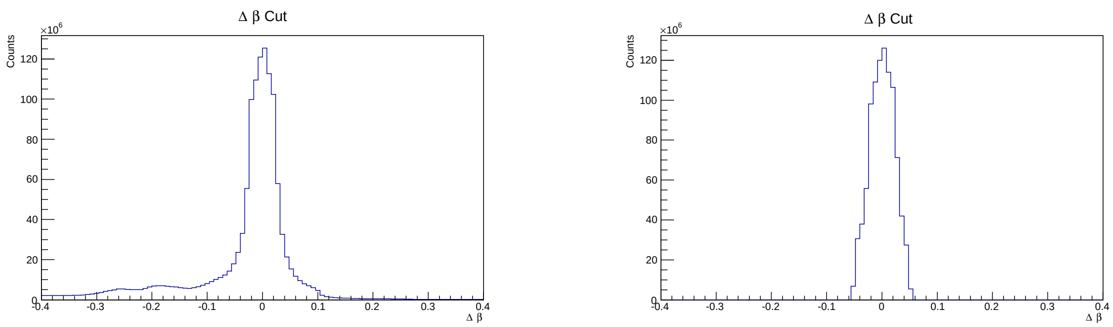

(a) Before (b) After

Figure 4.13: The $\Delta\beta$ cut one-dimensionally for all particles before (a) and after the cut (b).

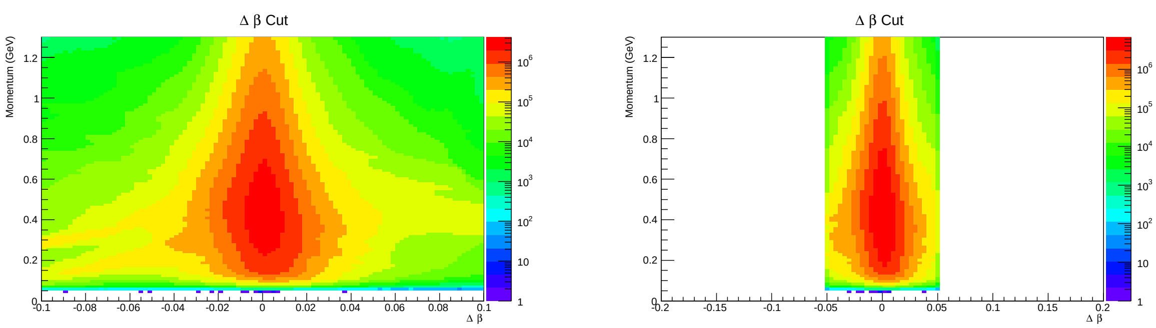

(a) Before (b) After

Figure 4.14: The momentum versus $\Delta\beta$ for all particles before (a) and after the cut (b).

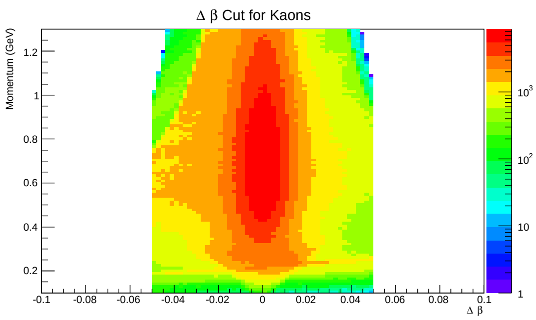

(a) Kaons

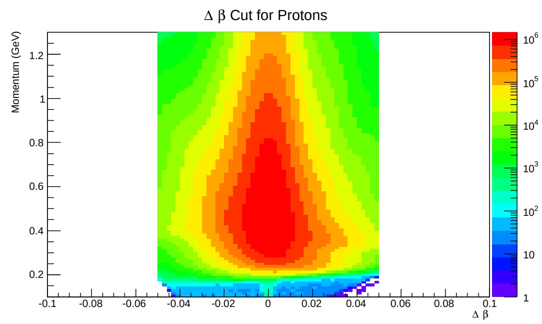

(b) Protons

Figure 4.15: The momentum versus $\Delta\beta$ cut for all kaons (a) and protons (b) after the momentum corrections are applied.

4.6 Fiducial Cuts

Geometrical fiducial cuts were applied to eliminate events where the detected particles fell into a region of CLAS where the acceptance was small and changed rapidly. This was the case near the edges of the CLAS drift chambers because the charged particle has partly avoided detection or failed track reconstruction due to the particle hitting a support frame or the cryostats of the torus magnet. Particle tracks in this region often have large reconstruction uncertainties.

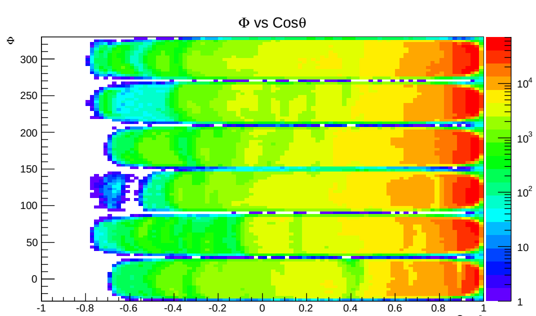

(a) Before Fiducial Cut

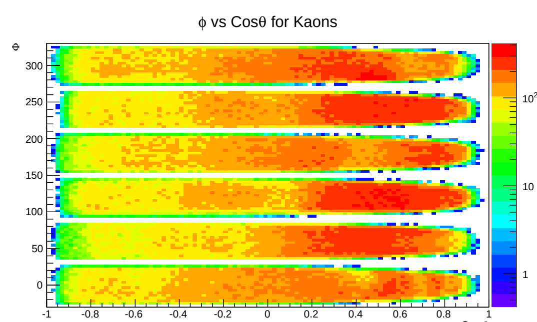

(b) After Fiducial Cut

Figure 4.16: ϕ versus $\cos\theta$ in all six sectors for all reconstructed kaon candidates before (a) and after (b) the fiducial cuts were applied.

The fiducial cuts used in this analysis were developed by looking at the azimuthal and polar angle distributions of the reconstructed tracks. In Fig. 4.16, the azimuthal distribution fits of the six sectors of CLAS can clearly be seen. The coverage of the drift chambers can be determined by looking at the azimuthal angle of the reconstructed track as a function of the polar angle. One can also see the angular coverage of the torus magnet cryostats, which results in stripes of low to no statistics. The torus coils can be seen at $\phi = 30°$, $90°$, $150°$, $210°$, $270°$ and $330°$. The equation used to define the fiducial cuts for each sector were given by:

$$|\phi_{sector}| < \begin{cases} 0 & \text{for} \quad \theta < \theta_{min} \\ \phi_{max}\left(\frac{\theta_{meas}-\theta_{min}}{\theta_{max}-\theta_{min}}\right)^{1/4} & \text{for} \quad \theta_{min} < \theta < \theta_{max} \\ \phi_{max} & \text{for} \quad \theta > \theta_{max} \end{cases}, \tag{4.8}$$

where ϕ_{sector} is the local relative azimuthal angle within a sector ranging from $-30°$ to $30°$, ϕ_{max} is the maximum ϕ_{sector} for the sector, θ_{min} is the minimum θ of the sector, θ_{max} is the maximum θ of the sector for which the correction is performed, and θ_{meas} is the measured θ from the reconstruction code. By using the equation, the fringe regions of low and variable acceptance were eliminated. The nominal values of θ_{min}, θ_{max}, and ϕ_{min} are given in Table 4.4.

Table 4.4: The parameters of the geometrical fiducial cuts for the positively charged tracks.

θ_{min}	θ_{max}	ϕ_{max}
9°	40°	25°

4.7 Energy Loss Corrections

When charged particles travel through matter, they lose energy due to ionizing or exciting the atoms in the material. The mean rate of energy loss can be described by the Bethe-Bloch formula [107]:

$$-\frac{dE}{dx} = \frac{Kz^2Z}{A\beta^2}\left[\frac{1}{2}\ln\frac{2m_ec^2\beta^2\gamma^2T_{max}}{I^2} - \beta^2 - \frac{\delta}{2}\right] , \tag{4.9}$$

where A is the atomic mass of the absorber, Z is the atomic number of the absorber, I is the mean excitation energy, z is the charge of the absorber, T_{max} is the maximum kinetic energy which can be given to a free electron in a single collision, and K is a constant that depends on the classical electron radius, Avogadro's number, and the mass of the electron. A software package, eLoss, was developed by Eugene Pasyuk at ASU to correct for the energy loss due to charged particles traveling through matter [108]. The eLoss package returns the particle momentum at the original creation point in the target. Since the momentum of a charged particle in CLAS was determined by tracking it through the drift chamber hits in the torus field, the drift chamber reconstruction software returns a value for an effective momentum between the Region 1 and Region 3 drift chambers, without energy loss. The eLoss software package calculates the path length of the particles in every material along the track between the event vertex and the Region 1 drift chambers such as the air gap before the Region 1 drift chambers, the start counter, the scattering chamber, the target cell wall, and the target material between the target wall and event vertex. The energy lost through each material is corrected depending on the particle mass and its measured momentum. In Fig. 4.17, the energy loss for reconstructed kaons and protons versus the particle's momentum is shown.

Some analyses apply energy loss corrections to all the particles because it is assumed that the associated tracks begin at the event origin. Due to the decay length of the Λ, $c\tau$=7.89 cm [5], and the decay $\Lambda \to p\pi^-$, the eLoss correction was only applied to the

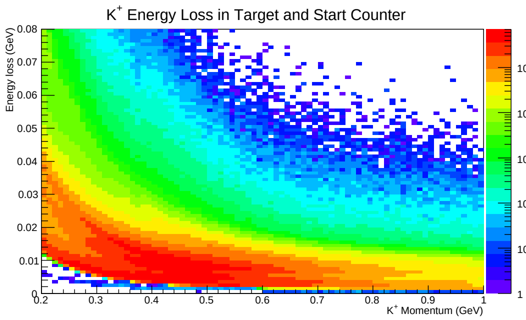

(a) Kaons

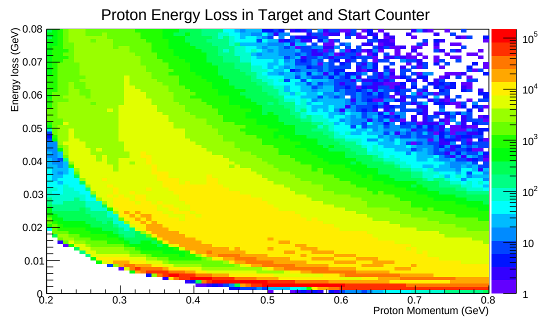

(b) Protons

Figure 4.17: Energy loss for reconstructed kaons (a) and protons (b) versus the momentum. In the proton (b) figure, two bands can be seen, which are due to the fact that the Λ can decay inside or outside of the target.

kaon along its full path, whereas the proton's energy loss was calculated from the Λ decay vertex, which was determined as follows: the vertex of the proton was calculated using its intersection with the Λ path, which was found by taking the opposite of the kaon vector in the center-of-mass frame. In theory, a point of intersection exists, but in practice, the point of the closest approach between the proton and the Λ paths was taken as the proton vertex and then the proton energy loss correction was applied. The correction eLoss was applied to particles before the final missing mass cuts were applied, as described in Section 4.10. The effect of energy loss correction, momentum correction, time-of-flight corrections, and missing mass cut (on π^-) can be seen in Fig. 4.18.

4.8 Event Vertex Cut

Another cut that needed to be applied after skimming the data is a cut on the event vertex, which established that the correct reconstructed event vertex location was consistent with particles produced within the FROST target. As previously mentioned in Section 2.7.3, the FROST target was a 5 cm long butanol target with its center at the center of CLAS (i.e. z=0). In Fig. 4.19, the butanol target and the carbon disks can clearly be seen along with

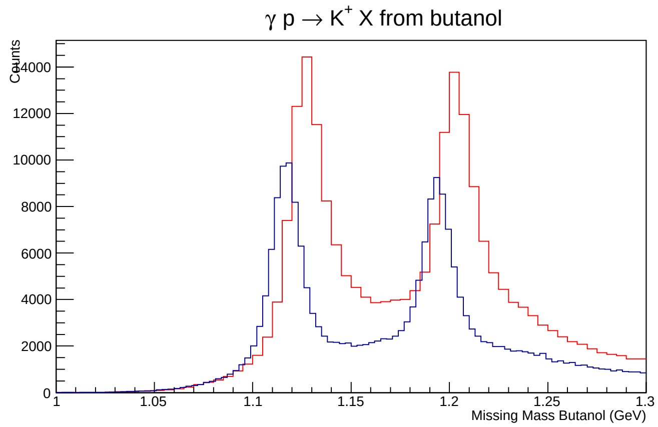

Figure 4.18: The comparison between events without eloss (red line) and events with eloss, TOF corrections, and momentum corrections applied (blue line) for $\gamma p \rightarrow K^+\Lambda$ can be seen. By including eloss and TOF and momentum corrections, the peak of the Λ and Σ^0 signals agree with the mass values from Ref. [5].

the heat shields present in the cryostat. The cuts that were applied to the butanol target were between -2.6 to 2.6 cm in the z-direction. The carbon foil target fell between 8.4 to 10.0 cm in the z-direction and the CH_2 target between 15.3 and 16.3 cm in the z-direction. The purpose of the different targets will be explained later in Section 4.11.

4.9 Momentum Corrections

The reconstructed momenta required small corrections for two reasons: one due to the fact that the torus field map was based on calculations for a single sector assuming that all magnet coils and all material inside the field were symmetric with respect to the six-fold sector geometry of CLAS and secondly, due to ambiguities in the drift chamber alignment that resulted in small shifts of momentum components of the order of 0.1 %. If one looked into the missing mass distributions as a function of ϕ, a clear azimuthal dependence was present, so a momentum correction was applied to remove these effects. The author worked with Michael Dugger from ASU and Priya Roy from FSU to devise corrections to be used

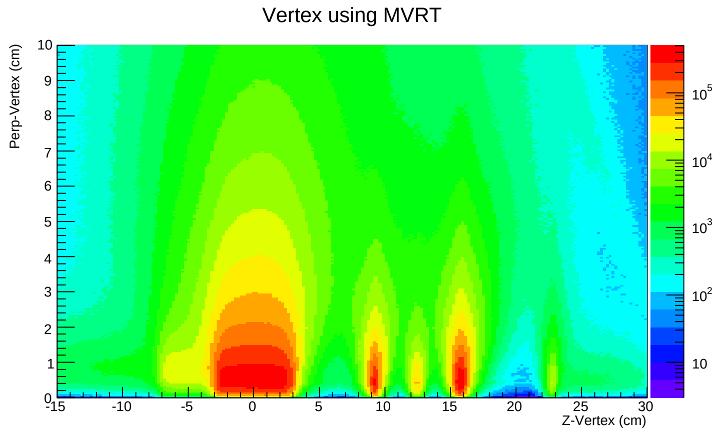

Figure 4.19: The vertex distribution of the reconstructed tracks. Around z=0, is the butanol target. To the right of the butanol is the carbon disk, heat shield, CH_2 disk, and heat shield in that order.

for the g9b experiment, and full details may be found in [109]. M. Dugger developed a two stage process to ensure the most accurate momentum corrections, starting with his reaction of $\gamma p \rightarrow \pi^+ n$, which yielded a momentum correction for the π^+ as a function of ϕ. The initial result before any correction can be seen in Fig. 4.20.

To find a correction for the proton, the reaction $\gamma p \rightarrow \pi^0 p$ was investigated, and more details can be found in Ref. [109]. In order to determine the correction, the azimuthal angle versus the difference between the calculated proton momentum and the momentum computed based on the reconstruction polar angle was studied. For each azimuthal angle bin, the average momentum difference was used to correct the measured proton momentum.

For the first stage, the momentum corrections were assumed to be only a function of the azimuthal angle ϕ. One can see the effect of these corrections for $\pi^+ X$ in Fig. 4.21, which shows that the new mass distributions have less dependence on the azimuthal angle. [109]

To remove the remaining azimuthal dependence, a second stage of corrections was applied, where the data was binned in momentum, polar angle, and CLAS sector, and a linear regression was used to decide the momentum correction for each bin. [109] The momentum

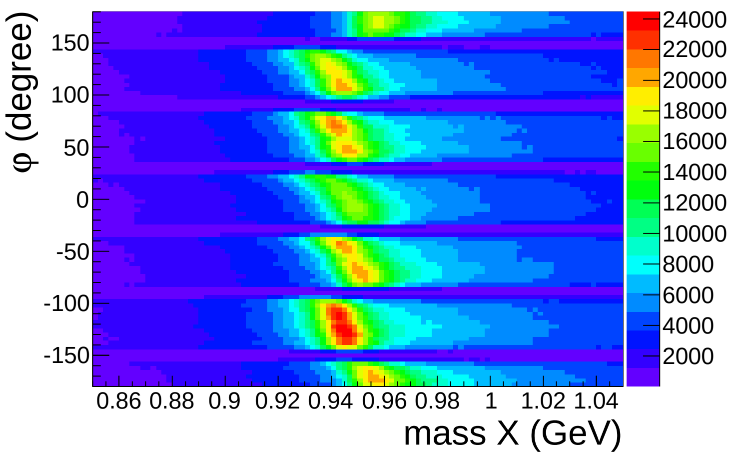

Figure 4.20: Azimuthal angle versus missing mass for the reaction $\gamma p \to \pi^+ X$ with no momentum corrections except for energy loss in the target and start counter. Figure taken from [109].

correction was taken to be:

$$\Delta P = m\phi + b, \tag{4.10}$$

where ϕ is the local azimuthal angle of the particle within a given sector (ranging from -30° to +30°), m the slope, and b the intercept. [109] In order to solve for m and b, the following equations were considered:

$$\begin{aligned} <\Delta P> &= m <\phi> +b && (4.11)\\ <\phi\Delta P> &= m <\phi^2> +b <\phi> . && (4.12) \end{aligned}$$

These two equations give rise to two unknowns, which can be solved:

$$\begin{aligned} m &= <\phi\Delta P> - <\delta P> <\phi> / <\phi^2> - <\phi>^2 && (4.13)\\ b &= <\Delta P> <\phi^2> - <\phi\Delta P> <\phi> / <\phi^2> - <\phi>^2 && (4.14) \end{aligned}$$

These two unknown terms were calculated for each bin of momentum, polar angle, and

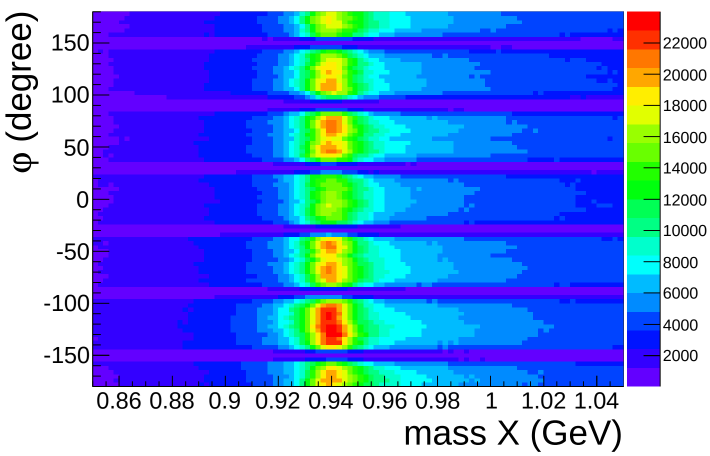

Figure 4.21: Azimuthal angle versus missing mass for the reaction $\gamma p \rightarrow \pi^+ X$ initial stage one momentum corrections were applied. Figure taken from [109].

sector. If N is the number of counts within any particular bin, we can see that:

$$< \Delta P > \;=\; N(\text{weighted by } \Delta P)/N \tag{4.15}$$

$$< \phi > \;=\; N(\text{weighted by } \phi)/N \tag{4.16}$$

$$< \phi\Delta P > \;=\; N(\text{weighted by } \phi\Delta P)/N \tag{4.17}$$

$$< \phi^2 > \;=\; N(\text{weighted by } \phi^2)/N. \tag{4.18}$$

These weighted equations described in Eqs. 4.15 to 4.18 are functions of a variable in missing mass X, which varies based on the final state reaction. To find the desired events, a mass dependent fraction of signal to total counts was created, which is denoted as F_S. The mass distribution was fit to the sum of a Gaussian and a third degree polynomial, where the resulting Gaussian was divided by the same mass distribution in order to calculate F_S. The weighted mass dependent count distributions that were used in the linear regression are multiplied by F_S to isolate the signal events. Once the weighted equations were setup, m and b were calculated. Even though F_S removes events that were not close to the desired signal, the background under the signal was still present in the weighted equations. For b, shaping the signal by using F_S was satisfactory in deciding values. However, for m, the background under the signal was featureless in terms of the azimuthal variable and the background acts as a dilution to the real value of m. [109]

The slope can be rewritten as:

$$m = \alpha_s m_s + \alpha_b m_b, \tag{4.19}$$

where s is the signal, b is the background, and α_s and α_b were the fraction of events of type s and b, respectively. If the background was featureless with regard to the azimuthal angle, then m_b=0 and m_s=m/α_s. The final corrections may be seen in Fig. 4.22.

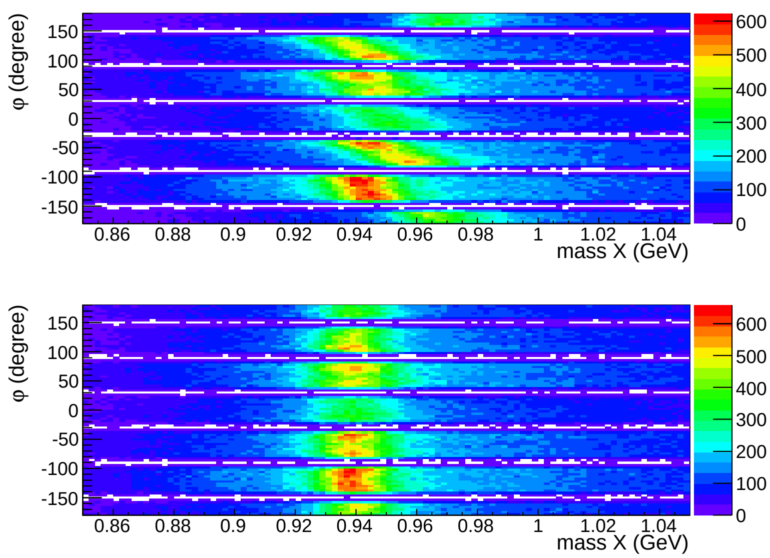

Figure 4.22: Azimuthal angle versus missing mass for the reaction $\gamma p \rightarrow \pi^+ X$ with no momentum corrections applied (top plot-before) and final (bottom plot-after) stage momentum corrections and target eLoss applied. Figure taken from [109].

Due to the low statistics of the reaction upon which this analysis is focused, momentum corrections specific to kaons were difficult to determine. Therefore, the corrections for the

π^+ found by M. Dugger were applied to the K^+. One can see the difference of the missing mass in $\gamma p \to K^+X$ with and without the momentum corrections applied in Fig. 4.23. Momentum corrections for momenta about 700 MeV and 1050 MeV can also be seen in Figs. 4.24 and 4.25 to check the validity of the corrections for different momenta. From these figures, the momentum corrected mass distributions as a function of the azimuthal angle are uniform, which implies that the π^+ correction is sufficient for K^+.

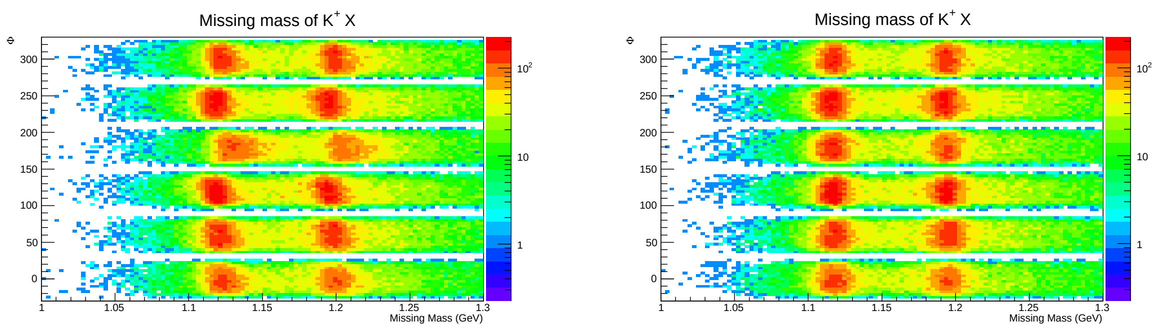

(a) Before (b) After

Figure 4.23: The azimuthal angle versus missing mass for $\gamma p \to K^+X$ before (a) the momentum corrections were applied and after (b) the corrections were applied.

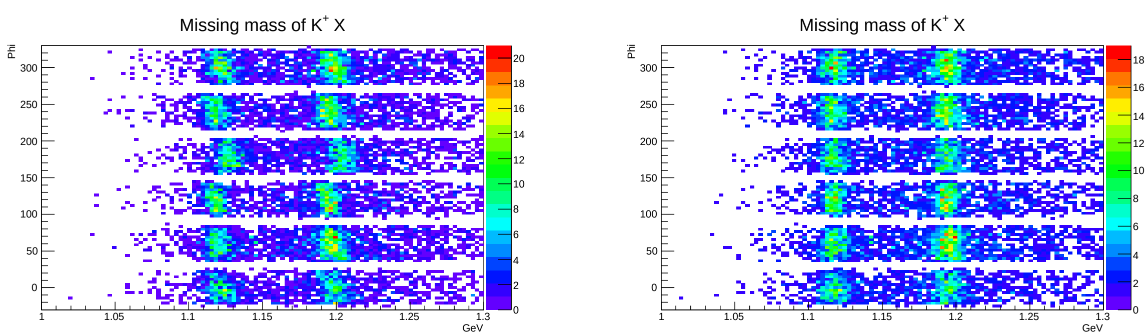

(a) Before (b) After

Figure 4.24: The azimuthal angle versus missing mass for $\gamma p \to K^+X$ for momentum about 700 MeV before (a) the momentum corrections were applied and after (b) the corrections were applied.

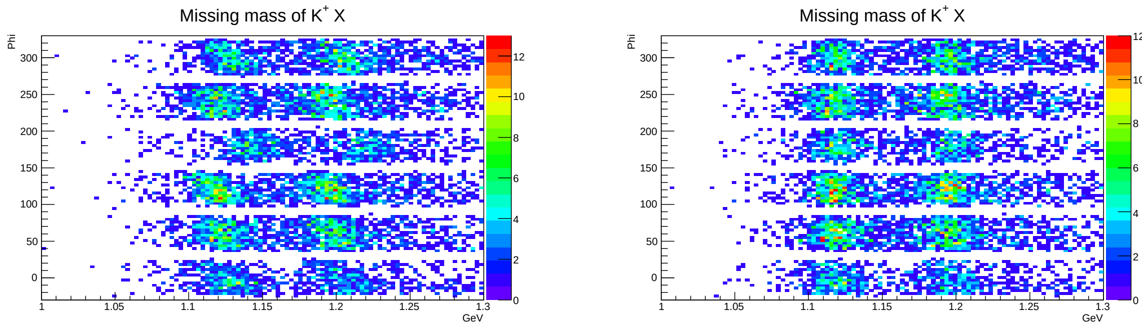

(a) Before (b) After

Figure 4.25: The azimuthal angle versus missing mass for $\gamma p \to K^+X$ for momentum about 1050 MeV before (a) the momentum corrections were applied and after (b) the corrections were applied.

4.10 Missing Mass Cuts

After the preliminary cuts and corrections were applied and the particle tracks in an event looped over, the K^+ and proton tracks were identified. While looping over the particle tracks in the event, the 4-momentum vectors were constructed, and the vertex vectors and the velocity of each particle were saved. Using this along with the tagged photon energy and the assumption the target proton was at rest, the center of mass energy associated with the $\gamma p \to K^+X$ state may be computed. The center-of-mass energy may be derived from the sum of the photon and target proton momentum vectors being conserved, which may be described as:

$$E_{CM} = M(\gamma p) = M[(E_\gamma + M_p, 0, 0, E_\gamma)] = \sqrt{(E_\gamma + M_p)^2 - E_\gamma^2}\ , \tag{4.20}$$

where the four vectors for the photon and target proton are given in the lab frame form of (E, p_x, p_y, p_z) with p_x=p_y=0 due to the beamline being along the z-axis. The invariant mass of any 4-momentum vector is given by M=$\sqrt{E^2 - p^2}$, regardless of whether the invariant mass is for a single particle or the sum of multiple particle momentum vectors. The invariant mass of the difference between the initial 4-momentum vector and the sum of the detected final state 4-momentum vectors is known as the missing mass.

The missing mass for photoproduction from a target proton at rest $\gamma p \rightarrow YX$ can be written as:

$$M(X) = M[(E_\gamma + M_p, 0, 0, E_\gamma) - p_4(Y)], \tag{4.21}$$

where X is the undetected particle, $p_4(Y)$ is the 4-momentum vector of Y, and Y is either a single detected particle or a group of detected particles. If Y is a group of particles, then $p_4(Y)$ is also used to calculate the invariant mass of these particles. In this current analysis, the missing mass of the K^+ could be equal to the mass of the Λ or the invariant mass of the proton and π^- momentum vector sum, thus $p_4(Y)$=$p_4(K^+)$. Otherwise, the invariant mass of the proton and the K^+ could be equal to the π^- mass, thus $p_4(Y)$=$p_4(K^+)+p_4(p)$. The same should be done for Σ^0 as well. The missing mass of the K^+ should be equal to the mass of the Σ^0 or the invariant mass of the proton, π^-, and γ momentum vector sum, thus $p_4(Y)$=$p_4(K^+)$. Otherwise, the invariant mass of the proton and the K^+ should be equal to the invariant mass of π^- and γ, thus $p_4(Y)$=$p_4(K^+) + p_4(p)$.

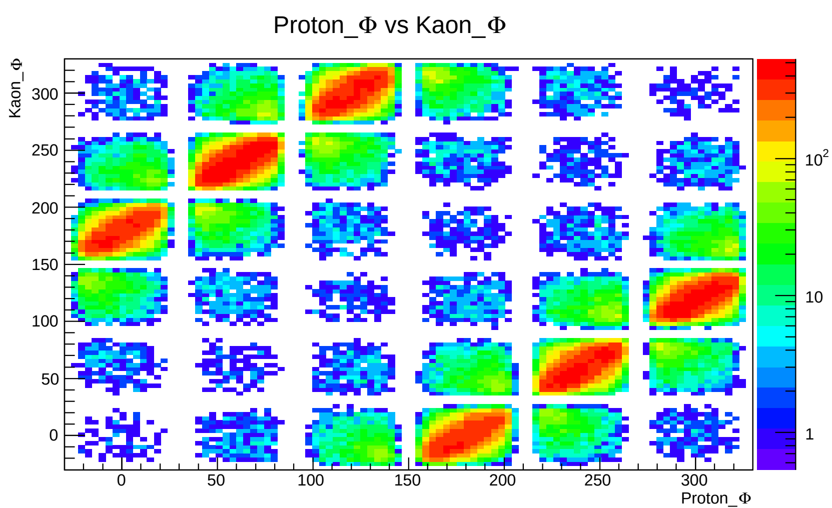

Figure 4.26: The proton and kaon tracks fall into opposite sectors. The six sectors of CLAS can be seen.

In the center-of-mass frame, the Λ must have opposite momentum to the K^+ because it is a two-particle reaction. The Λ decays into a proton and π^-, and the proton moves in a cone around the Λ direction when boosted into the lab frame. The azimuthal angle of the proton is around 180° different from the azimuthal angle of the kaon as shown in Fig. 4.26. Similarly, when the Σ^0 decays into $\Lambda\gamma$, then the Λ is moving in a cone around the Σ^0 direction when boosted into the lab frame.

In order to find the Λ decay vertex, the distance of closest approach of the proton track and the Λ direction was calculated and can be seen in Fig. 4.27 plotted versus the flight length of Λ. In principle, the proton track should intersect with the Λ propagation direction, but due to finite resolution of the detector, the tracks might not intersect. Unfortunately, the Σ^0 decay vertex cannot be determined because both decay products of the Σ^0, Λ and γ, are neutral and were not detected in CLAS.

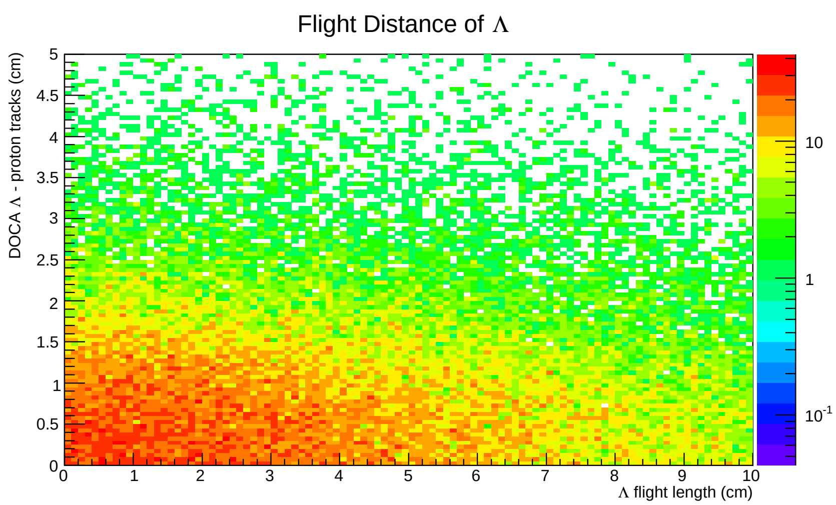

Figure 4.27: The distance of closest approach of the Λ and proton track versus the Λ flight length is shown.

The missing mass of π^- may be reconstructed after the energy loss, momentum and time-of-flight corrections were applied. As seen in Fig. 4.28(a), once a proton and a K^+ have been identified, the K^+pX missing mass distribution shows a clear peak at the pion mass. There is also a small hump, which is coming from the contribution of $\Sigma^0 \rightarrow \Lambda\gamma \rightarrow$

p π^- γ.

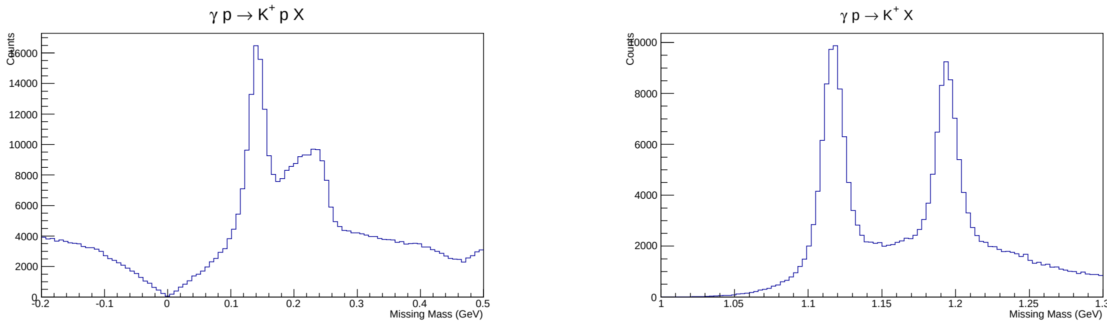

(a) $\gamma p \to K^+pX$ (b) $\gamma p \to K^+X$

Figure 4.28: The missing mass distribution for the butanol target for $\gamma p \to K^+pX$ (a) and then a cut is applied between 0.05 GeV and 0.30 GeV, which results in the distribution for $\gamma p \to K^+X$ (b).

In order to do a correct background subtraction, which will be described in Section 4.12, the contribution of the both the Λ and Σ^0 should be kept. In order to keep both signal contributions, a loose cut is made around the π^- mass between 0.05 GeV and 0.30 GeV. With this cut in mind, the Λ and Σ^0 signals can clearly be seen in the K^+X missing mass distribution shown in Fig. 4.28(b). A mass cut was then applied on the K^+ missing mass between 1.05 GeV and 1.30 GeV to select the hyperon events, and the events left in between are then used to calculate the background and the polarization observables, which will be discussed in Chapter 5. It can be seen that the Λ and Σ^0 peaks have non-negligible of background in between them. It is also useful to look at the missing mass squared of (K^+pX) versus the missing mass of (K^+X), which can be seen in Fig. 4.29 to check that the majority of the Y^* contributions (above the ground state hyperons) are cut from the analysis. When comparing Fig. 4.28 to a histogram using a pure liquid-hydrogen target, as from the CLAS experiment g1c, one can see the effect of having bound nucleons in the FROST target, as shown in Fig. 4.30. The effect of the background will be discussed next.

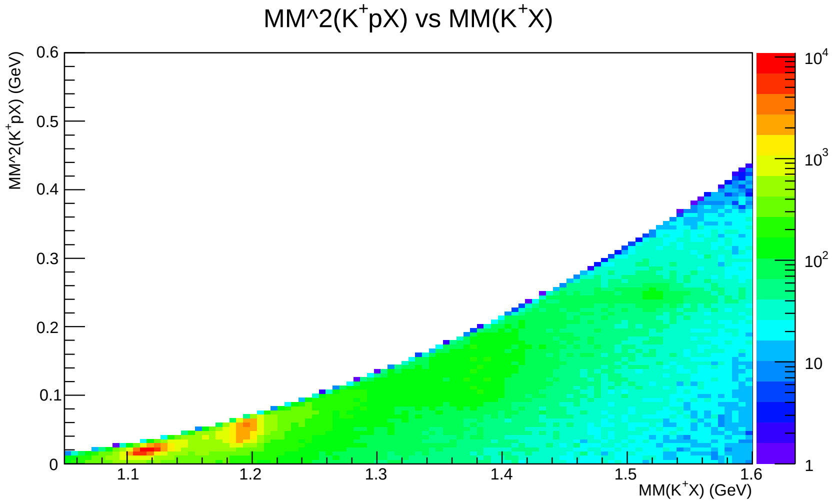

Figure 4.29: The missing mass squared of (K^+pX) versus the missing mass of (K^+X) is showing clear peaks for the Λ and Σ^0 hyperons. This plot also shows the smooth and feature background in the region above and below the hyperon peaks.

4.11 Carbon Background Study

Previous FROST analyses have used the carbon foil, described in Section 2.7, as a method for subtracting the signal from the background [110] [111]. As mentioned in Section 2.7, the FROST target has background not seen in other CLAS experiments due to the nature of the butanol target with its bound nucleons in addition to free protons. This approach was studied for the present analysis, but ultimately not used. As seen in Fig. 4.28(b), there is non-negligible background between the two hyperon mass peaks. If the same histogram using production off the carbon is studied, a different result is seen. Despite that the carbon foil target having only 5% of the density of the butanol target, Fig. 4.31 shows the result that quasi-free kaon production is suppressed on carbon [112].

When comparing the butanol target missing mass histograms to that of the carbon target missing mass histograms, there is a clear difference regarding the number of events as shown in Fig. 4.32. The carbon signal is barely seen in comparison to the butanol signal. Previous analyses such as [110] and [111] use the carbon events to scale it accordingly to

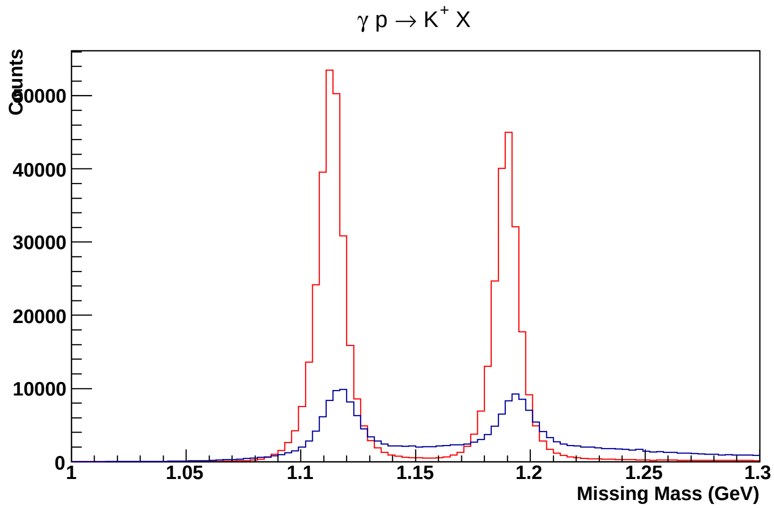

Figure 4.30: The missing mass distributions for $\gamma p \to K^+X$ for the g9b experiment using a butanol target (blue line) compared to the g1c experiment using a pure hydrogen target (red line). The g1c experiment had more events and much less background than the g9b experiment.

the butanol events to find a scaling or dilution factor. With this in mind, the author attempted to scale the carbon to the butanol over a large E_γ range. This scale factor was studied for the missing mass of K^+X, but due to the low statistics on carbon, the method was discarded because the resulting dilution factor was too uncertain. It also appears that there was an angular dependence of the scaling factors, shown in Fig. 4.33, but due to the large statistical uncertainty, a new more treatable method for dealing with the background subtraction was investigated, which is discussed in Section 4.12.

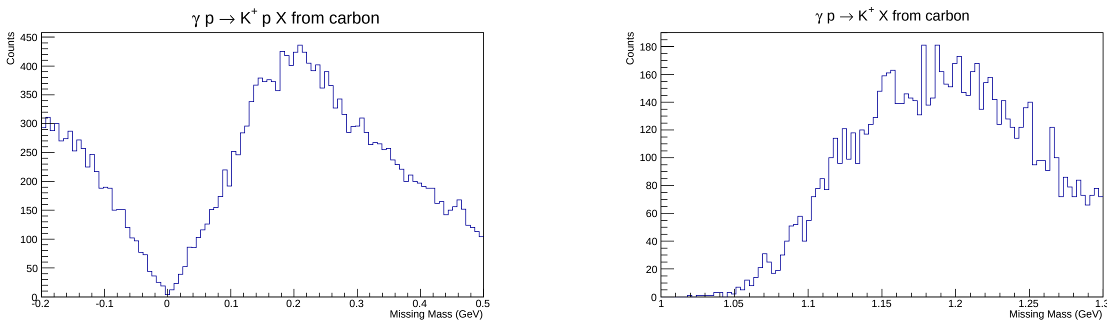

(a) $\gamma p \rightarrow K^{+}pX$ (b) $\gamma p \rightarrow K^{+}X$

Figure 4.31: The missing mass distribution for the carbon target for $\gamma p \rightarrow K^{+}pX$ (a) and then a cut is applied between 0.05 GeV and 0.30 GeV, which results in the distribution of $\gamma p \rightarrow K^{+}X$ (b).

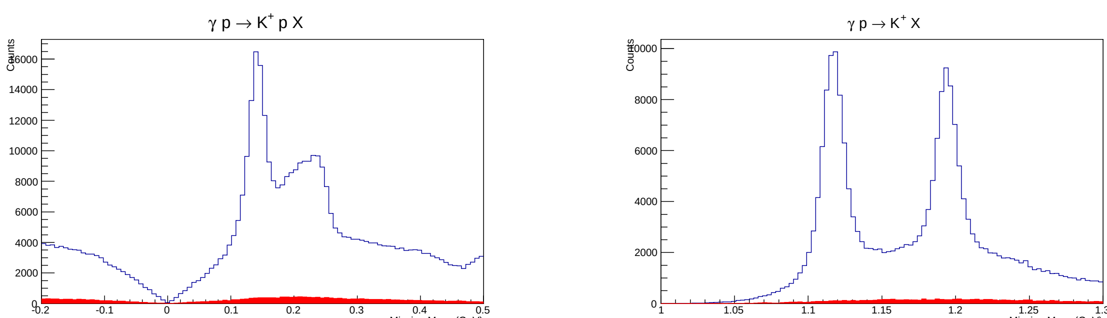

(a) $\gamma p \rightarrow K^{+}pX$ (b) $\gamma p \rightarrow K^{+}X$

Figure 4.32: The missing mass distribution for both the butanol (blue line) and the carbon (red line) target for $\gamma p \rightarrow K^{+}pX$ (a) and then a cut is applied between 0.05 GeV and 0.30 GeV, which results in the distribution of $\gamma p \rightarrow K^{+}X$ (b). There are clearly insufficient statistics from the carbon target compared to the butanol target assuming other parameters are properly normalized.

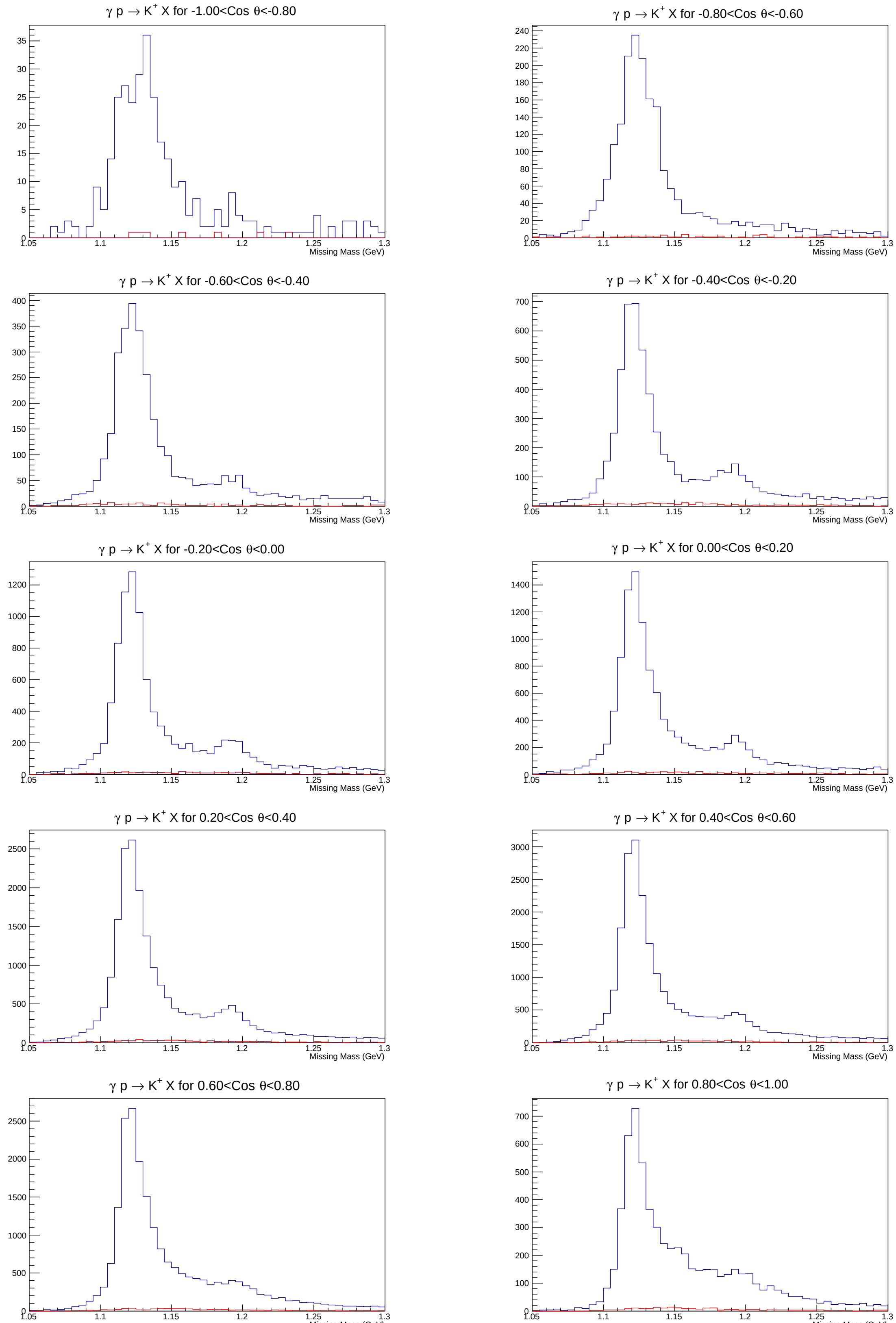

Figure 4.33: Missing Mass for $\gamma p \rightarrow K^+X$ with a cut on $|MM(K^+pX) - m_\pi| < 0.045$ GeV binned in $\Delta\cos\theta$=0.2 for all energies. The butanol events are in blue and the carbon events are in red.

4.12 Background Subtraction

As just described, the carbon background subtraction method given the small statistics cannot be used to subtract the background beneath the Λ and Σ^0 peaks for this analysis. Instead, an empirical fit function was used to separate the hyperon signals from the underlying background. The specific procedure for calculating the polarization observables will be described in Chapter 5. The Λ and Σ^0 peaks in the $\gamma p \to K^+ X$ missing mass spectrum were fit using Gaussian functions for the peak plus a constant background:

$$g_p(x) = c_p e^{-\frac{(x-m_p)^2}{2\sigma_p^2}} + b_p \ , \tag{4.22}$$

where p=(Λ, Σ^0), c_p are the amplitudes, m_p are the peak centroids, σ_p are the peak widths, and b_p are constant offsets. After disabling the peak entries in the histogram in the range $m_p - 2\sigma_p$ to $m_p + 2\sigma_p$ for both peaks, the background was fit to a third degree polynomial of the form:

$$f(x) = a_3 x^3 + a_2 x^2 + a_1 x + a_0 \ . \tag{4.23}$$

The Gaussian fits summed over all bins can be seen in Fig. 4.34(a) and the background fit for all bins can be seen in Fig. 4.34(b).

With both the Gaussians and the cubic polynomial calculated, a global fit was performed as shown in Fig. 4.34(c). The number of Λ and Σ^0 events was then determined from the area under the Gaussians above the background:

$$N_\Lambda = \frac{\sqrt{2\pi} c_\Lambda \sigma_\Lambda}{\text{binwidth}} \quad \text{and} \quad N_{\Sigma^0} = \frac{\sqrt{2\pi} c_\Sigma \sigma_\Sigma}{\text{binwidth}} \ . \tag{4.24}$$

The Gaussian plus background fit was performed for every W and $\cos\theta$ bin, with the binning scheme described in more detail in Section 7.1. More examples of the background subtraction can be found in Section 5.5. The systematic uncertainties of this fitting proce-

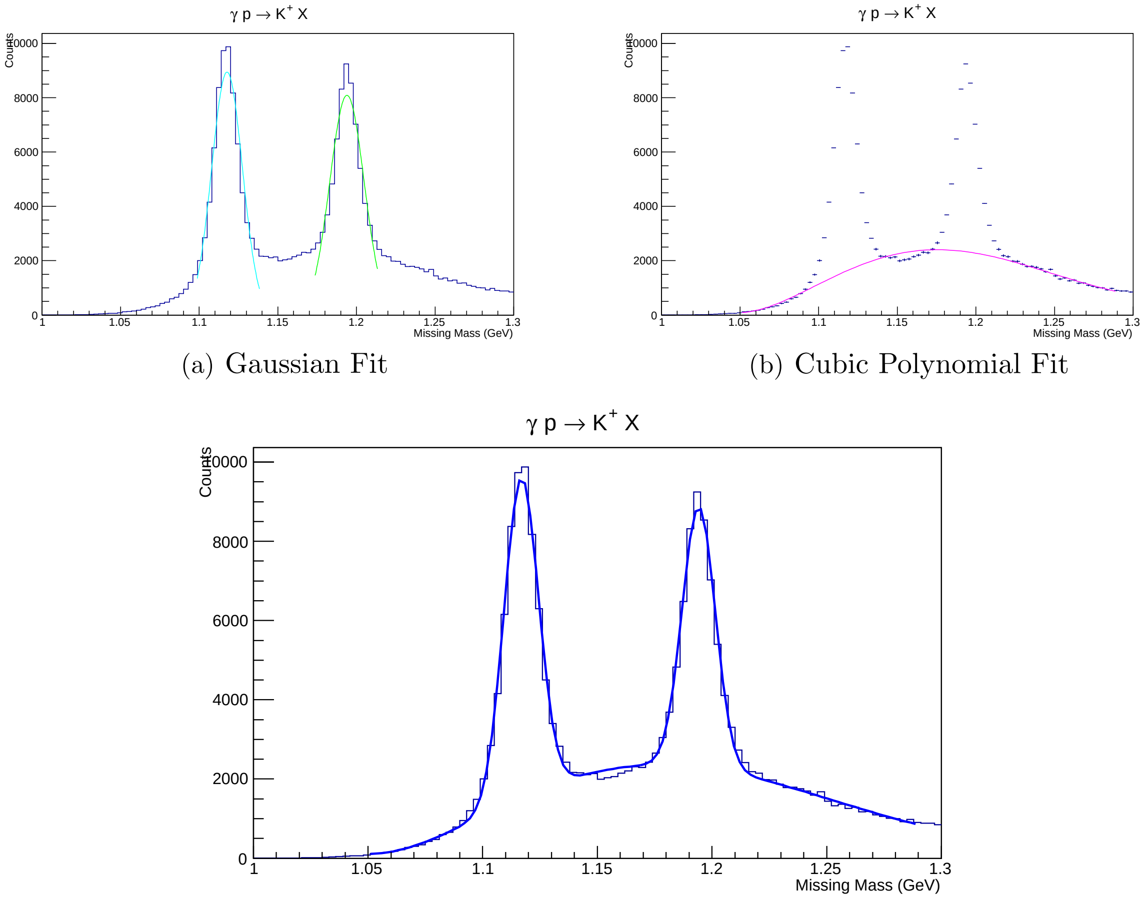

(a) Gaussian Fit

(b) Cubic Polynomial Fit

(c) Global Fit

Figure 4.34: The Gaussian fit (a), cubic polynomial fit (b), and global fit (c) can be seen for all energy and cosθ bins.

dure are discussed in Section 6.1.4.

4.13 Summary

This chapter has described the cuts applied to the analysis of the reactions $\gamma p \rightarrow K^+\Lambda$ and $K^+\Sigma^0$ and how the underlying background was accounted for. After the cuts were optimized, clear Λ and Σ^0 signals are seen in the $\gamma p \rightarrow K^+X$ missing mass spectra. After the hyperon yield fits were completed, the polarization observables could be measured.

Chapter 5

Moment Method

This chapter will describe how the observables were extracted. Typically, one may determine the polarization observables (or asymmetries) by fitting the measured differential cross-sections with a $\cos(m\phi)$ or $\sin(m\phi)$ function, but this requires high statistics and extensive corrections regarding detector acceptance and efficiencies. Another example of extracting the observable measurements would be the ϕ-bin method [113], which involves extracting the observables from the asymmetry distributions of the kaon azimuthal angle for two specific polarization states. This method has the advantage of canceling out acceptance effects in the detector system, which then removes the need to perform detailed acceptance calculations, but could result in large systematic uncertainties in the asymmetry calculation due to limited statistics, large ϕ bins, and holes in the CLAS ϕ acceptance.

Therefore, the author has decided to use a method for extraction of the observables known as the moment method. [114, 115] This method allows for extraction of the angle-dependent quantities without requiring large statistics. It is worth noting that the author attempted to use the ϕ-bin method, but due to the low statistics, the fits did not give stable results and resulted in large and unphysical bin-to-bin fluctuations of the asymmetries.

5.1 Differential Cross-Section for Kaon Photoproduction

The unpolarized differential cross-section $(\frac{d\sigma}{dEd\Omega})_u$ for $\gamma p \rightarrow K^+\Lambda$ and $\gamma p \rightarrow K^+\Sigma^0$ depends on energy, which can be the center-of-mass energy, $E_{cm} \equiv W$, or photon energy in the lab frame, E_γ, and on the K^+ production polar angle $\theta_{cm}(K^+)$. Fig. 5.1 shows the coordinate systems of $\gamma p \rightarrow K^+Y$ in addition to the spin orientations and momenta in the CM frame. There is no explicit dependence on the azimuthal angle, $\phi(K^+)$, of the production plane nor the decay angles since in the cross-section formula, Eq. 1.3, the squared matrix elements are averaged over initial spin orientations and summed over final spin states.

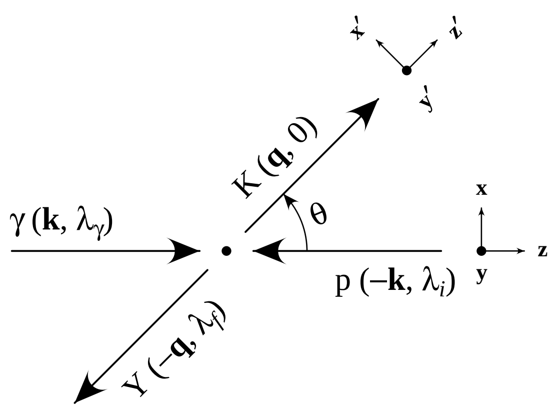

Figure 5.1: Coordinates for the reaction $\gamma p \rightarrow K^+Y$, where Y can be a Λ or Σ^0.

In these equations and throughout this analysis there are two coordinate systems used: (a) Center-of-Mass (CM) frame, for which the coordinate axes are defined by the photon momentum, $\vec{\mathbf{k}}_\gamma$, and the kaon momentum in the CM frame, $\vec{\mathbf{q}}^{cm}_{K^+}$:

$$\hat{z} = \frac{\vec{\mathbf{k}}_\gamma}{|\vec{\mathbf{k}}_\gamma|} \ , \quad \hat{y} = \frac{\vec{\mathbf{k}}_\gamma \times \vec{\mathbf{q}}^{cm}_{K^+}}{|\vec{\mathbf{k}}_\gamma \times \vec{\mathbf{q}}^{cm}_{K^+}|} \ , \quad \hat{x} = \hat{y} \times \hat{z} \ , \tag{5.1}$$

so that $\hat{z}$ defines the beamline direction, $\hat{y}$ is normal to the $K^+\Lambda$ or $K^+\Sigma^0$ production plane, and $\hat{x}$ is in the production plane, perpendicular to $\hat{z}$ and (b) Hyperon rest frame (primed symbols in Fig. 5.1), for which the z'-axis is along the kaon momentum in the CM frame and the y'-axis is again perpendicular to the production plane:

$$\hat{z}' = \frac{\vec{\mathbf{q}}^{cm}_{K^+}}{|\vec{\mathbf{q}}^{cm}_{K^+}|}\ , \quad \hat{y}' = \hat{y}\ , \quad \hat{x}' = \hat{y}' \times \hat{z}'\ . \tag{5.2}$$

For the case that the polarization of the initial or final state particles is known, the differential cross-section shows additional dependence on the K^+ azimuthal angle $\phi(K^+)$, the direction of the photon-beam polarization ψ, and the direction of the target polarization φ_0, and the direction of the hyperon spin (related to direction cosines $\cos\theta_{x',y',z'}$ of the decay proton in the Λ rest frame). The general form of the cross-section for $K^+\Lambda$ or $K^+\Sigma^0$ photoproduction [23] can be written as:

$$\begin{aligned}
\frac{d\sigma}{dW\ d\Omega} &= \left(\frac{d\sigma}{dW\ d\Omega}\right)_u \big(1 - P^\gamma_{cos}\mathbf{\Sigma} + P^{tg}_y\mathbf{T} + P^Y_{y'}\mathbf{P} \\
&- P^\gamma_c P^{tg}_z\mathbf{E} + P^\gamma_c P^{tg}_x\mathbf{F} + P^\gamma_{sin}P^{tg}_z\mathbf{G} + P^\gamma_{sin}P^{tg}_x\mathbf{H} - P^\gamma_{cos}P^{tg}_y\mathbf{P} \\
&+ P^\gamma_c P^Y_{x'}\mathbf{C_x} + P^\gamma_c P^Y_{z'}\mathbf{C_z} + P^\gamma_{sin}P^Y_{x'}\mathbf{O_x} - P^\gamma_{sin}P^Y_{y'}\mathbf{T} + P^\gamma_{sin}P^Y_{z'}\mathbf{O_z} \\
&+ P^{tg}_x P^Y_{x'}\mathbf{T_x} + P^{tg}_y P^Y_{y'}\mathbf{\Sigma}) + P^{tg}_x P^Y_{z'}\mathbf{T_z} + P^{tg}_z P^Y_{x'}\mathbf{L_x} + P^{tg}_z P^Y_{z'}\mathbf{L_z} \\
&- P^{tg}_x P^Y_{x'} P^\gamma_{cos}\mathbf{L_z} - P^{tg}_x P^Y_{y'} P^\gamma_{sin}\mathbf{E} + P^{tg}_x P^Y_{z'} P^\gamma_{cos}\mathbf{L_x} + P^{tg}_y P^Y_{x'} P^\gamma_{sin}\mathbf{C_z} \\
&- P^{tg}_y P^Y_{z'} P^\gamma_{sin}\mathbf{C_x} + P^{tg}_z P^Y_{x'} P^\gamma_{cos}\mathbf{T_z} + P^{tg}_z P^Y_{y'} P^\gamma_{sin}\mathbf{F} - P^{tg}_z P^Y_{z'} P^\gamma_{cos}\mathbf{T_x}\big)
\end{aligned} \tag{5.3}$$

with $\quad P^{tg}_x = P^{tg}_{xy}\ \cos(\varphi_0 - \phi), \qquad P^{tg}_y = P^{tg}_{xy}\ \sin(\varphi_0 - \phi)$

and $\quad P^\gamma_{cos} = P^\gamma_l \cos(2(\psi - \phi)), \quad P^\gamma_{sin} = P^\gamma_l \sin(2(\psi - \phi))\ .$

Here P^γ_c is the circular polarization of the beam photon ($P^\gamma_c = \lambda P^\gamma_\lambda$, where $\lambda = \pm 1$ is the photon helicity and P^γ_λ the degree of photon polarization), P^γ_l is the degree of linear polarization of the photon beam, ψ is the angle of the polarization or $\vec{\mathbf{E}}$ vector relative to the horizontal, P^{tg}_{xy} is the degree of transverse target polarization and φ_0 is its direction (relative to the horizontal), $\tilde{\varphi}$=ϕ-φ_0 is the azimuthal angle of the detected kaon relative to the target-polarization direction, and $P^Y_{x'}$=$\alpha_Y\cos\theta_{x'}$, $P^Y_{y'}$=$\alpha_Y\cos\theta_{y'}$, and $P^Y_{z'}$=$\alpha_Y\cos\theta_{z'}$ are the components of the hyperon polarization in the rest frame of the hyperon. The term α_Y is the (effective) weak-decay parameter of the hyperon: α_Λ=0.642 for the decay $\Lambda \to p\pi^-$ and $\alpha_{\Sigma^0} \approx -\frac{1}{3}\alpha_\Lambda$ for the decay $\Sigma^0 \to \Lambda\gamma \to p\pi^-\gamma$ [5], $\cos\theta_{z'}$=$c_{z'}$ is the direction cosine of the decay proton in the hyperon rest frame opposite to the flight direction of the hyperon, as explained in Section 4.10, and $\cos\theta_{x'}$=$c_{x'}$ is the direction cosine of the decay proton in the hyperon rest frame in the hyperon–proton plane perpendicular to $\hat{z}'$, $\cos\theta_{y'}$=$c_{y'}$ is the direction cosine of the decay proton in the hyperon rest frame perpendicular to the production plane. A more detailed view of the azimuthal plane perpendicular to the photon beam direction can be seen in Fig. 5.2.

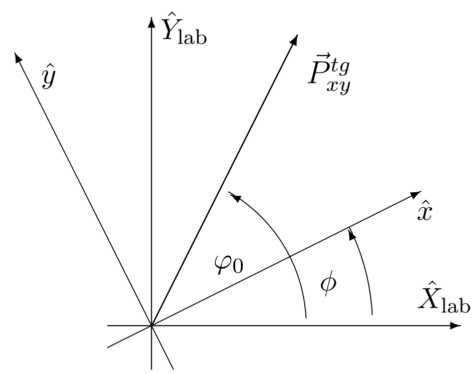

Figure 5.2: View of azimuthal plane perpendicular to beam direction ($\hat{z}$). The production plane makes an angle ϕ relative to the horizontal ($\hat{X}_{\text{lab}}$), the target polarization vector $\vec{P}^{tg}_{xy}$ is offset by an angle φ_0 relative to the horizontal.

For kaon production from a transversely polarized target using circularly polarized photons this expression is simplified to:

$$
\begin{aligned}
\frac{d\sigma}{d\Omega} &= \left(\frac{d\sigma}{d\Omega}\right)_u \Big(1 + P^{tg}_{xy}\sin\tilde{\varphi}\ \mathbf{T} + P^\gamma_c P^{tg}_{xy}\cos\tilde{\varphi}\ \mathbf{F} \\
&+ \alpha_Y c_{x'}\ (P^\gamma_c\ \mathbf{C_x} + P^{tg}_{xy}\cos\tilde{\varphi}\ \mathbf{T_x} - P^\gamma_c P^{tg}_{xy}\sin\tilde{\varphi}\ \mathbf{O_z}) \\
&+ \alpha_Y c_{y'}\ (\mathbf{P} + P^{tg}_{xy}\sin\tilde{\varphi}\ \mathbf{\Sigma} + P^\gamma_c P^{tg}_{xy}\cos\tilde{\varphi}\ \mathbf{G}) \\
&+ \alpha_Y c_{z'}\ (P^\gamma_c\mathbf{C_z} + P^{tg}_{xy}\cos\tilde{\varphi}\ \mathbf{T_z} + P^\gamma_c P^{tg}_{xy}\sin\tilde{\varphi}\ \mathbf{O_x})\Big)\ . \qquad (5.4)
\end{aligned}
$$

5.2 Moment Method for Beam and Target Polarization

Usually cross-sections are measured in kinematic bins (i, j, k) for W bin i (or E_γ bin i), $\cos\theta_{cm}$ bin j, ϕ_{cm} bin k:

$$\Delta\sigma^{(i,j,k)} = \frac{Y^{(i,j,k)}}{N_\gamma^i\ \rho_{tg}\ L_{tg} N_A\ \epsilon^{(i,j,k)}}\ , \tag{5.5}$$

where $Y^{(i,j,k)}$ is the background-subtracted yield in the bin (i, j, k), N_γ^i is the photon flux for this energy bin (i), $\rho_{tg}\ L_{tg} N_A$ is the target density of the number of target particles along the path of the beam photon, and $\epsilon^{(i,j,k)}$ is the detector acceptance for the kinematic bin (i, j, k). One can also define the normalized yield, which is used throughout this chapter:

$$\tilde{Y}^{(i,j,k)} = \frac{Y^{(i,j,k)}}{N_\gamma^i}\ . \tag{5.6}$$

One can modify equation (5.5) further to also be differential in the decay frame angles of the hyperon decay products by adding more dimensions to the kinematic bin definition: (i, j, k, l, m, n). Here, l is the index for the $c_{x'}$ bin, m the index for the $c_{y'}$ bin, and n the index for the $c_{z'}$ bin, such that the differential cross-section, the yield Y, and the detector acceptance ϵ are functions of $(W, \cos\theta_{cm}, \tilde{\varphi}, c_{x'}, c_{y'}, c_{z'})$. In order to account for all kinematic dimensions appearing in eq.(5.4), except for energy (index i) and production angle (index j), one may define a density function f^{ij} for each $(W, \cos\theta_{cm})$ bin:

$$f^{ij}(\tilde{\varphi}, c_{x'}, c_{y'}, c_{z'}) =$$
$$\rho_{tg} L_{tg} N_A \int_{W_{i-1}}^{W_i} dW \int_{\cos\theta_{j-1}}^{\cos\theta_j} d\cos\theta_{cm}\ \frac{d\sigma}{dW\ d\cos\theta_{cm}\ d\tilde{\varphi}\ dc_{x'}\ dc_{y'}\ dc_{z'}}\ \epsilon^{(i,j,k,l,m,n)}\ ,$$

so that the yield for this kinematic bin $(W_i, \cos\theta_j)$ is given by

$$Y^{ij} = N_\gamma^i\ \frac{1}{8} \int_{-1}^{1} dc_{x'} \int_{-1}^{1} dc_{y'} \int_{-1}^{1} dc_{z'} \int_0^{2\pi} d\tilde{\varphi}\ f^{ij}(\tilde{\varphi}, c_{x'}, c_{y'}, c_{z'})\ . \tag{5.7}$$

The density function is then expanded in a Fourier series to describe the $\tilde{\varphi}=\phi-\varphi_0$ dependence and into Legendre polynomials for the decay angles:

$$f^{ij} = \frac{1}{8\pi} \sum_{k',l',m',n'} (\tilde{Y}^{ij}_{k'l'm'n'} \cos(k'\tilde{\varphi}) + \tilde{Z}^{ij}_{klmn} \sin(k'\tilde{\varphi}))\ P_{l'}(c_{x'})\ P_{m'}(c_{y'})\ P_{n'}(c_{z'})\ , \qquad (5.8)$$

where $\tilde{Y}^{ij}_{k'l'm'n'}$ are the cosine–moments of the normalized yield and $\tilde{Z}^{ij}_{k'l'm'n'}$ are the sine–moments of the normalized yield, both weighted by the Legendre polynomials $P_{l'}(c_{x'})$, $P_{m'}(c_{y'})$, and $P_{n'}(c_{z'})$.

During the g9b experiment, experimental data were taken at all four combinations of circular beam polarization (positive and negative helicity) and transverse target polarization (target polarized upwards and downwards).

Setting	Beam Helicity	Target Polarization
(A)	$P_c^\gamma > 0$	$P_{xy}^{tg} > 0$
(B)	$P_c^\gamma < 0$	$P_{xy}^{tg} > 0$
(C)	$P_c^\gamma > 0$	$P_{xy}^{tg} < 0$
(D)	$P_c^\gamma < 0$	$P_{xy}^{tg} < 0$

For this analysis, the reactions $\gamma p \to K^+\Lambda$ and $K^+\Sigma^0$ were identified through detection of both the scattered K^+ and the decay proton from the hyperon, as described in Section 4.10. Since the proton from the Λ decay typically falls in the opposite sector of CLAS (cf. Fig. 4.26), in a tight cone around the Λ direction, it can be assumed that the acceptance of the decay proton is mainly related to the charged-particle acceptance of the CLAS sector opposite to the K^+ direction and not strongly correlated with the decay angle. Under this assumption the density functions for the four combinations of beam and target polarization in a given $(W, \cos\theta_{cm})$ bin are:

$$(A): \qquad f_A = f_u(1 + P_A T \sin\tilde{\varphi} + \lambda_A P_A F \cos\tilde{\varphi})$$
$$(B): \qquad f_B = f_u(1 + P_B T \sin\tilde{\varphi} - \lambda_B P_B F \cos\tilde{\varphi})$$
$$(C): \qquad f_C = f_u(1 - P_C T \sin\tilde{\varphi} - \lambda_C P_C F \cos\tilde{\varphi})$$
$$(D): \qquad f_D = f_u(1 - P_D T \sin\tilde{\varphi} + \lambda_D P_D F \cos\tilde{\varphi}) \ ,$$

where λ_i is the magnitude of the circular photon beam polarization and P_i is the magnitude of the transverse target polarization for the settings A, B, C, and D.

It is worth noting that settings A & B belong to the same data set, only with opposite helicity, thus the target polarization for both settings was the same, P_A=P_B. The measured beam charge asymmetry during the g9b run was always below 0.1% and the beam helicity was flipped rapidly at a rate of 30–240 Hz. The helicity was flipped rapidly due to a beam requirement set by Hall C and unfortunately, Hall B had to accept the requirement as well. Therefore, helicity dependent flux variations and acceptance effects can be ruled out and then λ_A=λ_B. Similarly, the settings C & D belong to the same data set, meaning that P_C=P_D and λ_C=λ_D. This simplifies the set of equations:

$$f_A = f_u(1 + P_A T \sin\tilde{\varphi} + \lambda_A P_A F \cos\tilde{\varphi}) = f_u + P_A f_T + \lambda_A P_A f_F \tag{5.9}$$
$$f_B = f_u(1 + P_A T \sin\tilde{\varphi} - \lambda_A P_A F \cos\tilde{\varphi}) = f_u + P_A f_T - \lambda_A P_A f_F \tag{5.10}$$
$$f_C = f_u(1 - P_C T \sin\tilde{\varphi} - \lambda_C P_C F \cos\tilde{\varphi}) = f_u - P_C f_T - \lambda_C P_C f_F \tag{5.11}$$
$$f_D = f_u(1 - P_C T \sin\tilde{\varphi} + \lambda_C P_C F \cos\tilde{\varphi}) = f_u - P_C f_T + \lambda_C P_C f_F. \tag{5.12}$$

Here, the simplified symbols f_T=$f_u T \sin\tilde{\varphi}$ and f_F=$f_u F \cos\tilde{\varphi}$ are used.

Combining the equations for the positive (A & B) and negative (C & D) target polarization, respectively, cancels out the helicity dependent terms containing f_F:

$$\begin{aligned} f_{AB} &= \frac{1}{2}(f_A + f_B) = f_u + P_A f_T \\ f_{CD} &= \frac{1}{2}(f_C + f_D) = f_u - P_C f_T. \end{aligned}$$

Solving these equations for f_T and f_u gives the following results:

$$\begin{aligned} f_T &= \frac{1}{P_A + P_C}(f_{AB} - f_{CD}) = \frac{1}{2(P_A + P_C)}(f_A + f_B - f_C - f_D) \qquad (5.13) \\ f_u &= \frac{P_A}{P_A + P_C} f_{AB} + \frac{P_C}{P_A + P_C} f_{CD} = \frac{P_A}{2(P_A + P_C)}(f_A + f_B) + \frac{P_C}{2(P_A + P_C)}(f_C + f_D). \end{aligned}$$

The moments are found by weighting the density functions f_T and f_u by $\cos(k\tilde{\varphi})$ and $\sin(k\tilde{\varphi})$ and integrating over $\tilde{\varphi}$ and the decay angles $\cos\theta_{x'}, \cos\theta_{y'}, \cos\theta_{z'}$:

$$\begin{aligned} \tilde{Y}_{u,k} &= \int_0^{2\pi} d\tilde{\varphi} \int_{-1}^{1} d\cos\theta_{x'} \int_{-1}^{1} d\cos\theta_{y'} \int_{-1}^{1} d\cos\theta_{z'}\; f_u \cos(k\tilde{\varphi}) \\ \tilde{Z}_{u,k} &= \int_0^{2\pi} d\tilde{\varphi} \int_{-1}^{1} d\cos\theta_{x'} \int_{-1}^{1} d\cos\theta_{y'} \int_{-1}^{1} d\cos\theta_{z'}\; f_u \sin(k\tilde{\varphi}) \\ \tilde{Y}_{T,k} &= \int_0^{2\pi} d\tilde{\varphi} \int_{-1}^{1} d\cos\theta_{x'} \int_{-1}^{1} d\cos\theta_{y'} \int_{-1}^{1} d\cos\theta_{z'}\; f_u T \sin\tilde{\varphi}\; \cos(k\tilde{\varphi}) \\ \tilde{Z}_{T,k} &= \int_0^{2\pi} d\tilde{\varphi} \int_{-1}^{1} d\cos\theta_{x'} \int_{-1}^{1} d\cos\theta_{y'} \int_{-1}^{1} d\cos\theta_{z'}\; f_u T \sin\tilde{\varphi}\; \sin(k\tilde{\varphi})\ . \end{aligned}$$

The integration over $d\cos\theta_{x'}, d\cos\theta_{y'}, d\cos\theta_{z'}$ gives simply a factor of 8, and the orthogonality of $\cos(k\phi)$ and $\sin(k\phi)$ makes $\tilde{Y}_{T,k}$=0. Here, the indices for the Legendre expansions

(l,n,m) are suppressed since only l=m=n=0 contribute. The other relations are:

$$\begin{aligned}
\tilde{Y}_{u,k} &= 8\int_0^{2\pi} d\tilde{\varphi}\ f_u\cos(k\tilde{\varphi}) = \frac{P_A}{2(P_A+P_C)}(\tilde{Y}_{A,k}+\tilde{Y}_{B,k}) + \frac{P_C}{2(P_A+P_C)}(\tilde{Y}_{C,k}+\tilde{Y}_{D,k}) \\
\tilde{Z}_{u,k} &= 8\int_0^{2\pi} d\tilde{\varphi}\ f_u\sin(k\tilde{\varphi}) = \frac{P_A}{2(P_A+P_C)}(\tilde{Z}_{A,k}+\tilde{Z}_{B,k}) + \frac{P_C}{2(P_A+P_C)}(\tilde{Z}_{C,k}+\tilde{Z}_{D,k}) \\
\tilde{Z}_{T,k} &= 8\int_0^{2\pi} d\tilde{\varphi}\ f_uT\sin\tilde{\varphi}\sin(k\tilde{\varphi}) = \frac{1}{2(P_A+P_C)}(\tilde{Z}_{A,k}+\tilde{Z}_{B,k}-\tilde{Z}_{C,k}-\tilde{Z}_{D,k}).
\end{aligned}$$

Of special interest is the k=1 moment because f_T depends on $\sin\tilde{\varphi}$. Then using the relation $\sin^2\phi = \frac{1}{2}(1-\cos 2\phi)$ results in the following:

$$\begin{aligned}
\tilde{Z}_{T,1} &= \frac{1}{2(P_A+P_C)}(\tilde{Z}_{A,1}+\tilde{Z}_{B,1}-\tilde{Z}_{C,1}-\tilde{Z}_{D,1}) = \frac{T}{2}(\tilde{Y}_{u,0}-\tilde{Y}_{u,2}) \\
&= T\tfrac{P_A}{4(P_A+P_C)}(\tilde{Y}_{A,0}+\tilde{Y}_{B,0}-\tilde{Y}_{A,2}-\tilde{Y}_{B,2}) + T\tfrac{P_C}{4(P_A+P_C)}(\tilde{Y}_{C,0}+\tilde{Y}_{D,0}-\tilde{Y}_{C,2}-\tilde{Y}_{D,2})
\end{aligned}$$

so that

$$T = 2\frac{\tilde{Z}_{A,1}+\tilde{Z}_{B,1}-\tilde{Z}_{C,1}-\tilde{Z}_{D,1}}{P_C(\tilde{Y}_{A,0}+\tilde{Y}_{B,0}-\tilde{Y}_{A,2}-\tilde{Y}_{B,2}) + P_A(\tilde{Y}_{C,0}+\tilde{Y}_{D,0}-\tilde{Y}_{C,2}-\tilde{Y}_{D,2})}\ . \tag{5.14}$$

Similarly, combining settings A & D and B & C, for which the product $P_c^\gamma P_{xy}^{tg}$ is positive and negative, respectively, and weighting by the target polarization such that the f_T terms cancel out, gives

$$\begin{aligned}
f_{AD} &= \frac{P_Cf_A+P_Af_D}{P_A+P_C} = f_u + \frac{P_AP_C(\lambda_A+\lambda_C)}{P_A+P_C}f_F = f_u + P_{AC}f_F \\
f_{BC} &= \frac{P_Cf_B+P_Af_C}{P_A+P_C} = f_u - \frac{P_AP_C(\lambda_A+\lambda_C)}{P_A+P_C}f_F = f_u - P_{AC}f_F\ .
\end{aligned}$$

Solving for f_F and f_u in these equations gives the following result:

$$\begin{aligned} f_F &= \frac{1}{2P_{AC}}(f_{AD} - f_{BC}) = \frac{1}{2P_A P_C(\lambda_A + \lambda_C)}\left(P_C(f_A - f_B) + P_A(f_D - f_C)\right) \\ f_u &= \frac{1}{2}(f_{AD} + f_{BC}) = \frac{1}{2(P_A + P_C)}\left(P_C(f_A + f_B) + P_A(f_D + f_C)\right). \end{aligned} \tag{5.15}$$

Again, weighting the density functions f_F and f_u by $\cos(k\tilde{\varphi})$ and $\sin(k\tilde{\varphi})$, respectively, and integrating over $\tilde{\varphi}$ and the decay angles, and using the orthogonality of $\cos(k\phi)$ and $\sin(k\phi)$, gives

$$\begin{aligned} \tilde{Y}_{F,k} &= \frac{1}{2P_A P_C(\lambda_A + \lambda_C)}\Big(P_C(\tilde{Y}_{A,k} - \tilde{Y}_{B,k}) + P_A(\tilde{Y}_{D,k} - \tilde{Y}_{C,k})\Big) \\ \tilde{Y}_{u,k} &= \frac{1}{2(P_A + P_C)}\Big(P_C(\tilde{Y}_{A,k} + \tilde{Y}_{B,k}) + P_A(\tilde{Y}_{C,k} + \tilde{Y}_{D,k})\Big). \end{aligned}$$

Since f_F depends on $\cos\tilde{\varphi}$, the first moment for F is considered and the relation of $\cos^2\phi = \frac{1}{2}(1 + \cos 2\phi)$ was used to obtain the result:

$$\begin{aligned} \tilde{Y}_{F,1} &= \frac{F}{2}(\tilde{Y}_{u,0} + \tilde{Y}_{u,2}) = \frac{1}{2P_A P_C(\lambda_A + \lambda_C)}\Big(P_C(\tilde{Y}_{A,1} - \tilde{Y}_{B,1}) + P_A(\tilde{Y}_{D,1} - \tilde{Y}_{C,1})\Big) \\ \text{with} \quad & \tilde{Y}_{u,0} = \frac{1}{2(P_A + P_C)}\Big(P_C(\tilde{Y}_{A,0} + \tilde{Y}_{B,0}) + P_A(\tilde{Y}_{C,0} + \tilde{Y}_{D,0})\Big) \\ \text{and} \quad & \tilde{Y}_{u,2} = \frac{1}{2(P_A + P_C)}\Big(P_C(\tilde{Y}_{A,2} + \tilde{Y}_{B,2}) + P_A(\tilde{Y}_{C,2} + \tilde{Y}_{D,2})\Big), \end{aligned}$$

such that

$$F = \frac{2(P_A + P_C)}{P_A P_C(\lambda_A + \lambda_C)} \frac{P_C(\tilde{Y}_{A,1} - \tilde{Y}_{B,1}) + P_A(\tilde{Y}_{D,1} - \tilde{Y}_{C,1})}{P_C(\tilde{Y}_{A,0} + \tilde{Y}_{B,0} + \tilde{Y}_{A,2} + \tilde{Y}_{B,2}) + P_A(\tilde{Y}_{C,0} + \tilde{Y}_{D,0} + \tilde{Y}_{C,2} + \tilde{Y}_{D,2})}. \tag{5.16}$$

5.3 Moment Method for Beam–Target and Recoil Polarization

Now the experimental condition for a polarized photon beam and polarized target and considering the recoil polarization will be described. For this running condition, "circ–trans", the contributing terms in eq.(5.4), separated for the four combinations of different beam and target polarization directions are given by:

$$\begin{aligned}
f_A &= f_u\,(1 + P_A T\sin\tilde{\varphi} + \lambda_A P_A F\cos\tilde{\varphi} \\
&+ \lambda_A\alpha_y c_{x'} C_x + P_A\alpha_Y c_{x'} T_x\cos\tilde{\varphi} - \lambda_A P_A\alpha_Y c_{x'} O_z\sin\tilde{\varphi} \\
&+ \alpha_y c_{y'} P + P_A\alpha_Y c_{y'}\Sigma\sin\tilde{\varphi} + \lambda_A P_A\alpha_Y c_{y'} G\cos\tilde{\varphi} \\
&+ \lambda_A\alpha_y c_{z'} C_z + P_A\alpha_Y c_{z'} T_z\cos\tilde{\varphi} + \lambda_A P_A\alpha_Y c_{z'} O_x\sin\tilde{\varphi}) \\
&= f_u + f_P^y + \lambda_A(f_{Cx}^x + f_{Cz}^z) + P_A(f_T + f_\Sigma^y + f_{Tx}^x + f_{Tz}^z) \\
&\qquad + \lambda_A P_A(f_F + f_G^y - f_{Oz}^x + f_{Ox}^z)
\end{aligned} \tag{5.17}$$

$$\begin{aligned}
f_B &= f_u + f_P^y - \lambda_B(f_{Cx}^x + f_{Cz}^z) + P_B(f_T + f_\Sigma^y + f_{Tx}^x + f_{Tz}^z) \\
&\qquad - \lambda_B P_B(f_F + f_G^y - f_{Oz}^x + f_{Ox}^z)
\end{aligned} \tag{5.18}$$

$$\begin{aligned}
f_C &= f_u + f_P^y + \lambda_C(f_{Cx}^x + f_{Cz}^z) - P_C(f_T + f_\Sigma^y + f_{Tx}^x + f_{Tz}^z) \\
&\qquad - \lambda_C P_C(f_F + f_G^y - f_{Oz}^x + f_{Ox}^z)
\end{aligned} \tag{5.19}$$

$$\begin{aligned}
f_D &= f_u + f_P^y - \lambda_D(f_{Cx}^x + f_{Cz}^z) - P_D(f_T + f_\Sigma^y + f_{Tx}^x + f_{Tz}^z) \\
&\qquad + \lambda_D P_D(f_F + f_G^y - f_{Oz}^x + f_{Ox}^z)\ ,
\end{aligned} \tag{5.20}$$

with abbreviations $f_T = f_u T\sin\tilde{\varphi}$, $f_F = f_u F\cos\tilde{\varphi}$, $f_P^y = f_u P\alpha_Y c_{y'}$, $f_{Cx}^x = f_u C_x\alpha_Y c_{x'}$, $f_{Cz}^x = f_u C_z\alpha_Y c_{z'}$, $f_{Tx}^x = f_u T_x\cos\tilde{\varphi}\alpha_Y c_{x'}$, $f_{Tz}^x = f_u T_z\cos\tilde{\varphi}\alpha_Y c_{z'}$, $f_\Sigma^y = f_u\Sigma\sin\tilde{\varphi}\alpha_Y c_{y'}$, $f_{Oz}^x = f_u O_z\sin\tilde{\varphi}\alpha_Y c_{x'}$, $f_G^y = f_u G\cos\tilde{\varphi}\alpha_Y c_{y'}$, and $f_{Ox}^z = f_u O_x\sin\tilde{\varphi}\alpha_Y c_{z'}$.

Note that for unpolarized target data, P and C_x, C_z can be obtained by combinations of f_A and f_B:

$$f_u + f_P^y = \frac{\lambda_B f_A + \lambda_A f_B}{\lambda_A + \lambda_B} = \frac{1}{2}(f_A + f_B) \quad \text{for} \quad \lambda_A = \lambda_B \tag{5.21}$$

$$f_{Cx}^x + f_{Cz}^z = \frac{f_A - f_B}{\lambda_A + \lambda_B} = \frac{1}{2\lambda_A}(f_A - f_B). \tag{5.22}$$

Weighting equation (5.22) by $\cos(k\tilde{\varphi})P_l(c_{x'})P_m(c_{y'})P_n(c_{z'})$ and integrating gives:

$$\begin{aligned}&\int_0^{2\pi} d\tilde{\varphi} \int_{-1}^{1} dc_{x'} \int_{-1}^{1} dc_{y'} \int_{-1}^{1} dc_{z'} \alpha_Y f_u (C_x c_{x'} + C_z c_{z'}) \cos(k\tilde{\varphi}) P_l(c_{x'}) P_m(c_{y'}) P_n(c_{z'}) \\ = \; & \frac{\alpha_Y}{(2l+1)(2m+1)(2n+1)} \left(C_x \left(\frac{l}{2l+1} \tilde{Y}_{u,k(l-1)mn} + \frac{l+1}{2l+1} \tilde{Y}_{u,k(l+1)mn} \right) + \right. \\ & \left. C_z \left(\frac{n}{2n+1} \tilde{Y}_{u,klm(n-1)} + \frac{n+1}{2n+1} \tilde{Y}_{u,klm(n+1)} \right) \right),\end{aligned}$$

and using $(n+1)P_{n+1}(x) = (2n+1)xP_n(x) - nP_n(x)$ and $\int_{-1}^{1} P_m(x)P_n(x)dx = \frac{2}{2n+1}\delta_{mn}$.

Of interest are the l=1 moment for C_x and the n=1 moment for C_z, since C_x and C_z depend linearly on $c_{x'}$ and $c_{z'}$, respectively. With $\tilde{Y}_{u,klmn} = \frac{1}{2}(\tilde{Y}_{A,klmn} + \tilde{Y}_{B,klmn})$, then C_x and C_z can be written as:

$$C_x = \frac{\tilde{Y}_{A,0100} - \tilde{Y}_{B,0100}}{\frac{2}{9}\alpha_Y \lambda_A (\tilde{Y}_{A,0000} + \tilde{Y}_{B,0000} + 2\tilde{Y}_{A,0200} + 2\tilde{Y}_{B,0200})} \tag{5.23}$$

$$C_z = \frac{\tilde{Y}_{A,0001} - \tilde{Y}_{B,0001}}{\frac{2}{9}\alpha_Y \lambda_A (\tilde{Y}_{,0000} + \tilde{Y}_{B,0000} + 2\tilde{Y}_{A,0002} + 2\tilde{Y}_{B,0002})}. \tag{5.24}$$

If the target is transversely polarized, groups of observables can be separated by combining the settings of beam and target polarization, that is eqs. (5.9) to (5.12), in matrix form:

$$\begin{pmatrix} f_A \\ f_B \\ f_C \\ f_D \end{pmatrix} = \begin{pmatrix} 1 & \lambda_A & P_A & \lambda_A P_A \\ 1 & -\lambda_A & P_A & -\lambda_A P_A \\ 1 & \lambda_C & -P_C & -\lambda_C P_C \\ 1 & -\lambda_C & -P_C & \lambda_C P_C \end{pmatrix} \begin{pmatrix} f_u + f_P^y \\ f_{Cx}^x + f_{Cz}^z \\ f_T + f_{Tx}^x + f_\Sigma^y + f_{Tz}^z \\ f_F - f_{Oz}^x + f_G^y + f_{Ox}^z \end{pmatrix}. \tag{5.25}$$

Inverting the coefficient matrix ($\mathbf{A}$) gives the dependence of the density functions on the weighted combinations of the 4 settings of beam and target polarization:

$$\begin{pmatrix} f_u + f_P^y \\ f_{Cx}^x + f_{Cz}^z \\ f_T + f_{Tx}^x + f_\Sigma^y + f_{Tz}^z \\ f_F - f_{Oz}^x + f_G^y + f_{Ox}^z \end{pmatrix} = \mathbf{A}^{-1} \begin{pmatrix} f_A \\ f_B \\ f_C \\ f_D \end{pmatrix}, \tag{5.26}$$

with

$$\mathbf{A}^{-1} = \frac{1}{2\lambda_A\lambda_C(P_A + P_C)} \begin{pmatrix} \lambda_A\lambda_C P_C & \lambda_A\lambda_C P_C & \lambda_A\lambda_C P_A & \lambda_A\lambda_C P_A \\ \lambda_C P_C & -\lambda_C P_C & \lambda_A P_A & -\lambda_A P_A \\ \lambda_A\lambda_C & \lambda_A\lambda_C & -\lambda_A\lambda_C & -\lambda_A\lambda_C \\ \lambda_C & -\lambda_C & -\lambda_A & \lambda_A \end{pmatrix}. \tag{5.27}$$

The groups of density functions with the same dependence on target and beam polarization can be separated as:

$$f_u + f_P^y = \frac{P_C}{2(P_A+P_C)}(f_A+f_B) + \frac{P_A}{2(P_A+P_C)}(f_C+f_D) \tag{5.28}$$

$$f_{Cx}^x + f_{Cz}^z = \frac{P_C}{2\lambda_A(P_A+P_C)}(f_A-f_B) + \frac{P_A}{2\lambda_C(P_A+P_C)}(f_C-f_D) \tag{5.29}$$

$$f_T + f_{Tx}^x + f_\Sigma^y + f_{Tz}^z = \frac{1}{2(P_A+P_C)}\ (f_A+f_B-f_C-f_D) \tag{5.30}$$

$$f_F - f_{Oz}^x + f_G^y + f_{Ox}^z = \frac{1}{2\lambda_A(P_A+P_C)}(f_A-f_B) - \frac{1}{2\lambda_C(P_A+P_C)}(f_C-f_D). \tag{5.31}$$

Weighting eq. (5.30) by $\cos(k\tilde{\varphi})P_l(c_{x'})P_m(c_{y'})P_n(c_{z'})$ and integrating gives the target–recoil observables T_x and T_z:

$$T_x = \frac{\tilde{Y}_{AB,1100} - \tilde{Y}_{CD,1100}}{\frac{1}{9}\alpha_Y(P_C X_{AB} + P_A X_{CD})}\ , \tag{5.32}$$

$$T_z = \frac{\tilde{Y}_{AB,1001} - \tilde{Y}_{CD,1001}}{\frac{1}{9}\alpha_Y(P_C Z_{AB} + P_A Z_{CD})} \tag{5.33}$$

where

$$\begin{aligned}
X_{AB} &= \tilde{Y}_{AB,0000} + \tilde{Y}_{AB,2000} + 2\tilde{Y}_{AB,0200} + 2\tilde{Y}_{AB,2200} \\
X_{CD} &= \tilde{Y}_{CD,0000} + \tilde{Y}_{CD,2000} + 2\tilde{Y}_{CD,0200} + 2\tilde{Y}_{CD,2200} \\
Z_{AB} &= \tilde{Y}_{AB,0000} + \tilde{Y}_{AB,2000} + 2\tilde{Y}_{AB,0002} + 2\tilde{Y}_{AB,2002} \\
Z_{CD} &= \tilde{Y}_{CD,0000} + \tilde{Y}_{CD,2000} + 2\tilde{Y}_{CD,0002} + 2\tilde{Y}_{CD,2002}
\end{aligned}$$

and $\quad \tilde{Y}_{AB,klmn} = \tilde{Y}_{A,klmn} + \tilde{Y}_{B,klmn}\ , \quad \tilde{Y}_{CD,klmn} = \tilde{Y}_{C,klmn} + \tilde{Y}_{D,klmn}.$

5.4 Statistical Uncertainties

In order to calculate the associated statistical uncertainty for the polarization asymmetries from Fourier or Legendre moments, an arbitrary bin $\tilde{Y}_{k,p}$ of the cosine–moment histogram

$\tilde{Y}_k$ may be considered. Let n_p be the total number of events in this bin and $w_{k,p,q}$ the weight of the q-th Poisson-distributed event of the k-th cosine–moment within the p-th mass bin of the distribution $\tilde{Y}_k$, then

$$\tilde{Y}_{k,p} = \frac{1}{N_\gamma}\sum_{q=1}^{n_p} w_{k,p,q} = \frac{1}{N_\gamma}\sum_{q=1}^{n_p}\cos(k\tilde{\varphi}_q)$$

and the 0-th moment within the p-th mass bin is simply

$$\tilde{Y}_{o,p} = \frac{1}{N_\gamma}\sum_{q=1}^{n_p} 1 = \frac{n_p}{N_\gamma} = \frac{Y_{0,p}}{N_\gamma}\ .$$

The variance of $\tilde{Y}_{0,p}$ is given by

$$\sigma^2_{\tilde{Y}_{0,p}} = \frac{1}{N_\gamma^2}\ \sum_{q=1}^{n_p} 1^2 = \frac{Y_{k,p}}{N_\gamma^2} = \frac{\tilde{Y}_{k,p}}{N_\gamma}\ . \tag{5.34}$$

For the other moments the relation $\cos^2(\phi)=\frac{1}{2}(1+\cos(2\phi))$ is used:

$$\begin{aligned}
\sigma^2_{\tilde{Y}_{k,p}} &= \frac{1}{N_\gamma^2}\ \sum_{q=1}^{n_p}\cos^2(k\tilde{\varphi}_q) \\
&= \frac{1}{2N_\gamma^2}\ \sum_{q=1}^{n_p}(1+\cos(2k\tilde{\varphi}_q)) = \frac{1}{2N_\gamma}\left(\tilde{Y}_{0,p}+\tilde{Y}_{2k,p}\right). \qquad (5.35)
\end{aligned}$$

The covariance of the different cosine–moments of the mass bin p is

$$cov(\tilde{Y}_{k_1,p},\tilde{Y}_{k_2,p}) = \frac{1}{N_\gamma^2}\ \sum_{q=1}^{n_p}\cos(k_1\tilde{\varphi}_q)\cos(k_2\tilde{\varphi}_q)\ ,$$

in particular

$$
\begin{aligned}
cov(\tilde{Y}_{k,p}, \tilde{Y}_{2k,p}) &= \frac{1}{N_\gamma^2} \sum_{q=1}^{n_p} \cos(k\tilde{\varphi}_q)\cos(2k\tilde{\varphi}_q) = \frac{1}{2N_\gamma^2} \sum_{q=1}^{n_p} (\cos(k\tilde{\varphi}_q) + \cos(3k\tilde{\varphi}_q)) \\
&= \frac{1}{2N_\gamma} \left(\tilde{Y}_{k,p} + \tilde{Y}_{3k,p} \right). && (5.36) \\
cov(\tilde{Y}_{0,p}, \tilde{Y}_{k,p}) &= \frac{1}{N_\gamma^2} \sum_{q=1}^{n_p} \cos(k\tilde{\varphi}_q) = \frac{1}{N_\gamma} \tilde{Y}_{k,p}, && (5.37)
\end{aligned}
$$

using the relation $\cos(\alpha)\cos(\beta) = \frac{1}{2}(\cos(\alpha - \beta) + \cos(\alpha + \beta))$. Similarly the sine–moments $\tilde{Z}_{m,p}$ for the mass bin p have

$$
\begin{aligned}
\sigma^2_{\tilde{Z}_{k,p}} &= \frac{1}{N_\gamma^2} \sum_{q=1}^{n_p} \sin^2(k\tilde{\varphi}_q) \\
&= \frac{1}{2N_\gamma^2} \sum_{q=1}^{n_p} (1 - \cos(2k\tilde{\varphi}_q)) = \frac{1}{2N_\gamma} \left(\tilde{Y}_{0,p} - \tilde{Y}_{2k,p} \right) \;, && (5.38)
\end{aligned}
$$

$$
\begin{aligned}
cov(\tilde{Z}_{k,p}, \tilde{Z}_{2k,p}) &= \frac{1}{N_\gamma^2} \sum_{q=1}^{n_p} \sin(k\tilde{\varphi}_q)\sin(2k\tilde{\varphi}_q) = \frac{1}{2N_\gamma^2} \sum_{q=1}^{n_p} (\cos(k\tilde{\varphi}_q) - \cos(3k\tilde{\varphi}_q)) \\
&= \frac{1}{2N_\gamma} \left(\tilde{Y}_{k,p} - \tilde{Y}_{3k,p} \right). && (5.39) \\
cov(\tilde{Z}_{k,p}, \tilde{Y}_{2k,p}) &= \frac{1}{N_\gamma^2} \sum_{q=1}^{n_p} \sin(k\tilde{\varphi}_q)\cos(2k\tilde{\varphi}_q) = \frac{1}{N_\gamma} \left(\tilde{Z}_{3k,p} - \tilde{Z}_{k,p} \right). && (5.40)
\end{aligned}
$$

Asymmetries are written as numerator N and denominator D relations. Then the statistical uncertainty in the measured asymmetry can be calculated from

$$
A = \frac{N}{D} \;\rightarrow\; \sigma_A^2 = A^2 \left(\frac{\sigma_N^2}{N^2} + \frac{\sigma_D^2}{D^2} - 2\frac{cov(N,D)}{ND} \right) \;, \tag{5.41}
$$

where σ_N^2 and σ_D^2 are calculated using Gaussian error propagation.

Calling $N_\gamma^{(A)}$ ($=N_\gamma^{(B)}$) the flux during the runs on positively polarized target (settings A & B) and $N_\gamma^{(C)}$ ($=N_\gamma^{(D)}$) the flux during the runs on negatively polarized target (settings C & D), the variance for T is given by

$$\begin{aligned}
N_T &= 2(\tilde{Z}_{A,1}+\tilde{Z}_{B,1}-\tilde{Z}_{C,1}-\tilde{Z}_{D,1}) \\
D_T &= P_C(\tilde{Y}_{A,0}+\tilde{Y}_{B,0}-\tilde{Y}_{A,2}-\tilde{Y}_{B,2})+P_A(\tilde{Y}_{C,0}+\tilde{Y}_{D,0}-\tilde{Y}_{C,2}-\tilde{Y}_{D,2})
\end{aligned} \tag{5.42}$$

$$\begin{aligned}
\sigma^2_{N_T} &= \frac{1}{N_\gamma^{(A)}}\left(\tilde{Y}_{A,0}-\tilde{Y}_{A,2}+\tilde{Y}_{B,0}-\tilde{Y}_{B,2}\right)+\frac{1}{N_\gamma^{(C)}}\left(\tilde{Y}_{C,0}-\tilde{Y}_{C,2}+\tilde{Y}_{D,0}-\tilde{Y}_{D,2}\right) \\
\sigma^2_{D_T} &= P_C^2(\sigma^2_{\tilde{Y}_{A,0}}+\sigma^2_{\tilde{Y}_{A,2}}+\sigma^2_{\tilde{Y}_{B,0}}+\sigma^2_{\tilde{Y}_{B,2}}-2cov(\tilde{Y}_{A,0},\tilde{Y}_{A,2})-2cov(\tilde{Y}_{B,0},\tilde{Y}_{B,2})) \\
&\quad +P_A^2(\sigma^2_{\tilde{Y}_{C,0}}+\sigma^2_{\tilde{Y}_{C,2}}+\sigma^2_{\tilde{Y}_{D,0}}+\sigma^2_{\tilde{Y}_{D,2}}-2cov(\tilde{Y}_{C,0},\tilde{Y}_{C,2})-2cov(\tilde{Y}_{D,0},\tilde{Y}_{D,2})) \\
&= \frac{P_C^2}{2N_\gamma^{(A)}}(3\tilde{Y}_{A,0}-2\tilde{Y}_{A,2}+\tilde{Y}_{A,4}+3\tilde{Y}_{B,0}-2\tilde{Y}_{B,2}+\tilde{Y}_{B,4}) \\
&\quad +\frac{P_A^2}{2N_\gamma^{(C)}}(3\tilde{Y}_{C,0}-2\tilde{Y}_{C,2}+\tilde{Y}_{C,4}+3\tilde{Y}_{D,0}-2\tilde{Y}_{D,2}+\tilde{Y}_{D,4}) \\
cov(N_T,D_T) &= \frac{P_C^2}{N_\gamma^{(A)}}(\tilde{Z}_{A,1}+\tilde{Z}_{A,3}+\tilde{Z}_{B,1}+\tilde{Z}_{B,3})+\frac{P_A^2}{N_\gamma^{(C)}}(\tilde{Z}_{C,1}+\tilde{Z}_{C,3}+\tilde{Z}_{D,1}+\tilde{Z}_{D,3}) \\
\rightarrow\ \sigma^2_T &= \frac{\sigma^2_{N_T}}{D_T^2}+\frac{\sigma^2_{D_T}N_T^2}{D_T^4}-2cov(N_T,D_T)\frac{N_T}{D_T^3},
\end{aligned} \tag{5.43}$$

and for F by

$$\begin{aligned}
N_F &= 2\left(P_C(\tilde{Y}_{A,1} - \tilde{Y}_{B,1}) + P_A(\tilde{Y}_{D,1} - \tilde{Y}_{C,1})\right). \\
D_F &= \frac{P_A P_C(\lambda_A + \lambda_C)}{P_A + P_C}\Big(P_C(\tilde{Y}_{A,0} + \tilde{Y}_{A,2} + \tilde{Y}_{B,0} + \tilde{Y}_{B,2}) \\
&\quad + P_A(\tilde{Y}_{C,0} + \tilde{Y}_{C,2} + \tilde{Y}_{D,0} + \tilde{Y}_{D,2})\Big). \\
\sigma^2_{N_F} &= \frac{2P_C^2}{N_\gamma^{(A)}}\left(\tilde{Y}_{A,0} + \tilde{Y}_{A,2} + \tilde{Y}_{B,0} + \tilde{Y}_{B,2}) + \frac{2P_A^2}{N_\gamma^{(C)}}\left(\tilde{Y}_{C,0} + \tilde{Y}_{C,2} + \tilde{Y}_{D,0} + \tilde{Y}_{D,2}\right)\right) \\
\sigma^2_{D_F} &= \frac{P_A^2 P_C^2(\lambda_A + \lambda_C)^2}{2(P_A + P_C)^2}\left(\frac{P_C^2}{N_\gamma^{(A)}}\left(3\tilde{Y}_{A,0} + 2\tilde{Y}_{A,2} + \tilde{Y}_{A,4} + 3\tilde{Y}_{B,0} + 2\tilde{Y}_{B,2} + \tilde{Y}_{B,4}\right).\right. \\
&\quad \left. + \frac{P_A^2}{N_\gamma^{(C)}}\left(3\tilde{Y}_{C,0} + 2\tilde{Y}_{C,2} + \tilde{Y}_{C,4} + 3\tilde{Y}_{D,0} + 2\tilde{Y}_{D,2} + \tilde{Y}_{D,4}\right)\right).
\end{aligned}$$

$$\begin{aligned}
cov(N_F, D_F) &= \frac{P_A + P_C}{2P_A P_C(\lambda_A + \lambda_C)}\left(\frac{P_C^2}{N_\gamma^{(A)}}\left(3\tilde{Y}_{A,1} + \tilde{Y}_{A,3} - 3\tilde{Y}_{B,1} - \tilde{Y}_{B,3}\right).\right. \\
&\quad \left. + \frac{P_A^2}{N_\gamma^{(C)}}\left(3\tilde{Y}_{C,1} + \tilde{Y}_{C,3} - 3\tilde{Y}_{D,1} - \tilde{Y}_{D,3}\right)\right) \\
\rightarrow\ \sigma^2_F &= \frac{\sigma^2_{N_F}}{D_F^2} + \frac{\sigma^2_{D_F} N_F^2}{D_F^4} - 2cov(N_F, D_F)\frac{N_F}{D_F^3}.
\end{aligned} \tag{5.44}$$

5.5 Illustration of the Yield Extraction

Now that the procedure for extracting the various moments has been described, an illustrative example would be beneficial for a specific bin in order to understand the procedure more fully. For this, the bin $W = 1875$ MeV was chosen, due to the high statistics for both of the reaction channels of this analysis. The following figures then show the various cosθ bins for this energy bin. Shown first is the fitting of signal and background in the denominator and later the calculated moments are shown as well for the energy bin.

In Figs. 5.3 to 5.11, (a) shows the Gaussian fit to the Λ and Σ^0 peaks, (b) shows the third degree polynomial fit to the background, and (c) shows the global fit in $\cos\theta$ bins of 0.2.

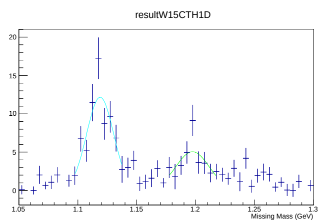

(a) Gaussian Fit

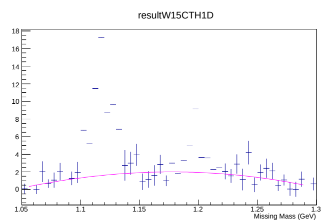

(b) Background Fit

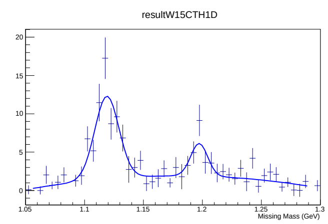

(c) Global Fit

Figure 5.3: Fits for $W = 1875$ MeV in $\cos\theta = -0.7$.

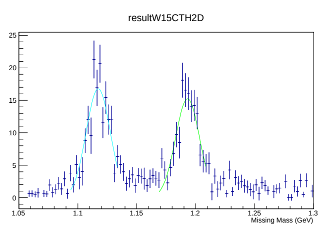

(a) Gaussian Fit

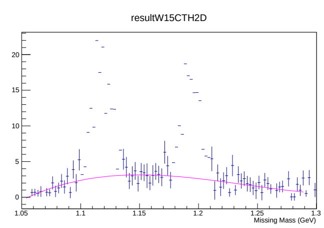

(b) Background Fit

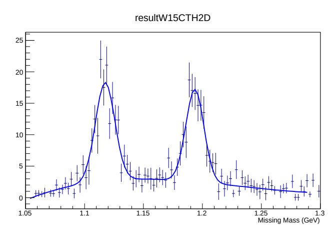

(c) Global Fit

Figure 5.4: Fits for $W = 1875$ MeV in $\cos\theta = -0.5$.

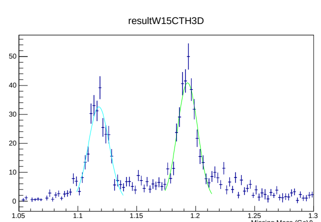

(a) Gaussian Fit

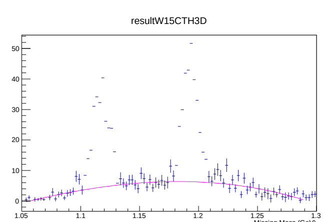

(b) Background Fit

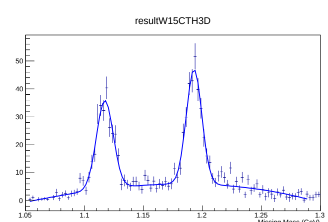

(c) Global Fit

Figure 5.5: Fits for $W = 1875$ MeV in $\cos\theta = -0.3$.

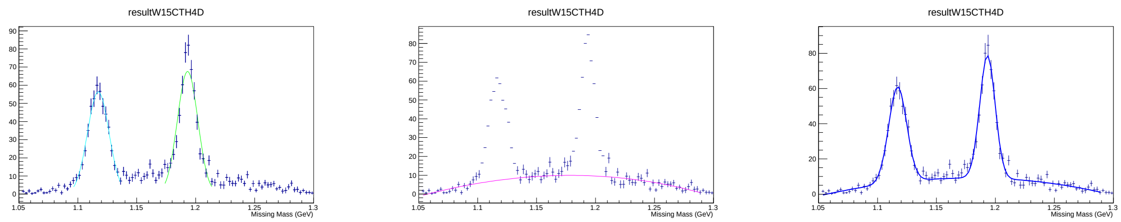

(a) Gaussian Fit (b) Background Fit (c) Global Fit

Figure 5.6: Fits for $W = 1875$ MeV in $\cos\theta = -0.1$.

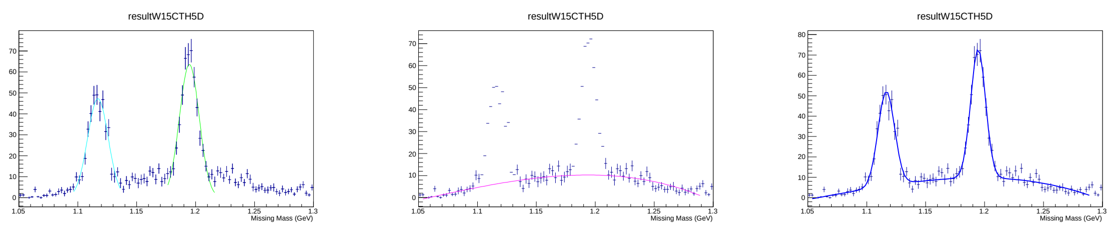

(a) Gaussian Fit (b) Background Fit (c) Global Fit

Figure 5.7: Fits for $W = 1875$ MeV in $\cos\theta = 0.1$.

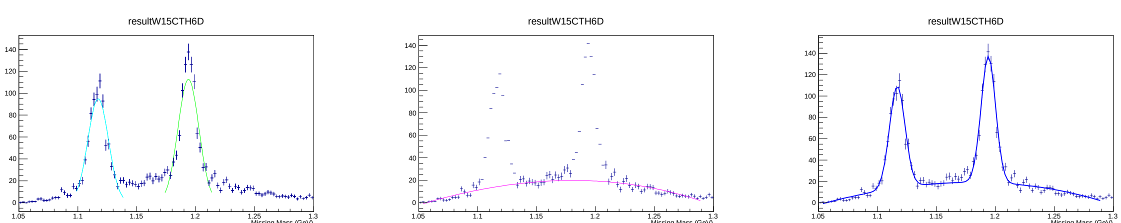

(a) Gaussian Fit (b) Background Fit (c) Global Fit

Figure 5.8: Fits for $W = 1875$ MeV in $\cos\theta = 0.3$.

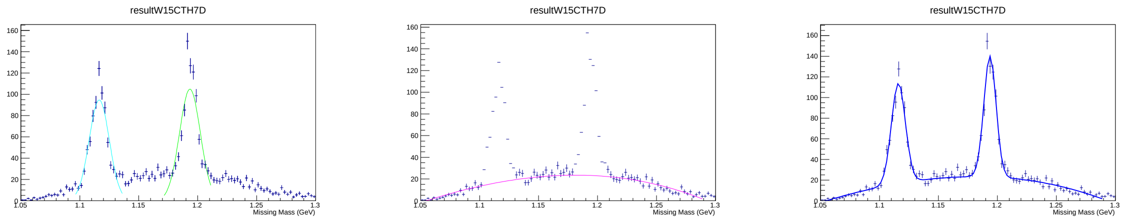

(a) Gaussian Fit (b) Background Fit (c) Global Fit

Figure 5.9: Fits for $W = 1875$ MeV in $\cos\theta = 0.5$.

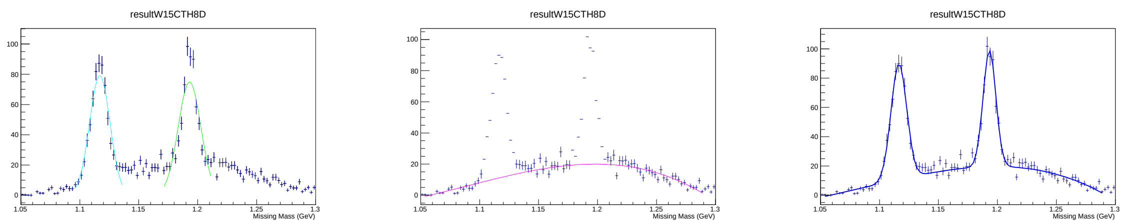

(a) Gaussian Fit (b) Background Fit (c) Global Fit

Figure 5.10: Fits for $W = 1875$ MeV in $\cos\theta = 0.7$.

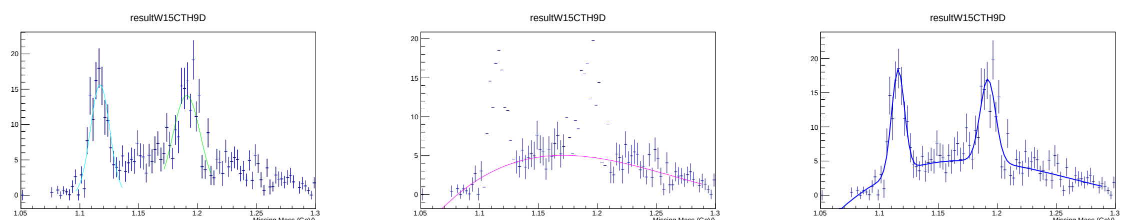

(a) Gaussian Fit (b) Background Fit (c) Global Fit

Figure 5.11: Fits for $W = 1875$ MeV in $\cos\theta = 0.9$.

Now that the signal and background for the energy bin $W = 1875$ MeV has been shown, the moments used to extract the observables for three various $\cos\theta$ bins will be shown. We note that only a small set of moments is used to calculate the polarization observables; other moments should be zero as long as there is no strong correlation between this moment and the CLAS acceptance. This was easily verified by checking that such 'unphysical' moments average out to zero. In Figs. 5.12 to 5.14, (a) shows the 0th moment, (b) shows the 1st cosine moment, (c) shows the 1st sine moment, (d) shows the 2nd cosine moment, (e) shows the 3rd sine moment, and (f) shows the 4th cosine moment.

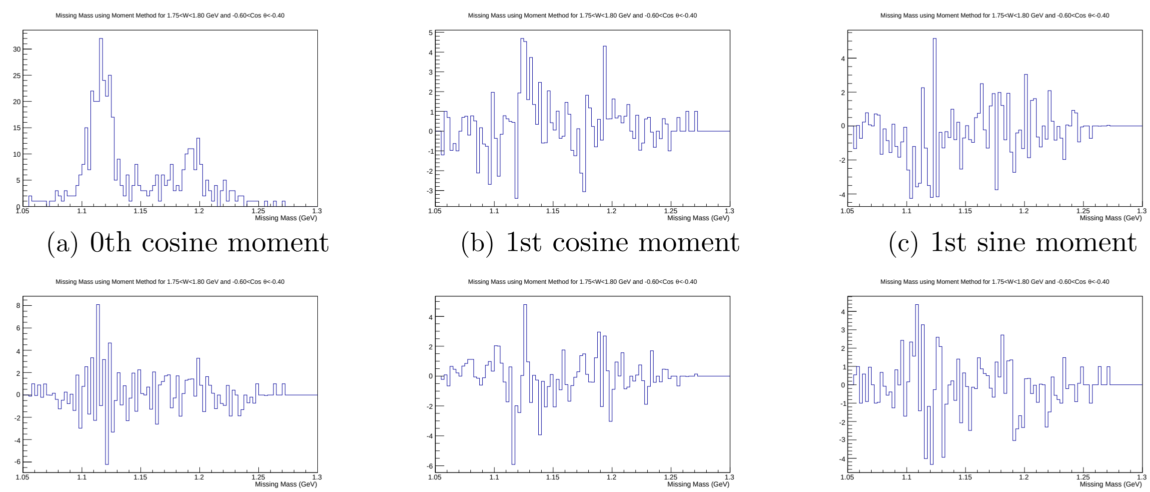

(a) 0th cosine moment

(b) 1st cosine moment

(c) 1st sine moment

(d) 2nd cosine moment

(e) 3rd sine moment

(f) 4th cosine moment

Figure 5.12: Moments for $W = 1875$ MeV and $\cos\theta = -0.5$.

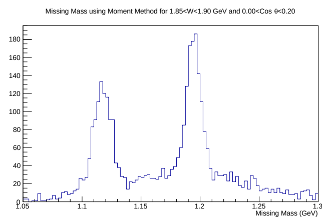

(a) 0th cosine moment

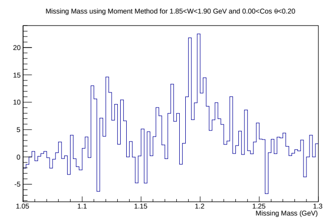

(b) 1st cosine moment

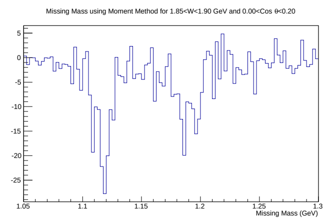

(c) 1st sine moment

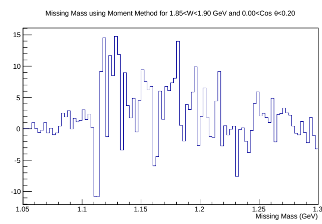

(d) 2nd cosine moment

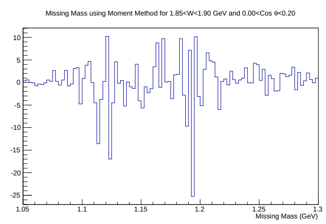

(e) 3rd sine moment

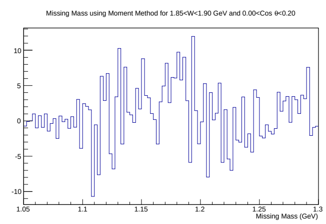

(f) 4th cosine moment

Figure 5.13: Moments for $W = 1875$ MeV and $\cos\theta = 0.1$.

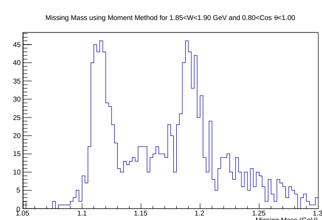

(a) 0th cosine moment

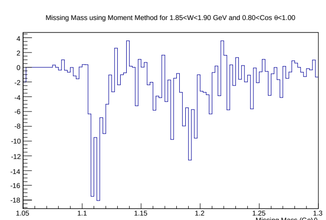

(b) 1st cosine moment

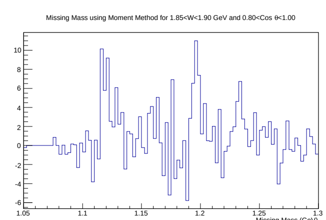

(c) 1st sine moment

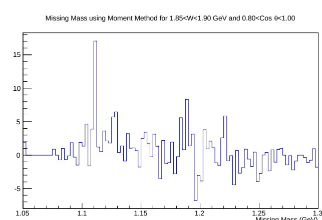

(d) 2nd cosine moment

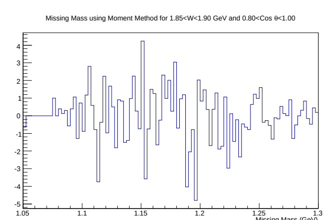

(e) 3rd sine moment

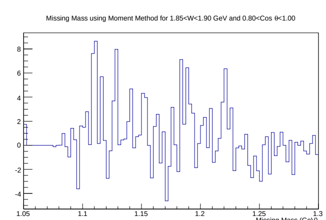

(f) 4th cosine moment

Figure 5.14: Moments for $W = 1875$ MeV and $\cos\theta = 0.9$.

There are only published data for target asymmetry in $\gamma p \to K^+\Lambda$ to which results of this analysis can be compared to, see Section 7.3. And in principle, a comparison of moment method and ϕ-bin method should be performed but due to the low statistics of $\gamma p \to K^+\Lambda$ and $\gamma p \to K^+\Sigma^0$ the reader is referred to the comparison of both methods for $\gamma p \to \pi^+ n$ by M. Dugger [116].

The observables T_x and T_z rely on Λ polarization components in the production plane. The only published data related to these components are beam-recoil polarization data, in particular C_x and C_z, which also require a circularly polarized photon beam. Obviously, the published C_X and C_z results were extracted from pure hydrogen target data [48], whereas g9b employed a butanol target. In addition, the published data used a coordinate system with z along the beamline, whereas this analysis uses the propagation direction of K^+ in the c.m. frame as z' axis. A bin-by-bin rotation of g9b results by

$$\begin{aligned} C_{x*} &= C_{x'} \cos\theta_{cm} + C_{z'} \sin\theta_{cm} \\ C_{z*} &= -C_{x'} \sin\theta_{cm} + C_{z'} \cos\theta_{cm} \end{aligned} \tag{5.45}$$

provides the observable in the frame of Ref. [48]. The observable C_x in this reference frame is shown for two W bins in Fig. 5.15. It is acknowledged that the observables for all W bins should be compared to the published results and that the CLAS-g1c data should be re-analyzed using the moment method in order to have a direct comparison of the methods.

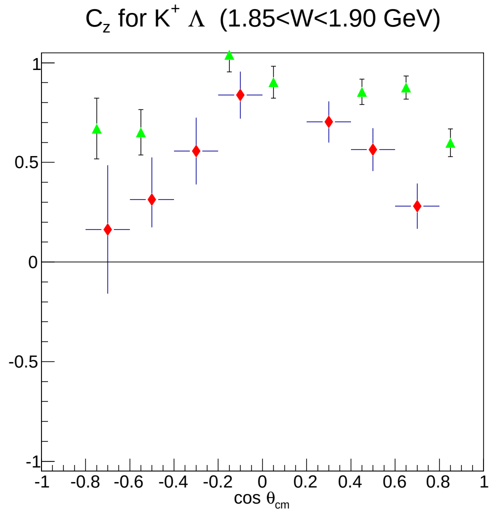

(a) for $1.85 < W < 1.90$ GeV

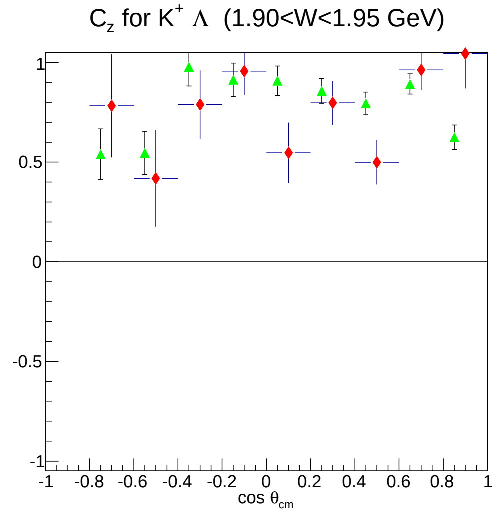

(b) for $1.90 < W < 1.95$ GeV

Figure 5.15: Comparison of C_z from CLAS-g9b with published data from CLAS-g1c [48] for two W bins.

5.6 Summary

This chapter has described the method for extracting the various polarization observables, T, T_x, T_z, and F and has discussed why the method is the most advantageous procedure for this current analysis. The next chapters will describe the uncertainty associated with the measurements and then finally, the results themselves.

Chapter 6

Systematic Studies

Before extracting the final results for the observables, the cuts previously described must be checked for their effects on the final results. Systematic studies serve to quantify any biases in the measurements and also allow for maximizing the final yield, that is obtaining the most events of interest, while still maintaining quality data. Although it would be more useful to study all energy and $\cos\theta$ bins, only three energy bins (each of width $\Delta W = 50$ MeV), $W = 1875$ MeV, $W = 2075$ MeV, and $W = 2225$ MeV, and three $\cos\theta$ bins (each covering $\Delta\cos\theta = 0.2$), $\cos\theta = -0.5$, $\cos\theta = 0.1$, and $\cos\theta = 0.9$, were chosen due to time constraints. The effects of changing certain cuts and how these changes effect the extracted results are described in this chapter.

6.1 Varying the Cuts

In order to maximize the yield, the author has chosen to vary multiple cuts discussed in Chapter 4. First, only one variation of a given cut (such as a looser or tighter cut) was applied at a time, in order to study each cut separately. Then all of the proposed cuts (all loose cuts or all tight cuts) were tried in combination to the study the resulting hyperon yields. This process will become more evident in Section 6.1.5. The yields for various bins were examined to see if the cuts had a systematic effect based on energy (in W) or K^+ (in $\cos\theta$), such as the backward, central, or forward angles. Also, the resulting measured T asymmetry was examined to see the effect of the change on the asymmetry. Although the effect of changing the cuts should be examined for all asymmetries, T, T_x, T_z, and F, the following sections describe an initial study of the uncertainties. Finally, this will also allow to calculate the total systematic uncertainty.

The tables in this chapter contain yields and T asymmetries for these specific bins together with measures to quantify the changes:

$$\text{for yields:} \quad \frac{\Delta Y}{Y_0} = \frac{Y_{\text{varied}} - Y_{\text{normal}}}{Y_{\text{normal}}} \quad (\text{in } \%) \quad , \tag{6.1}$$

$$\text{for asymmetries:} \quad \text{DSR} = \frac{T_{\text{varied}} - T_{\text{normal}}}{\sqrt{\sigma^2_{T_{\text{varied}}} + \sigma^2_{T_{\text{normal}}}}} \ . \tag{6.2}$$

The Difference-to-Standard-deviation Ratio (DSR), a variation of the more familiar SSR (Signal-to-Standard-deviation ratio = $Y_{\text{Signal}}/\sqrt{Y_{\text{background}}}$), is used to account for the uncertainty in the value of the extracted asymmetry. As a rough estimate for the significance of the change a DSR>0.5 means that the 'varied' asymmetry value is not within the error bars of the 'normal' one, a DSR>1 means that error bars are not overlapping.

In addition, at the end of the tables the standard deviation for all $\cos\theta$ bins in this W bin by adding the differences for all $\cos\theta$ bins in quadrature, weighted by the variance of the 'normal' value:

$$\sigma_T = \sqrt{\left(\sum_{i=1}^{10} \frac{1}{(\delta T^{(i)}_{\text{normal}})^2}\right)^{-1} \sum_{i=1}^{10} \frac{(T^{(i)}_{\text{varied}} - T^{(i)}_{\text{normal}})^2}{(\delta T^{(i)}_{\text{normal}})^2}} \ . \tag{6.3}$$

Note that "n/a" refers to a bin for which a Λ or Σ^0 signal could not be extracted and the resulting DSR could not be determined.

6.1.1 Optimizing Fiducial Cuts

The geometrical fiducial cuts were previously described in Section 4.6. The fiducial cut equation applied to each sector was of the form:

$$|\phi_{sector}| < \begin{cases} 0 & \text{for} \quad \theta < \theta_{min} \\ \phi_{max}\left(\frac{\theta_{meas}-\theta_{min}}{\theta_{max}-\theta_{min}}\right)^{1/4} & \text{for} \quad \theta_{min} < \theta < \theta_{max} \\ \phi_{max} & \text{for} \quad \theta > \theta_{max} \end{cases} , \tag{6.4}$$

where ϕ_{sector} is the local azimuthal angle within a sector ranging from $-30°$ to $30°$, ϕ_{max} is the maximum accepted value of ϕ_{sector} for the sector, θ_{min} is the minimum θ of the sector, θ_{max} is the maximum θ of the sector for which the correction is performed, and θ_{meas} is the measured θ from the reconstruction code. The nominal values of θ_{min}, θ_{max}, and ϕ_{min} are given in Table 4.4.

In order to check the sensitivity of the extracted observables to the parameters used for the fiducial cut, a loose and a tighter range of θ_{min}, θ_{max}, and ϕ_{max} were considered. To see the effect, the same fits were performed as in Section 4.12, more specifically, Gaussians to the signals, a cubic polynomial for the background polynomial, and a global fit for the events passing through the new and old cuts. The cut limits and results are listed in Tables 6.1, 6.2, and 6.3. The global fit results from the tighter and looser cuts may be seen in Figs. 6.1 to 6.9.

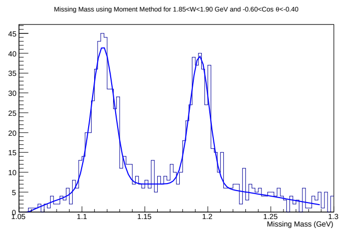

(a) Normal Fiducial Cut

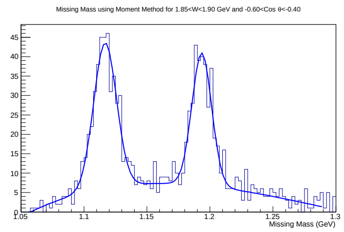

(b) Loose Fiducial Cut

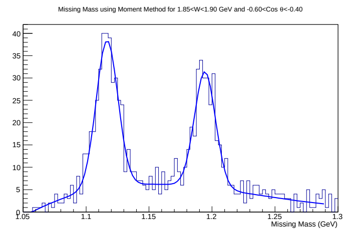

(c) Tight Fiducial Cut

Figure 6.1: Comparison of the global fits of the varied fiducial cuts applied for W = 1875 MeV and $\cos\theta$=-0.5.

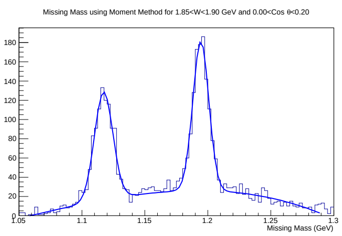

(a) Normal Fiducial Cut

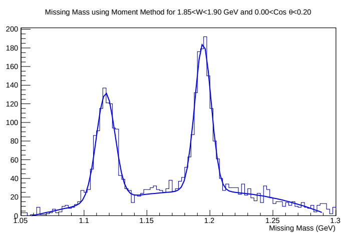

(b) Loose Fiducial Cut

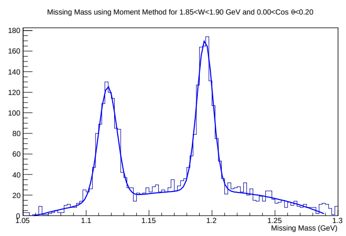

(c) Tight Fiducial Cut

Figure 6.2: Comparison of the global fits of the loose fiducial cuts applied for W = 1875 MeV and various $\cos\theta$=0.1.

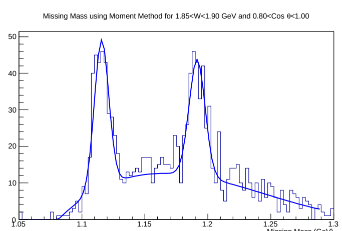

(a) Normal Fiducial Cut

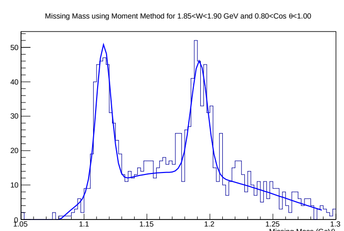

(b) Loose Fiducial Cut

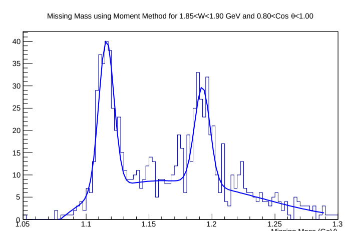

(c) Tight Fiducial Cut

Figure 6.3: Comparison of the global fits of the varied fiducial cuts applied for W = 1875 MeV and $\cos\theta$=0.9.

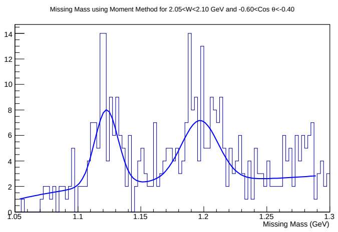

(a) Normal Fiducial Cut

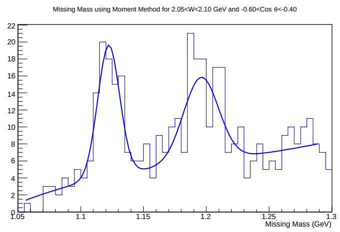

(b) Loose Fiducial Cut

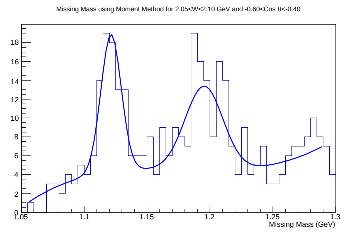

(c) Tight Fiducial Cut

Figure 6.4: Comparison of the global fits of the varied fiducial cuts applied for W = 2075 MeV and $\cos\theta$=-0.5.

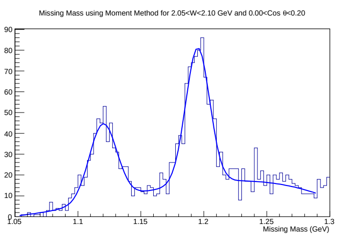

(a) Normal Fiducial Cut

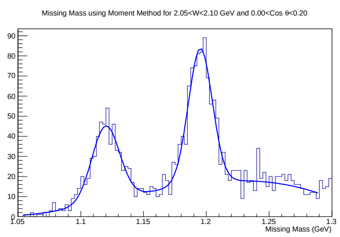

(b) Loose Fiducial Cut

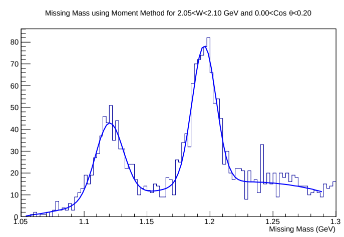

(c) Tight Fiducial Cut

Figure 6.5: Comparison of the global fits of the loose fiducial cuts applied for W = 2075 MeV and various $\cos\theta$=0.1.

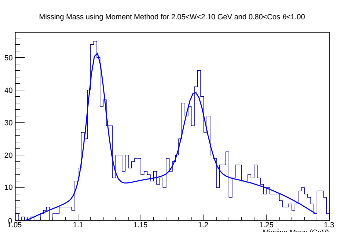

(a) Normal Fiducial Cut

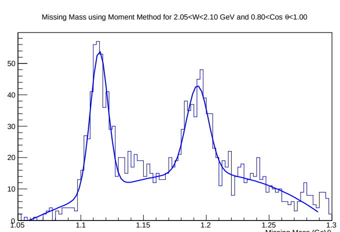

(b) Loose Fiducial Cut

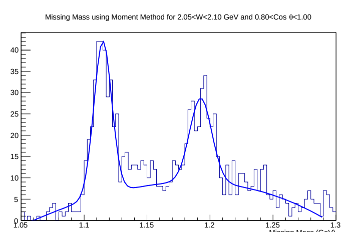

(c) Tight Fiducial Cut

Figure 6.6: Comparison of the global fits of the varied fiducial cuts applied for W = 2075 MeV and $\cos\theta$=0.9.

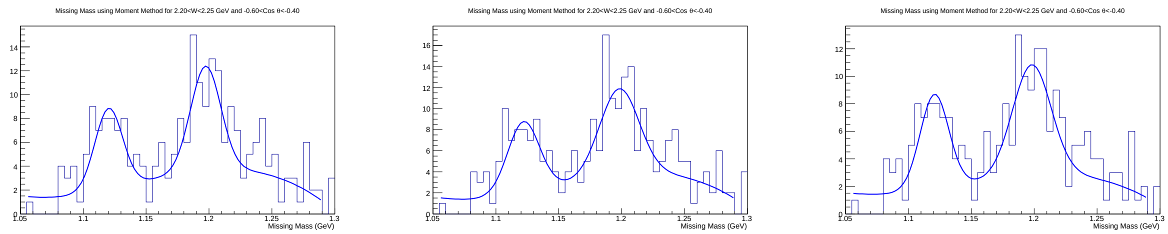

(a) Normal Fiducial Cut (b) Loose Fiducial Cut (c) Tight Fiducial Cut

Figure 6.7: Comparison of the global fits of the varied fiducial cuts applied for $W = 2225$ MeV and $\cos\theta$=-0.5.

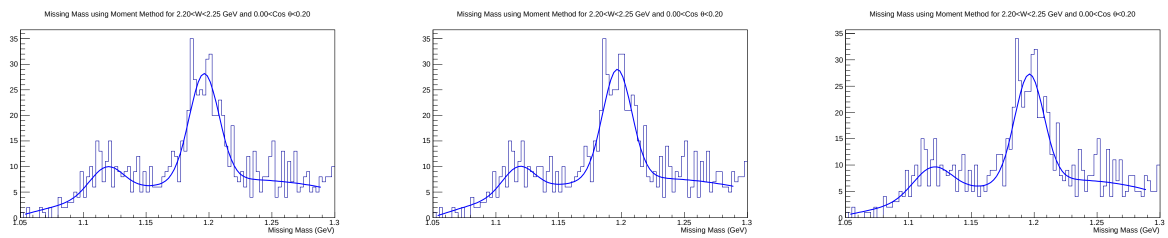

(a) Normal Fiducial Cut (b) Loose Fiducial Cut (c) Tight Fiducial Cut

Figure 6.8: Comparison of the global fits of the loose fiducial cuts applied for $W = 2225$ MeV and various $\cos\theta$=0.1.

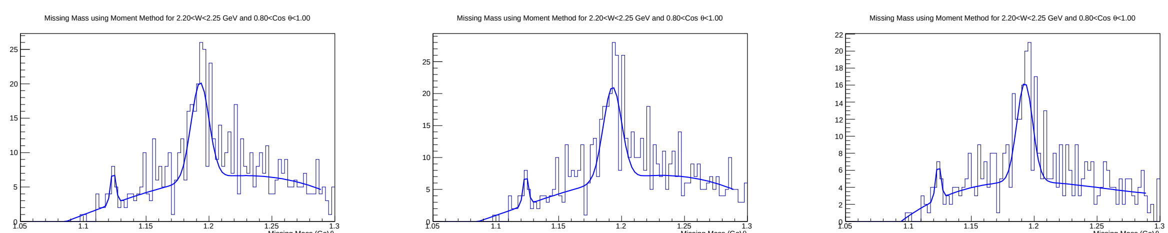

(a) Normal Fiducial Cut (b) Loose Fiducial Cut (c) Tight Fiducial Cut

Figure 6.9: Comparison of the global fits of the varied fiducial cuts applied for $W = 2225$ MeV and $\cos\theta$=0.9.

Table 6.1: Extracted yields of Λ and Σ^0 events depending on the applied fiducial cut for energy bin $W = 1875$ MeV and various $\cos\theta_{K^+}$ bins.

$\theta_{min};\theta_{max};\phi_{max}$	Normal Cuts: $9°;40°;25°$	Loose Cuts: $7°;42°;26°$	Tight Cuts: $11°;38°;24°$
$W = 1875$ MeV, $\cos\theta_{K^+} = -0.5$			
Λ yield (background):	319 (84)	339 (88)	285 (75)
Λ gain/loss %:		6.27 (4.76)	-10.66 (-10.71)
Σ^0 yield (background):	255 (80)	268 (85)	217 (73)
Σ^0 gain/loss %:		5.10 (6.25)	-14.90 (-8.75)
χ^2/NDF:	0.76	0.80	0.68
T Λ asymmetry:	0.240±0.117	0.206±0.113	0.161±0.123
T Λ change (DSR):		-0.209	-0.465
T Σ^0 asymmetry:	0.158±0.125	0.151±0.121	0.059±0.134
T Σ^0 change (DSR):		-0.040	-0.540
$W = 1875$ MeV, $\cos\theta_{K^+} = 0.1$			
Λ yield (background):	825 (189)	848 (192)	807 (179)
Λ gain/loss %:		2.79 (1.59)	-2.18 (-5.29)
Σ^0 yield (background):	991 (264)	1030 (275)	940 (249)
Σ^0 gain/loss %:		3.94 (4.17)	-5.15 (-5.68)
χ^2/NDF:	1.29	1.37	1.30
T Λ asymmetry:	-0.260±0.069	-0.262±0.067	-0.275±0.068
T Λ change (DSR):		-0.021	-0.155
T Σ^0 asymmetry:	0.203±0.066	0.200±0.064	0.235±0.066
T Σ^0 change (DSR):		-0.033	0.343
$W = 1875$ MeV, $\cos\theta_{K^+} = 0.9$			
Λ yield (background):	232 (78)	244 (84)	206 (61)
Λ gain/loss %:		5.17 (7.69)	-11.21 (-21.79)
Σ^0 yield (background):	202 (118)	216 (135)	135 (77)
Σ^0 gain/loss %:		6.93 (14.41)	-33.17 (-34.75)
χ^2/NDF:	1.38	1.36	1.12
T Λ asymmetry:	-0.390±0.134	-0.372±0.133	-0.306±0.146
T Λ change (DSR):		0.095	0.424
T Σ^0 asymmetry:	-0.082±0.144	-0.111±0.138	-0.165±0.171
T Σ^0 change (DSR):		-0.145	-0.371
σ_T (Λ):		0.015	0.052
σ_T (Σ^0):		0.020	0.032

Table 6.2: Extracted yields of Λ and Σ^0 events depending on the applied fiducial cut for energy bin W = 2075 MeV and various $\cos\theta_{K^+}$ bins. "n/a" refers to a bin for which a Λ or Σ^0 signal could not be extracted and the resulting DSR could not be determined.

	Normal Cuts:	Loose Cuts:	Tight Cuts:
$\theta_{min}; \theta_{max}; \phi_{max}$	$9°; 40°; 25°$	$7°; 42°; 26°$	$11°; 38°; 24°$
$W = 2075$ MeV, $\cos\theta_{K^+} = -0.5$			
Λ yield (background):	55 (27)	48 (32)	49 (25)
Λ gain/loss %:		-12.73 (18.52)	-10.91 (-7.41)
Σ^0 yield (background):	69 (41)	47 (57)	68 (32)
Σ^0 gain/loss %:		-31.88 (39.02)	-1.45 (-21.95)
χ^2/NDF:	0.95	1.01	0.95
T Λ asymmetry:	n/a	n/a	n/a
T Λ change (DSR):			
T Σ^0 asymmetry:	-0.087±0.273	-0.037±0.265	-0.123±0.294
T Σ^0 change (DSR):		0.131	-0.090
$W = 2075$ MeV, $\cos\theta_{K^+} = 0.1$			
Λ yield (background):	405 (118)	415 (117)	395 (116)
Λ gain/loss %:		2.47 (-0.85)	-2.53 (-1.69)
Σ^0 yield (background):	618 (241)	639 (248)	607 (226)
Σ^0 gain/loss %:		3.40 (2.90)	-1.78 (-6.22)
χ^2/NDF:	0.98	0.93	1.01
T Λ asymmetry:	-0.660±0.074	-0.598±0.079	-0.628±0.078
T Λ change (DSR):		0.573	0.298
T Σ^0 asymmetry:	-0.210±0.084	-0.194±0.081	-0.218±0.084
T Σ^0 change (DSR):		0.137	-0.067
$W = 2075$ MeV, $\cos\theta_{K^+} = 0.9$			
Λ yield (background):	308 (97)	316 (101)	257 (66)
Λ gain/loss %:		2.60 (4.12)	-16.56 (-31.96)
Σ^0 yield (background):	221 (191)	246 (211)	173 (124)
Σ^0 gain/loss %:		11.31 (10.47)	-21.72 (-35.08)
χ^2/NDF:	1.22	1.18	1.32
T Λ asymmetry:	-0.597±0.090	-0.571±0.089	-0.586±0.098
T Λ change (DSR):		0.205	0.083
T Σ^0 asymmetry:	-0.211±0.142	-0.204±0.133	0.005±0.164
T Σ^0 change (DSR):		0.036	0.996
σ_T (Λ):		0.029	0.042
σ_T (Σ^0):		0.031	0.058

Table 6.3: Extracted yields of Λ and Σ^0 events depending on the applied fiducial cut for energy bin $W = 2225$ MeV and various $\cos\theta_{K^+}$ bins. "n/a" refers to a bin for which a Λ or Σ^0 signal could not be extracted and the resulting DSR could not be determined.

$\theta_{min}; \theta_{max}; \phi_{max}$	Normal Cuts: $9°; 40°; 25°$	Loose Cuts: $7°; 42°; 26°$	Tight Cuts: $11°; 38°; 24°$
$W = 2225$ MeV, $\cos\theta_{K^+} = -0.5$			
Λ yield (background):	29 (29)	29 (31)	24 (29)
Λ gain/loss %:		0 (6.90)	-17.24 (0)
Σ^0 yield (background):	14 (16)	15 (16)	15 (16)
Σ^0 gain/loss %:		7.14 (0)	7.14 (0)
χ^2/NDF:	0.72	0.81	0.62
T Λ asymmetry:	n/a	n/a	n/a
T Λ change (DSR):			
T Σ^0 asymmetry:	n/a	n/a	n/a
T Σ^0 change (DSR):			
$W = 2225$ MeV, $\cos\theta_{K^+} = 0.1$			
Λ yield (background):	74 (74)	66 (79)	87 (65)
Λ gain/loss %:		-10.81 (6.76)	17.57 (-12.16)
Σ^0 yield (background):	248 (121)	249 (125)	238 (115)
Σ^0 gain/loss %:		0.04 (3.31)	-4.03 (-4.96)
χ^2/NDF:	0.96	1.01	1.03
T Λ asymmetry:	-0.707±0.13	-0.723±0.104	-0.613±0.151
T Λ change (DSR):		-0.096	0.472
T Σ^0 asymmetry:	-0.472±0.114	-0.507±0.104	-0.468±0.111
T Σ^0 change (DSR):		-0.227	0.025
$W = 2225$ MeV, $\cos\theta_{K^+} = 0.9$			
Λ yield (background):	10 (8)	10 (8)	8 (8)
Λ gain/loss %:			-20.0 (0)
Σ^0 yield (background):	100 (69)	106 (75)	72 (46)
Σ^0 gain/loss %:		6 (8.70)	-28 (-33.33)
χ^2/NDF:	1.42	1.55	1.19
T Λ asymmetry:	n/a	n/a	n/a
T Λ change (DSR):			
T Σ^0 asymmetry:	0.181±0.178	0.130±0.172	0.066±0.211
T Σ^0 change (DSR):		-0.206	-0.417
σ_T (Λ):		0.063	0.072
σ_T (Σ^0):		0.039	0.097

By examining the global fits, yields, and change in the T asymmetry for both looser and tighter fiducial cuts, one can clearly see that the current *normal* cuts are within reason. If too loose fiducial cuts are used, more background is present in the Λ and Σ^0 peaks. If too tight fiducial cuts are used, more events are lost, which is undesirable, as the events from the Λ and Σ^0 signals are used to calculate the asymmetry measurements. More specifically, for $W = 1875$ MeV, a large change occurs in the yields of Λ and Σ^0 in the backward and forward angles chosen, but the overall change of the T asymmetry is negligible. Fiducial cuts that were too tight were not good due to the bias in the backward and forward direction angles.

6.1.2 Optimizing the Particle ID

In order to study the optimum particle identification, it is useful to vary the momentum dependent β cut. The particle identification using momentum dependent β ranges was previously discussed in Section 4.5. In order to ensure that the best particle identification is used, the cuts on β of the pion, kaon, and proton may be varied, again applying looser and tighter cuts. To see the effect, the same fits as performed in Section 4.12, more specifically, Gaussians for the signals, a cubic polynomial to the background, and a global fit were performed. The global fit result from the tighter and looser cuts may be seen in Figs. 6.10 to 6.18. The cut parameters and results are listed in Tables 6.4, 6.5, and 6.6.

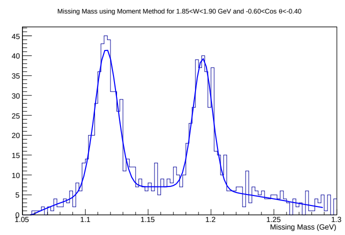

(a) Normal β Cuts

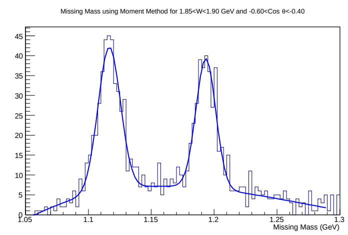

(b) Loose β Cuts

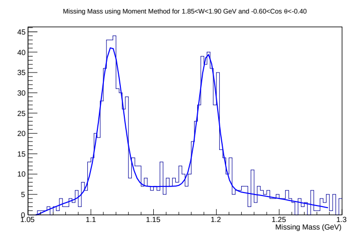

(c) Tight β Cuts

Figure 6.10: Comparison of the global fits of the varied β cuts applied for W = 1875 MeV and $\cos\theta$=-0.5.

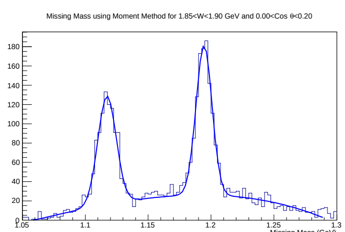

(a) Normal β Cuts

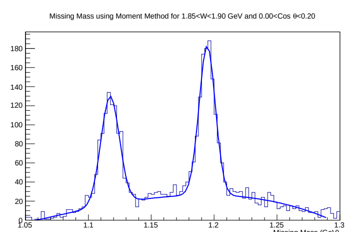

(b) Loose β Cuts

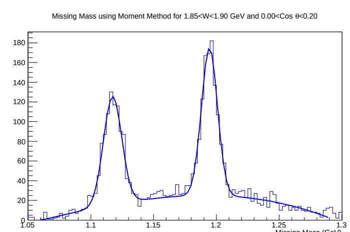

(c) Tight β Cuts

Figure 6.11: Comparison of the global fits of the varied β cuts applied for W = 1875 MeV and $\cos\theta$=0.1.

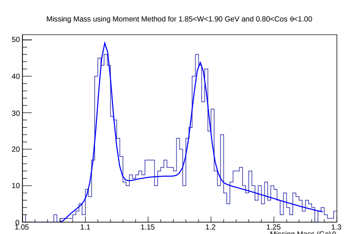

(a) Normal β Cuts

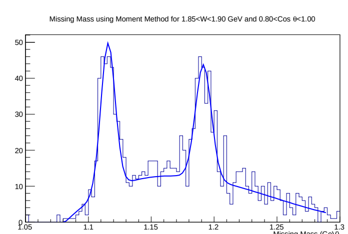

(b) Loose β Cuts

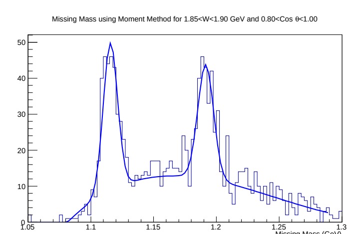

(c) Tight β Cuts

Figure 6.12: Comparison of the global fits of the varied β cuts applied for W = 1875 MeV and $\cos\theta$=0.9.

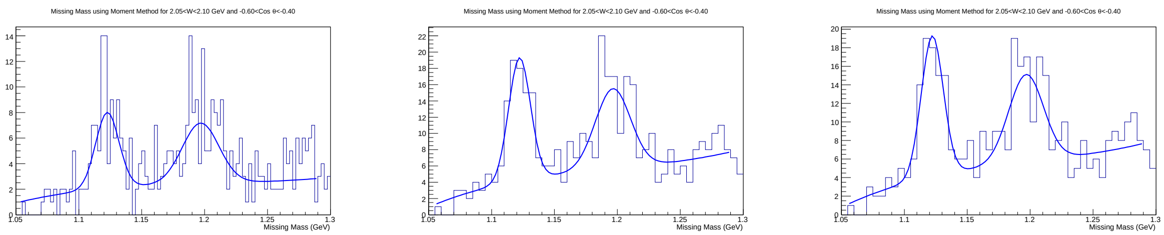

(a) Normal β Cuts (b) Loose β Cuts (c) Tight β Cuts

Figure 6.13: Comparison of the global fits of the varied β cuts applied for $W = 2075$ MeV and $\cos\theta$=-0.5.

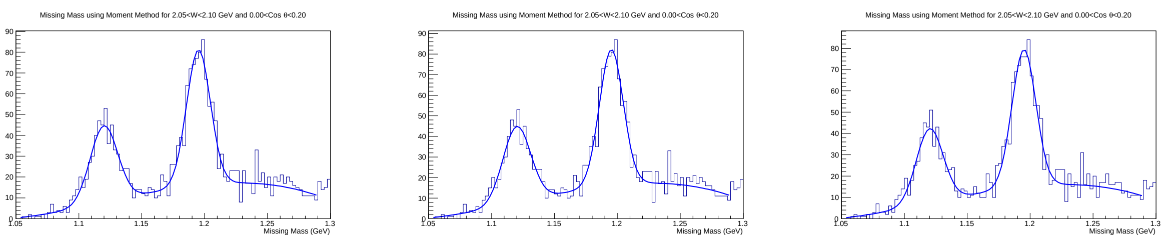

(a) Normal β Cuts (b) Loose β Cuts (c) Tight β Cuts

Figure 6.14: Comparison of the global fits of the varied β cuts applied for $W = 2075$ MeV and $\cos\theta$=0.1.

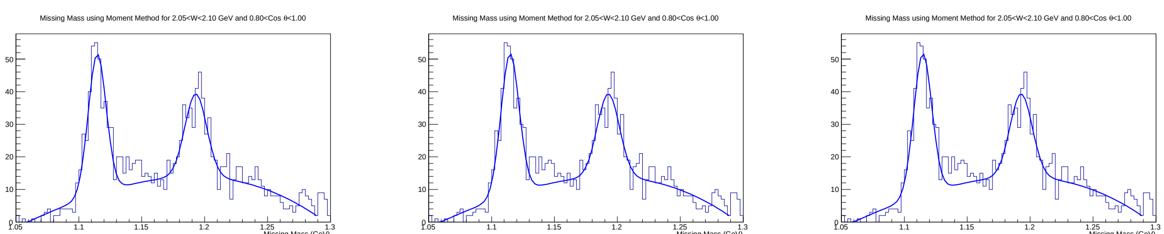

(a) Normal β Cuts (b) Loose β Cuts (c) Tight β Cuts

Figure 6.15: Comparison of the global fits of the varied β cuts applied for $W = 2075$ MeV and $\cos\theta$=0.9.

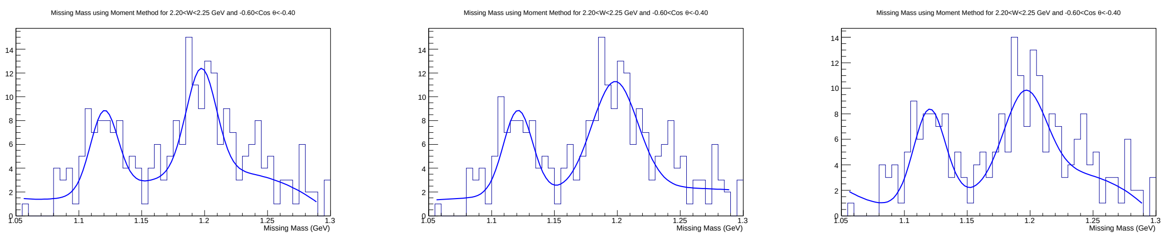

(a) Normal β Cuts (b) Loose β Cuts (c) Tight β Cuts

Figure 6.16: Comparison of the global fits of the varied β cuts applied for W = 2225 MeV and $\cos\theta$=-0.5.

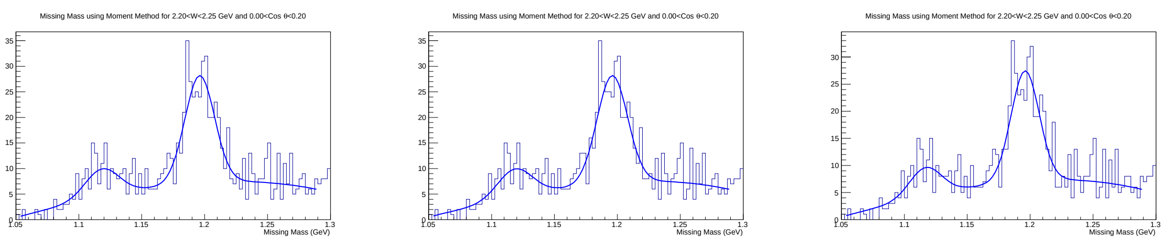

(a) Normal β Cuts (b) Loose β Cuts (c) Tight β Cuts

Figure 6.17: Comparison of the global fits of the varied β cuts applied for W = 2225 MeV and $\cos\theta$=0.1.

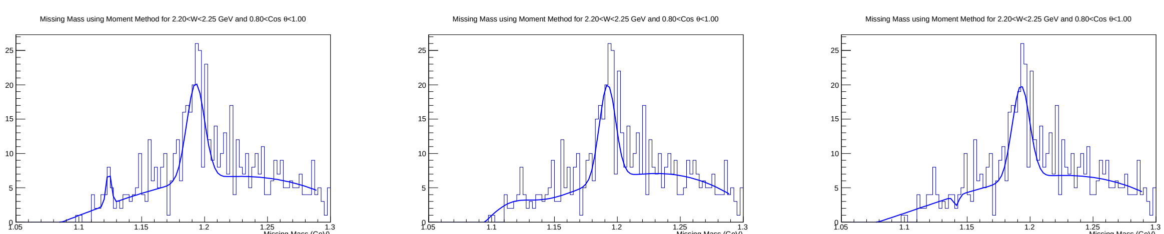

(a) Normal β Cuts (b) Loose β Cuts (c) Tight β Cuts

Figure 6.18: Comparison of the global fits of the varied β cuts applied for W = 2225 MeV and $\cos\theta$=0.9.

Table 6.4: Extracted yields of Λ and Σ^0 events and the resulting T asymmetry depending on the β cuts applied for energy bin $W = 1875$ MeV and various $\cos\theta_{K^+}$ bins.

	Normal Cuts:	Loose Cuts:	Tight Cuts:
π range	0.11-0.2	0.06-0.25	0.11-0.17
K range	0.44-0.55	0.39-0.60	0.46-0.54
p range	0.85-1.05	0.80-1.10	0.9-1.0
$W = 1875$ MeV, $\cos\theta_{K^+} = -0.5$			
Λ yield (background):	319 (84)	322 (85)	311 (81)
Λ gain/loss %:		0.94 (1.19)	-2.51 (-3.57)
Σ^0 yield (background):	255 (80)	256 (83)	252 (79)
Σ^0 gain/loss %:		0.39 (3.75)	-1.18 (-1.25)
χ^2/NDF:	0.76	0.75	0.78
T Λ asymmetry:	0.240±0.117	0.231±0.115	0.259±0.117
T Λ change (DSR):		-0.055	0.115
T Σ^0 asymmetry:	0.158±0.125	0.163±0.123	0.154±0.124
T Σ^0 change (DSR):		0.029	-0.023
$W = 1875$ MeV, $\cos\theta_{K^+} = 0.1$			
Λ yield (background):	825 (189)	837 (191)	803 (183)
Λ gain/loss %:		1.45 (1.06)	-2.67 (-3.17)
Σ^0 yield (background):	991 (264)	1014 (272)	958 (254)
Σ^0 gain/loss %:		2.32 (3.03)	-3.33 (-3.79)
χ^2/NDF:	1.29	1.29	1.31
T Λ asymmetry:	-0.260±0.069	-0.250±0.068	-0.252±0.068
T Λ change (DSR):		0.103	0.083
T Σ^0 asymmetry:	0.203±0.066	0.171±0.065	0.213±0.066
T Σ^0 change (DSR):		-0.345	0.107
$W = 1875$ MeV, $\cos\theta_{K^+} = 0.9$			
Λ yield (background):	232 (78)	234 (79)	221 (70)
Λ gain/loss %:		0.86 (1.28)	-4.74 (-10.26)
Σ^0 yield (background):	202 (118)	199 (120)	195 (114)
Σ^0 gain/loss %:		-1.46 (1.69)	-3.47 (-3.39)
χ^2/NDF:	1.38	1.39	1.48
T Λ asymmetry:	-0.39±0.134	-0.369±0.133	-0.326±0.138
T Λ change (DSR):		0.111	0.333
T Σ^0 asymmetry:	-0.082±0.144	-0.08±0.143	-0.097±0.145
T Σ^0 change (DSR):		0.00986	-0.0734
σ_T (Λ):		0.024	0.030
σ_T (Σ^0):		0.020	0.015

Table 6.5: Extracted yields of Λ and Σ^0 events and the resulting T asymmetry depending on the β cuts applied for energy bin $W = 2075$ MeV and various $\cos\theta_{K^+}$ bins. "n/a" refers to a bin for which a Λ or Σ^0 signal could not be extracted and the resulting DSR could not be determined.

	Normal Cuts:	Loose Cuts:	Tight Cuts:
π range	0.11-0.2	0.06-0.25	0.11-0.17
K range	0.44-0.55	0.39-0.60	0.46-0.54
p range	0.85-1.05	0.80-1.10	0.9-1.0
$W = 2075$ MeV, $\cos\theta_{K^+} = -0.5$			
Λ yield (background):	55 (27)	55 (27)	55 (27)
Λ gain/loss %:			
Σ^0 yield (background):	69 (41)	70 (41)	66 (41)
Σ^0 gain/loss %:		1.45 (0)	-4.35 (0)
χ^2/NDF:	0.95	0.96	0.92
T Λ asymmetry:	n/a	n/a	n/a
T Λ change (DSR):			
T Σ^0 asymmetry:	-0.087±0.273	-0.022±0.267	-0.094±0.273
T Σ^0 change (DSR):	0	0.17	-0.0181
$W = 2075$ MeV, $\cos\theta_{K^+} = 0.1$			
Λ yield (background):	405 (118)	411 (118)	374 (110)
Λ gain/loss %:		1.48 (0)	- 7.65 (-6.78)
Σ^0 yield (background):	618 (241)	628 (242)	613 (225)
Σ^0 gain/loss %:		1.62 (0.41)	-0.81 (-6.64)
χ^2/NDF:	0.98	0.98	1.08
T Λ asymmetry:	-0.66±0.074	-0.63±0.075	-0.834±0.027
T Λ change (DSR):		0.285	-2.21
T Σ^0 asymmetry:	-0.21±0.084	-0.203±0.082	-0.189±0.084
T Σ^0 change (DSR):		0.0596	0.177
$W = 2075$ MeV, $\cos\theta_{K^+} = 0.9$			
Λ yield (background):	308 (97)	313 (28)	307 (95)
Λ gain/loss %:		1.62 (-71.13)	-0.32 (-2.06)
Σ^0 yield (background):	221 (191)	226 (194)	218 (186)
Σ^0 gain/loss %:		2.26 (1.57)	-1.36 (-2.62)
χ^2/NDF:	1.22	1.24	1.13
T Λ asymmetry:	-0.597±0.09	-0.567±0.091	-0.542±0.094
T Λ change (DSR):		0.234	0.423
T Σ^0 asymmetry:	-0.211±0.142	-0.16±0.14	-0.202±0.141
T Σ^0 change (DSR):		0.256	0.045
σ_T (Λ):		0.030	0.070
σ_T (Σ^0):		0.016	0.036

Table 6.6: Extracted yields of Λ and Σ^0 events and the resulting T asymmetry depending on the β cuts applied for energy bin $W = 2225$ MeV and various $\cos\theta_{K^+}$ bins. "n/a" refers to a bin for which a Λ or Σ^0 signal could not be extracted and the resulting DSR could not be determined.

	Normal Cuts:	Loose Cuts:	Tight Cuts:
π range	0.11-0.2	0.06-0.25	0.11-0.17
K range	0.44-0.55	0.39-0.60	0.46-0.54
p range	0.85-1.05	0.80-1.10	0.9-1.0
$W = 2225$ MeV, $\cos\theta_{K^+} = -0.5$			
Λ yield (background):	29 (29)	31 (28)	25 (28)
Λ gain/loss %:		6.90 (-3.45)	-13.79 (-3.45)
Σ^0 yield (background):	14 (16)	14 (16)	15 (8)
Σ^0 gain/loss %:			7.14 (-50.0)
χ^2/NDF:	0.72	0.75	0.67
T Λ asymmetry:	n/a	n/a	n/a
T Λ change (DSR):			
T Σ^0 asymmetry:	n/a	n/a	n/a
T Σ^0 change (DSR):			
$W = 2225$ MeV, $\cos\theta_{K^+} = 0.1$			
Λ yield (background):	74 (74)	76 (72)	68 (73)
Λ gain/loss %:		2.70 (-2.70)	-10.81 (-1.35)
Σ^0 yield (background):	248 (121)	255 (121)	228 (117)
Σ^0 gain/loss %:		2.82 (0)	-8.06 (-3.31)
χ^2/NDF:	0.96	0.96	1.05
T Λ asymmetry:	-0.707±0.13	-0.679±0.13	-0.683±0.13
T Λ change (DSR):		0.152	0.131
T Σ^0 asymmetry:	-0.472±0.114	-0.435±0.115	-0.564±0.101
T Σ^0 change (DSR):		0.228	-0.604
$W = 2225$ MeV, $\cos\theta_{K^+} = 0.9$			
Λ yield (background):	10 (8)	47 (6)	-3 (0)
Λ gain/loss %:		370 (-25)	-130 (-100)
Σ^0 yield (background):	100 (69)	90 (63)	95 (69)
Σ^0 gain/loss %:		-10 (-8.70)	-5 (0)
χ^2/NDF:	1.42	1.43	1.43
T Λ asymmetry:	n/a	n/a	n/a
T Λ change (DSR):			
T Σ^0 asymmetry:	0.181±0.178	0.187±0.179	0.216±0.175
T Σ^0 change (DSR):		0.0238	0.14
σ_T (Λ):		0.019	0.089
σ_T (Σ^0):		0.020	0.042

Once again, by looking at the global fits, yields, and change of asymmetry for both looser and tighter β versus momentum cuts, one can clearly see that the current *normal* cuts are within reason. If too loose β cuts are used, more background is present in the Λ and Σ^0 peaks. For loose cuts, the extracted asymmetry appears systematically lower in magnitude. For tight β cuts the yield is reduced, but the asymmetries stay unchanged. When comparing the yields for the various energies, there is no significant change in the yields and the same effect occurs when comparing the change in asymmetries. The change in asymmetry calculations was negligible, and by trying to optimize the particle identification using looser or tighter cuts, did not produce a noticeable effect and the current cuts are reasonable.

6.1.3 Optimizing Missing Mass Cuts

The missing mass cuts performed in the analysis were previously described in Section 4.10. To study the optimal missing mass cut, the cut was varied to be looser and tighter. Normally, a very loose cut was applied around $\gamma p \rightarrow K^+ p X$ from 0.05 to 0.30 GeV to extract the Λ and Σ^0 signals. After the looser and tighter cuts were applied, the same process was performed to fit the Λ and Σ^0 signals, a Gaussian, a cubic polynomial and a global fit. The yield fits showed that when making a looser missing mass cut, in many bins a slight loss on the Σ^0 signal occurred. The yield, on the other hand, increased when making a tight missing mass cut, a gain on Λ and Σ^0 signals occurred, together with a decrease in the background. Due to this unexpected result, an even tighter cut was applied. The unexpected result is likely due to the variations in the signal/background ratio when changing the π^- cuts or on the fact that the background outside of the hyperon peaks for the normal cuts is lost and allows for better constraints for the background function. However, the end effect on the asymmetry was not as noticeable except in the $\cos\theta = 0.1$ bin at $W = 2225$ MeV, where a systematic decrease in T was observed. The yields and change in asymmetries are listed in Tables 6.7, 6.8, and 6.9. The global fit of the looser missing mass cuts, tight missing mass cuts, and tighter missing mass cuts can be seen in Figs. 6.19 to 6.27.

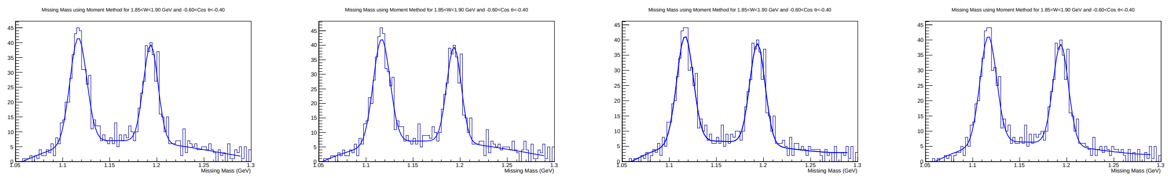

(a) Normal Missing Mass Cut (b) Loose Missing Mass Cut (c) Tight Missing Mass Cut (d) Tighter Missing Mass Cut

Figure 6.19: Comparison of the global fits of the varied missing mass cuts applied for $W = 1875$ MeV and $\cos\theta$=-0.5.

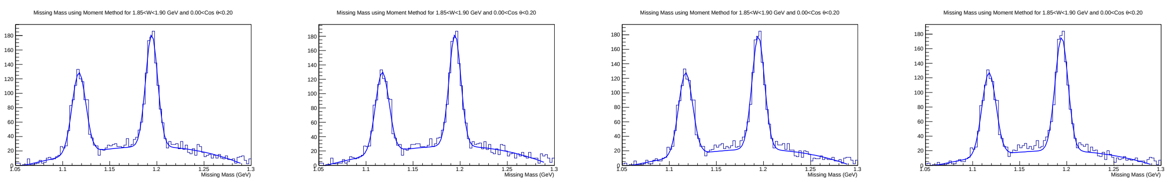

(a) Normal Missing Mass Cut (b) Loose Missing Mass Cut (c) Tight Missing Mass Cut (d) Tighter Missing Mass Cut

Figure 6.20: Comparison of the global fits of the varied missing mass cuts applied for $W = 1875$ MeV and $\cos\theta$=0.1

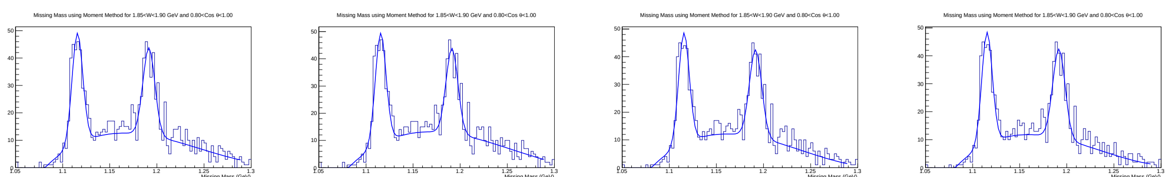

(a) Normal Missing Mass Cut (b) Loose Missing Mass Cut (c) Tight Missing Mass Cut (d) Tighter Missing Mass Cut

Figure 6.21: Comparison of the global fits of the varied missing mass cuts applied for $W = 1875$ MeV and $\cos\theta$=0.9.

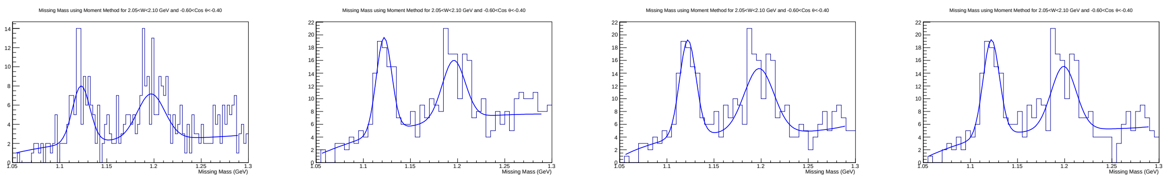

(a) Normal Missing Mass Cut (b) Loose Missing Mass Cut (c) Tight Missing Mass Cut (d) Tighter Missing Mass Cut

Figure 6.22: Comparison of the global fits of the varied missing mass cuts applied for $W = 2075$ MeV and $\cos\theta$=-0.5.

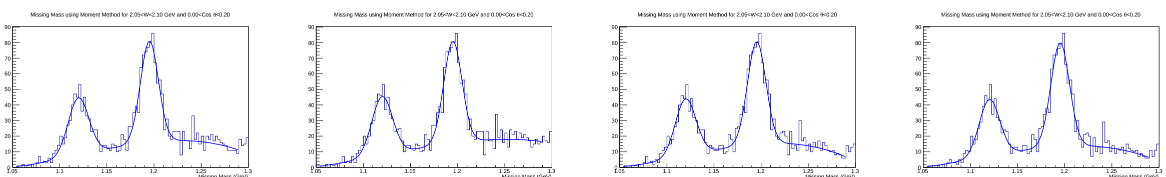

(a) Normal Missing Mass Cut (b) Loose Missing Mass Cut (c) Tight Missing Mass Cut (d) Tighter Missing Mass Cut

Figure 6.23: Comparison of the global fits of the varied missing mass cuts applied for $W = 2075$ MeV and $\cos\theta$=0.1

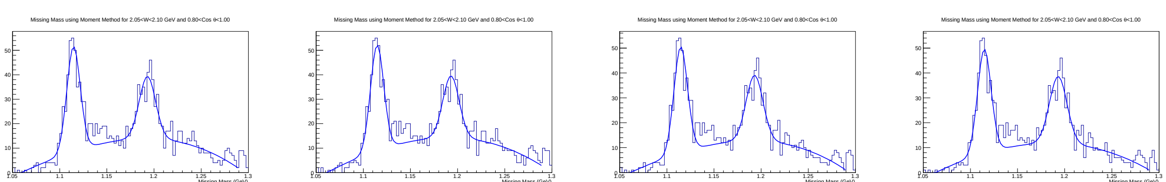

(a) Normal Missing Mass Cut (b) Loose Missing Mass Cut (c) Tight Missing Mass Cut (d) Tighter Missing Mass Cut

Figure 6.24: Comparison of the global fits of the varied missing mass cuts applied for $W = 2075$ MeV and $\cos\theta$=0.9.

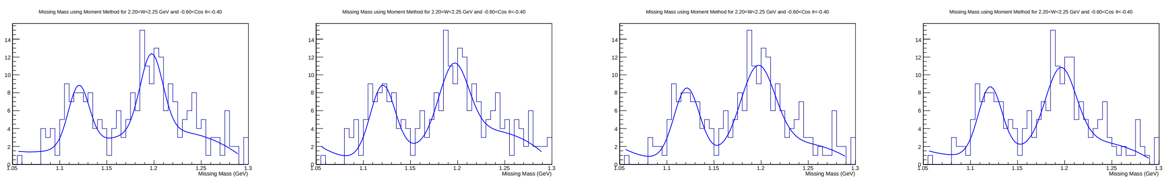

(a) Normal Missing Mass Cut (b) Loose Missing Mass Cut (c) Tight Missing Mass Cut (d) Tighter Missing Mass Cut

Figure 6.25: Comparison of the global fits of the varied missing mass cuts applied for $W = 2225$ MeV and $\cos\theta$=-0.5.

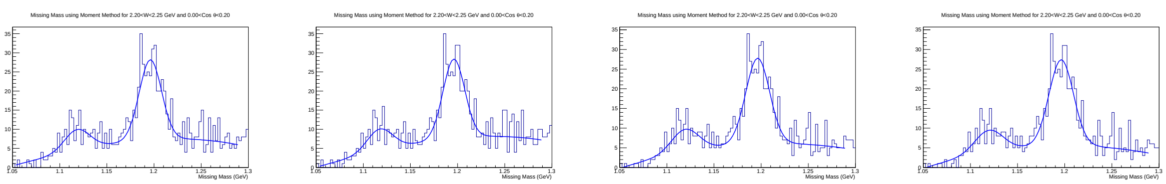

(a) Normal Missing Mass Cut (b) Loose Missing Mass Cut (c) Tight Missing Mass Cut (d) Tighter Missing Mass Cut

Figure 6.26: Comparison of the global fits of the varied missing mass cuts applied for $W = 2225$ MeV and $\cos\theta$=0.1

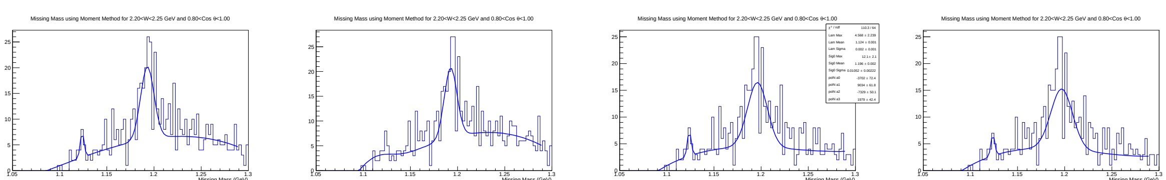

(a) Normal Missing Mass Cut (b) Loose Missing Mass Cut (c) Tight Missing Mass Cut (d) Tighter Missing Mass Cut

Figure 6.27: Comparison of the global fits of the varied missing mass cuts applied for $W = 2225$ MeV and $\cos\theta$=0.9.

Table 6.7: Extracted yields of Λ and Σ^0 events and the resulting T asymmetry depending on the missing mass cuts for energy bin $W = 1875$ MeV and various $\cos\theta_{K^+}$ bins.

Cut on π (GeV):	Normal Cuts: 0.05-0.30	Loose Cuts: 0.03-0.32	Tight Cuts: 0.07-0.28	Tighter Cuts: 0.08-0.27
$W = 1875$ MeV, $\cos\theta_{K^+} = -0.5$				
Λ yield (background):	319 (84)	321 (84)	308 (83)	312 (79)
Λ gain/loss %:		0.63 (0)	-3.45 (-1.19)	-2.19 (-5.95)
Σ^0 yield (background):	255 (80)	253 (81)	269 (74)	270 (72)
Σ^0 gain/loss %:		-0.78 (1.25)	5.49 (-7.50)	5.88 (-10)
χ^2/NDF:	0.76	0.89	0.70	0.67
T Λ asymmetry:	0.24±0.117	0.255±0.115	0.237±0.117	0.257±0.117
T Λ change (DSR):		0.0914	-0.0181	0.103
T Σ^0 asymmetry:	0.158±0.125	0.154±0.124	0.148±0.122	0.14±0.123
T Σ^0 change (DSR):		-0.0227	-0.0573	-0.103
$W = 1875$ MeV, $\cos\theta_{K^+} = 0.1$				
Λ yield (background):	825 (189)	821 (199)	849 (162)	849 (155)
Λ gain/loss %:		-0.48 (5.29)	2.91 (-14.29)	2.91 (-17.99)
Σ^0 yield (background):	991 (264)	982 (269)	1044 (234)	1071 (219)
Σ^0 gain/loss %:		-0.91 (1.89)	5.35 (-11.36)	8.07 (-17.04)
χ^2/NDF:	1.29	1.32	1.68	1.82
T Λ asymmetry:	-0.26±0.069	-0.255±0.068	-0.237±0.068	-0.245±0.069
T Λ change (DSR):		0.0516	0.237	0.154
T Σ^0 asymmetry:	0.203±0.066	0.204±0.065	0.196±0.064	0.193±0.064
T Σ^0 change (DSR):		0.0108	-0.0761	-0.109
$W = 1875$ MeV, $\cos\theta_{K^+} = 0.9$				
Λ yield (background):	232 (78)	232 (79)	227 (77)	223 (75)
Λ gain/loss %:		0 (1.28)	-2.16 (-1.28)	-3.88 (-3.85)
Σ^0 yield (background):	202 (118)	197 (126)	206 (114)	209 (108)
Σ^0 gain/loss %:		-2.48 (6.78)	1.98 (-3.39)	3.47 (-8.47)
χ^2/NDF:	1.38	1.29	1.49	1.36
T Λ asymmetry:	-0.39±0.134	-0.42±0.131	-0.431±0.131	-0.439±0.134
T Λ change (DSR):		-0.16	-0.219	-0.259
T Σ^0 asymmetry:	-0.082±0.144	-0.058±0.144	-0.039±0.14	-0.068±0.14
T Σ^0 change (DSR):		0.118	0.214	0.0697
σ_T (Λ):		0.025	0.014	0.010
σ_T (Σ^0):		0.009	0.012	0.012

Table 6.8: Extracted yields of Λ and Σ^0 events and the resulting T asymmetry depending on the missing mass cuts for energy bin $W = 2075$ MeV and various $\cos\theta_{K^+}$ bins. "n/a" refers to a bin for which a Λ or Σ^0 signal could not be extracted and the resulting DSR could not be determined.

Cut on π (GeV):	Normal Cuts: 0.05-0.30	Loose Cuts: 0.03-0.32	Tight Cuts: 0.07-0.28	Tighter Cuts: 0.08-0.27
$W = 2075$ MeV, $\cos\theta_{K^+} = -0.5$				
Λ yield (background):	55 (27)	49 (30)	53 (28)	54 (27)
Λ gain/loss %:		-10.91 (11.11)	-3.64 (3.70)	-1.82 (0)
Σ^0 yield (background):	69 (41)	53 (53)	69 (40)	71 (34)
Σ^0 gain/loss %:		-23.19 (29.27)	0 (-2.44)	2.90 (-17.07)
χ^2/NDF:	0.95	0.98	1.00	
T Λ asymmetry:	n/a	n/a	n/a	n/a
T Λ change (DSR):				
T Σ^0 asymmetry:	-0.087±0.273	-0.127±0.26	-0.046±0.263	-0.096±0.257
T Σ^0 change (DSR):		-0.106	0.108	-0.024
$W = 2075$ MeV, $\cos\theta_{K^+} = 0.1$				
Λ yield (background):	405 (118)	416 (117)	402 (110)	395 (107)
Λ gain/loss %:		2.96 (-0.85)	-0.74 (-6.78)	-2.47 (-9.32)
Σ^0 yield (background):	618 (241)	631 (237)	640 (228)	654 (208)
Σ^0 gain/loss %:		1.91 (-1.66)	3.56 (-5.39)	5.83 (-13.69)
χ^2/NDF:	0.98	0.99	0.96	0.98
T Λ asymmetry:	-0.66±0.074	-0.585±0.081	-0.622±0.076	-0.641±0.077
T Λ change (DSR):		0.684	0.358	0.178
T Σ^0 asymmetry:	-0.21±0.084	-0.19±0.082	-0.201±0.081	-0.208±0.082
T Σ^0 change (DSR):		0.17	0.0771	0.017
$W = 2075$ MeV, $\cos\theta_{K^+} = 0.9$				
Λ yield (background):	308 (97)	305 (100)	307 (90)	302 (27)
Λ gain/loss %:		-0.97 (3.09)	-0.32 (-7.22)	-1.95 (-72.16)
Σ^0 yield (background):	221 (191)	218 (194)	235 (181)	249 (173)
Σ^0 gain/loss %:		-1.36 (1.57)	6.33 (-5.24)	12.67 (-9.42)
χ^2/NDF:	1.22	1.27	1.29	1.33
T Λ asymmetry:	-0.597±0.09	-0.617±0.086	-0.603±0.087	-0.576±0.093
T Λ change (DSR):		-0.161	-0.0479	0.162
T Σ^0 asymmetry:	-0.211±0.142	-0.219±0.14	-0.153±0.137	-0.113±0.137
T Σ^0 change (DSR):		-0.0401	0.294	0.497
σ_T (Λ):		0.035	0.040	0.026
σ_T (Σ^0):		0.017	0.025	0.031

Table 6.9: Extracted yields of Λ and Σ^0 events and the resulting T asymmetry depending on the missing mass cut for energy bin $W = 2225$ MeV and various $\cos\theta_{K^+}$ bins. "n/a" refers to a bin for which a Λ or Σ^0 signal could not be extracted and the resulting DSR could not be determined.

Cut on π (GeV):	Normal Cuts: 0.05-0.30	Loose Cuts: 0.03-0.32	Tight Cuts: 0.07-0.28	Tighter Cuts: 0.08-0.27
$W = 2225$ MeV, $\cos\theta_{K^+} = -0.5$				
Λ yield (background):	29 (29)	24 (32)	30 (26)	29 (26)
Λ gain/loss %:		-17.24 (10.34)	3.45 (-10.34)	0 (-10.34)
Σ^0 yield (background):	14 (16)	15 (8)	14 (16)	16 (8)
Σ^0 gain/loss %:		7.14 (-50)	0 (0)	14.28 (-50)
χ^2/NDF:	0.72	0.69	0.66	0.58
T Λ asymmetry:	n/a	n/a	n/a	n/a
T Λ change (DSR):				
T Σ^0 asymmetry:	n/a	n/a	n/a	n/a
T Σ^0 change (DSR):				
$W = 2225$ MeV, $\cos\theta_{K^+} = 0.1$				
Λ yield (background):	74 (74)	78 (32)	83 (65)	84 (63)
Λ gain/loss %:		5.41 (-56.76)	12.16 (-12.16)	13.51 (-14.86)
Σ^0 yield (background):	248 (121)	240 (127)	275 (101)	282 (94)
Σ^0 gain/loss %:		-3.23 (4.96)	10.89 (-16.53)	13.71 (-22.31)
χ^2/NDF:	0.96	1.02	0.91	0.99
T Λ asymmetry:	-0.707±0.13	-0.735±0.097	-0.583±0.167	-0.511±0.19
T Λ change (DSR):		-0.173	0.586	0.851
T Σ^0 asymmetry:	-0.472±0.114	-0.43±0.114	-0.412±0.114	-0.403±0.115
T Σ^0 change (DSR):		0.261	0.372	0.426
$W = 2225$ MeV, $\cos\theta_{K^+} = 0.9$				
Λ yield (background):	10 (8)	55 (3)	9 (8)	8 (9)
Λ gain/loss %:		450 (-62.5)	-10 (0)	0 (12.5)
Σ^0 yield (background):	100 (69)	95 (71)	128 (69)	129 (66)
Σ^0 gain/loss %:		-5 (2.90)	28 (0)	29 (-4.35)
χ^2/NDF:	1.42	1.43	1.72	1.77
T Λ asymmetry:	n/a	n/a	n/a	n/a
T Λ change (DSR):				
T Σ^0 asymmetry:	0.181±0.178	0.248±0.169	0.181±0.165	0.191±0.168
T Σ^0 change (DSR):		0.273	0	0.0409
σ_T (Λ):		0.033	0.064	0.081
σ_T (Σ^0):		0.031	0.032	0.038

Here, one can see that by applying tighter cuts, the yields on both the Λ and Σ^0 yields increase and the background decreases, which is a desirable effect. However, in some bins the χ^2 increases as well, which implies that the fits are not optimal. The overall effect on the asymmetry is negligible, so it doesn't appear to make sense to change the cut. More specifically, for the lower energy ranges there is no significant change in the yields or asymmetries. But at the higher energy range (W = 2225 MeV), the yields and the asymmetries of the tightest cuts change sharply. Therefore, it would appear that once again, the current *normal* cuts are within reason. Although more events and less background are the most desirable, a high χ^2 is not.

6.1.4 Optimizing the Background

The background subtraction method was previously described in Section 4.12, where a third degree polynomial was used for the background fit. In order to check the validity of using a third order polynomial, the degree of the polynomial was varied and then the yields of the Λ and Σ^0 signals were compared along with the resulting asymmetries and are listed in Tables 6.10, 6.11, and 6.12. The global fit of the different degrees of polynomials compared to each other can be seen in Figs. 6.28 to 6.36.

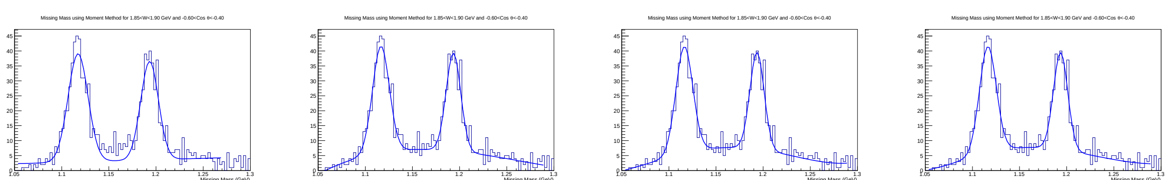

(a) 1st Deg. Pol. (b) 3rd Deg. Poly. (c) 4th Deg. Pol. (d) 5th Deg. Pol.

Figure 6.28: Comparison of the global fit of various degrees of background fits for W = 1875 MeV and $\cos\theta$=-0.5.

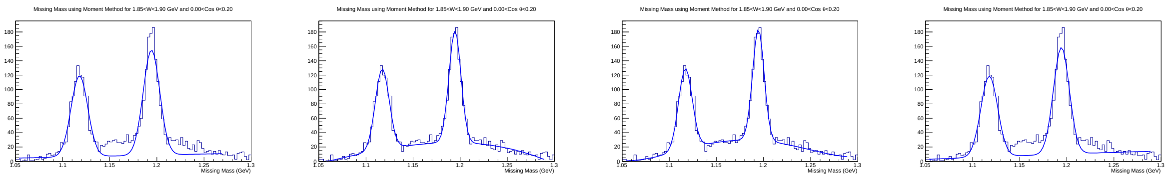

(a) 1st Deg. Pol. (b) 3rd Deg. Pol. (c) 4th Deg. Pol. (d) 5th Deg. Pol.

Figure 6.29: Comparison of the global fit of various degrees of background fits for W = 1875 MeV and $\cos\theta$=0.1.

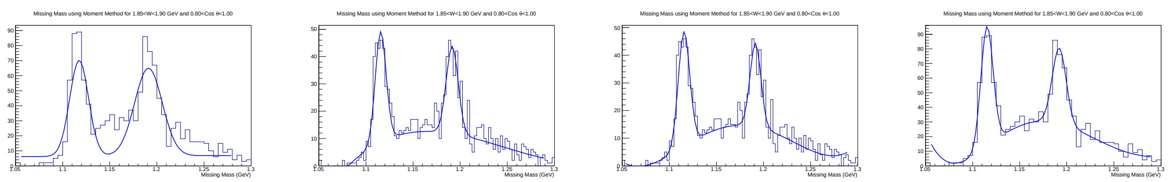

(a) 1st Deg. Pol. (b) 3rd Deg. Pol. (c) 4th Deg. Pol. (d) 5th Deg. Pol.

Figure 6.30: Comparison of the global fit of various degrees of background fits for W = 1875 MeV and $\cos\theta$=0.9.

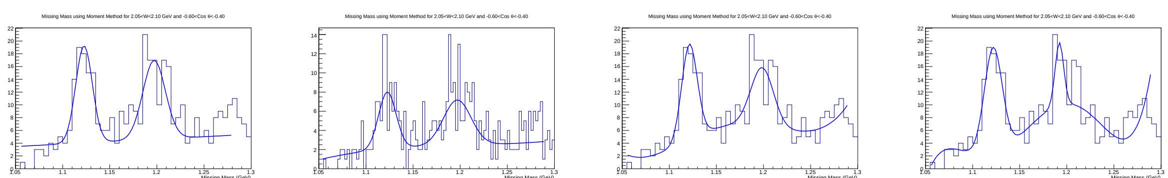

(a) 1st Deg. Pol. (b) 3rd Deg. Pol. (c) 4th Deg. Pol. (d) 5th Deg. Pol.

Figure 6.31: Comparison of the global fit of various degrees of background fits for W = 2075 MeV and $\cos\theta$=-0.5.

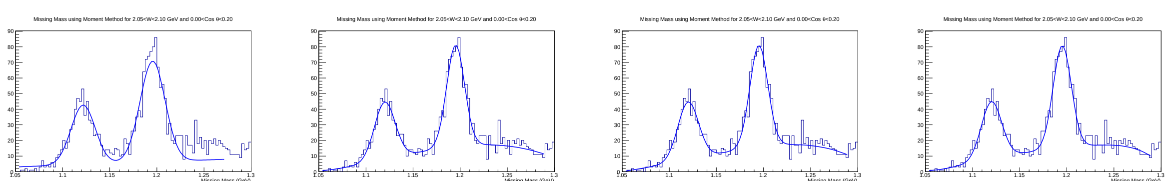

(a) 1st Deg. Pol. (b) 3rd Deg. Pol. (c) 4th Deg. Pol. (d) 5th Deg. Pol.

Figure 6.32: Comparison of the global fit of various degrees of background fits for W = 2075 MeV and $\cos\theta$=0.1.

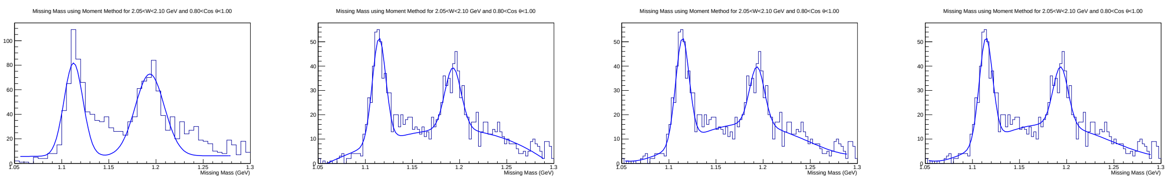

(a) 1st Deg. Pol. (b) 3rd Deg. Pol. (c) 4th Deg. Pol. (d) 5th Deg. Pol.

Figure 6.33: Comparison of the global fit of various degrees of background fits for W = 2075 MeV and $\cos\theta$=0.9.

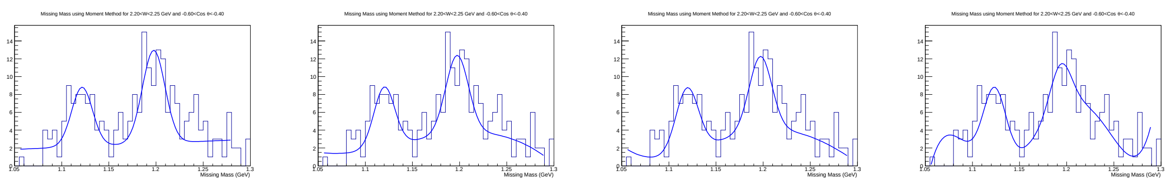

(a) 1st Deg. Pol. (b) 3rd Deg. Pol. (c) 4th Deg. Pol. (d) 5th Deg. Pol.

Figure 6.34: Comparison of the global fit of various degrees of background fits for W = 2225 MeV and $\cos\theta$=-0.5.

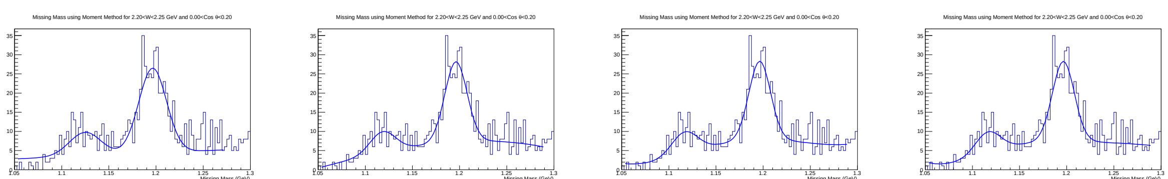

(a) 1st Deg. Pol. (b) 3rd Deg. Pol. (c) 4th Deg. Pol. (d) 5th Deg. Pol.

Figure 6.35: Comparison of the global fit of various degrees of background fits for W = 2225 MeV and $\cos\theta$=0.1.

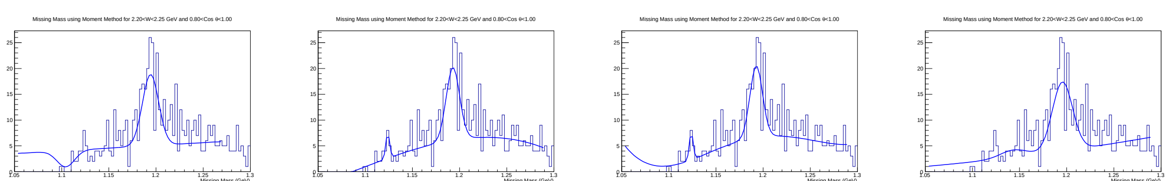

(a) 1st Deg. Pol. (b) 3rd Deg. Pol. (c) 4th Deg. Pol. (d) 5th Deg. Pol.

Figure 6.36: Comparison of the global fit of various degrees of background fits for W = 2225 MeV and $\cos\theta$=0.9.

Table 6.10: Extracted yields of Λ and Σ^0 events and the resulting T asymmetry depending on the background fit for energy bin $W = 1875$ MeV and various $\cos\theta_{K^+}$ bins.

	Normal (3rd deg.):	1st Degree:	4th Degree:	5th Degree:
$W = 1875$ MeV, $\cos\theta_{K^+} = -0.5$				
Λ yield (background):	319 (84)	383 (47)	322 (82)	320 (84)
Λ gain/loss %:		20.06 (-44.05)	0.94 (-2.38)	0.31 (0)
Σ^0 yield (background):	255 (80)	311 (54)	245 (85)	247 (84)
Σ^0 gain/loss %:		21.96 (-32.5)	-3.92 (6.25)	-3.14 (5)
χ^2/NDF:	0.76	1.14	0.74	0.75
T Λ asymmetry:	0.24±0.117	0.209±0.11	0.238±0.116	0.24±0.117
T Λ change (DSR):		-0.193	-0.0121	0
T Σ^0 asymmetry:	0.158±0.125	0.14±0.119	0.16±0.126	0.159±0.126
T Σ^0 change (DSR):		-0.104	0.0113	0.00563
$W = 1875$ MeV, $\cos\theta_{K^+} = 0.1$				
Λ yield (background):	825 (189)	1003 (92)	814 (195)	1008 (88)
Λ gain/loss %:		21.58 (-51.32)	-1.33 (3.17)	22.18 (-53.44)
Σ^0 yield (background):	991 (264)	1287 (121)	951 (283)	1258 (135)
Σ^0 gain/loss %:		29.87 (-54.17)	-4.04 (7.20)	26.94 (-48.86)
χ^2/NDF:	1.29	5.46	1.03	4.89
T Λ asymmetry:	-0.26±0.069	-0.227±0.066	-0.262±0.069	-0.25±0.068
T Λ change (DSR):		0.346	-0.0205	0.103
T Σ^0 asymmetry:	0.203±0.066	0.165±0.06	0.21±0.067	0.22±0.068
T Σ^0 change (DSR):		-0.426	0.0744	0.179
$W = 1875$ MeV, $\cos\theta_{K^+} = 0.9$				
Λ yield (background):	232 (78)	287 (12)	253 (68)	252 (68)
Λ gain/loss %:		23.71 (-84.62)	9.05 (-12.82)	8.62 (-12.82)
Σ^0 yield (background):	202 (118)	633 (35)	173 (128)	175 (128)
Σ^0 gain/loss %:		213.37 (-70.34)	-14.36 (8.47)	-13.37 (8.47)
χ^2/NDF:	1.38	2.27	1.18	1.15
T Λ asymmetry:	-0.39±0.134	-0.268±0.117	-0.356±0.13	-0.357±0.13
T Λ change (DSR):		0.686	0.182	0.177
T Σ^0 asymmetry:	-0.082±0.144	-0.05±0.113	-0.092±0.153	-0.09±0.152
T Σ^0 change (DSR):		0.175	-0.0476	-0.0382
σ_T (Λ):		0.099	0.007	0.032
σ_T (Σ^0):		0.024	0.005	0.008

Table 6.11: Extracted yields of Λ and Σ^0 events and the resulting T asymmetry depending on the background fit for energy bin $W = 2075$ MeV and various $\cos\theta_{K^+}$ bins. "n/a" refers to a bin for which a Λ or Σ^0 signal could not be extracted and the resulting DSR could not be determined.

	Normal (3rd deg.):	1st Degree:	4th Degree:	5th Degree:
$W = 2075$ MeV, $\cos\theta_{K^+} = -0.5$				
Λ yield (background):	55 (27)	62 (24)	54 (28)	60 (24)
Λ gain/loss %:		12.73 (-11.11)	-1.82 (3.70)	9.09 (-11.11)
Σ^0 yield (background):	69 (41)	83 (34)	55 (51)	45 (57)
Σ^0 gain/loss %:		20.29 (-17.07)	-20.29 (24.39)	-34.78 (34.04)
χ^2/NDF:	0.95	0.86	0.98	1.05
T Λ asymmetry:	n/a	n/a	n/a	n/a
T Λ change (DSR):				
T Σ^0 asymmetry:	-0.087±0.273	-0.086±0.272	-0.071±0.246	-0.045±0.196
T Σ^0 change (DSR):		0.00259	0.0435	0.125
$W = 2075$ MeV, $\cos\theta_{K^+} = 0.1$				
Λ yield (background):	405 (118)	489 (74)	407 (117)	393 (126)
Λ gain/loss %:		20.74 (-37.29)	0.49 (-0.84)	-2.96 (6.78)
Σ^0 yield (background):	618 (241)	865 (105)	623 (239)	637 (232)
Σ^0 gain/loss %:		39.97 (-56.43)	0.81 (-0.83)	3.07 (-3.73)
χ^2/NDF:	0.98	2.81	0.99	0.97
T Λ asymmetry:	-0.66±0.074	-0.575±0.083	-0.661±0.074	-0.861±0.045
T Λ change (DSR):		0.764	-0.00956	-2.32
T Σ^0 asymmetry:	-0.21±0.084	-0.175±0.077	-0.21±0.084	-0.183±0.079
T Σ^0 change (DSR):		0.307	0	0.234
$W = 2075$ MeV, $\cos\theta_{K^+} = 0.9$				
Λ yield (background):	308 (97)	353 (18)	309 (97)	306 (99)
Λ gain/loss %:		14.61 (-81.44)	0.32 (0)	-0.65 (2.06)
Σ^0 yield (background):	221 (191)	847 (26)	189 (198)	192 (197)
Σ^0 gain/loss %:		283 (-86.39)	-14.48 (3.66)	-13.12 (3.14)
χ^2/NDF:	1.22	1.84	1.04	1.05
T Λ asymmetry:	-0.597±0.09	-0.453±0.091	-0.599±0.09	-0.606±0.089
T Λ change (DSR):		1.13	-0.0157	-0.0711
T Σ^0 asymmetry:	-0.211±0.142	-0.12±0.108	-0.236±0.149	-0.233±0.148
T Σ^0 change (DSR):		0.51	-0.121	-0.107
σ_T (Λ):		0.102	0.022	0.086
σ_T (Σ^0):		0.063	0.022	0.033

Table 6.12: Extracted yields of Λ and Σ^0 events and the resulting T asymmetry depending on the background fit for energy bin $W = 2225$ MeV and various $\cos\theta_{K^+}$ bins. "n/a" refers to a bin for which a Λ or Σ^0 signal could not be extracted and the resulting DSR could not be determined.

	Normal (3rd deg.):	1st Degree:	4th Degree:	5th Degree:
$W = 2225$ MeV, $\cos\theta_{K^+} = -0.5$				
Λ yield (background):	29 (29)	34 (26)	36 (24)	39 (21)
Λ gain/loss %:		17.24 (-10.34)	24.14 (-17.24)	34.48 (-27.59)
Σ^0 yield (background):	14 (16)	44 (28)	14 (16)	10 (10)
Σ^0 gain/loss %:		214 (75)	0 (0)	-28.57 (37.5)
χ^2/NDF:	0.72	0.74	0.73	0.71
T Λ asymmetry:	n/a	n/a	n/a	n/a
T Λ change (DSR):				
T Σ^0 asymmetry:	n/a	-1.04±0.224	-1.54±0.575	-1.75±0.732
T Σ^0 change (DSR):				
$W = 2225$ MeV, $\cos\theta_{K^+} = 0.1$				
Λ yield (background):	74 (74)	104 (60)	77 (71)	72 (74)
Λ gain/loss %:		40.54 (-18.92)	4.05 (-4.05)	-2.70 (0)
Σ^0 yield (background):	248 (121)	328 (74)	236 (128)	242 (124)
Σ^0 gain/loss %:		32.26 (-38.84)	-4.84 (5.79)	-2.42 (2.48)
χ^2/NDF:	0.96	1.25	0.96	0.97
T Λ asymmetry:	-0.707±0.13	-0.62±0.158	-0.687±0.138	-0.79±0.071
T Λ change (DSR):		0.425	0.105	-0.56
T Σ^0 asymmetry:	-0.472±0.114	-0.415±0.113	-0.481±0.114	-0.457±0.114
T Σ^0 change (DSR):		0.355	-0.0558	0.093
$W = 2225$ MeV, $\cos\theta_{K^+} = 0.9$				
Λ yield (background):	10 (8)	-29 (46)	11 (7)	20 (22)
Λ gain/loss %:		-390 (475)	10 (-12.5)	100 (175)
Σ^0 yield (background):	100 (69)	119 (69)	93 (70)	144 (65)
Σ^0 gain/loss %:		19 (0)	-7.00 (1.45)	44 (-5.80)
χ^2/NDF:	1.42	1.71	1.46	1.74
T Λ asymmetry:	n/a	n/a	n/a	n/a
T Λ change (DSR):				
T Σ^0 asymmetry:	0.181±0.178	0.149±0.164	0.166±0.172	0.153±0.166
T Σ^0 change (DSR):		-0.132	-0.0606	-0.115
σ_T (Λ):		0.129	0.020	0.042
σ_T (Σ^0):		0.053	0.008	0.015

Although, sometimes, it appears that the yield when applying a first degree polynomial fit to the background is high for Λ and Σ^0, by actually looking at the fit, as shown in Figs. 6.28 to 6.36, specifically at $\cos\theta = 0.9$, one can see that the fit did not actually work. This is also reflected in a larger χ^2 for many bins. In the energy bin $W = 2075$ MeV, the first order yields and asymmetries have large discrepancies. Also, in the same energy bin, the fifth degree polynomial results in only a small change in the yield at $\cos\theta = 0.1$, but a dramatic change in the T asymmetry.

6.1.5 All Cuts Simultaneously

It is also worth it to examine the results of the yields if ALL the tight cuts previously described in Sections 6.1.1, 6.1.2, 6.1.3 are applied, that is to apply tight fiducial cuts, tight cuts on β, and tight missing mass cuts, and to extract the yields in the same way as previously described and to do the same for ALL the loose cuts. The global fit of applying all tight cuts can be seen in Fig. 6.37 to 6.45. The yields and resulting asymmetries after applying all wide or tighter cuts is listed in Tables 6.13, 6.14, 6.15.

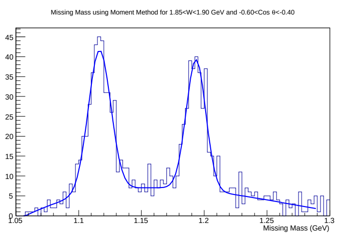

(a) Normal Cuts

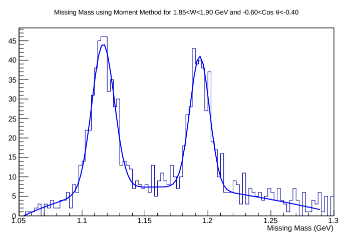

(b) All Loose Cuts

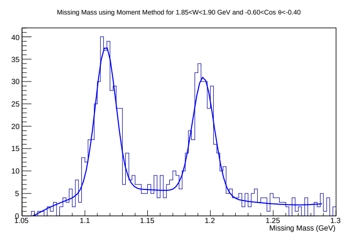

(c) All Tight Cuts

Figure 6.37: Comparison of the global fits for all cuts applied simultaneously for W = 1875 MeV and $\cos\theta$=-0.5.

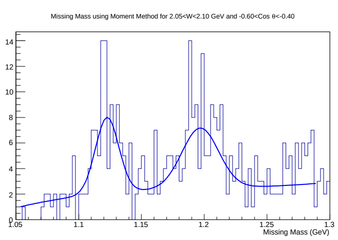

(a) Normal Cuts

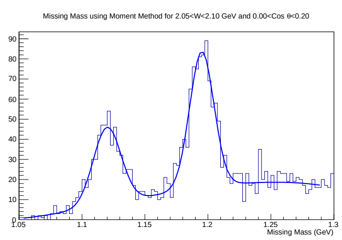

(b) All Loose Cuts

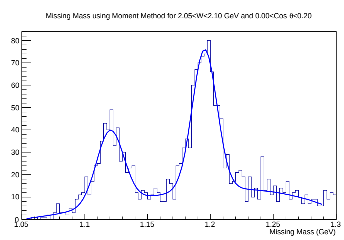

(c) All Tight Cuts

Figure 6.38: Comparison of the global fits for all cuts applied simultaneously for W = 2075 MeV and $\cos\theta$=0.1.

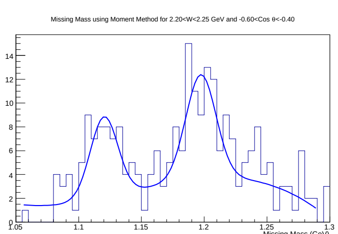

(a) Normal Cuts

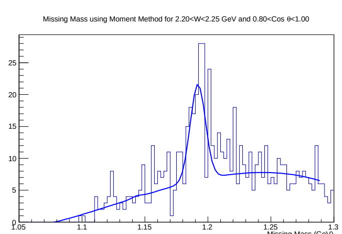

(b) All Loose Cuts

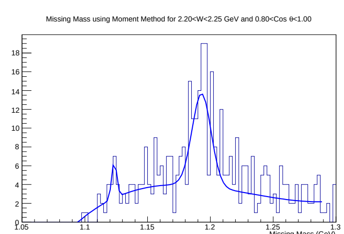

(c) All Tight Cuts

Figure 6.39: Comparison of the global fits for all cuts applied simultaneously for W = 2225 MeV and $\cos\theta$=0.9.

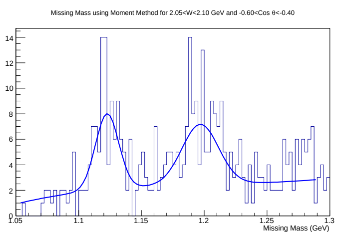

(a) Normal Cuts

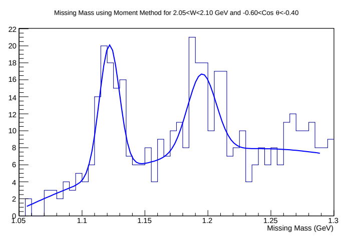

(b) All Loose Cuts

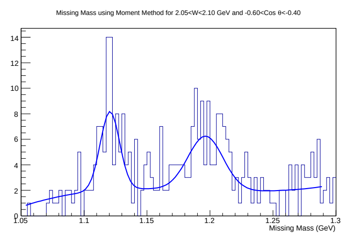

(c) All Tight Cuts

Figure 6.40: Comparison of the global fits for all cuts applied simultaneously for W = 2075 MeV and $\cos\theta$=-0.5.

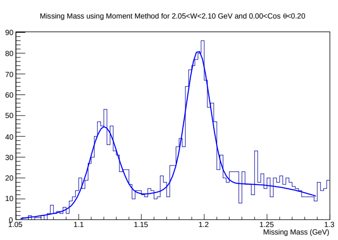

(a) Normal Cuts

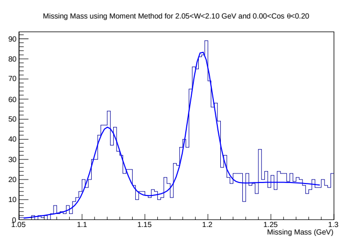

(b) All Loose Cuts

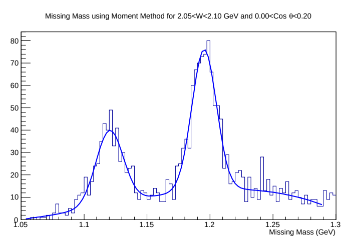

(c) All Tight Cuts

Figure 6.41: Comparison of the global fits for all cuts applied simultaneously for W = 2075 MeV and $\cos\theta$=0.1.

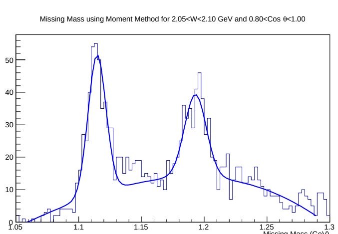

(a) Normal Cuts

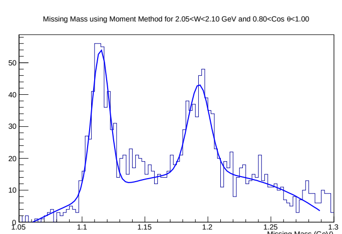

(b) All Loose Cuts

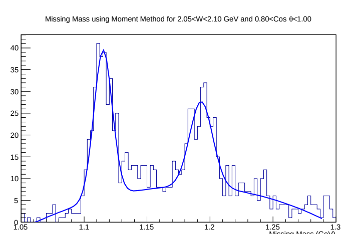

(c) All Tight Cuts

Figure 6.42: Comparison of the global fits for all cuts applied simultaneously for W = 2075 MeV and $\cos\theta$=0.9.

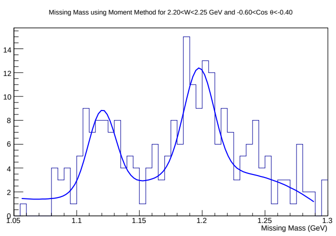

(a) Normal Cuts

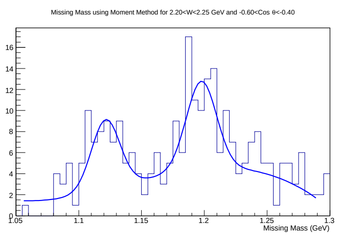

(b) All Loose Cuts

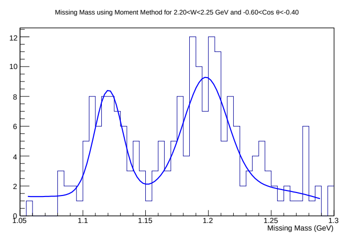

(c) All Tight Cuts

Figure 6.43: Comparison of the global fits for all cuts applied simultaneously for $W = 2225$ MeV and $\cos\theta$=-0.5.

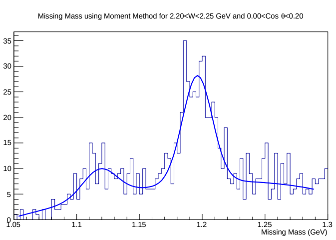

(a) Normal Cuts

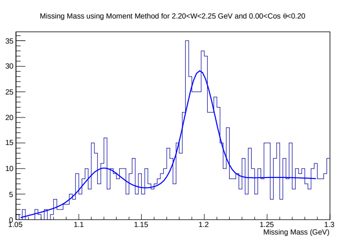

(b) All Loose Cuts

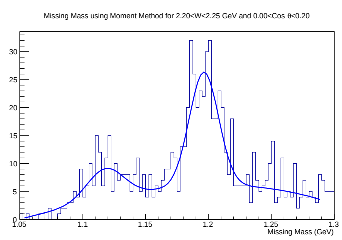

(c) All Tight Cuts

Figure 6.44: Comparison of the global fits for all cuts applied simultaneously for $W = 2225$ MeV and $\cos\theta$=0.1.

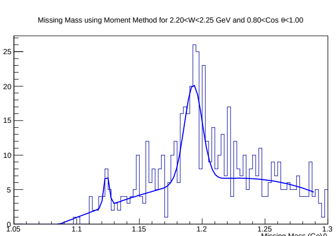

(a) Normal Cuts

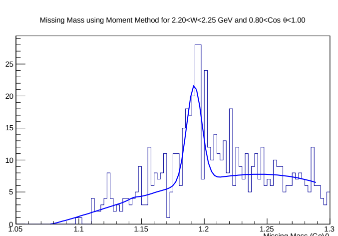

(b) All Loose Cuts

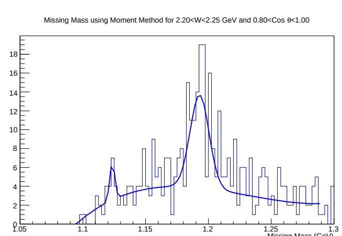

(c) All Tight Cuts

Figure 6.45: Comparison of the global fits for all cuts applied simultaneously for $W = 2225$ MeV and $\cos\theta$=0.9.

Table 6.13: Extracted yields of Λ and Σ^0 events and the resulting T asymmetry depending on all cuts applied simultaneously for energy bin $W = 1875$ MeV and $\cos\theta_{K^+}$ bins.

	Normal Cuts:	All Wide Cuts	All Tight Cuts:
$W = 1875$ MeV, $\cos\theta_{K^+} = -0.5$			
Λ yield (background):	319 (84)	340 (89)	265 (71)
Λ gain/loss %:		6.58 (5.95)	-16.93 (-15.48)
Σ^0 yield (background):	255 (80)	266 (85)	228 (64)
Σ^0 gain/loss %:		4.31 (6.25)	-10.59 (-20)
χ^2/NDF:	0.76	0.86	0.72
T Λ asymmetry:	0.24±0.117	0.226±0.112	0.189±0.126
T Λ change (DSR):		-0.0864	-0.297
T Σ^0 asymmetry:	0.158±0.125	0.152±0.121	0.058±0.133
T Σ^0 change (DSR):		-0.0345	-0.548
$W = 1875$ MeV, $\cos\theta_{K^+} = 0.1$			
Λ yield (background):	825 (189)	843 (202)	805 (150)
Λ gain/loss %:		2.18 (6.88)	-2.42 (-20.63)
Σ^0 yield (background):	991 (264)	1022 (280)	965 (207)
Σ^0 gain/loss %:		3.13 (6.06)	-2.62 (-21.59)
χ^2/NDF:	1.29	1.78	1.30
T Λ asymmetry:	-0.26±0.069	-0.267±0.067	-0.257±0.069
T Λ change (DSR):		-0.0728	0.0307
T Σ^0 asymmetry:	0.203±0.066	0.207±0.064	0.237±0.066
T Σ^0 change (DSR):		0.0435	0.364
$W = 1875$ MeV, $\cos\theta_{K^+} = 0.9$			
Λ yield (background):	232 (78)	244 (85)	193 (56)
Λ gain/loss %:		5.17 (8.79)	-16.81 (-28.21)
Σ^0 yield (background):	202 (118)	210 (143)	135 (68)
Σ^0 gain/loss %:		3.96 (21.19)	-33.17 (-42.37)
χ^2/NDF:	1.38	1.29	1.18
T Λ asymmetry:	-0.39±0.134	-0.414±0.13	-0.313±0.15
T Λ change (DSR):		-0.129	0.383
T Σ^0 asymmetry:	-0.082±0.144	-0.086±0.139	-0.054±0.174
T Σ^0 change (DSR):		-0.02	0.124
σ_T (Λ):		0.023	0.055
σ_T (Σ^0):		0.018	0.026

Table 6.14: Extracted yields of Λ and Σ^0 events and the resulting T asymmetry depending on all cuts applied simultaneously for energy bin W = 2075 MeV and $\cos\theta_{K^+}$ bins. “n/a” refers to a bin for which a Λ or Σ^0 signal could not be extracted and the resulting DSR could not be determined.

	Normal Cuts:	All Loose Cuts:	All Tight Cuts:
$W = 2075$ MeV, $\cos\theta_{K^+} = -0.5$			
Λ yield (background):	55 (27)	58 (26)	47 (25)
Λ gain/loss %:		5.45 (-3.70)	-12.73 (-7.41)
Σ^0 yield (background):	69 (41)	63 (48)	59 (34)
Σ^0 gain/loss %:		-8.70 (17.07)	-14.49 (-17.07)
χ^2/NDF:	0.95	0.98	0.83
T Λ asymmetry:	n/a	n/a	n/a
T Λ change (DSR):			
T Σ^0 asymmetry:	-0.087±0.273	-0.082±0.261	-0.093±0.306
T Σ^0 change (DSR):		0.0132	-0.0146
$W = 2075$ MeV, $\cos\theta_{K^+} = 0.1$			
Λ yield (background):	405 (118)	425 (116)	359 (103)
Λ gain/loss %:		4.94 (-1.69)	-11.36 (-12.71)
Σ^0 yield (background):	618 (241)	652 (243)	615 (203)
Σ^0 gain/loss %:		5.50 (0.83)	-0.49 (-15.77)
χ^2/NDF:	0.98	0.94	1.03
T Λ asymmetry:	-0.66±0.074	-0.558±0.084	-0.828±0.019
T Λ change (DSR):		0.911	-2.2
T Σ^0 asymmetry:	-0.21±0.084	-0.182±0.081	-0.203±0.084
T Σ^0 change (DSR):		0.24	0.0589
$W = 2075$ MeV, $\cos\theta_{K^+} = 0.9$			
Λ yield (background):	308 (97)	315 (103)	249 (64)
Λ gain/loss %:		2.27 (6.19)	-19.16 (-34.02)
Σ^0 yield (background):	221 (191)	242 (215)	179 (116)
Σ^0 gain/loss %:		9.50 (12.57)	-19.00 (-39.27)
χ^2/NDF:	1.22	1.25	1.21
T Λ asymmetry:	-0.597±0.09	-0.591±0.088	-0.584±0.099
T Λ change (DSR):		0.0477	0.0972
T Σ^0 asymmetry:	-0.211±0.142	-0.219±0.133	0.074±0.16
T Σ^0 change (DSR):		-0.0411	1.33
σ_T (Λ):		0.047	0.076
σ_T (Σ^0):		0.027	0.080

Table 6.15: Extracted yields of Λ and Σ^0 events and the resulting T asymmetry depending on all cuts applied simultaneously for energy bin $W = 2225$ MeV and various $\cos\theta_{K^+}$ bins. "n/a" refers to a bin for which a Λ or Σ^0 signal could not be extracted and the resulting DSR could not be determined.

	Normal Cuts:	All Wide Cuts	All Tight Cuts:
$W = 2225$ MeV, $\cos\theta_{K^+} = -0.5$			
Λ yield (background):	29 (29)	22 (35)	35 (18)
Λ gain/loss %:		-24.14 (20.69)	20.69 (-37.93)
Σ^0 yield (background):	14 (16)	17 (9)	32 (29)
Σ^0 gain/loss %:		21.43 (-43.75)	129 (81.25)
χ^2/NDF:	0.72	0.78	0.56
T Λ asymmetry:	n/a	n/a	n/a
T Λ change (DSR):			
T Σ^0 asymmetry:	n/a	n/a	n/a
T Σ^0 change (DSR):			
$W = 2225$ MeV, $\cos\theta_{K^+} = 0.1$			
Λ yield (background):	74 (74)	83 (69)	80 (60)
Λ gain/loss %:		9.46 (-6.76)	8.11 (-18.92)
Σ^0 yield (background):	248 (121)	256 (123)	236 (99)
Σ^0 gain/loss %:		3.23 (1.65)	-4.84 (-18.18)
χ^2/NDF:	0.96	1.06	1.08
T Λ asymmetry:	-0.707±0.13	-0.773±0.07	-0.547±0.181
T Λ change (DSR):		-0.447	0.718
T Σ^0 asymmetry:	-0.472±0.114	-0.464±0.109	-0.52±0.106
T Σ^0 change (DSR):		0.0507	-0.308
$W = 2225$ MeV, $\cos\theta_{K^+} = 0.9$			
Λ yield (background):	10 (8)	1 (2)	8 (8)
Λ gain/loss %:		-90 (-75)	-20 (0)
Σ^0 yield (background):	100 (69)	91 (63)	74 (46)
Σ^0 gain/loss %:		-9.00 (-8.70)	-26 (-33.33)
χ^2/NDF:	1.42	1.54	1.30
T Λ asymmetry:	n/a	n/a	n/a
T Λ change (DSR):			
T Σ^0 asymmetry:	0.181±0.178	0.235±0.171	0.176±0.199
T Σ^0 change (DSR):		0.219	-0.0187
σ_T (Λ):		0.061	0.013
σ_T (Σ^0):		0.040	0.059

In the case of all the loose cuts or all the tight cuts being applied simultaneously, there is an overall small change in most energy and $\cos\theta$ bins. The biggest noticeable change is in the Λ and Σ^0 yields, which shows a dramatic event loss when applying all of the tight cuts simultaneously, especially in comparison to the normal and loose cuts. When applying all the cuts, either tight or loose, the change in the yields and T asymmetry are overall small. Therefore, the normal cuts applied are within reason.

6.2 Uncertainty Associated with the Target

Due to the complex nature of the target, there is naturally some uncertainty associated with the measurements of the target polarization and the target offset.

6.2.1 Target Polarization

The main sources of uncertainty in the target polarization measurement were the contamination of the target material with other materials containing molecular protons, changes in the NMR coils used to measure the polarization, and changes in the target temperature. These were investigated and are described in Ref. [99].

6.2.2 Target Polarization Offset Angle

As previously mentioned, the target used in the g9b experiment was a transversely polarized butanol target. Due to the transverse holding field, the symmetry axis was not aligned parallel to the floor. Therefore, when extracting the polarization observables, the target offset angle, ϕ_0, must be known. As described in Section 3.8, the target offset was found to be $63.9^\circ \pm 0.4^\circ$. In order to study the target offset, the author varied the offset to be either 60° or 63° and then examined the effect on the yield for the Λ and Σ^0 signals and resulting asymmetries. Details are listed in Tables 6.16, 6.17, and 6.18.

Table 6.16: Extracted yields of Λ and Σ^0 events and the resulting T asymmetry depending on the target polarization angle offset for energy bin $W = 1875$ MeV and various $\cos\theta_{K^+}$ bins.

	Target Offset=63°:	Target Offset=60°:
$W = 1875$ MeV, $\cos\theta_{K^+} = -0.5$		
Λ yield (background):	319 (84)	319 (84)
Λ gain/loss %:		
Σ^0 yield (background):	255 (80)	255 (80)
Σ^0 gain/loss %:		
χ^2/NDF:	0.76	0.76
T Λ asymmetry:	0.24±0.117	0.233±0.116
T Λ change (DSR):		-0.0425
T Σ^0 asymmetry:	0.158±0.125	0.153±0.124
T Σ^0 change (DSR):		-0.0284
$W = 1875$ MeV, $\cos\theta_{K^+} = 0.1$		
Λ yield (background):	825 (189)	825 (189)
Λ gain/loss %:		
Σ^0 yield (background):	991 (264)	991 (264)
Σ^0 gain/loss %:		
χ^2/NDF:	1.29	1.29
T Λ asymmetry:	-0.26±0.069	-0.251±0.068
T Λ change (DSR):		0.0929
T Σ^0 asymmetry:	0.203±0.066	0.197±0.065
T Σ^0 change (DSR):		-0.0648
$W = 1875$ MeV, $\cos\theta_{K^+} = 0.9$		
Λ yield (background):	232 (78)	232 (78)
Λ gain/loss %:		
Σ^0 yield (background):	202 (118)	202 (118)
Σ^0 gain/loss %:		
χ^2/NDF:	1.38	1.38
T Λ asymmetry:	-0.39±0.134	-0.379±0.134
T Λ change (DSR):		0.058
T Σ^0 asymmetry:	-0.082±0.144	-0.08±0.143
T Σ^0 change (DSR):		0.00986
σ_T (Λ):		0.018
σ_T (Σ^0):		0.004

Table 6.17: Extracted yields of Λ and Σ^0 events and the resulting T asymmetry depending on the target polarization angle offset for energy bin $W = 2075$ MeV and various $\cos\theta_{K^+}$ bins. "n/a" refers to a bin for which a Λ or Σ^0 signal could not be extracted and the resulting DSR could not be determined.

	Target Offset=63°:	Target Offset=60°:
$W = 2075$ MeV, $\cos\theta_{K^+} = -0.5$		
Λ yield (background):	55 (27)	55 (27)
Λ gain/loss %:		
Σ^0 yield (background):	69 (41)	69 (41)
Σ^0 gain/loss %:		
χ^2/NDF:	0.95	0.95
T Λ asymmetry:	n/a	n/a
T Λ change (DSR):		
T Σ^0 asymmetry:	-0.087±0.273	-0.083±0.267
T Σ^0 change (DSR):		0.0105
$W = 2075$ MeV, $\cos\theta_{K^+} = 0.1$		
Λ yield (background):	405 (118)	405 (118)
Λ gain/loss %:		
Σ^0 yield (background):	618 (241)	618 (241)
Σ^0 gain/loss %:		
χ^2/NDF:	0.98	0.98
T Λ asymmetry:	-0.66±0.074	-0.628±0.075
T Λ change (DSR):		0.304
T Σ^0 asymmetry:	-0.21±0.084	-0.203±0.083
T Σ^0 change (DSR):		0.0593
$W = 2075$ MeV, $\cos\theta_{K^+} = 0.9$		
Λ yield (background):	308 (97)	308 (97)
Λ gain/loss %:		
Σ^0 yield (background):	221 (191)	221 (191)
Σ^0 gain/loss %:		
χ^2/NDF:	1.22	1.22
T Λ asymmetry:	-0.597±0.09	-0.585±0.089
T Λ change (DSR):		0.0948
T Σ^0 asymmetry:	-0.211±0.142	-0.203±0.14
T Σ^0 change (DSR):		0.0401
σ_T (Λ):		0.025
σ_T (Σ^0):		0.015

Table 6.18: Extracted yields of Λ and Σ^0 events and the resulting T asymmetry depending on the target polarization angle offset for energy bin $W = 2225$ MeV and $\cos\theta_{K^+}$ bins. "n/a" refers to a bin for which a Λ or Σ^0 signal could not be extracted and the resulting DSR could not be determined.

	Target Offset=63°:	Target Offset=60°:
$W = 2225$ MeV, $\cos\theta_{K^+} = -0.5$		
Λ yield (background):	29 (29)	23 (29)
Λ gain/loss %:		
Σ^0 yield (background):	14 (16)	14 (16)
Σ^0 gain/loss %:		
χ^2/NDF:	0.72	0.72
T Λ asymmetry:	n/a	n/a
T Λ change (DSR):		
T Σ^0 asymmetry:	n/a	n/a
T Σ^0 change (DSR):		
$W = 2225$ MeV, $\cos\theta_{K^+} = 0.1$		
Λ yield (background):	74 (74)	74 (74)
Λ gain/loss %:		
Σ^0 yield (background):	248 (121)	248 (121)
Σ^0 gain/loss %:		
χ^2/NDF:	0.96	0.96
T Λ asymmetry:	-0.707±0.13	-0.709±0.114
T Λ change (DSR):		-0.0116
T Σ^0 asymmetry:	-0.472±0.114	-0.461±0.112
T Σ^0 change (DSR):		0.0688
$W = 2225$ MeV, $\cos\theta_{K^+} = 0.9$		
Λ yield (background):	10 (8)	10 (8)
Λ gain/loss %:		
Σ^0 yield (background):	100 (69)	100 (69)
Σ^0 gain/loss %:		
χ^2/NDF:	1.42	1.42
T Λ asymmetry:	n/a	n/a
T Λ change (DSR):		
T Σ^0 asymmetry:	0.181±0.178	0.176±0.175
T Σ^0 change (DSR):		-0.02
σ_T (Λ):		0.021
σ_T (Σ^0):		0.009

After changing the target offset, the yields and asymmetries have a minimal change in all energy and cosine bins. There is no serious effect on the final asymmetries by changing the target offset ϕ_0.

6.2.3 Before and After the Quench

As mentioned in Section 2.7.5, the target quenched during the running of the g9b experiment, which required a repair. Since a lapse in time occurred, it was possible that the detector or target parameters may have changed and could have an effect on the data. In order to check the consistency throughout the experiment, the data was divided into two parts, before the quench and after the quench. Only the circularly polarized runs are taken into account since only circularly polarized runs were taken after the quench. The first comparison concerned the missing mass distribution of $\gamma p \rightarrow K^+X$ from before and after the quench, as shown in Fig. 6.46. The only difference in the missing mass distribution before and after the quench is the statistics, which was expected due to the shorter running time after the quench.

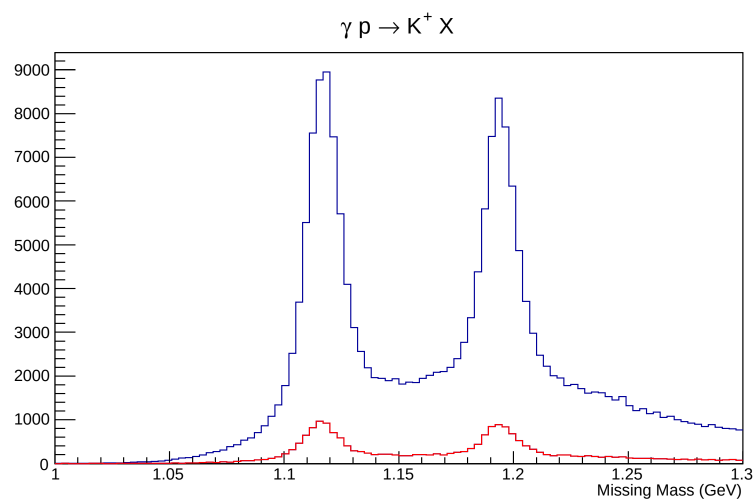

Figure 6.46: The missing mass distribution of $\gamma p \rightarrow K^+X$ before the quench (blue line) compared to after the quench (red line).

Shown in Figs. 6.47(a) and 6.47(b) are the missing mass distribution of $\gamma p \rightarrow K^+X$ versus ϕ. This test ensured that the momentum corrections applied in Section 4.4 work for data sets, taken before and after the quench.

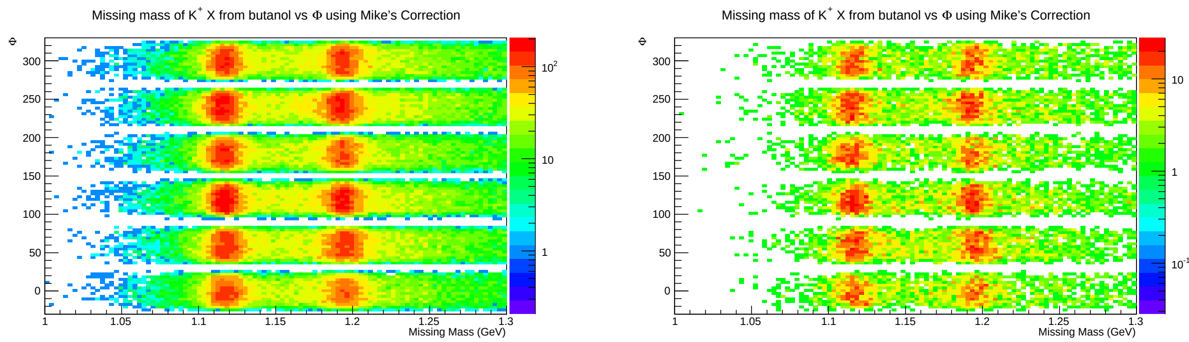

(a) Before Quench (b) After Quench

Figure 6.47: The missing mass distribution of $\gamma p \rightarrow K^+X$ versus ϕ before the quench (a) and after the quench (b).

In addition, the vertex distribution was compared before and after the quench as shown in Fig. 6.48. Here, a difference is seen to the left of the butanol around -6 cm due to a different target stick being used. Otherwise, there appears to be no clear difference in the vertex distribution of the target before and after the quench.

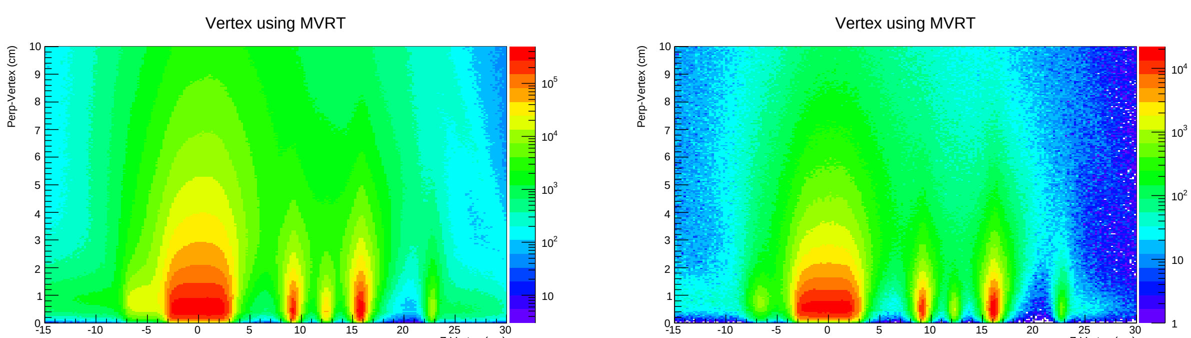

(a) Before Quench (b) After Quench

Figure 6.48: Comparison of the vertex distribution before (a) and after (b) the quench. A slight difference around -6.0 cm is visible due to the use of a different target stick.

One last consistency check was the β versus momentum distributions, described in Section 4.5 to check if the time-of-flight corrections described in Section 4.4 are valid for both before and after the quench. Figures 6.49(a) and 6.49(b) show the distribution before any corrections were applied, both before and after the quench. Figures 6.50(a) and 6.50(b) show the distribution after the energy loss, momentum, and time-of-flight corrections have been applied for before and after the quench. The main difference for the β versus momentum distributions for before and after the quench is the statistics, which as previously mentioned, was expected due to the shorter run time.

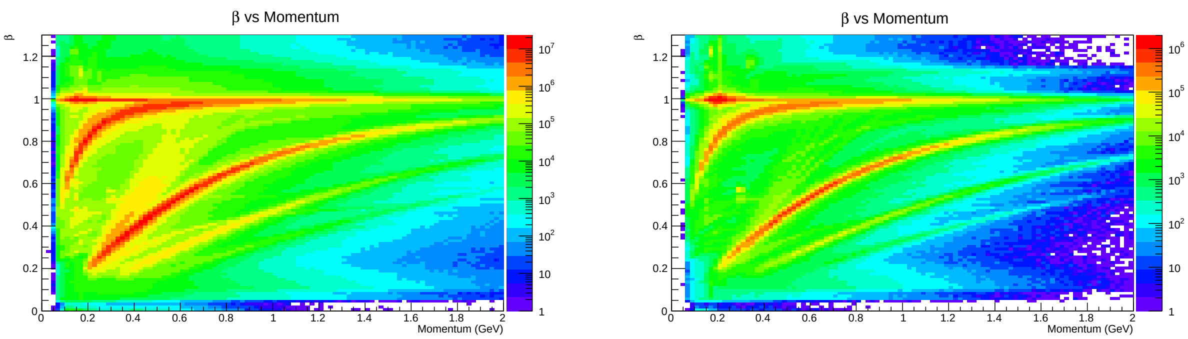

(a) Before Quench (b) After Quench

Figure 6.49: β versus momentum for before any energy loss or timing corrections are applied before (a) the quench and after (b) the quench.

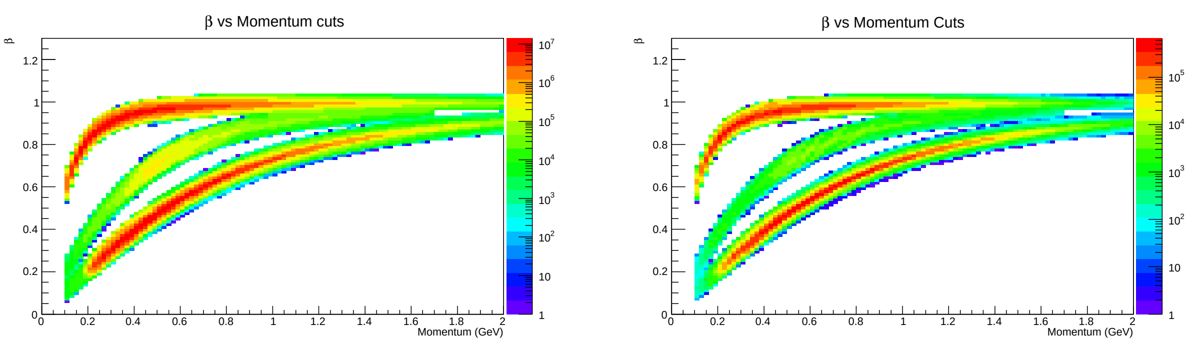

(a) Before Quench (b) After Quench

Figure 6.50: β versus momentum is shown here for after energy loss and timing corrections have been applied before (a) the quench and after (b) the quench.

It would also be beneficial to compare the T asymmetry before and after the quench, but due to low statistics taken after the quench, that is not possible. Too many re-polarization cycles occurred after the quench and due to time constraints, only three weeks of data were taken after the quench.

6.3 Normalization

The polarization of the free protons in the FROST target could be in the positive (upward) or negative (downward) direction, depending on the desired setting, which was previously described in Table 4.1. Because the two polarization settings were used to extract the polarization observables, a relative normalization factor between the two must be introduced because the number of incident photons for the positive setting was not the same as the number of incident photons for the negative polarization setting. The photon flux appears in the normalized yields used in the moment method (eq.5.6). Since the photon flux on target was difficult to estimate for this experiment because of tight collimation of the photon beam, the number of triggers during positive and negative target polarization settings was used. This was possible since the CLAS Level-1 and Level-2 trigger settings were not changed during the run. In order to study the normalization that was being used, it is useful to study a combination of other relative normalization factors that could be used. The different settings for the normalization are described in Table 6.19. For this purpose, the *"normal"* normalization setting was considered for each energy bin W separately, that is, counting all triggers in the positive and negative target polarization settings for both butanol and carbon (referred to as $flag0$) for each W bin. $flag1$ refers to the relative normalization using all reconstructed events independent of energy for each target polarization setting. $flag2$ refers to the number of all reconstructed events from butanol only, independent of energy. $flag4$ refers to the number of all reconstructed events from carbon only, independent of energy. $flag14$ refers to all reconstructed events from butanol, carbon and CH_2, independent of energy. By changing the relative normalization, the resulting T

asymmetries were examined and the results are listed in Tables 6.20, 6.21, and 6.22.

Table 6.19: The various flags defining the different normalization settings for energy bin W=1875 MeV. The flags are defined in Section 6.3.

Flag:	Pos. Events:	Neg. Events:	Scale Pos. by:
0	1.00663e+08	8.38861e+07	0.833333
1	1.00663e+08	8.38861e+07	0.833333
2	5.39366e+07	5.32113e+07	0.986553
4	5.82188e+06	5.19749e+06	0.892751
14	6.73161e+07	6.51748e+07	0.96819

Table 6.20: The resulting T asymmetry of Λ and Σ^0 events depending on the relative normalization for energy bin $W = 1875$ MeV and various $\cos\theta_{K^+}$ bins. The flags are defined in Section 6.3.

	Normal ($flag0$):	$flag1$:	$flag2$:	$flag4$:	$flag14$:
$W = 1875$ MeV, $\cos\theta_{K^+} = -0.5$					
T Λ asymmetry:	0.24±0.117	0.274±0.115	0.138±0.122	0.221±0.121	0.154±0.121
T Λ change (DSR):		0.207	-0.603	-0.113	-0.735
T Σ^0 asymmetry:	0.158±0.125	0.163±0.124	0.144±0.13	0.155±0.126	0.146±0.129
T Σ^0 change (DSR):		0.0284	-0.0776	-0.0169	-0.0668
$W = 1875 MeV$, $\cos\theta_{K^+} = 0.1$					
T Λ asymmetry:	-0.26±0.069	-0.22±0.069	-0.382±0.069	-0.282±0.069	-0.363±0.069
T Λ change (DSR):		0.41	-1.25	-0.225	-0.472
T Σ^0 asymmetry:	0.203±0.066	0.222±0.065	0.144±0.068	0.192±0.066	0.153±0.068
T Σ^0 change (DSR):		0.205	-0.623	-0.118	-0.528
$W = 1875$ MeV, $\cos\theta_{K^+} = 0.9$					
T Λ asymmetry:	-0.39±0.134	-0.42±0.132	-0.304±0.142	-0.376±0.141	-0.318±0.141
T Λ change (DSR):		-0.159	0.440	0.072	0.270
T Σ^0 asymmetry:	-0.082±0.144	-0.106±0.142	-0.008±0.15	-0.068±0.145	-0.02±0.149
T Σ^0 change (DSR):		-0.119	0.356	0.0685	0.299
σ_T (Λ):		0.016	0.048	0.009	0.041
σ_T (Σ^0):		0.016	0.048	0.009	0.040

Table 6.21: The resulting T asymmetry of Λ and Σ^0 events depending on the relative normalization for energy bin $W = 2075$ MeV and various $\cos\theta_{K^+}$ bins. The flags are defined in Section 6.3. "n/a" refers to a bin for which a Λ or Σ^0 signal could not be extracted and the resulting DSR could not be determined.

	Normal ($flag0$):	$flag1$:	$flag2$:	$flag4$:	$flag14$:
$W = 2075$ MeV, $\cos\theta_{K^+} = -0.5$					
T Λ asymmetry:	n/a	n/a	n/a	n/a	
T Λ change (DSR):					
T Σ^0 asymmetry:	-0.087±0.273	-0.066±0.272	-0.18±0.278	-0.11±0.274	-0.167±0.277
T Σ^0 change (DSR):		0.0545	-0.239	-0.0595	-0.206
$W = 2075$ MeV, $\cos\theta_{K^+} = 0.1$					
T Λ asymmetry:	-0.66±0.074	-0.643±0.074	-0.733±0.074	-0.673±0.074	-0.721±0.074
T Λ change (DSR):		0.162	-0.698	-0.124	-0.128
T Σ^0 asymmetry:	-0.21±0.084	-0.207±0.083	-0.229±0.087	-0.215±0.085	-0.226±0.087
T Σ^0 change (DSR):		0.0254	-0.157	-0.0418	-0.132
$W = 2075$ MeV, $\cos\theta_{K^+} = 0.9$					
T Λ asymmetry:	-0.597±0.09	-0.602±0.088	-0.577±0.097	-0.592±0.096	-0.58±0.096
T Λ change (DSR):		-0.0397	0.151	0.038	0.084
T Σ^0 asymmetry:	-0.211±0.142	-0.23±0.14	-0.125±0.148	-0.19±0.143	-0.138±0.147
T Σ^0 change (DSR):		-0.0953	0.419	0.104	0.357
σ_T (Λ):		0.010	0.043	0.010	0.036
σ_T (Σ^0):		0.016	0.073	0.018	0.062

Table 6.22: The resulting T asymmetry of Λ and Σ^0 events depending on the relative normalization for energy bin $W = 2225$ MeV and various $\cos\theta_{K^+}$ bins. The flags are defined in Section 6.3. "n/a" refers to a bin for which a Λ or Σ^0 signal could not be extracted and the resulting DSR could not be determined.

	Normal ($flag0$):	$flag1$:	$flag2$:	$flag4$:	$flag14$:
	$W = 2225MeV$, $\cos\theta_{K^+} = -0.5$				
T Λ asymmetry:	n/a	n/a	n/a	n/a	n/a
T Λ change (DSR):					
T Σ^0 asymmetry:	n/a	n/a	n/a	n/a	n/a
T Σ^0 change (DSR):					
	$W = 2225$ MeV, $\cos\theta_{K^+} = 0.1$				
T Λ asymmetry:	-0.707±0.13	-0.664±0.136	-0.826±0.114	-0.723±0.117	-0.807±0.117
T Λ change (DSR):		0.229	-0.688	-0.0915	-0.679
T Σ^0 asymmetry:	-0.472±0.114	-0.441±0.114	-0.562±0.114	-0.487±0.114	-0.547±0.114
T Σ^0 change (DSR):		0.192	-0.558	-0.093	-0.465
	$W = 2225$ MeV, $\cos\theta_{K^+} = 0.9$				
T Λ asymmetry:	n/a	n/a	n/a	n/a	n/a
T Λ change (DSR):					
T Σ^0 asymmetry:	0.181±0.178	0.135±0.177	0.313±0.181	0.203±0.179	0.292±0.18
T Σ^0 change (DSR):		-0.183	0.52	0.0872	0.438
σ_T (Λ):		0.020	0.055	0.085	0.046
σ_T (Σ^0):		0.032	0.093	0.016	0.078

6.4 Total Systematic Uncertainty

Now that the various cuts have been applied and the uncertainty associated with them have been studied for the T asymmetry, the total systematic uncertainty can be calculated. These uncertainties are an overall systematic error for all energies and angles. More precise studies will be performed in the future for the final publication using simulated data, but Table 6.23 gives a good beginning estimate to the systematic uncertainty associated with this analysis for the T asymmetry. The same studies should also be done to find the total systematic uncertainty associated with the F, T_x, and T_z asymmetries.

How the uncertainties were calculated will now be described. The first uncertainties described are not specific to this particular analysis, but the overall experiment. The uncertainty associated with the electron beam polarization due to the Møller measurement was estimated to be 3% using simulation of the Møller polarimeter [102]. Due to this uncertainty, there is then a systematic uncertainty associated with the photon beam polarization of 3% since the photon beam polarization is derived from the electron beam polarization using Eq. (2.2). The beam charge asymmetry was previously discussed in Section 4.1.2 and the uncertainty was determined to be $< 0.1\%$ [102]. The extraction of the target polarization from the NMR signal had a systematic uncertainty of 1.7% [99] and the overall systematic uncertainty in using the Q-meters and NMR coils was estimated to be $\approx$ 3% [86].

The next uncertainties to be discussed are particular to this analysis since they are based on the cuts applied throughout the analysis. To estimate the systematic uncertainties, the Λ and Σ^0 yields and the T asymmetry results have been compared and the standard deviation of all extracted asymmetries for varied cuts from those for 'normal' cuts within the W bins 1.85-1.90 GeV, 2.05-2.10 GeV, and 2.20-2.25 GeV calculated. The standard deviation (σ_T) from Eq.(6.3) is used to estimate the uncertainty of the T asymmetries for $K^+\Lambda$ and $K^+\Sigma^0$ for all $\cos\theta$ bins within a given W bin, as reported in the tables in previous sections of this chapter. The following ranges of σ_T reflect the average of σ_T for both reactions in the chosen three W bins. The standard deviations associated with varying the fiducial cuts (cf. Tables 6.1 to 6.3), the particle identification (β) cuts (cf. Tables 6.4 to 6.6), the missing mass cuts (cf. Tables 6.7 to 6.9), and all cuts simultaneously (cf. Tables 6.13 to 6.15) were between $\pm$ 0.02 to $\pm$ 0.06 (absolute). A variation of the target offset ϕ_0 by more than 3° resulted in a negligible change of the extracted asymmetries by $\pm$ 0.01–0.02 (cf. Tables 6.16 to 6.18). A comparison of results before and the quench showed small variations, which is estimated to lead to an uncertainty of less than 2%. Changing the degree of the polynomial for the background fit resulted in variations of $\pm$0.035–0.12. To calculate the final uncertainty only the standard deviations for the 4th and 5th degree fits are used, larger deviations occurred when using a linear background fit (cf. Tables 6.10 to 6.12). A change of the relative normalization between data from positive and negative target polarization settings, previously described in Section 6.3, resulted in a standard deviation of $\pm$ 0.04–0.05.

Table 6.23: Total Systematic Uncertainty in T asymmetry

Systematics	Effect on T
Photon Beam Polarization	3%
Beam Charge Asymmetry	$<$ 0.1%
Target Polarization	$\approx$ 4-5%
Target Quench	$<$ 2 %
Target Offset	$<$ 0.02 (absolute)
Fiducial Cuts	$\approx$ 0.04 (absolute)
β Cuts	$<$ 0.04 (absolute)
Missing Mass Cuts	$\approx$ 0.03 (absolute)
All Cuts Simultaneously	$\approx$ 0.05 (absolute)
Background Fit	$<$ 0.05 (absolute)
Normalization	$<$ 0.05 (absolute)
Overall Uncertainty	$\pm$0.09 (absolute) $\pm$ 7%

Finally, the overall uncertainty is calculated by adding the individual errors in quadrature except for fiducial cut, β cut, and missing mass cut because these are included in 'All Cuts Simultaneously'. The result can be seen in Table 6.23. Systematic errors are reported in form of two values, a relative 7%, mainly associated with uncertainties of beam and target polarization, the other an absolute uncertainty of 0.09, based on studies of various cuts used in this analysis. Both uncertainties have to be considered when accounting for the systematic uncertainty of asymmetry results shown in Chapter 7 and listed in Appendix B.

6.5 Summary

This section has described the uncertainty associated with the polarization observable measurements due to cuts and detector performance. It appears that by varying the fiducial cut, missing mass cut, or β cuts, that a significant change in yield of signal does not occur. Cuts have been varied and the re-calculated T asymmetry has been checked against the *normal* observable measurements. This should be done for all polarization observables, not just T, but this chapter has demonstrated a reasonable start to the systematic studies. The results are presented in Chapter 7 and the impact of these results is also discussed.

Chapter 7

Results

Once the events have been selected, the method for extracting the observables discussed, and the uncertainty associated with the measurements estimated, the results can be presented. These results will hopefully provide answers or more clues as to the physics of the two reactions, $\gamma p \rightarrow K^+ + \Lambda$ and $K^+ + \Sigma^0$. One of the main motivations for this analysis is to search for missing resonances and it is expected that these results will allow for improvement in the models and their fits, as well as to strengthen the evidence for the N^* and Δ^* states that couple to KY. These results are also useful to constrain the parameters of existing 3-star and 4-star resonances, as shown in Tables 1.1 and 1.2.

7.1 Binning of the Results

In Section 5.1, the kinematics for kaon photoproduction were shown. In order to realize final results, independent kinematic variables must be chosen. For this particular analysis, the following two were chosen: the K^+ scattering angle in the center-of-mass frame, $\cos\theta_K^{cm}$, and the center-of-mass energy, W. For most energy bins, W was binned into 50-MeV wide bins, low-statistics bins (such as below $W < 1800$ MeV or > 2200 MeV) in 100 MeV wide bins. Both the T and F observables for $K^+ + \Lambda$ has 12 energy bins covering a range from

1650 to 2300 MeV and for $K^+ + \Lambda$, 10 energy bins ranging from 1700 to 2300 MeV are shown. Due to the low statistics of T_x and T_z, the W range covered is less than that of the T and F asymmetries for both $K^+ + \Lambda$ and $K^+ + \Sigma$. The T_x observable for $K^+ + \Lambda$ has 10 energy bins ranging from 1650 to 2250 MeV and $K^+ + \Sigma$ has 10 energy bins ranging from 1750 to 2300 MeV. The T_z observable for $K^+ + \Lambda$ has 9 energy bins ranging from 1650 to 2200 MeV and $K^+ + \Sigma$ has 8 energy bins ranging from 1750 to 2250 MeV. For $\cos\theta_K^{cm}$, 10 equally sized bins were used, covering a range from -1 to 1.

7.2 Nomenclature

The following sections will show the T, T_x, T_z, and F asymmetries for both $K^+ + \Lambda$ and $K^+ + \Sigma^0$. For all plots, the same designation of data and model curves is used and only statistical errors are included. The data of this analysis are denoted by red solid diamonds, the Bonn-Althoff data [55] are denoted by black solid circles, and the GRAAL data [52] are denoted by green solid upside-down triangles. The BOGA model predictions [17] are shown as the magenta solid curves, the KAON-MAID model predictions [16] as blue solid curves, and the RPR-Ghent model predictions [117] as red dashed curves.

7.3 T Results for $K^+ + \Lambda$

The first result to discuss is the T asymmetry for $K^+ + \Lambda$. The T asymmetry is the only asymmetry that will be presented in this analysis along with published data from Bonn and GRAAL, discussed in Sections 1.6.9 and 1.6.8, respectively. As a reminder, the Bonn data were also acquired using a polarized target and the GRAAL data were extracted using double-polarization data. The data have been compared to three separate models, KAON-Maid, Bonn-Gatchina, and Ghent, previously described in Sections 1.7.1, 1.7.2, 1.7.3, respectively. All energy bins are binned in 50 MeV except the last bin, which is binned in 100 MeV due to the low statistics. At energies between $W = 1750$ to 2100 MeV, the current data agrees with the BOGA model or are at least of the same trend in sign. Above 2000 MeV, the data agree best with the RPR-Ghent model. However, it is clear that the current theory models are inadequate to describe the data at higher energies, >2150 MeV. The results as a function of $\cos\theta_K^{cm}$ can be seen in Figs. 7.1 and 7.2 ranging from 1650 – 2300 MeV in W. In the lower energy bins, there is minimal consistency with the GRAAL data. However, increasing in W, better agreement is seen, specifically around $W = 1875$ MeV. Despite the Bonn data only consisting of three data points, the CLAS data agrees with them, especially at $W = 1725$ MeV, within error bars. Below 2000 MeV, the current data is consistently lower than the GRAAL data. Beyond $W = 1975$ MeV, no GRAAL data exists and the CLAS data has a clear trend of being positive in the backward direction and negative in the forward direction. However, at higher energies, $W > 2125$ MeV, there is a clear breakdown in the consistency of the data with large fluctuations in $\cos\theta_K^{cm}$, but there are less statistics at these energies, which could explain the large variations.

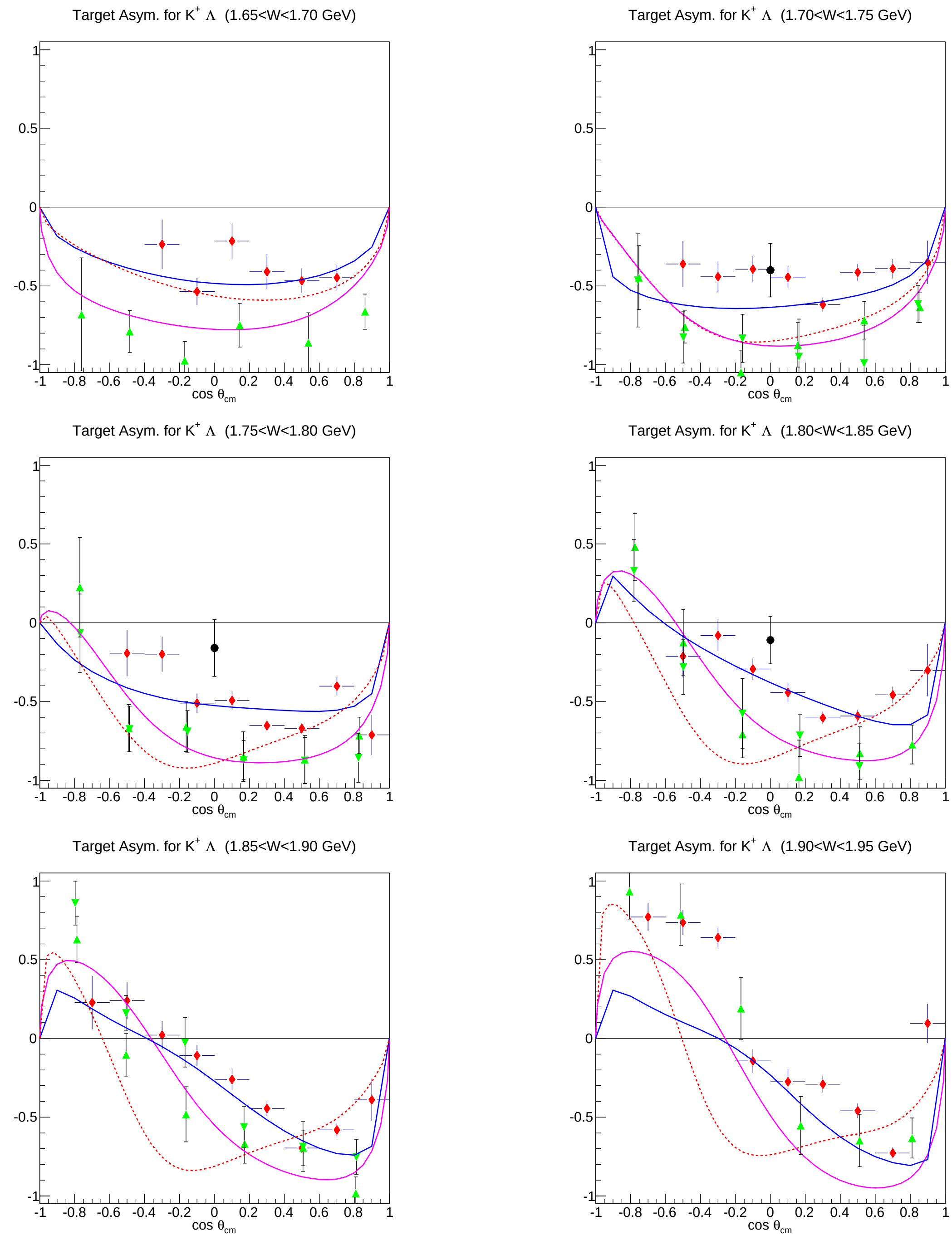

Figure 7.1: T asymmetry for $\gamma p \to K^+\Lambda$ for $W = 1650$ to 1950 MeV. Red diamond data points are from this analysis and include only statistical errors, green triangle data points are from GRAAL, black circle data points are from Bonn, the dashed red model curve is from RPR-Ghent, the solid blue model curve is from KAON-MAID, and the solid magenta model curve is from BOGA, all data and models are previously described in Section 7.2.

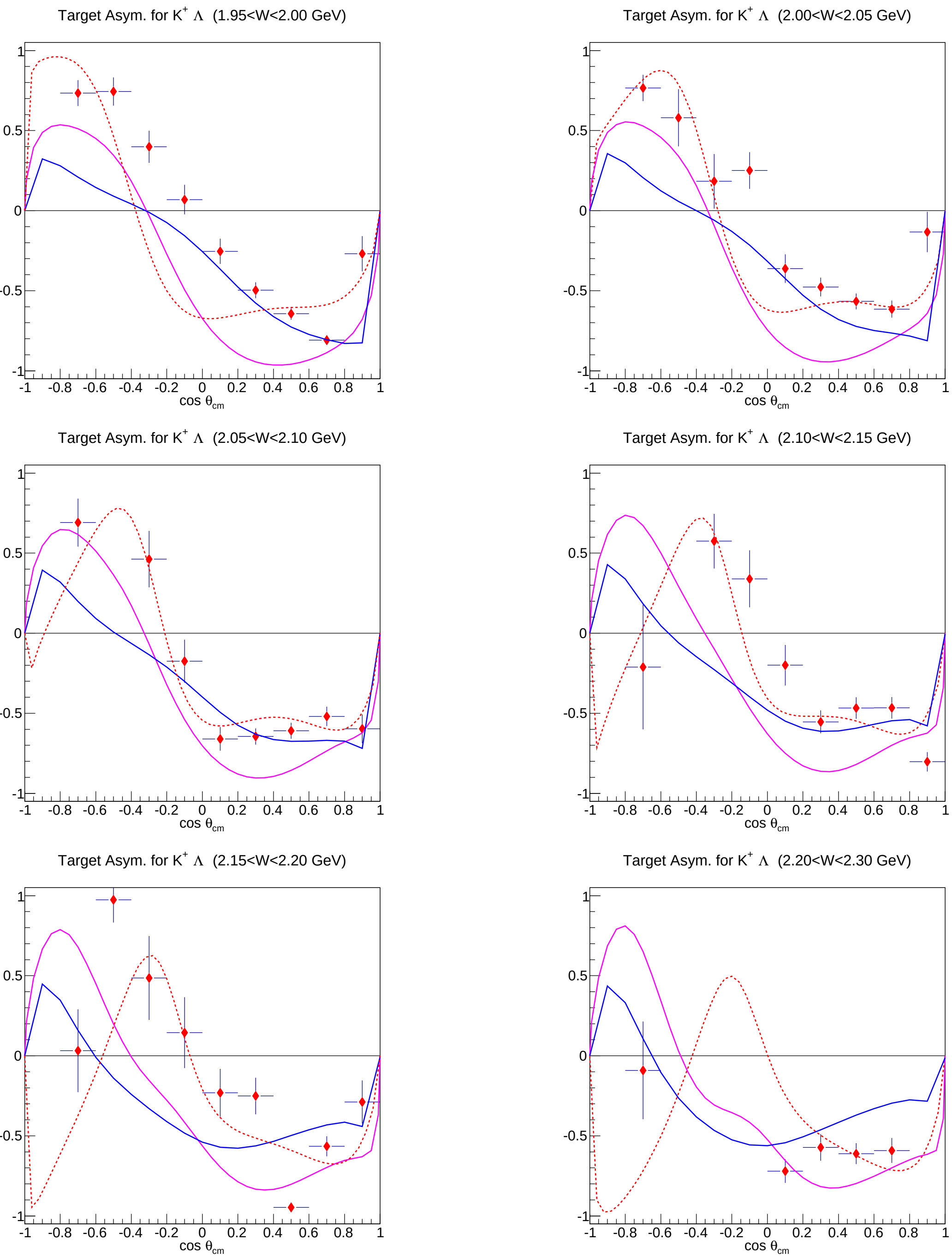

Figure 7.2: T asymmetry for $\gamma p \rightarrow K^+\Lambda$ for $W = 1950$ to 2300 MeV. Red diamond data points are from this analysis and include only statistical errors, green triangle data points are from GRAAL, the dashed red model curve is from RPR-Ghent, the solid blue model curve is from KAON-MAID, and the solid magenta model curve is from BOGA, all data and models are previously described in Section 7.2.

7.4 T Results for $K^+ + \Sigma^0$

The results for the T asymmetry for $K^+ + \Sigma^0$ are presented in this section. The models again are the KAON-MAID, Bonn-Gatchina, and Ghent models, previously described in Sections 1.7.1, 1.7.2, 1.7.3, respectively. There are no previous experimental data and those included here are the first results for this observable. The results can be seen in Figs. 7.3 and 7.4 and range from 1700 – 2300 MeV in W. The first and last energy bins are binned in 100 MeV due to low statistics, but the bins in between are binned in 50 MeV. Here, it can be seen that at lower energies, that is $W < 1875$ MeV, no consistency of data appears and none of the models come close to representing the data, but at $W > 1875$ MeV, a trend exists of the data with a dip in the data around $\cos\theta_K^{cm} = 0.3$. At $W > 1875$ MeV, none of the theory agree with the data. The data appears to have the same shape as the BOGA model from $W = 2075$ to 2225 MeV, but overall is still in poor agreement with the present data. Once again, at higher energies, the results have less statistics that at lower energies.

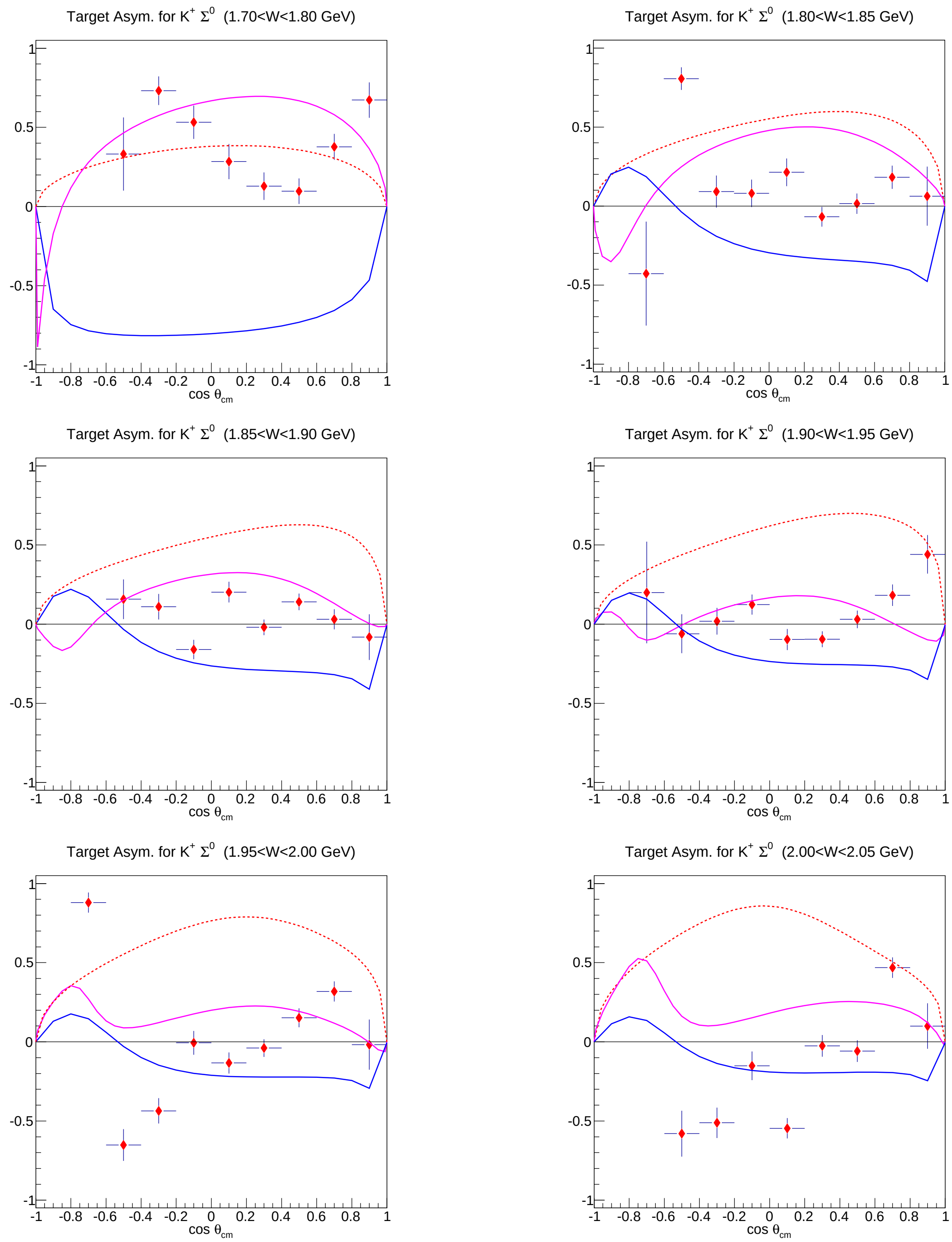

Figure 7.3: T asymmetry for $\gamma p \rightarrow K^+\Sigma^0$ for $W = 1700$ to 2050 MeV. Red diamond data points are from this analysis and include only statistical errors, the dashed red model curve is from RPR-Ghent, the solid blue model curve is from KAON-MAID, and the solid magenta model curve is from BOGA, all data and models are previously described in Section 7.2.

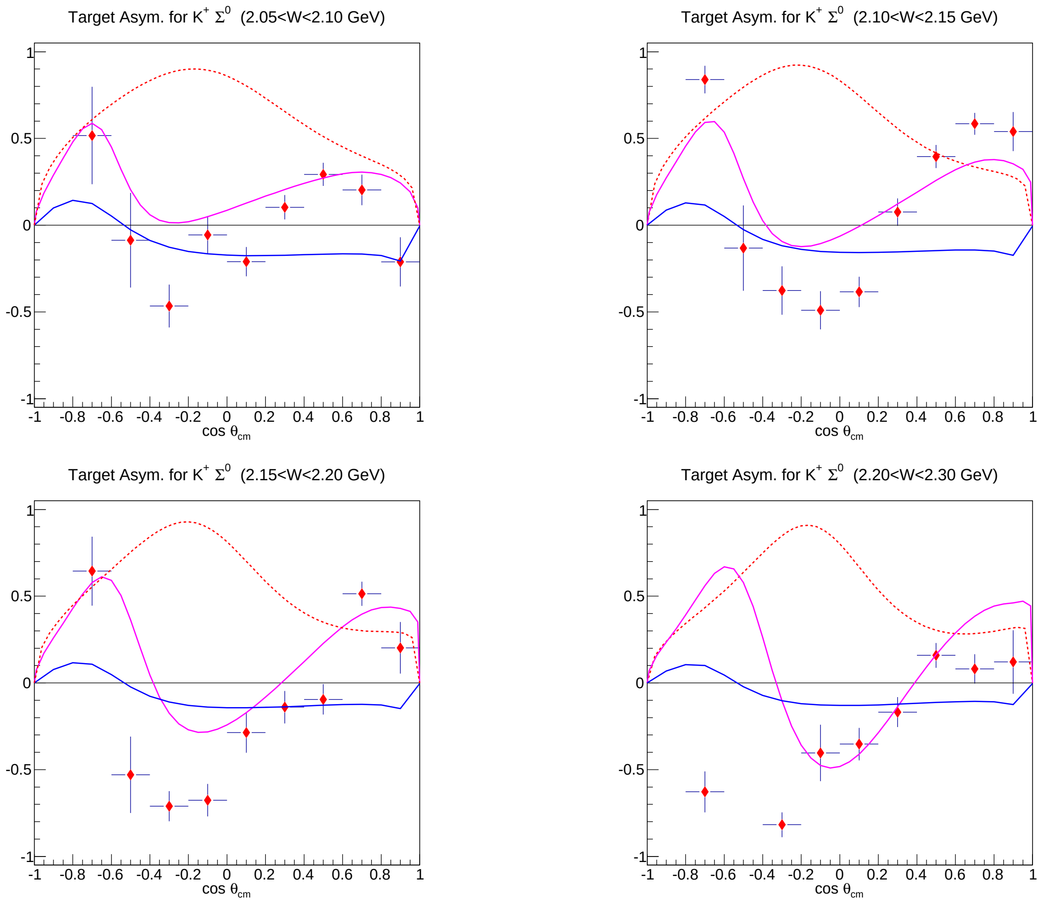

Figure 7.4: T asymmetry for $\gamma p \to K^+\Sigma^0$ for $W = 2050$ to 2300 MeV. Red diamond data points are from this analysis, the dashed red model curve is from RPR-Ghent, the solid blue model curve is from KAON-MAID, and the solid magenta model curve is from BOGA, all data and models are previously described in Section 7.2.

7.5 T_x Results for $K^+ + \Lambda$

The results for T_x for $K^+ + \Lambda$ are shown here. The models again are the KAON-MAID, Bonn-Gatchina, and Ghent models, previously described in Sections 1.7.1, 1.7.2, 1.7.3, respectively. There are no previous experimental data and those included here are the first results for this observable. The results can be seen in Figs. 7.5 and 7.6 and range from

1650 – 2200 MeV in W. The first and last energy bins are binned in 100 MeV due to low statistics, but the energy bins in between are binned in 50 MeV. For T_x, there is no agreement with any of the models at any energy range.

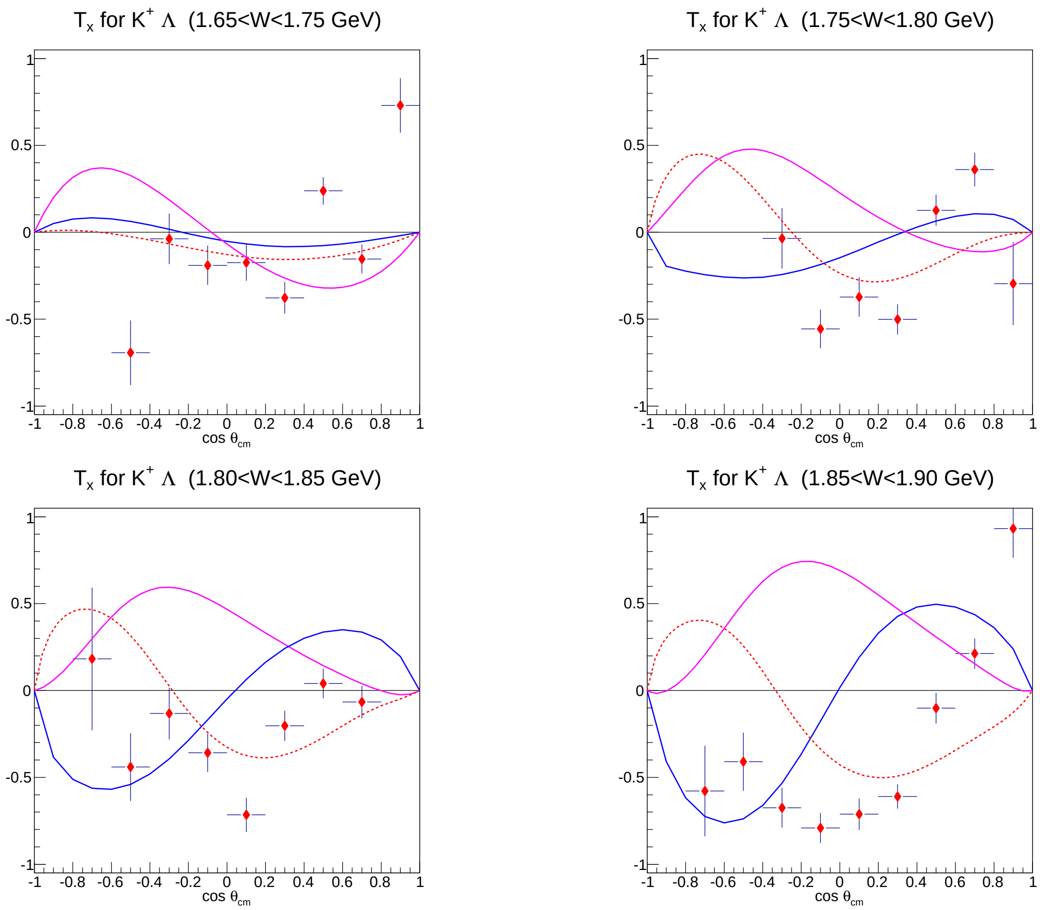

Figure 7.5: T_x asymmetry for $\gamma p \to K^+\Lambda$ for $W = 1650$ to 1900 MeV. Red diamond data points are from this analysis and include only statistical errors, the dashed red model curve is from RPR-Ghent, the solid blue model curve is from KAON-MAID, and the solid magenta model curve is from BOGA, all data and models are previously described in Section 7.2.

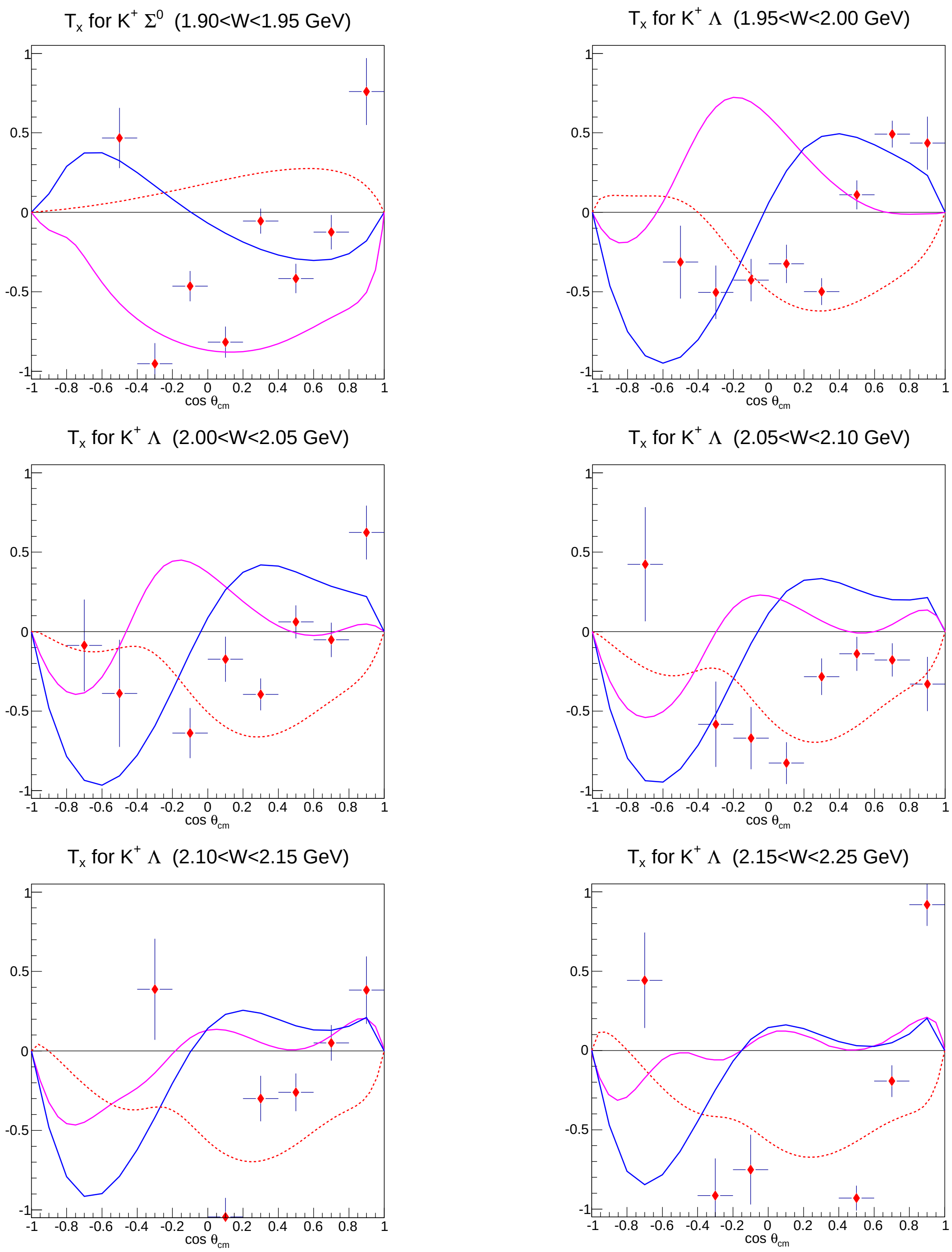

Figure 7.6: T_x asymmetry for $\gamma p \to K^+\Lambda$ for $W = 1900$ to 2250 MeV. Red diamond data points are from this analysis and include only statistical errors, the dashed red model curve is from RPR-Ghent, the solid blue model curve is from KAON-MAID, and the solid magenta model curve is from BOGA, all data and models are previously described in Section 7.2.

7.6 T_x Results for $K^+ + \Sigma^0$

The results for T_x for $K^+ + \Sigma^0$ are shown here. The models again are the KAON-MAID, Bonn-Gatchina, and Ghent models, previously described in Sections 1.7.1, 1.7.2, 1.7.3, respectively. There are no previous experimental data and those included here are the first results for this observable. The results can be seen in Figs. 7.7 and 7.8 and range from 1750 – 2200 MeV in W. The first energy bin is binned in 100 MeV due to low statistics, but the remaining energy bins are binned in 50 MeV. Again, there is no agreement with any model at any energy range. The measurement of polarization data depending on the recoiling hyperon for $\gamma p \to K^+\Sigma^0$ does not directly use the polarization direction of Σ^0, but instead the decay particle Λ while averaging over the polarization direction of the other decay particle γ, which could not be detected. Therefore the measurement of T_x for $K^+ + \Sigma^0$ is not as accurate as the measurement for $K^+ + \Lambda$.

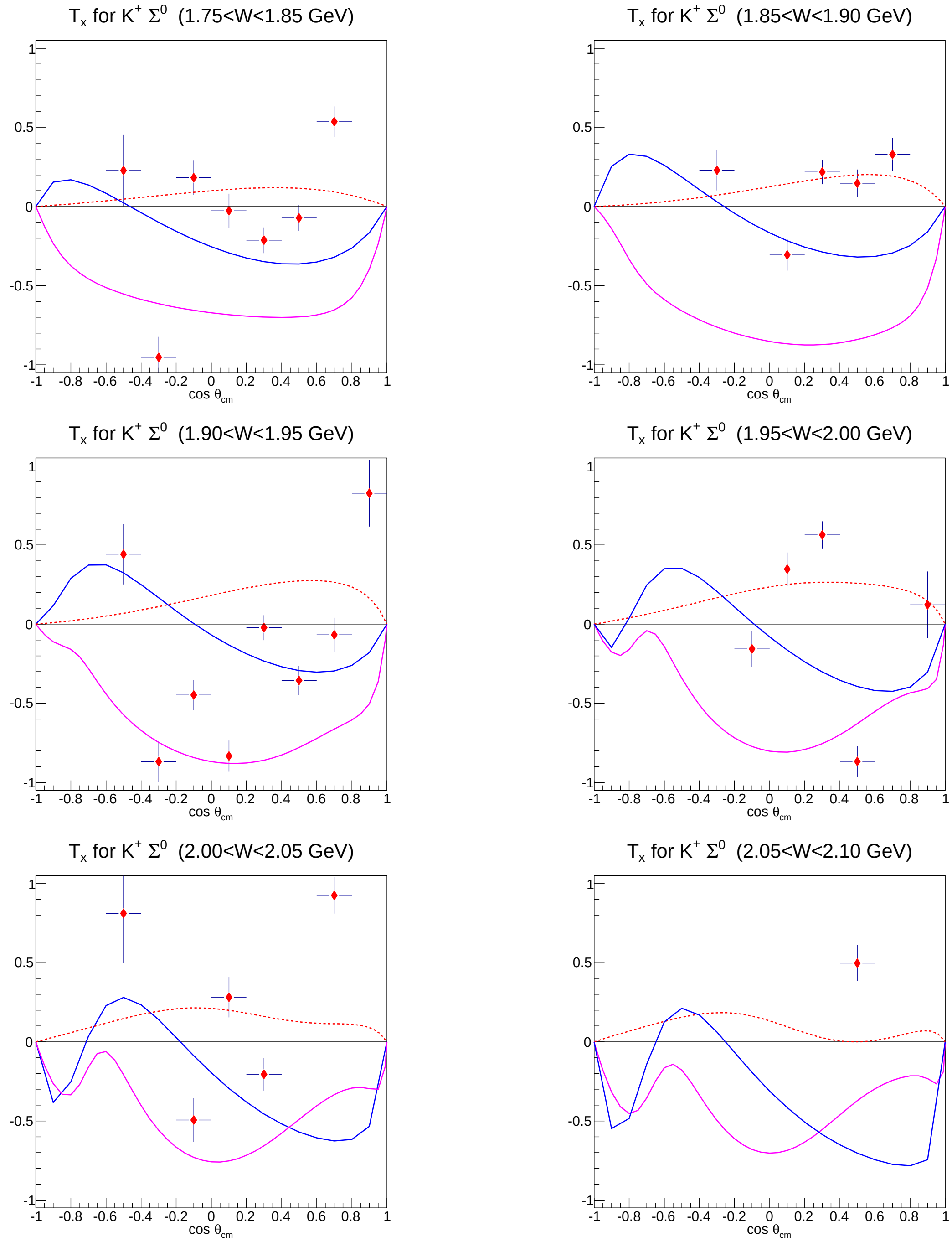

Figure 7.7: T_x asymmetry for $\gamma p \rightarrow K^+\Sigma^0$ for W = 1750 to 2100 MeV. Red diamond data points are from this analysis and include only statistical errors, the dashed red model curve is from RPR-Ghent, the solid blue model curve is from KAON-MAID, and the solid magenta model curve is from BOGA, all data and models are previously described in Section 7.2.

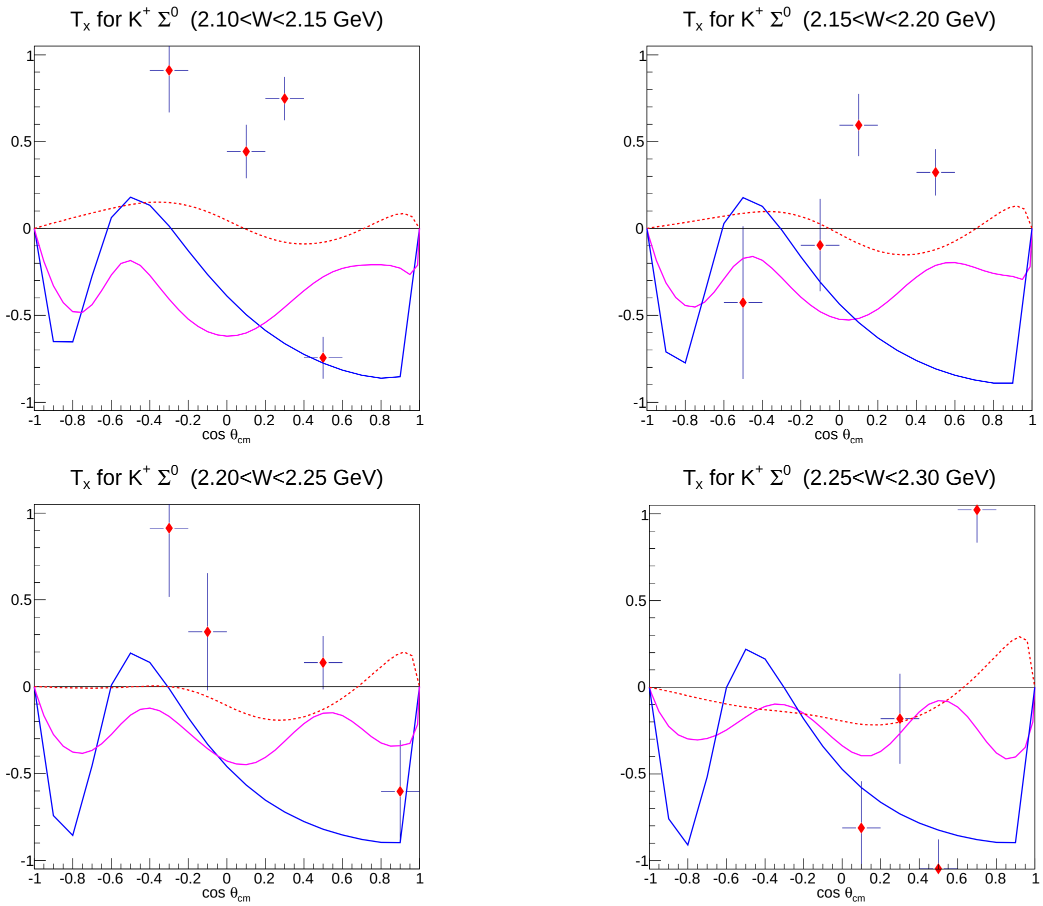

Figure 7.8: T_x asymmetry for $\gamma p \rightarrow K^+\Sigma^0$ for $W = 2100$ to 2300 MeV. Red diamond data points are from this analysis and include only statistical errors, the dashed red model curve is from RPR-Ghent, the solid blue model curve is from KAON-MAID, and the solid magenta model curve is from BOGA, all data and models are previously described in Section 7.2.

7.7 T_z Results for $K^+ + \Lambda$

The results for T_z for $K^+ + \Lambda$ are shown here. The models again are the KAON-MAID, Bonn-Gatchina, and Ghent models, previously described in Sections 1.7.1, 1.7.2, 1.7.3, respectively. There are no previous experimental data and those included here are the first results for this observable. The results can be seen in Figs. 7.9 and 7.10 and range from

1650 – 2300 MeV in W. The first and last energy bin are binned in 100 MeV due to low statistics and the energy bins in between are binned in 50 MeV. It appears that T_z has a trend at lower energies being positive in the backward angles and negative in the forward angles, but a breakdown occurs at $W > 2100$ MeV due to a lack of statistics causing large fluctuations in the data. Once again, it can be seen that the theoretical calculations do not agree with the measurements.

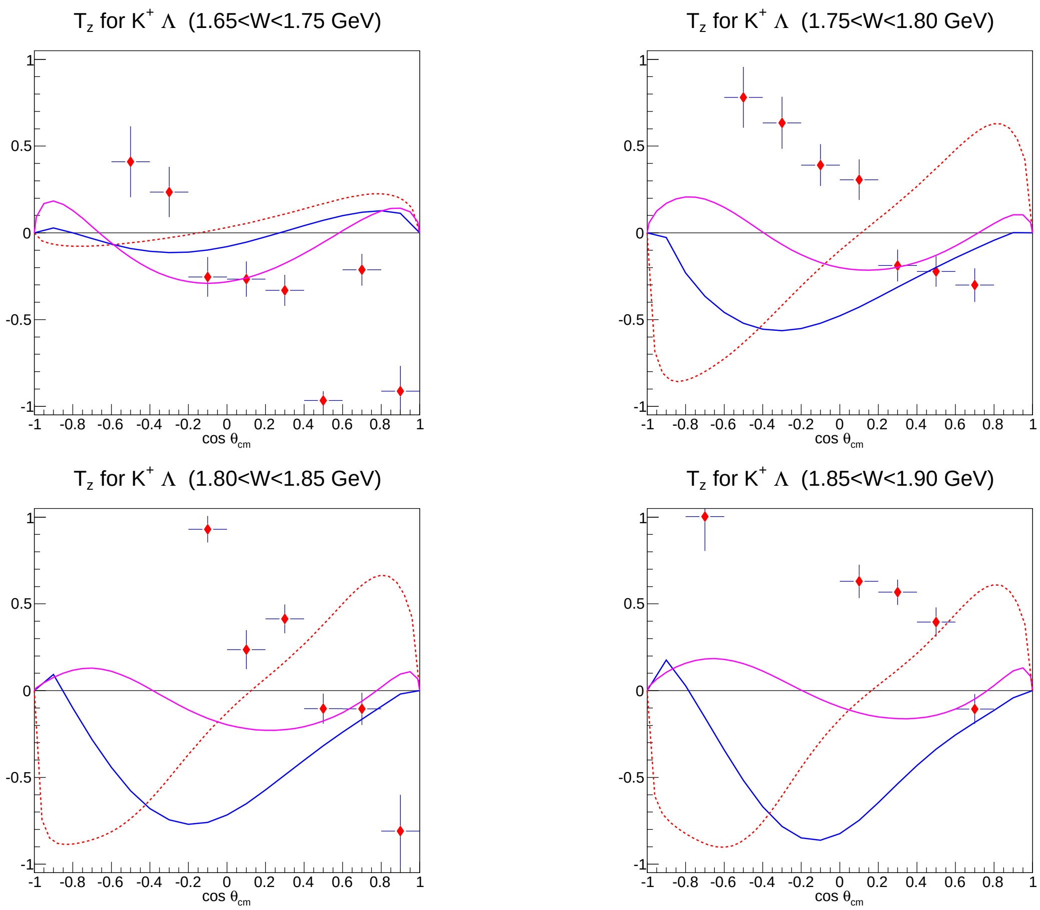

Figure 7.9: T_z asymmetry for $\gamma p \rightarrow K^+\Lambda$ for $W = 1650$ to 1900 MeV. Red diamond data points are from this analysis and include only statistical errors, the dashed red model curve is from RPR-Ghent, the solid blue model curve is from KAON-MAID, and the solid magenta model curve is from BOGA, all data and models are previously described in Section 7.2.

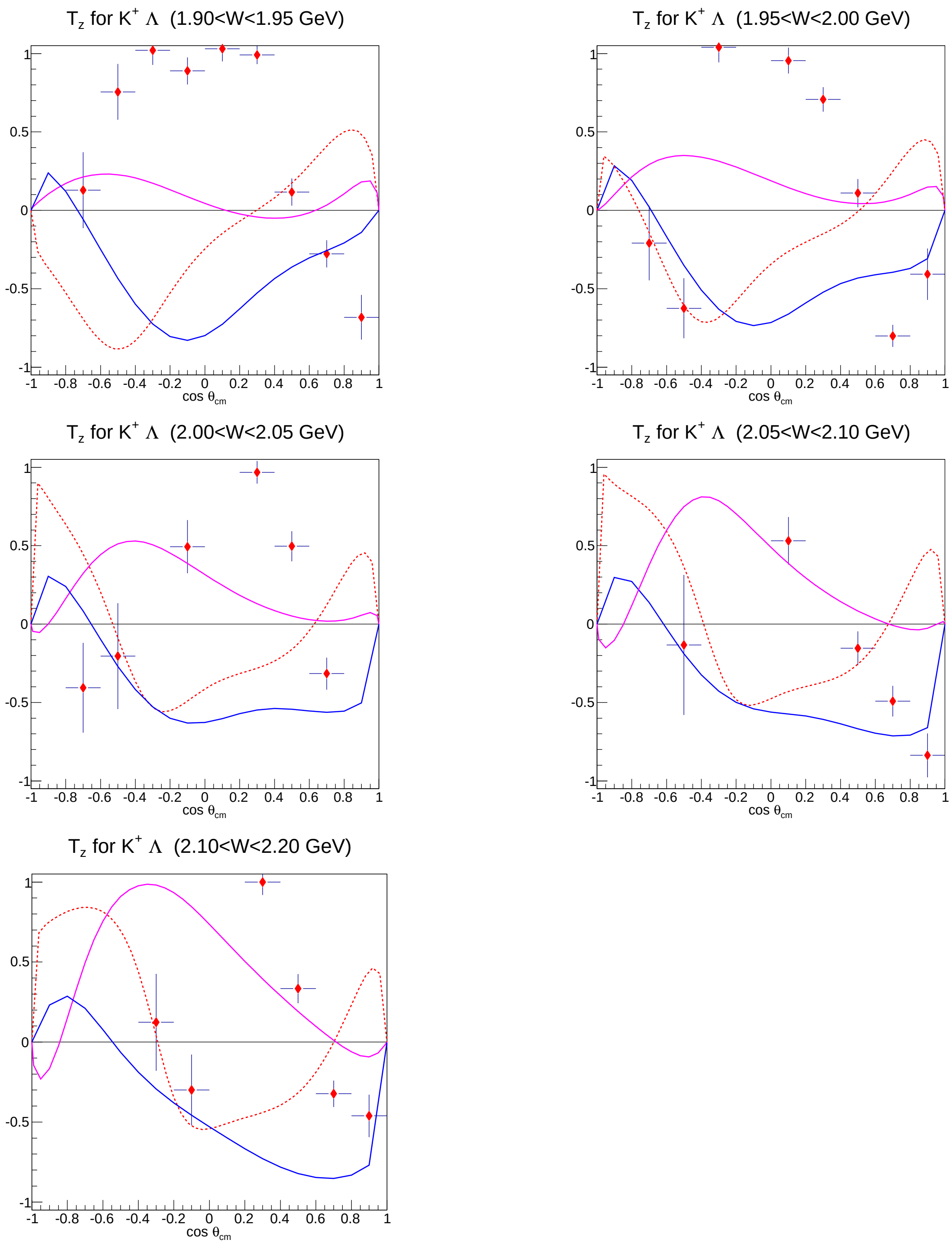

Figure 7.10: T_z asymmetry for $\gamma p \to K^+\Lambda$ for $W = 1900$ to 2200 MeV. Red diamond data points are from this analysis and include only statistical errors, the dashed red model curve is from RPR-Ghent, the solid blue model curve is from KAON-MAID, and the solid magenta model curve is from BOGA, all data and models are previously described in Section 7.2.

7.8 T_z Results for $K^+ + \Sigma^0$

The results for T_z for $K^+ + \Sigma^0$ are shown here. The models again are the KAON-MAID, Bonn-Gatchina, and Ghent models, previously described in Sections 1.7.1, 1.7.2, 1.7.3, respectively. There are no previous experimental data and those included here are the first results for this observable. The results can be seen in Figs. 7.11 and 7.12 and range from 1750 – 2300 MeV in W. Due to low statistics, more energy bins are binned in 100 MeV, with only five energy bins binned in 50 MeV. Here, the data in all energy bins seems to have large fluctuations and no data in any energy bin correspond to the models.

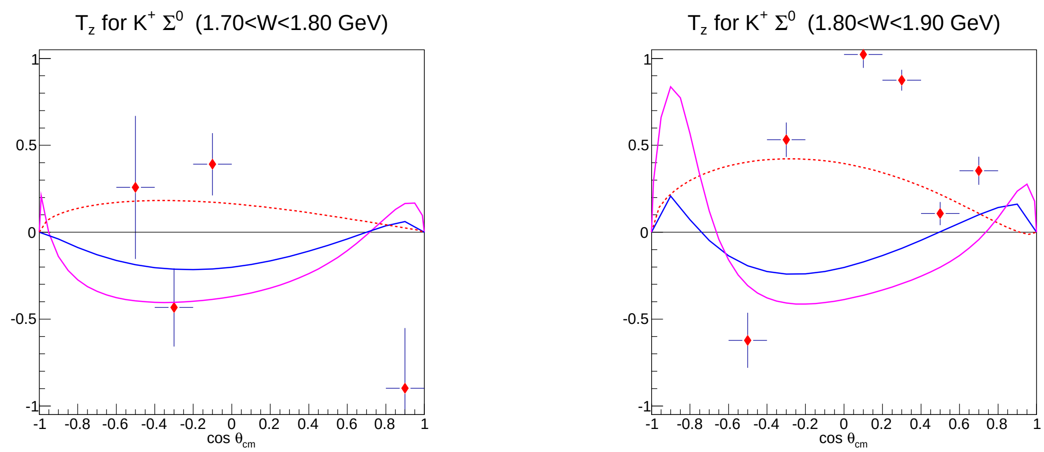

Figure 7.11: T_z asymmetry for $\gamma p \rightarrow K^+\Sigma^0$ for W = 1700 to 1900 MeV. Red diamond data points are from this analysis and include only statistical errors, the dashed red model curve is from RPR-Ghent, the solid blue model curve is from KAON-MAID, and the solid magenta model curve is from BOGA, all data and models are previously described in Section 7.2.

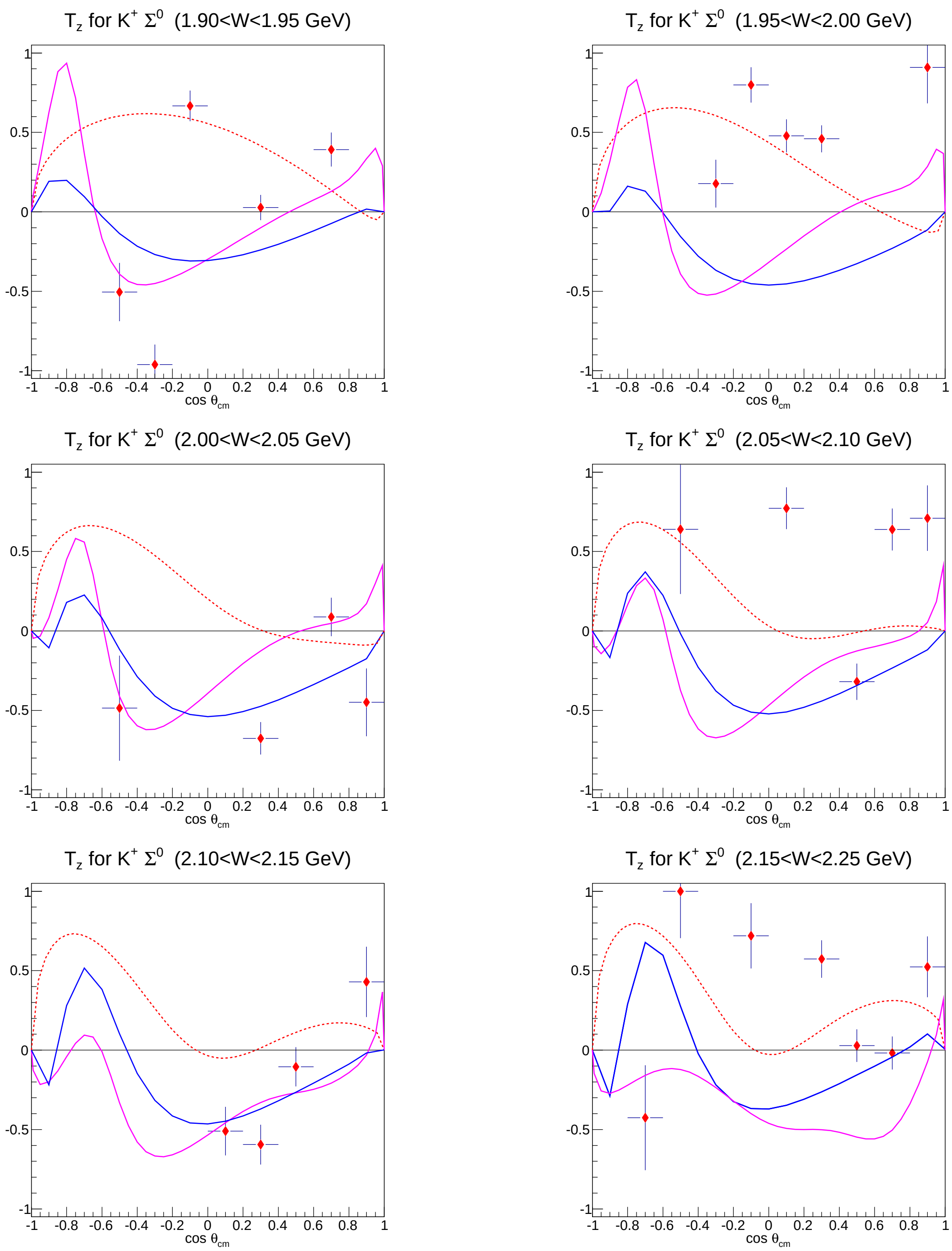

Figure 7.12: T_z asymmetry for $\gamma p \to K^+\Sigma^0$ for $W = 1900$ to 2250 MeV. Red diamond data points are from this analysis and include only statistical errors, the dashed red model curve is from RPR-Ghent, the solid blue model curve is from KAON-MAID, and the solid magenta model curve is from BOGA, all data and models are previously described in Section 7.2.

7.9 F Results for $K^+ + \Lambda$

Here results for F for $K^+ + \Lambda$ are presented. The models again are the KAON-MAID, Bonn-Gatchina, and Ghent models, previously described in Sections 1.7.1, 1.7.2, 1.7.3, respectively. There are no previous experimental data and those included here are the first results for this observable. The results can be seen in Figs. 7.13 to 7.15 and range from 1650 – 2250 MeV in W. The first and last energy bins are binned in 100 MeV due to low statistics and the energy bins in between are binned in 50 MeV. In most energy bins, there is not enough statistics in the very backward angles to obtain a measurement. In almost all energy bins, a trend occurs with the F asymmetry being positive in the backward angles and around $\cos\theta_K^{cm} = 0$ and then becoming negative in the very forward angles. Also, around $\cos\theta_K^{cm} = 0.1$, there is a small peak around energies $W > 2075$ MeV. No models show any agreement with the data.

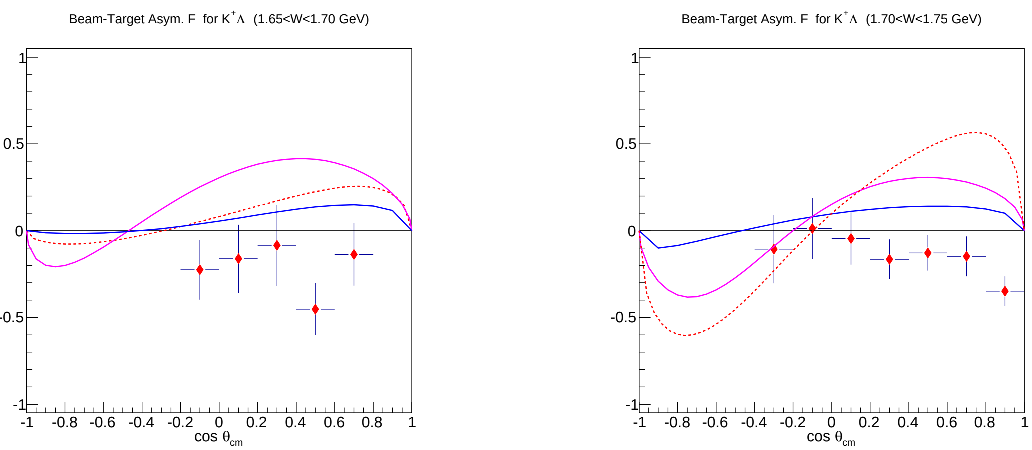

Figure 7.13: F asymmetry for $\gamma p \to K^+\Lambda$ for $W = 1650$ to 1750 MeV. Red diamond data points are from this analysis and include only statistical errors, the dashed red model curve is from RPR-Ghent, the solid blue model curve is from KAON-MAID, and the solid magenta model curve is from BOGA, all data and models are previously described in Section 7.2.

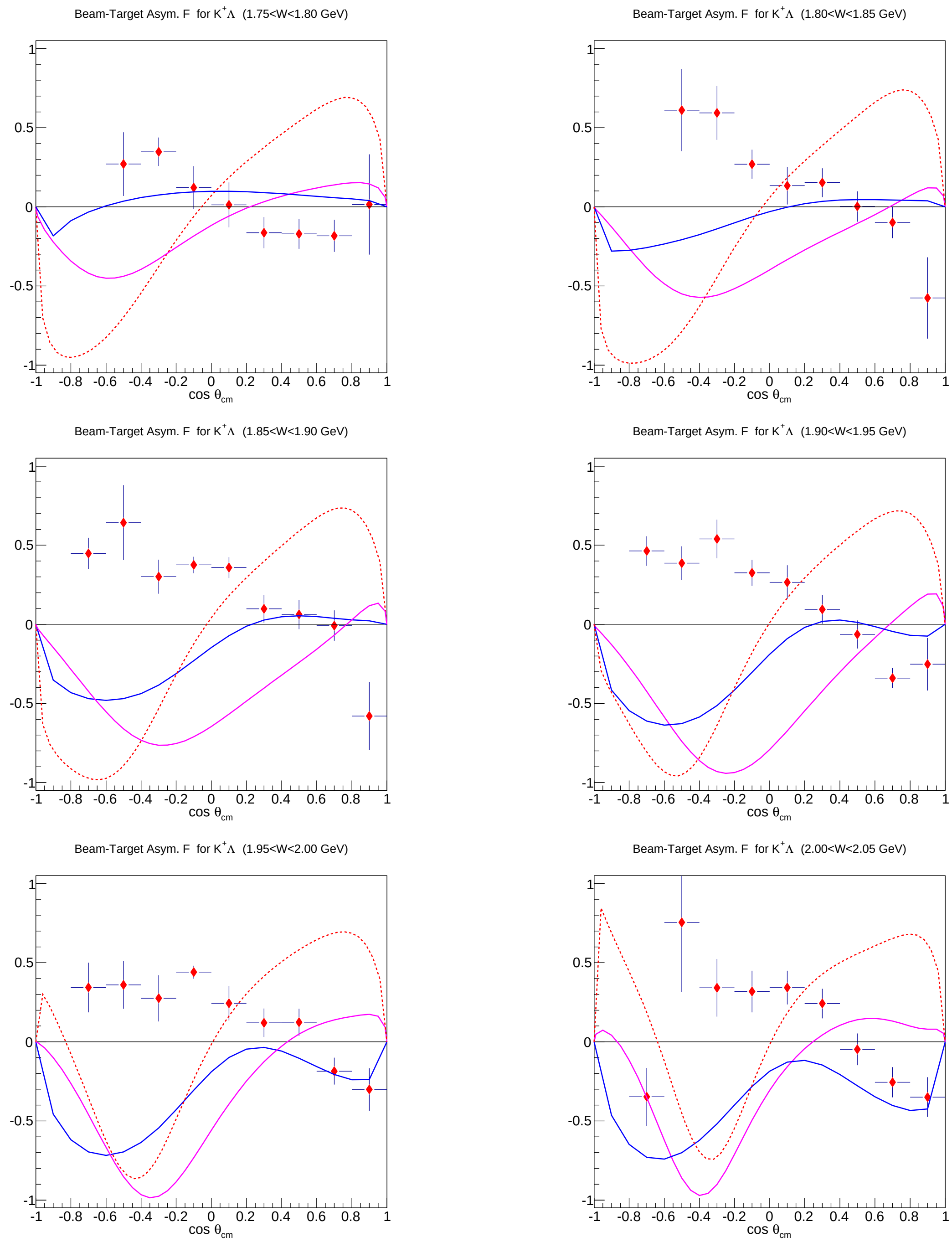

Figure 7.14: F asymmetry for $\gamma p \to K^+\Lambda$ for $W = 1750$ to 2050 MeV. Red diamond data points are from this analysis and include only statistical errors, the dashed red model curve is from RPR-Ghent, the solid blue model curve is from KAON-MAID, and the solid magenta model curve is from BOGA, all data and models are previously described in Section 7.2.

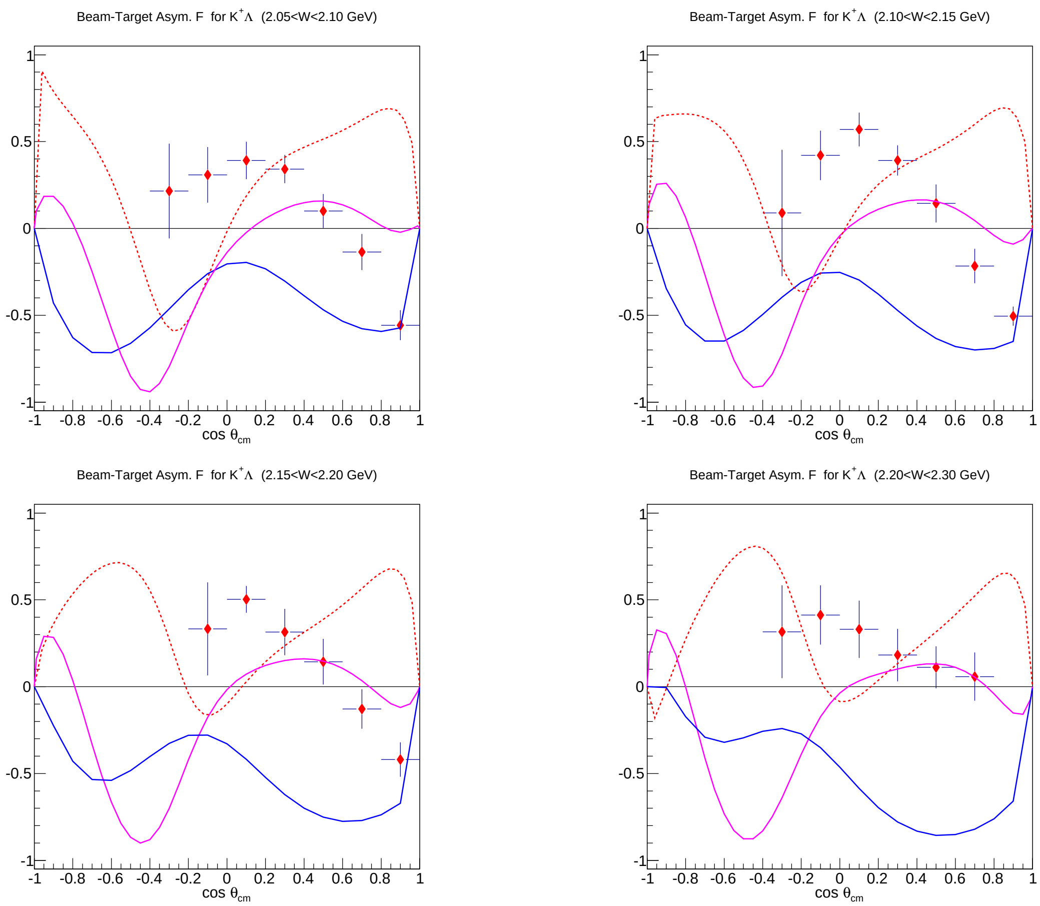

Figure 7.15: F asymmetry for $\gamma p \rightarrow K^+\Lambda$ for $W = 2050$ to 2300 MeV. Red diamond data points are from this analysis and include only statistical errors, the dashed red model curve is from RPR-Ghent, the solid blue model curve is from KAON-MAID, and the solid magenta model curve is from BOGA, all data and models are previously described in Section 7.2.

7.10 F Results for $K^+ + \Sigma^0$

Here results for F for $K^+ + \Sigma^0$ are presented. The models again are the KAON-MAID, Bonn-Gatchina, and Ghent models, previously described in Sections 1.7.1, 1.7.2, 1.7.3, respectively. There are no previous experimental data and this would be the first results for this observable and can be seen in Figs. 7.16 and 7.17. The first and last energy bins are binned in 100 MeV due to low statistics and the energy bins in between are binned in 50 MeV. At lower energies, $W < 1900$ MeV, there is some agreement between the data and the Ghent-RPR model for values of $\cos\theta_K^{cm}$ greater than zero. At higher energies, $W > 2075$ MeV, there is some agreement between the data and the KAON-MAID model in the forward angle. At the higher energies, there is not enough statistics in the backward angles to obtain a measurement of the asymmetry.

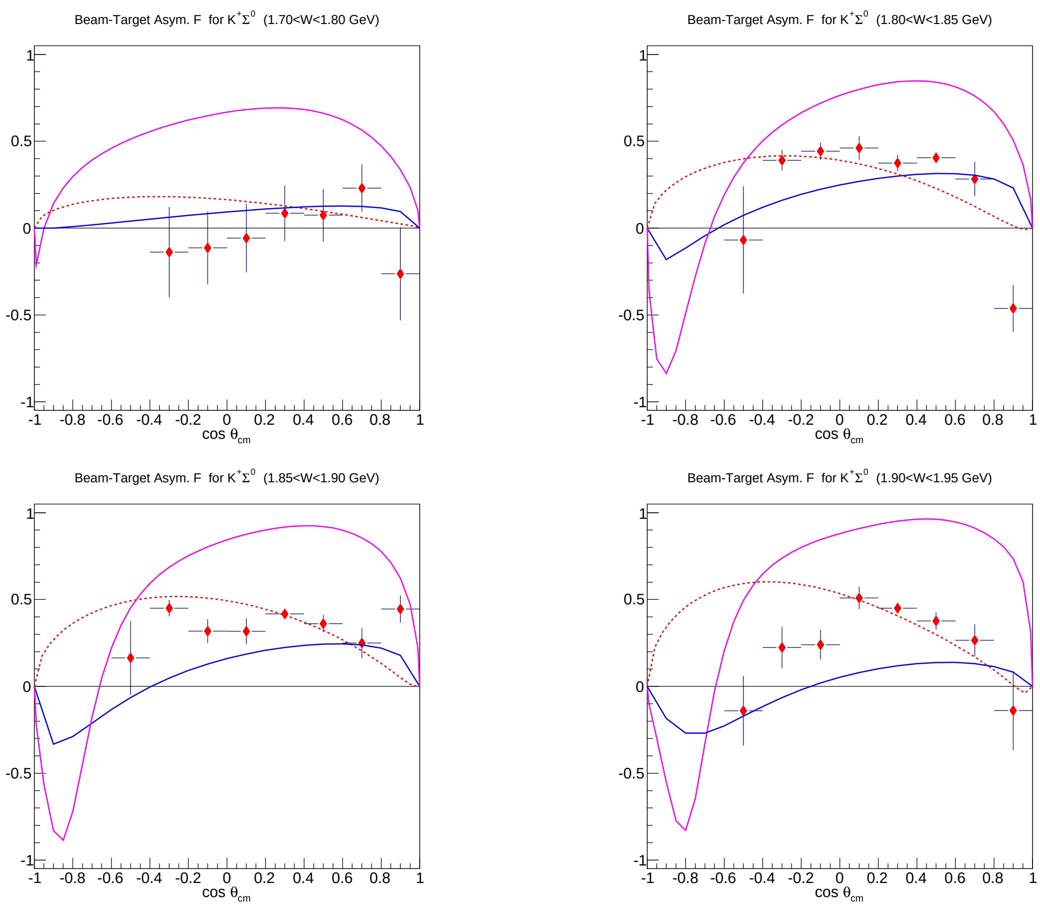

Figure 7.16: F asymmetry for $\gamma p \to K^+\Sigma^0$ for $W = 1700$ to 1950 MeV. Red diamond data points are from this analysis and include only statistical errors, the dashed red model curve is from RPR-Ghent, the solid blue model curve is from KAON-MAID, and the solid magenta model curve is from BOGA, all data and models are previously described in Section 7.2.

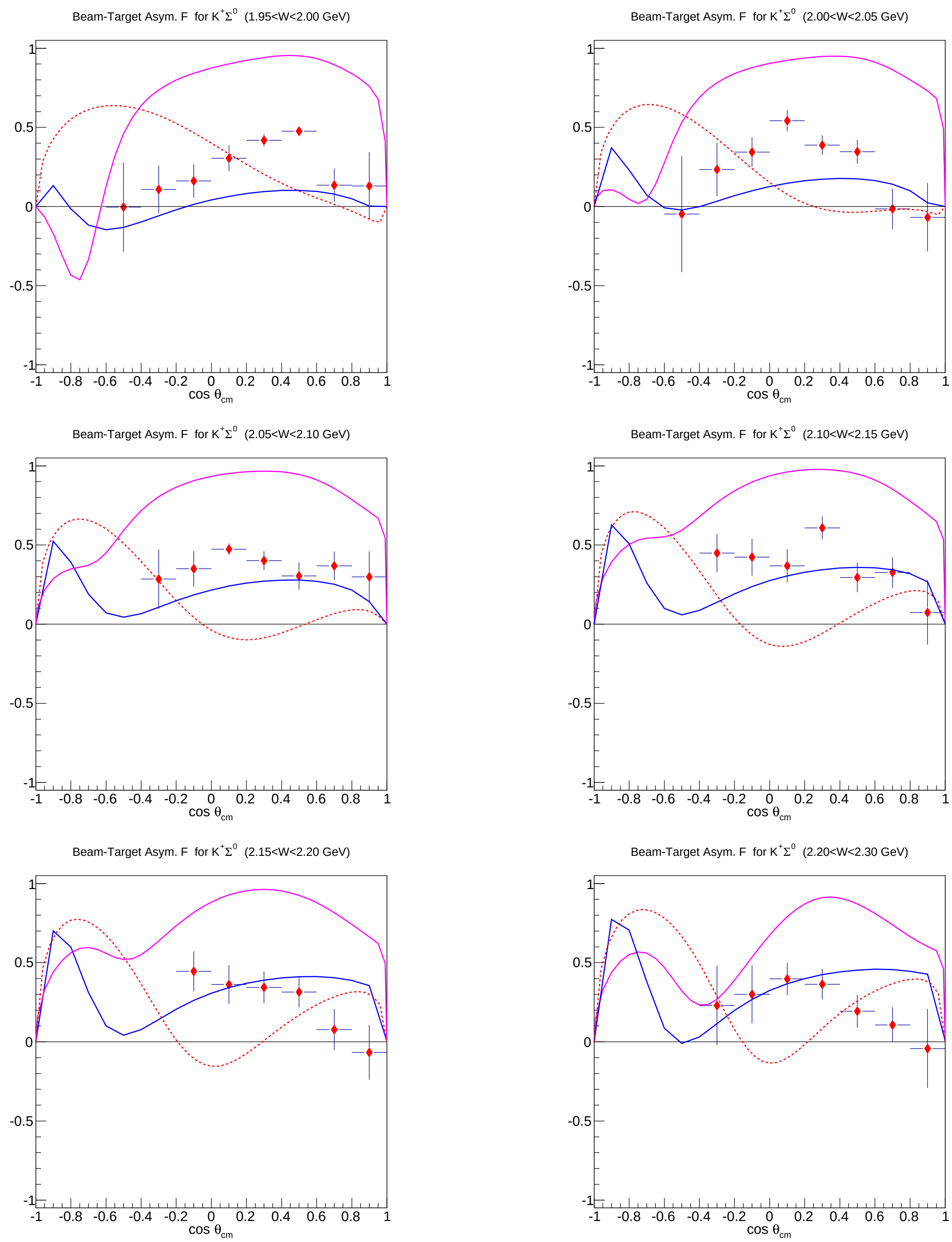

Figure 7.17: F asymmetry for $\gamma p \rightarrow K^+\Sigma^0$ for $W = 1950$ to 2300 MeV. Red diamond data points are from this analysis and include only statistical errors, the dashed red model curve is from RPR-Ghent, the solid blue model curve is from KAON-MAID, and the solid magenta model curve is from BOGA, all data and models are previously described in Section 7.2.

7.11 Summary

This chapter has showed results for the T, T_x, T_z, and F asymmetries for $\gamma p \rightarrow K^+\Lambda$ and $\gamma p \rightarrow K^+\Sigma^0$ over wide angular ranges and wide energy ranges. Never before have results for these asymmetries been obtained with this binning or to this high statistical precision. These results are indeed the most precise as of now and can offer significant impact on future measurements and models. Although T is not in complete agreement with GRAAL, some agreement does occur in energy bins W between 1875 to 1925 MeV. The impact of these results will be discussed next, which includes but is not limited to providing answers to the missing resonances of the spectrum.

Chapter 8

Conclusion

This analysis described the selection of both $\gamma\, p \to K^+ + \Lambda$ and $K^+ + \Sigma^0$ events and the extraction of the polarization observables T, T_x, T_z, and F from CLAS data produced from the transversely polarized butanol target FROST. This work was performed at Jefferson Lab and the analysis used data collected during the g9b experiment. A circularly polarized photon beam was produced by incoherent bremsstrahlung and the reaction products were detected in CLAS. The events were selected using the missing mass technique and polarization observables were extracted using the moment method. The uncertainty associated with the analysis has been described. Never before have results been obtained over such a large kinematic range for T, T_x, T_z, and F and with such precision. These results will no doubt have a substantial impact on the world database and will help to fix parameters in the theoretical models associated therewith.

8.1 Discussion of the Presented Results

As previously mentioned, these results are over a large kinematic range. By presenting polarization observable measurements for T, T_x, T_z, and F for $\gamma p \to K^+\Lambda$ and $\gamma p \to K^+\Sigma^0$ a more accurate PWA can be performed. Previous PWA had only a few polarization data to utilize and some with low statistics or small energy ranges. By using the data presented in this analysis, the PWA will be more detailed and hopefully information about the 'missing resonances' can be obtained. Strong deviations of model predictions from the measured asymmetries may give hints for additional strength in specific partial waves, which might be accounted for by including additional resonances in the fit.

Coupling strength of resonant states cannot be directly extracted from this data. However, it is expected that with the presentation of this data, the models of Bonn-Gatchina [17], KAON-MAID [16], and Ghent [117] will be updated by incorporating these data. It is unclear at this time, whether or not the models will provide useful information regarding certain resonances.

With regards to the previously measured observables, for example T by GRAAL, one must admit there is a discrepancy in lower energy bins. GRAAL did not have a polarized target, but instead utilized the properties of polarization observables and their dependency upon one another in order to extract T. At GRAAL T was extracted together with O_x and O_z in a combined fit. Inaccuracy in the measurement of any of these observables would have resulted in an inaccurate T asymmetry. The data of this analysis are consistent within error bars with the T asymmetry measured by Bonn, where the experimental conditions were similar. This analysis, on the other hand, suffers from low statistics in many W and $\cos\theta$ bins and a systematic uncertainty dominated by fit quality and normalization concerns. However, it is clear that more systematic studies of these data will have to be performed in order to have final results for publication.

8.2 Outlook

The FROST experiment was the first experiment with a transversely polarized proton target in a large acceptance detector. For the $\gamma\, p \rightarrow K^+ + \Lambda$ and $K^+ + \Sigma^0$ reaction channels, it is possible to measure all 16 polarization observables. This work alone has determined the T, T_x, T_z, and F observables. C_x and C_z were previously published by Bradford et al. [48] and P and $d\sigma/d\Omega$ were also previously published by McCracken et al. [43]. Although not published, a CLAS thesis has determined preliminary results for the E, L_x, and L_z observables [110]. Another CLAS thesis yet to be published has also measured the Σ and G observables [111]. It is also possible to extract the H observable from the FROST data, but this requires a more in-depth analysis due to the use of a linearly polarized beam.

8.3 Summary

The results presented in this analysis will likely have an impact on models describing the reactions $\gamma p \rightarrow K^+\Lambda$ and $\gamma p \rightarrow K^+\Sigma^0$. These results are an obvious step towards a 'complete set' of measurements for $K^+ + \Lambda$ and $K^+ + \Sigma^0$ channels. The PWA will, no doubt, be constrained by these results.

Appendix A

Target Polarization per Run for g9b

Table A.1: Target polarization per run

Run Number	Target Pol.	Fit Error
62207	0.8292	0.0200
62209	0.8290	0.0200
62211	0.8278	0.0200
62212	0.8269	0.0200
62213	0.8267	0.0200
62214	0.8265	0.0200
62215	0.8257	0.0200
62216	0.8247	0.0200
62217	0.8245	0.0200
62218	0.8241	0.0143
62220	0.8231	0.0143
62225	0.8211	0.0142
62226	0.8205	0.0142
62227	0.8198	0.0142
62230	0.8188	0.0143
62231	0.8188	0.0142
62232	0.8182	0.0142
62233	0.8175	0.0142
62240	0.8167	0.0142
62241	0.8159	0.0142
62242	0.8152	0.0142
62243	0.8146	0.0141
62246	0.8140	0.0141

Run Number	Target Pol.	Fit Error
62247	0.8131	0.0142
62248	0.8126	0.0141
62249	0.8121	0.0141
62252	0.8117	0.0141
62253	0.8114	0.0141
62254	0.8105	0.0141
62256	0.8102	0.0141
62257	0.8095	0.0140
62258	0.8088	0.0140
62262	0.8085	0.0140
62263	0.8078	0.0140
62264	0.8071	0.0141
62267	0.8063	0.0140
62268	0.8058	0.0140
62271	0.8050	0.0139
62280	0.8039	0.0139
62281	0.8038	0.0139
62282	0.8028	0.0139
62283	0.8019	0.0139
62287	0.8013	0.0139
62288	0.8010	0.0138
62289	0.8007	0.0138

Run Number	Target Pol.	Fit Error
62298	-0.8607	0.0158
62299	-0.8591	0.0161
62300	-0.8575	0.0163
62301	-0.8565	0.0163
62304	-0.8561	0.0159
62306	-0.8541	0.0160
62308	-0.8525	0.0159
62311	-0.8516	0.0161
62312	-0.8519	0.0157
62314	-0.8505	0.0158
62316	-0.8497	0.0156
62317	-0.8488	0.0155
62321	-0.8475	0.0156
62322	-0.8466	0.0155
62323	-0.8455	0.0154
62324	-0.8443	0.0155
62328	-0.8415	0.0151
62329	-0.8409	0.0151
62330	-0.8403	0.0151
62332	-0.8383	0.0074
62333	-0.8373	0.0111
62334	-0.8363	0.0148
62335	-0.8350	0.0149
62336	-0.8343	0.0148
62337	-0.8329	0.0148
62338	-0.8318	0.0147
62339	-0.8264	0.0144
62341	-0.8220	0.0141
62342	-0.8204	0.0141
62343	-0.8191	0.0141
62344	-0.8178	0.0140
62346	-0.8169	0.0140
62347	-0.8163	0.0140
62348	-0.8152	0.0140
62349	-0.8142	0.0140
62351	-0.8134	0.0140
62352	-0.8123	0.0140
62353	-0.8112	0.0139
62354	-0.8101	0.0139

Run Number	Target Pol.	Fit Error
62356	-0.8092	0.0139
62357	-0.8085	0.0139
62358	-0.8074	0.0139
62362	-0.8048	0.0139
62363	-0.8048	0.0139
62364	-0.8039	0.0139
62366	-0.8023	0.0138
62367	-0.8018	0.0139
62368	-0.8007	0.0138
62369	-0.8001	0.0138
62371	-0.7990	0.0138
62372	-0.7986	0.0138
62374	0.7915	0.0158
62375	0.7906	0.0161
62376	0.7885	0.0168
62378	0.7875	0.0170
62379	0.7866	0.0170
62380	0.7864	0.0168
62381	0.7853	0.0168
62383	0.7844	0.0167
62384	0.7837	0.0166
62385	0.7833	0.0164
62386	0.7826	0.0165
62387	0.7824	0.0163
62388	0.7822	0.0161
62389	0.7815	0.0161
62390	0.7808	0.0161
62392	0.7802	0.0160
62393	0.7795	0.0160
62394	0.7791	0.0158
62395	0.7778	0.0157
62398	0.7767	0.0153
62399	0.7766	0.0152
62400	0.7759	0.0153
62402	0.7754	0.0152
62403	0.7748	0.0152
62404	0.7744	0.0151
62406	0.7736	0.0150
62407	0.7732	0.0149

Run Number	Target Pol.	Fit Error
62408	0.7724	0.0149
62409	0.7719	0.0148
62410	0.7716	0.0148
62411	0.7711	0.0147
62412	0.7703	0.0147
62417	0.7692	0.0146
62419	0.7684	0.0143
62420	0.7678	0.0143
62424	0.7676	0.0139
62425	0.7664	0.0141
62427	0.7659	0.0139
62428	0.7655	0.0138
62429	0.7649	0.0138
62430	0.7645	0.0137
62432	0.7637	0.0137
62438	0.7625	0.0137
62439	0.7620	0.0137
62440	0.7613	0.0137
62441	0.7609	0.0136
62443	0.7604	0.0135
62444	0.7596	0.0136
62445	0.7594	0.0136
62446	0.7590	0.0135
62448	0.7583	0.0135
62449	0.7579	0.0135
62450	0.7572	0.0134
62451	0.7568	0.0134
62453	0.7561	0.0133
62454	0.7543	0.0134
62455	0.3755	0.0067
62456	0.7528	0.0135
62458	0.7524	0.0135
62459	0.7518	0.0135
62460	0.7510	0.0135
62461	0.7507	0.0134
62463	0.3760	0.0065
62464	0.7520	0.0130
62504	-0.8109	0.0158
62505	-0.8110	0.0156

Run Number	Target Pol.	Fit Error
62506	-0.8102	0.0157
62507	-0.8096	0.0157
62508	-0.8091	0.0156
62510	-0.8088	0.0155
62512	-0.8081	0.0156
62513	-0.8075	0.0155
62515	-0.8071	0.0153
62516	-0.8066	0.0153
62517	-0.8062	0.0152
62518	-0.8058	0.0151
62520	-0.8052	0.0150
62521	-0.8049	0.0149
62525	-0.8041	0.0146
62526	-0.8034	0.0146
62527	-0.8028	0.0146
62529	-0.8026	0.0145
62530	-0.8020	0.0145
62531	-0.8012	0.0145
62532	-0.8005	0.0145
62534	-0.8005	0.0143
62536	-0.7997	0.0144
62538	-0.7990	0.0143
62539	-0.7989	0.0142
62540	-0.7984	0.0142
62541	-0.7986	0.0141
62543	-0.7980	0.0141
62544	-0.7979	0.0140
62545	-0.7976	0.0139
62546	-0.7969	0.0139
62548	-0.7963	0.0139
62549	-0.7962	0.0139
62550	-0.7956	0.0138
62551	-0.7951	0.0138
62553	-0.7946	0.0137
62554	-0.7941	0.0137
62555	-0.7937	0.0137
62556	-0.7933	0.0137
62559	-0.7923	0.0137
62560	-0.7921	0.0136

Run Number	Target Pol.	Fit Error
62561	-0.7915	0.0136
62562	-0.7910	0.0136
62564	-0.7906	0.0136
62565	-0.7900	0.0136
62566	-0.7897	0.0136
62567	-0.7893	0.0136
62569	-0.7886	0.0135
62570	-0.7883	0.0135
62573	-0.7880	0.0135
62574	-0.7876	0.0135
62575	-0.7874	0.0135
62577	-0.7870	0.0135
62578	-0.7866	0.0135
62579	-0.7861	0.0135
62580	-0.7855	0.0135
62582	-0.7851	0.0135
62584	-0.7845	0.0135
62585	-0.7841	0.0135
62587	-0.7832	0.0134
62588	-0.7831	0.0135
62589	-0.7825	0.0134
62591	-0.7821	0.0134
62592	-0.7815	0.0134
62593	-0.7811	0.0134
62594	-0.7806	0.0134
62596	-0.7794	0.0134
62597	-0.7785	0.0134
62599	-0.7779	0.0134
62601	-0.7774	0.0133
62602	-0.7767	0.0133
62603	-0.7764	0.0133
62604	-0.7757	0.0133
62609	0.8559	0.0156
62610	0.8534	0.0160
62612	0.8521	0.0161
62613	0.8509	0.0161
62614	0.8500	0.0159
62615	0.8493	0.0158
62620	0.8483	0.0156
62622	0.8468	0.0155

Run Number	Target Pol.	Fit Error
62624	0.8447	0.0152
62627	0.8429	0.0151
62628	0.8419	0.0151
62629	0.8400	0.0153
62630	0.8400	0.0149
62632	0.8380	0.0147
62633	0.8368	0.0144
62634	0.8360	0.0144
62635	0.8351	0.0143
62636	0.8343	0.0143
62638	0.8333	0.0143
62640	0.8322	0.0143
62641	0.8312	0.0143
62642	0.8300	0.0142
62643	0.8287	0.0142
62647	0.8276	0.0142
62652	0.8260	0.0142
62653	0.8255	0.0142
62656	0.8246	0.0142
62657	0.8238	0.0142
62658	0.8230	0.0142
62659	0.8220	0.0142
62661	0.8215	0.0142
62662	0.8203	0.0142
62665	0.8192	0.0142
62666	0.8184	0.0142
62667	0.8176	0.0142
62668	0.8167	0.0142
62670	0.8158	0.0141
62671	0.8150	0.0141
62676	0.8115	0.0140
62677	0.8101	0.0139
62678	0.8091	0.0139
62679	0.8081	0.0139
62681	0.8069	0.0139
62682	0.8059	0.0139
62683	0.8053	0.0139
62684	0.8043	0.0138
62685	0.8032	0.0138
62686	0.8021	0.0138

Run Number	Target Pol.	Fit Error
62687	0.8011	0.0138
62689	0.8002	0.0138
62690	0.7996	0.0137
62693	0.7989	0.0137
62694	0.7976	0.0137
62696	0.7967	0.0137
62697	0.7957	0.0137
62698	0.7945	0.0136
62699	0.7938	0.0136
62701	0.7929	0.0136
62702	0.7918	0.0136
62704	0.7899	0.0136
63508	0.7700	0.0900
63509	0.7300	0.0900
63510	0.7000	0.0800
63516	0.6800	0.0800
63518	0.6600	0.0700
63519	0.6500	0.0700
63523	0.6100	0.0600
63524	0.5900	0.0500
63525	0.5820	0.0520
63529	-0.5596	0.0173
63530	-0.5506	0.0165
63531	-0.5456	0.0151
63532	-0.5411	0.0135
63533	-0.5350	0.0115
63536	-0.5272	0.0086
63537	-0.5233	0.0072
63539	-0.5161	0.0053
63540	-0.5123	0.0045
63541	-0.5083	0.0041
63542	-0.5080	0.0057
63543	0.7419	0.0210
63544	0.7256	0.0222
63545	0.7164	0.0215
63546	0.7078	0.0203
63547	0.6958	0.0193
63549	0.6820	0.0163
63550	0.6707	0.0145
63551	0.6618	0.0135

Run Number	Target Pol.	Fit Error
63552	0.6517	0.0121
63553	0.6409	0.0108
63555	0.6302	0.0093
63557	0.6201	0.0082
63558	0.6100	0.0070
63559	0.6008	0.0061
63560	0.5906	0.0052
63561	0.5814	0.0047
63562	0.5725	0.0046
63563	0.5644	0.0046
63564	0.5565	0.0053
63566	-0.7033	0.0145
63567	-0.6978	0.0141
63568	-0.6925	0.0129
63569	-0.6849	0.0115
63570	-0.6797	0.0107
63571	-0.6749	0.0100
63572	-0.6682	0.0093
63573	-0.6624	0.0083
63574	-0.6567	0.0076
63575	-0.6496	0.0071
63576	-0.6437	0.0066
63577	-0.6390	0.0060
63578	-0.6338	0.0055
63580	-0.6216	0.0050
63581	-0.6419	0.0262
63582	-0.4833	0.1078
63583	0.4809	0.1008
63586	0.4798	0.0960
63588	0.4772	0.0840
63589	0.4745	0.0706
63590	0.4729	0.0604
63591	0.4718	0.0550
63592	0.4708	0.0509
63593	0.4690	0.0433
63594	0.4670	0.0356
63595	0.4651	0.0270
63596	0.4636	0.0197
63597	0.4621	0.0133
63598	0.4606	0.0073

Appendix B

Asymmetry Results for $K^+ + \Lambda$ and $K^+ + \Sigma^0$

Table B.1: T asymmetry for $\gamma p \rightarrow K^+ + \Lambda$

W (GeV)	E_γ (GeV)	$\cos\theta_{cm}$	T	Statistical Error
1.675	1.024	-0.3	-0.235	0.157
1.675	1.024	-0.1	-0.535	0.086
1.675	1.024	0.1	-0.215	0.116
1.675	1.024	0.3	-0.410	0.110
1.675	1.024	0.5	-0.467	0.078
1.675	1.024	0.7	-0.447	0.082
1.725	1.115	-0.5	-0.361	0.146
1.725	1.115	-0.3	-0.442	0.095
1.725	1.115	-0.1	-0.394	0.082
1.725	1.115	0.1	-0.443	0.068
1.725	1.115	0.3	-0.618	0.045
1.725	1.115	0.5	-0.414	0.052
1.725	1.115	0.7	-0.390	0.063
1.725	1.115	0.9	-0.350	0.137
1.775	1.208	-0.5	-0.193	0.147
1.775	1.208	-0.3	-0.199	0.111
1.775	1.208	-0.1	-0.511	0.061
1.775	1.208	0.1	-0.493	0.061
1.775	1.208	0.3	-0.653	0.036
1.775	1.208	0.5	-0.671	0.035
1.775	1.208	0.7	-0.402	0.055
1.775	1.208	0.9	-0.712	0.128
1.825	1.304	-0.5	-0.212	0.134
1.825	1.304	-0.3	-0.081	0.097
1.825	1.304	-0.1	-0.293	0.067
1.825	1.304	0.1	-0.442	0.061
1.825	1.304	0.3	-0.605	0.040
1.825	1.304	0.5	-0.592	0.041
1.825	1.304	0.7	-0.457	0.051
1.825	1.304	0.9	-0.302	0.165
1.875	1.402	-0.7	0.227	0.170
1.875	1.402	-0.5	0.240	0.117
1.875	1.402	-0.3	0.021	0.089
1.875	1.402	-0.1	-0.108	0.066
1.875	1.402	0.1	-0.260	0.069
1.875	1.402	0.3	-0.446	0.046
1.875	1.402	0.5	-0.696	0.033
1.875	1.402	0.7	-0.581	0.044
1.875	1.402	0.9	-0.390	0.134
1.925	1.503	-0.7	0.771	0.088
1.925	1.503	-0.5	0.736	0.078
1.925	1.503	-0.3	0.640	0.063
1.925	1.503	-0.1	-0.144	0.075
1.925	1.503	0.1	-0.275	0.081

Table B.2: T asymmetry for $\gamma p \rightarrow K^+ + \Lambda$ (continued).

W (GeV)	E_γ (GeV)	$\cos\theta_{cm}$	T	Statistical Error
1.925	1.503	0.3	-0.291	0.054
1.925	1.503	0.5	-0.460	0.047
1.925	1.503	0.7	-0.727	0.035
1.925	1.503	0.9	0.095	0.123
1.975	1.607	-0.7	0.735	0.081
1.975	1.607	-0.5	0.744	0.088
1.975	1.607	-0.3	0.399	0.101
1.975	1.607	-0.1	0.069	0.092
1.975	1.607	0.1	-0.254	0.079
1.975	1.607	0.3	-0.497	0.049
1.975	1.607	0.5	-0.643	0.039
1.975	1.607	0.7	-0.809	0.026
1.975	1.607	0.9	-0.269	0.110
2.025	1.713	-0.7	0.766	0.082
2.025	1.713	-0.5	0.580	0.178
2.025	1.713	-0.3	0.183	0.171
2.025	1.713	-0.1	0.250	0.115
2.025	1.713	0.1	-0.362	0.089
2.025	1.713	0.3	-0.477	0.059
2.025	1.713	0.5	-0.567	0.050
2.025	1.713	0.7	-0.615	0.053
2.025	1.713	0.9	-0.134	0.126
2.075	1.822	-0.7	0.691	0.150
2.075	1.822	-0.3	0.463	0.176
2.075	1.822	-0.1	-0.175	0.135
2.075	1.822	0.1	-0.660	0.074
2.075	1.822	0.3	-0.645	0.051

W (GeV)	E_γ (GeV)	$\cos\theta_{cm}$	T	Statistical Error
2.075	1.822	0.5	-0.609	0.050
2.075	1.822	0.7	-0.519	0.060
2.075	1.822	0.9	-0.597	0.090
2.125	1.934	-0.7	-0.211	0.390
2.125	1.934	-0.3	0.575	0.171
2.125	1.934	-0.1	0.339	0.178
2.125	1.934	0.1	-0.199	0.127
2.125	1.934	0.3	-0.554	0.072
2.125	1.934	0.5	-0.467	0.067
2.125	1.934	0.7	-0.466	0.067
2.125	1.934	0.9	-0.803	0.061
2.175	2.048	-0.7	0.032	0.259
2.175	2.048	-0.5	0.974	0.142
2.175	2.048	-0.3	0.486	0.262
2.175	2.048	-0.1	0.144	0.222
2.175	2.048	0.1	-0.231	0.149
2.175	2.048	0.3	-0.251	0.115
2.175	2.048	0.5	-0.946	0.029
2.175	2.048	0.7	-0.565	0.062
2.175	2.048	0.9	-0.289	0.135
2.250	2.225	-0.7	-0.091	0.305
2.250	2.225	-0.3	1.078	0.137
2.250	2.225	-0.1	1.096	0.177
2.250	2.225	0.1	-0.720	0.074
2.250	2.225	0.3	-0.572	0.083
2.250	2.225	0.5	-0.611	0.065
2.250	2.225	0.7	-0.591	0.078

Table B.3: F asymmetry for $\gamma p \to K^+ + \Lambda$

W (GeV)	E_γ (GeV)	$\cos\theta_{cm}$	F	Statistical Error	W (GeV)	E_γ (GeV)	$\cos\theta_{cm}$	F	Statistical Error
1.675	1.024	-0.1	-0.225	0.173	1.975	1.607	-0.7	0.343	0.157
1.675	1.024	0.1	-0.162	0.196	1.975	1.607	-0.5	0.360	0.151
1.675	1.024	0.3	-0.084	0.234	1.975	1.607	-0.3	0.275	0.146
1.675	1.024	0.5	-0.452	0.150	1.975	1.607	-0.1	0.440	0.041
1.675	1.024	0.7	-0.137	0.180	1.975	1.607	0.1	0.244	0.110
1.725	1.115	-0.3	-0.107	0.197	1.975	1.607	0.3	0.120	0.090
1.725	1.115	-0.1	0.012	0.175	1.975	1.607	0.5	0.124	0.086
1.725	1.115	0.1	-0.045	0.151	1.975	1.607	0.7	-0.186	0.085
1.725	1.115	0.3	-0.165	0.114	1.975	1.607	0.9	-0.301	0.134
1.725	1.115	0.5	-0.128	0.103	2.025	1.713	-0.7	-0.348	0.183
1.725	1.115	0.7	-0.148	0.115	2.025	1.713	-0.5	0.755	0.440
1.725	1.115	0.9	-0.349	0.086	2.025	1.713	-0.3	0.342	0.182
1.775	1.208	-0.5	0.270	0.201	2.025	1.713	-0.1	0.318	0.131
1.775	1.208	-0.3	0.348	0.090	2.025	1.713	0.1	0.343	0.106
1.775	1.208	-0.1	0.121	0.136	2.025	1.713	0.3	0.242	0.093
1.775	1.208	0.1	0.0120	0.142	2.025	1.713	0.5	-0.048	0.101
1.775	1.208	0.3	-0.163	0.099	2.025	1.713	0.7	-0.255	0.096
1.775	1.208	0.5	-0.172	0.093	2.025	1.713	0.9	-0.349	0.126
1.775	1.208	0.7	-0.183	0.102	2.075	1.822	-0.3	0.216	0.273
1.775	1.208	0.9	0.015	0.317	2.075	1.822	-0.1	0.309	0.160
1.825	1.304	-0.5	0.610	0.259	2.075	1.822	0.1	0.392	0.108
1.825	1.304	-0.3	0.594	0.170	2.075	1.822	0.3	0.342	0.081
1.825	1.304	-0.1	0.269	0.092	2.075	1.822	0.5	0.101	0.098
1.825	1.304	0.1	0.133	0.118	2.075	1.822	0.7	-0.136	0.104
1.825	1.304	0.3	0.153	0.091	2.075	1.822	0.9	-0.558	0.086
1.825	1.304	0.5	0.002	0.096	2.125	1.934	-0.3	0.089	0.364
1.825	1.304	0.7	-0.099	0.101	2.125	1.934	-0.1	0.420	0.143
1.825	1.304	0.9	-0.576	0.257	2.125	1.934	0.1	0.570	0.097
1.875	1.402	-0.7	0.448	0.099	2.125	1.934	0.3	0.392	0.087
1.875	1.402	-0.5	0.643	0.236	2.125	1.934	0.5	0.144	0.109
1.875	1.402	-0.3	0.301	0.107	2.125	1.934	0.7	-0.216	0.099
1.875	1.402	-0.1	0.375	0.052	2.125	1.934	0.9	-0.505	0.055
1.875	1.402	0.1	0.359	0.066	2.175	2.048	-0.1	0.333	0.268
1.875	1.402	0.3	0.098	0.088	2.175	2.048	0.1	0.503	0.077
1.875	1.402	0.5	0.062	0.092	2.175	2.048	0.3	0.315	0.133
1.875	1.402	0.7	-0.008	0.096	2.175	2.048	0.5	0.144	0.132
1.875	1.402	0.9	-0.580	0.215	2.175	2.048	0.7	-0.128	0.114
1.925	1.503	-0.7	0.464	0.094	2.175	2.048	0.9	-0.419	0.099
1.925	1.503	-0.5	0.387	0.106	2.225	2.165	0.1	0.560	0.091
1.925	1.503	-0.3	0.539	0.122	2.225	2.165	0.3	0.392	0.135
1.925	1.503	-0.1	0.326	0.082	2.225	2.165	0.5	0.257	0.145
1.925	1.503	0.1	0.266	0.107	2.225	2.165	0.7	0.040	0.149
1.925	1.503	0.3	0.095	0.091	2.275	2.285	0.1	0.330	0.236
1.925	1.503	0.5	-0.064	0.089	2.275	2.285	0.3	0.491	0.129
1.925	1.503	0.7	-0.340	0.063	2.275	2.285	0.5	0.133	0.184
1.925	1.503	0.9	-0.252	0.166	2.275	2.285	0.7	-0.092	0.423

Table B.4: T_x asymmetry for $\gamma p \rightarrow K^+ + \Lambda$

W (GeV)	E_γ (GeV)	$\cos\theta_{cm}$	T_x	Statistical Error
1.7	1.069	-0.5	-0.694	0.186
1.7	1.069	-0.3	-0.038	0.145
1.7	1.069	-0.1	-0.190	0.114
1.7	1.069	0.1	-0.175	0.104
1.7	1.069	0.3	-0.377	0.091
1.7	1.069	0.5	0.239	0.079
1.7	1.069	0.7	-0.154	0.083
1.7	1.069	0.9	0.730	0.157
1.775	1.208	-0.3	-0.035	0.174
1.775	1.208	-0.1	-0.556	0.111
1.775	1.208	0.1	-0.373	0.114
1.775	1.208	0.3	-0.501	0.087
1.775	1.208	0.5	0.126	0.090
1.775	1.208	0.7	0.361	0.097
1.775	1.208	0.9	-0.296	0.239
1.825	1.304	-0.7	0.182	0.41
1.825	1.304	-0.5	-0.441	0.195
1.825	1.304	-0.3	-0.132	0.149
1.825	1.304	-0.1	-0.358	0.11
1.825	1.304	0.1	-0.716	0.098
1.825	1.304	0.3	-0.203	0.087
1.825	1.304	0.5	0.040	0.086
1.825	1.304	0.7	-0.066	0.093
1.875	1.402	-0.7	-0.578	0.26
1.875	1.402	-0.5	-0.410	0.168
1.875	1.402	-0.3	-0.675	0.114
1.875	1.402	-0.1	-0.791	0.087
1.875	1.402	0.1	-0.712	0.091
1.875	1.402	0.3	-0.610	0.070
1.875	1.402	0.5	-0.101	0.088
1.875	1.402	0.7	0.213	0.088
1.875	1.402	0.9	0.933	0.169
1.925	1.503	-0.7	0.089	0.247
1.925	1.503	-0.5	0.533	0.183
1.925	1.503	-0.3	-0.455	0.145
1.925	1.503	-0.1	-0.725	0.095
1.925	1.503	0.1	-0.691	0.102
1.925	1.503	0.3	-0.265	0.086
1.925	1.503	0.5	0.049	0.089

W (GeV)	E_γ (GeV)	$\cos\theta_{cm}$	T_x	Statistical Error
1.925	1.503	0.7	0.811	0.078
1.925	1.503	0.9	-0.907	0.136
1.975	1.607	-0.5	-0.314	0.229
1.975	1.607	-0.3	-0.504	0.168
1.975	1.607	-0.1	-0.426	0.133
1.975	1.607	0.1	-0.325	0.121
1.975	1.607	0.3	-0.499	0.084
1.975	1.607	0.5	0.110	0.091
1.975	1.607	0.7	0.492	0.085
1.975	1.607	0.9	0.435	0.167
2.025	1.713	-0.7	-0.087	0.289
2.025	1.713	-0.5	-0.388	0.337
2.025	1.713	-0.1	-0.638	0.158
2.025	1.713	0.1	-0.174	0.142
2.025	1.713	0.3	-0.395	0.101
2.025	1.713	0.5	0.061	0.104
2.025	1.713	0.7	-0.052	0.108
2.025	1.713	0.9	0.624	0.169
2.075	1.822	-0.7	0.424	0.359
2.075	1.822	-0.3	-0.583	0.268
2.075	1.822	-0.1	-0.67	0.195
2.075	1.822	0.1	-0.827	0.132
2.075	1.822	0.3	-0.284	0.115
2.075	1.822	0.5	-0.140	0.107
2.075	1.822	0.7	-0.178	0.105
2.075	1.822	0.9	-0.330	0.170
2.125	1.934	-0.3	0.388	0.318
2.125	1.934	0.1	-1.044	0.119
2.125	1.934	0.3	-0.299	0.143
2.125	1.934	0.5	-0.260	0.119
2.125	1.934	0.7	0.051	0.112
2.125	1.934	0.9	0.383	0.212
2.200	2.106	-0.7	0.442	0.301
2.200	2.106	-0.3	-0.914	0.233
2.200	2.106	-0.1	-0.751	0.220
2.200	2.106	0.5	-0.931	0.078
2.200	2.106	0.7	-0.193	0.101
2.200	2.106	0.9	0.919	0.134

Table B.5: T_z asymmetry for $\gamma p \rightarrow K^+ + \Lambda$

W (GeV)	E_γ (GeV)	$\cos\theta_{cm}$	T_z	Statistical Error
1.75	1.161	-0.7	0.617	0.346
1.75	1.161	-0.5	0.592	0.152
1.75	1.161	-0.3	0.523	0.113
1.75	1.161	-0.1	0.267	0.095
1.75	1.161	0.1	-0.004	0.088
1.75	1.161	0.3	-0.201	0.069
1.75	1.161	0.5	-0.538	0.059
1.75	1.161	0.7	-0.240	0.074
1.825	1.304	-0.1	0.930	0.076
1.825	1.304	0.1	0.237	0.112
1.825	1.304	0.3	0.414	0.084
1.825	1.304	0.5	-0.104	0.087
1.825	1.304	0.7	-0.105	0.093
1.825	1.304	0.9	-0.809	0.209
1.875	1.402	-0.7	1.003	0.198
1.875	1.402	0.1	0.630	0.096
1.875	1.402	0.3	0.568	0.073
1.875	1.402	0.5	0.396	0.085
1.875	1.402	0.7	-0.106	0.086
1.925	1.503	-0.7	0.128	0.242
1.925	1.503	-0.5	0.756	0.178
1.925	1.503	-0.3	1.02	0.093
1.925	1.503	-0.1	0.889	0.086
1.925	1.503	0.1	1.030	0.081
1.925	1.503	0.3	0.992	0.059
1.925	1.503	0.5	0.116	0.087
1.925	1.503	0.7	-0.277	0.087

W (GeV)	E_γ (GeV)	$\cos\theta_{cm}$	T_z	Statistical Error
1.925	1.503	0.9	-0.682	0.143
1.975	1.607	-0.7	-0.209	0.237
1.975	1.607	-0.5	-0.624	0.191
1.975	1.607	-0.3	1.039	0.096
1.975	1.607	0.1	0.955	0.083
1.975	1.607	0.3	0.707	0.078
1.975	1.607	0.5	0.110	0.090
1.975	1.607	0.7	-0.801	0.07
1.975	1.607	0.9	-0.407	0.164
2.025	1.713	-0.7	-0.406	0.286
2.025	1.713	-0.5	-0.204	0.338
2.025	1.713	-0.1	0.493	0.169
2.025	1.713	0.3	0.968	0.072
2.025	1.713	0.5	0.496	0.096
2.025	1.713	0.7	-0.316	0.103
2.075	1.822	-0.5	-0.133	0.446
2.075	1.822	0.1	0.531	0.152
2.075	1.822	0.5	-0.154	0.108
2.075	1.822	0.7	-0.492	0.098
2.075	1.822	0.9	-0.837	0.14
2.150	1.991	-0.3	0.123	0.303
2.150	1.991	-0.1	-0.300	0.222
2.150	1.991	0.3	0.999	0.080
2.150	1.991	0.5	0.334	0.091
2.150	1.991	0.7	-0.323	0.083
2.150	1.991	0.9	-0.461	0.133

Table B.6: T asymmetry for $\gamma p \rightarrow K^+ + \Sigma^0$

W (GeV)	E_γ (GeV)	$\cos\theta_{cm}$	T	Statistical Error
1.75	1.161	-0.5	0.331	0.231
1.75	1.161	-0.3	0.731	0.091
1.75	1.161	-0.1	0.532	0.105
1.75	1.161	0.1	0.284	0.111
1.75	1.161	0.3	0.129	0.087
1.75	1.161	0.5	0.097	0.081
1.75	1.161	0.7	0.377	0.082
1.75	1.161	0.9	0.672	0.112
1.825	1.304	-0.7	-0.428	0.330
1.825	1.304	-0.5	0.806	0.072
1.825	1.304	-0.3	0.091	0.102
1.825	1.304	-0.1	0.081	0.087
1.825	1.304	0.1	0.214	0.088
1.825	1.304	0.3	-0.068	0.062
1.825	1.304	0.5	0.015	0.065
1.825	1.304	0.7	0.182	0.073
1.825	1.304	0.9	0.062	0.187
1.875	1.402	-0.5	0.158	0.125
1.875	1.402	-0.3	0.110	0.081
1.875	1.402	-0.1	-0.160	0.061
1.875	1.402	0.1	0.203	0.066
1.875	1.402	0.3	-0.020	0.049
1.875	1.402	0.5	0.141	0.053
1.875	1.402	0.7	0.031	0.064
1.875	1.402	0.9	-0.082	0.144
1.925	1.503	-0.7	0.200	0.321
1.925	1.503	-0.5	-0.060	0.123
1.925	1.503	-0.3	0.018	0.084
1.925	1.503	-0.1	0.124	0.063
1.925	1.503	0.1	-0.097	0.067
1.925	1.503	0.3	-0.095	0.050
1.925	1.503	0.5	0.030	0.055
1.925	1.503	0.7	0.183	0.068
1.925	1.503	0.9	0.441	0.122
1.975	1.607	-0.7	0.880	0.063
1.975	1.607	-0.5	-0.652	0.101
1.975	1.607	-0.3	-0.436	0.080
1.975	1.607	-0.1	-0.006	0.075
1.975	1.607	0.1	-0.134	0.067
1.975	1.607	0.3	-0.039	0.056
1.975	1.607	0.5	0.152	0.059
1.975	1.607	0.7	0.318	0.064
1.975	1.607	0.9	-0.018	0.158

W (GeV)	E_γ (GeV)	$\cos\theta_{cm}$	T	Statistical Error
2.025	1.713	-0.5	-0.580	0.145
2.025	1.713	-0.3	-0.512	0.096
2.025	1.713	-0.1	-0.152	0.091
2.025	1.713	0.1	-0.546	0.065
2.025	1.713	0.3	-0.026	0.068
2.025	1.713	0.5	-0.059	0.068
2.025	1.713	0.7	0.468	0.065
2.025	1.713	0.9	0.100	0.144
2.075	1.822	-0.7	0.517	0.281
2.075	1.822	-0.5	-0.087	0.273
2.075	1.822	-0.3	-0.466	0.123
2.075	1.822	-0.1	-0.056	0.109
2.075	1.822	0.1	-0.210	0.084
2.075	1.822	0.3	0.103	0.070
2.075	1.822	0.5	0.293	0.067
2.075	1.822	0.7	0.203	0.088
2.075	1.822	0.9	-0.211	0.142
2.125	1.934	-0.7	0.839	0.080
2.125	1.934	-0.5	-0.132	0.246
2.125	1.934	-0.3	-0.377	0.139
2.125	1.934	-0.1	-0.490	0.111
2.125	1.934	0.1	-0.384	0.087
2.125	1.934	0.3	0.076	0.079
2.125	1.934	0.5	0.396	0.066
2.125	1.934	0.7	0.585	0.063
2.125	1.934	0.9	0.540	0.112
2.175	2.048	-0.7	0.645	0.199
2.175	2.048	-0.5	-0.530	0.220
2.175	2.048	-0.3	-0.711	0.087
2.175	2.048	-0.1	-0.676	0.093
2.175	2.048	0.1	-0.286	0.116
2.175	2.048	0.3	-0.140	0.094
2.175	2.048	0.5	-0.095	0.088
2.175	2.048	0.7	0.514	0.070
2.175	2.048	0.9	0.202	0.149
2.250	2.225	-0.7	-0.628	0.118
2.250	2.225	-0.3	-0.817	0.072
2.250	2.225	-0.1	-0.404	0.163
2.250	2.225	0.1	-0.353	0.094
2.250	2.225	0.3	-0.168	0.086
2.250	2.225	0.5	0.159	0.072
2.250	2.225	0.7	0.081	0.084
2.250	2.225	0.9	0.121	0.182

Table B.7: F asymmetry for $\gamma p \to K^+\Sigma^0$

W (GeV)	E_γ (GeV)	$\cos\theta_{cm}$	F	Statistical Error
1.675	1.024	0.3	0.039	0.425
1.725	1.115	0.7	0.462	0.305
1.775	1.208	-0.3	0.371	0.095
1.775	1.208	-0.1	0.632	0.296
1.775	1.208	0.1	0.396	0.038
1.775	1.208	0.3	0.237	0.137
1.775	1.208	0.5	0.661	0.229
1.775	1.208	0.7	0.299	0.118
1.775	1.208	0.9	-0.135	0.371
1.825	1.304	-0.5	-0.068	0.309
1.825	1.304	-0.3	0.390	0.059
1.825	1.304	-0.1	0.443	0.05
1.825	1.304	0.1	0.461	0.069
1.825	1.304	0.3	0.375	0.047
1.825	1.304	0.5	0.405	0.026
1.825	1.304	0.7	0.283	0.098
1.825	1.304	0.9	-0.463	0.135
1.875	1.402	-0.5	0.164	0.213
1.875	1.402	-0.3	0.450	0.047
1.875	1.402	-0.1	0.318	0.069
1.875	1.402	0.1	0.317	0.074
1.875	1.402	0.3	0.417	0.017
1.875	1.402	0.5	0.362	0.049
1.875	1.402	0.7	0.250	0.086
1.875	1.402	0.9	0.445	0.077
1.925	1.503	-0.5	-0.140	0.201
1.925	1.503	-0.3	0.224	0.119
1.925	1.503	-0.1	0.241	0.085
1.925	1.503	0.1	0.510	0.064
1.925	1.503	0.3	0.451	0.022
1.925	1.503	0.5	0.377	0.048
1.925	1.503	0.7	0.266	0.091
1.925	1.503	0.9	-0.139	0.228
1.975	1.607	-0.5	-0.003	0.283
1.975	1.607	-0.3	0.108	0.15
1.975	1.607	-0.1	0.162	0.106
1.975	1.607	0.1	0.304	0.081
1.975	1.607	0.3	0.418	0.037
1.975	1.607	0.5	0.476	0.018
1.975	1.607	0.7	0.135	0.105
1.975	1.607	0.9	0.130	0.214
2.025	1.713	-0.5	-0.048	0.366
2.025	1.713	-0.3	0.234	0.168
2.025	1.713	-0.1	0.344	0.094
2.025	1.713	0.1	0.542	0.067
2.025	1.713	0.3	0.388	0.061
2.025	1.713	0.5	0.346	0.076
2.025	1.713	0.7	-0.015	0.128
2.025	1.713	0.9	-0.068	0.216
2.075	1.822	-0.3	0.285	0.187
2.075	1.822	-0.1	0.350	0.113
2.075	1.822	0.1	0.473	0.036
2.075	1.822	0.3	0.401	0.059
2.075	1.822	0.5	0.305	0.087
2.075	1.822	0.7	0.369	0.090
2.075	1.822	0.9	0.299	0.161
2.125	1.934	-0.3	0.449	0.121
2.125	1.934	-0.1	0.423	0.116
2.125	1.934	0.1	0.368	0.105
2.125	1.934	0.3	0.608	0.072
2.125	1.934	0.5	0.295	0.094
2.125	1.934	0.7	0.326	0.098
2.125	1.934	0.9	0.074	0.204
2.175	2.048	-0.1	0.446	0.126
2.175	2.048	0.1	0.363	0.122
2.175	2.048	0.3	0.344	0.100
2.175	2.048	0.5	0.315	0.098
2.175	2.048	0.7	0.077	0.130
2.175	2.048	0.9	-0.067	0.172
2.225	2.165	0.1	0.602	0.097
2.225	2.165	0.3	0.499	0.061
2.225	2.165	0.5	0.313	0.123
2.225	2.165	0.7	0.129	0.136
2.225	2.165	0.9	-0.064	0.244
2.275	2.285	0.1	0.215	0.201
2.275	2.285	0.3	0.632	0.117
2.275	2.285	0.5	0.174	0.151
2.275	2.285	0.7	0.043	0.173

Table B.8: T_x asymmetry for $\gamma p \rightarrow K^+ + \Sigma^0$

W (GeV)	E_γ (GeV)	$\cos\theta_{cm}$	T_x	Statistical Error
1.8	1.255	-0.5	0.228	0.227
1.8	1.255	-0.3	-0.953	0.129
1.8	1.255	-0.1	0.182	0.108
1.8	1.255	0.1	-0.027	0.108
1.8	1.255	0.3	-0.213	0.082
1.8	1.255	0.5	-0.072	0.082
1.8	1.255	0.7	0.536	0.097
1.875	1.402	-0.3	0.229	0.127
1.875	1.402	0.1	-0.306	0.099
1.875	1.402	0.3	0.218	0.077
1.875	1.402	0.5	0.147	0.087
1.875	1.402	0.7	0.329	0.103
1.925	1.503	-0.5	0.468	0.190
1.925	1.503	-0.3	-0.953	0.130
1.925	1.503	-0.1	-0.464	0.095
1.925	1.503	0.1	-0.817	0.098
1.925	1.503	0.3	-0.055	0.079
1.925	1.503	0.5	-0.416	0.093
1.925	1.503	0.7	-0.125	0.108
1.925	1.503	0.9	0.760	0.210
1.975	1.607	-0.1	-0.156	0.114
1.975	1.607	0.1	0.348	0.105
1.975	1.607	0.3	0.564	0.086
1.975	1.607	0.5	-0.868	0.097

W (GeV)	E_γ (GeV)	$\cos\theta_{cm}$	T_x	Statistical Error
1.975	1.607	0.9	0.122	0.211
2.025	1.713	-0.5	0.812	0.312
2.025	1.713	-0.1	-0.494	0.138
2.025	1.713	0.1	0.281	0.127
2.025	1.713	0.3	-0.205	0.103
2.025	1.713	0.7	0.925	0.115
2.075	1.822	0.5	0.497	0.114
2.125	1.934	-0.3	0.910	0.241
2.125	1.934	0.1	0.443	0.154
2.125	1.934	0.3	0.747	0.125
2.125	1.934	0.5	-0.744	0.121
2.175	2.048	-0.5	-0.427	0.440
2.175	2.048	-0.1	-0.096	0.266
2.175	2.048	0.1	0.595	0.180
2.175	2.048	0.5	0.323	0.133
2.225	2.165	-0.3	0.913	0.396
2.225	2.165	-0.1	0.316	0.338
2.225	2.165	0.5	0.139	0.154
2.225	2.165	0.9	-0.603	0.295
2.275	2.285	0.1	-0.811	0.269
2.275	2.285	0.3	-0.182	0.260
2.275	2.285	0.5	-1.047	0.170
2.275	2.285	0.7	1.023	0.189

Table B.9: T_z asymmetry for $\gamma p \rightarrow K^+ + \Sigma^0$

W (GeV)	E_γ (GeV)	$\cos\theta_{cm}$	T_z	Statistical Error
1.75	1.161	-0.5	0.258	0.411
1.75	1.161	-0.3	-0.433	0.225
1.75	1.161	-0.1	0.392	0.179
1.75	1.161	0.5	-1.061	0.124
1.75	1.161	0.9	-0.898	0.346
1.85	1.352	-0.5	-0.622	0.159
1.85	1.352	-0.3	0.532	0.099
1.85	1.352	0.1	1.023	0.077
1.85	1.352	0.3	0.875	0.060
1.85	1.352	0.5	0.108	0.067
1.85	1.352	0.7	0.354	0.081
1.925	1.503	-0.5	-0.505	0.183
1.925	1.503	-0.3	-0.962	0.127
1.925	1.503	-0.1	0.667	0.097
1.925	1.503	0.3	0.027	0.080
1.925	1.503	0.7	0.392	0.107
1.975	1.607	-0.3	0.178	0.151
1.975	1.607	-0.1	0.799	0.111
1.975	1.607	0.1	0.479	0.104
1.975	1.607	0.3	0.460	0.085
1.975	1.607	0.9	0.909	0.226
2.025	1.713	-0.5	-0.486	0.330
2.025	1.713	0.3	-0.676	0.102
2.025	1.713	0.7	0.088	0.121
2.025	1.713	0.9	-0.449	0.213
2.075	1.822	-0.5	0.640	0.407
2.075	1.822	0.1	0.773	0.132
2.075	1.822	0.3	1.066	0.107
2.075	1.822	0.5	-0.319	0.114
2.075	1.822	0.7	0.639	0.132
2.075	1.822	0.9	0.710	0.206
2.125	1.934	0.1	-0.510	0.153
2.125	1.934	0.3	-0.595	0.126
2.125	1.934	0.5	-0.105	0.123
2.125	1.934	0.9	0.430	0.221
2.200	2.106	-0.7	-0.426	0.33
2.200	2.106	-0.5	0.999	0.294
2.200	2.106	-0.3	1.063	0.244
2.200	2.106	-0.1	0.720	0.206
2.200	2.106	0.3	0.573	0.118
2.200	2.106	0.5	0.029	0.103
2.200	2.106	0.7	-0.018	0.104
2.200	2.106	0.9	0.524	0.192

Bibliography

[1] M. Kaku, "QUANTUM FIELD THEORY. A Modern Introduction", New York, 1993.

[2] R.G. Edwards *et al.*, "Flavor structure of the excited baryon spectra from lattice QCD", Phys. Rev. D **87**, 054506 (2013).

[3] H. Fritzsch, "The history of QCD", CERN COURIER, Sept. 27, 2012.

[4] N. Bohr, "On the Constitution of Atoms and Molecules", Philosophical Magazine **6**, 26 (1913).

[5] K.A. Olive *et al.* (Particle Data Group), "2014 Review of Particle Physics", Chin. Phys. C **38**, 090001 (2014).

[6] M.E. McCracken, "A Study of $K^+\Lambda$ Photoproduction in the CLAS *g11a* Dataset: Differential Cross Section, Recoil Polarization, and a Partial-Wave Analysis", Carnegie Mellon University, Dec.22, 2008.

[7] S.U. Chung, J. Brose, R. Hackmann, E. Klempt, S. Spanier, and C. Strassburger, "Partial wave analysis in K-matrix formalism", Annalen der Physik **507**, 404 (1995).

[8] S. Capstick and W. Roberts, "Photo- and electroproduction of nonstrange baryon resonances in the relativized quark model", Phys. Rev. D **46**, 2864 (1992).

[9] S. Capstick and W. Roberts, "Quasi-two-body decays of nonstrange baryons", Phys. Rev. D **49**, 4570 (1994).

[10] S. Capstick and W. Roberts, "Strange decays of nonstrange baryons", Phys. Rev. D **58**, 074011 (1998).

[11] S. Capstick and W. Roberts, "Quark Models of Baryon Masses and Decays", Prog. Part. Nucl. Phys. **45**, 5241 (2000).

[12] R.E. Cutkosky and R.E. Hendrick, "Does the baryon spectrum reveal a diquark structure?", Phys. Rev. D **16**, 2902 (1977);

[13] D.B. Lichtenberg, W. Namgung, E. Predazzi, and J.G. Wills, "Baryon Masses in a Relativistic Quark–Diquark Model", Phys. Rev. Lett. **48**, 1653 (1982).

[14] M. Oettel, G. Hellstern, R. Alkofer, H. Reinhardt, "Octet and Decuplet Baryons in a Confining and Covariant Diquark-Quark Model", Phys. Rev. C **58**, 2459 (1998).

[15] J. Ferretti, A. Vassallo, and E. Santopinto, "Relativistic quark-diquark model of baryons", Phys. Rev. C **83**, 065204 (2011).

[16] T. Mart, C. Bennhold, H. Haberzettl, and L. Tiator, "Kaon-MAID". Available from http://www.kph.uni-mainz.de/MAID/kaon/kaonmaid.html.

[17] Bonn-Gatchina Partial-Wave Analysis. Available from http://pwa.hiskp.uni-bonn.de.

[18] T. Corthals, J.Ryckebusch, and T. Van Cauteren, "Forward-angle $K^+\Lambda$ photoproduction in a Regge–plus–resonance approach", Phys. Rev. C **73**, 045207 (2006).

[19] T. Corthals, D.G. Ireland, T. Van Cauteren, J. Ryckebusch, "Regge-plus-resonance treatment of the $\mathrm{p}(\gamma, K^+)\Sigma^0$ and $\mathrm{p}(\gamma, K^0)\Sigma^+$ reactions at forward kaon angles", Phys. Rev. C **75**, 045204 (2007).

[20] Cf. A.V. Anisovich *et al.*, "Energy-independent PWA of the reaction $\gamma p \to K^+\Lambda$", arXiv:1404.4587 (2014); S. Ceci, *et al.*, "PWA tools in Hadronic Spectroscopy", arXiv:1304.5896 (2013); R.L. Workman, "Multipole analysis of kaon photoproduction data", arXiv:1105.2967 (2011).

[21] C.G. Fasano, F. Tabakin, and B. Saghai, "Spin observables at threshold for meson photoproduction", Phys. Rev. C **46**, 2430 (1992).

[22] I.S. Barker, A. Donnachie, J.K. Storrow, "Complete experiments in pseudoscalar photoproduction", Nucl. Phys. **B75**, 347 (1975).

[23] G. Knöchlein, D. Drechsel, and L. Tiator, "Photoproduction and electroproduction of eta mesons", Z. Phys. A **352**, 327 (1995).

[24] W.-T. Chiang and F. Tabakin, "Completeness rules for spin observables in pseudoscalar meson photoproduction", Phys. Rev. C **55**, 2054 (1997).

[25] G.F. Chew, M.L. Goldberger, F.E. Low, and Y. Nambu, "Application of Dispersion Relations to Low-Energy Meson-Nucleon Scattering", Phys. Rev. **106**, 1345 (1957).

[26] R.L. Anderson *et al.*, Phys. Rev. Lett. **9**, 131 (1962); C.W. Peck, Phys. Rev. **135**, 830 (1964); S. Mori, Ph.D. thesis, Cornell University, 1966; H. Thom, a compilation, Phys. Rev. **151** 1322 (1966); N.B. Mistry *et al.*, Phys. Rev. Lett. B **24** 528 (1967); D.E.

Groom, J.H. Marshall, Phys. Rev. **159**, 1213 (1967); A. Bleckmann *et al.*, Z. Phys. **239**, 1 (1970); T. Fujii *et al.*, Preprint (INS, Univ. of Tokyo, 1970); P. Feller *et al.*, Nucl. Phys. B **39** 413 (1972); M. Grilli *et al.*, Nuovo Cim. **38** 1467 (1965); R. Haas *et al.*, Nucl. Phys. B **137** 261 (1978); D. Decamp *et al.*, L.A.L. 1236 (1970).

[27] R. Erbe *et al.* (ABBHHM Collaboration), "Multipion and Strange-Particle Photoproduction on Protons at Energies up to 5.8 GeV", Phys. Rev. **188**, 2060 (1969).

[28] H. Landolt and R. Börnstein, "Numerical Data and Functional Relationships in Science and Technology." New Series I/12b, 1988.

[29] J. Cohen, Phys. Rev. C **37**, 187 (1988); I. Tanabe, U. Kohno, and C. Bennhold, Mainz preprint 1988; R.A. Adelseck and L.E.Wright, Phys. Rev. C **38**, 1965 (1988).

[30] TJNAF experiment E-89-004, "Electromagnetic Prodcution of Hyperons", spokesperson R. Schumacher (1989).

[31] W.J. Schwille *et al.* (SAPHIR Collaboration), "Design and construction of the SAPHIR detector", Nucl. Instr. Meth. A **344**, 470 (1994).

[32] M. Bockhorst *et al.* (SAPHIR Collaboration), "Measurement of $\gamma p \to K^+\Lambda$ and $\gamma p \to K^+\Sigma^0$ at photon energies up to 1.47 GeV", Z. Phys. C **63**, 37 (1994).

[33] M.Q. Tran *et al.* (SAPHIR Collaboration), "Measurement of $\gamma p \to K^+\Lambda$ and $\gamma p \to K^+\Sigma^0$ at photon energies up to 2 GeV", Phys. Lett. B **445**, 20 (1998).

[34] K.-H. Glander *et al.* (SAPHIR Collaboration), "Measurement of $\gamma p \to K^+\Lambda$ and $\gamma p \to K^+\Sigma^0$ at photon energies up to 2.6 GeV", Eur. Phys. J **A19**, 251 (2004).

[35] T. Mart and C. Bennhold, "Evidence for a missing nucleon resonance in kaon photoproduction", Phys. Rev. C **61**, 012201 (2000).

[36] T. Mizutani, C. Fayard, G.-H. Lamot, and B. Saghai, "Off-shell effects in the electromagnetic production of strangeness", Phys. Rev. C **58**,75 (1998).

[37] V. Shklyar, H. Lenske, and U. Mosel, "A coupled-channel analysis of $K\Lambda$ production in the nucleon resonance region", Phys. Rev. C **72**,015210 (2005).

[38] A.V. Anisovich, V. Kleber, E. Klempt, V.A. Nikonov, A.V. Sarantsev, U. Thoma, "Baryon resonances and polarization transfer in hyperon photoproduction", Eur. Phys. J. A **34**, 243 (2007).

[39] B. Juliá-Díaz *et al.*, "Dynamical coupled-channels approach to hadronic and electromagnetic kaon-hyperon production on the proton", Phys. Rev. C **73**, 055204 (2006).

[40] R. Bradford *et. al* (CLAS Collaboration), "Differential cross sections for $\gamma + p \rightarrow K^+ + Y$ for Λ and Σ^0 hyperons", Phys. Rev. C **73**, 035202 (2006).

[41] J. McNabb, "Photoproduction of Λ and Σ^0 Hyperons off Protons in the Nucleon Resonance Region using CLAS at Jefferson Lab", Ph.D. thesis, Carnegie Mellon University, Dec. 2002.

[42] R. Bradford, "Measurement of Differential Cross Sections and C_x and C_z for $\gamma p \rightarrow K^+\Lambda$ and $\gamma p \rightarrow K^+\Sigma^0$ Using CLAS at Jefferson Lab", Ph.D. thesis, Carnegie Mellon University, May 2005.

[43] M.E. McCracken *et al.* (CLAS Collaboration), "Differential cross section and recoil polarization measurements for the $\gamma p \rightarrow K^+\Lambda$ reaction using CLAS at Jefferson Lab", Phys. Rev. C **81**, 025201 (2010).

[44] "LEPS – Laser Electron Photon Experiment at SPring-8". Available from http://www.rcnp.osaka-u.ac.jp/Divisions/np1-b.

[45] M. Sumihama *et al.* (LEPS Collaboration), "The $\gamma p \rightarrow K^+\Lambda$ and $\gamma p \rightarrow K^+\Sigma^0$ reactions at forward angles with photon energies from 1.5-GeV to 2.4-GeV", Phys. Rev. C **73**, 035214 (2006).

[46] K. Hicks, T. Mibe, M. Sumihama, *et al.* (LEPS Collaboration), "Measurement of the polarized $\gamma p \rightarrow K^+\Lambda$ reaction at backward angles", Phys. Rev. C **76**, 042201 (2007).

[47] T.C. Jude, D.I. Glazier, D.P. Watts, *et al.* (Crystal-Ball Collaboration), "$K^+\Lambda$ and $K^+\Sigma^0$ photoproduction with fine center-of-mass energy resolution", submitted to Phys. Lett. **B**, (2014).

[48] R. Bradford *et al.* (CLAS Collaboration), "First measurement of beam-recoil observables C_x and C_z in hyperon photoproduction," Phys. Rev. C **75**, 035205 (2007).

[49] F. Arqueros, *et al.* (GRAAL Collaboration), "The GRAAL Experiment", Proceedings of the XXXth International Meeting of Fundamentals Physics, Nucl. Phys. B **114**, Suppl, 253 (2003).

[50] A. Lleres *et al.* (GRAAL Collaboration), "Polarization observable measurements for $\gamma p \rightarrow K^+\Lambda$ and $\gamma p \rightarrow K^+\Sigma^0$ for energies up to 1.5-GeV," Eur. Phys. J. A **31**, 79 (2007).

[51] R. G. T. Zegers *et al.* (LEPS Collaboration), "Beam polarization asymmetries for the $\mathrm{p}(\gamma, K^+)\Lambda$ and $\mathrm{p}(\gamma, K^+)\Sigma^0$ reactions at E_γ = 1.5-GeV - 2.4-GeV", Phys. Rev. Lett. **91**, 092001 (2003).

[52] A. Lleres *et al.* (GRAAL Collaboration), "Measurement of beam-recoil observables O_x, O_z and target asymmetry for the reaction $\gamma p \to K^+\Lambda$", Eur. Phys. J. A **39**, 149 (2009).

[53] L. De Cruz, "Bayesian model selection for electromagnetic kaon production in the Regge–plus–resonance framework", Ph.D. thesis, Ghent University 2012. Available from http://inwpent5.ugent.be/papers/phdlesley.pdf.

[54] A.V. Anisovich, E. Klempt, V.A. Nikonov, A.V. Sarantsev, U. Thoma, "Nucleon resonances in the fourth resonance region", Eur. Phys. J. A **47**, 153 (2011).

[55] K. Althoff *et. al*, "Photoproduction of $K^+\Lambda$ on polarized protons", Nucl. Phys. **B137**, 269 (1978).

[56] H. Haberzettl, "Gauge-invariant theory of pion photoproduction with dressed hadrons", Phys. Rev. C **56**, 2041 (1997).

[57] F.X. Lee, T. Mart, C. Bennhold, H. Haberzettl, and L.E. Wright "Quasifree Kaon Photoproduction on Nuclei", Nucl. Phys. A **695**, 237 (2001).

[58] K. Miyagawa *et al.*, "Electromagnetic K+ production on the deuteron with hyperon recoil polarization", Nucl. Phys. A **691**, 64 (2001).

[59] A. Salam *et al.*, "Rescattering effects and two-step process in kaon photoproduction on the deuteron", Talk given at the Workshop SNP2004, Osaka, Japan (July 29-31, 2004).

[60] T. Mart, personal communication.

[61] A.V. Anisovich, R. Beck, E. Klempt, V.A. Nikonov, A.V. Sarantsev, U. Thoma, "Properties of baryon resonances from a multichannel partial wave analysis", Eur. Phys. J. A **48**, 15 (2012).

[62] B. Dey *et al.* (CLAS Collaboration), "Differential cross sections and recoil polarizations for the reaction $\gamma p \to K^+\Sigma^0$", Phys. Rev. **C82** 025202 (2010).

[63] B. Carnahan, "Strangeness photoproduction in the $\gamma p \to K^0\Sigma^+$ reaction," Ph.D. thesis, Catholic University, UMI-31-0909682, 2003.

[64] R. Lawall *et al.* (SAPHIR Collaboration), "Measurement of the reaction $\gamma p \to K^0\Sigma^+$ at photon energies up to 2.6-GeV," Eur. Phys. J. A **24**, 275 (2005).

[65] R. Castelijns *et al.* (SAPHIR Collaboration), "Nucleon resonance decay by the $K^0\Sigma^+$ channel", Eur. Phys. J. A **35**, 39 (2008).

[66] R. Ewald *et al.* (CB-ELSA/TAPS Collaboration), "Photoproduction of $\Sigma^+K^0(S)$ with the CBELSA/TAPS-setup", AIP Conf. Proc. **1257**, 566 (2010).

[67] P. D. B. Collins, "An Introduction to Regge Theory and High Energy Physics", Cambridge, MA, 1977.

[68] T. Corthals, "Regge–plus–resonance approach to kaon production from the proton", Ph.D. thesis, Ghent University 2007. Available from http://inwpent5.ugent.be/papers/phdtamara.pdf.

[69] F.J. Klein *et al.*, "Search for Missing Nucleon Resonances in the Photoproduction of Hyperons using a Polarized Photon Beam and a Polarized Target", JLab Experiment E-02-112 (2002).

[70] C.W. Leemann, "The Continuous Electron Beam Accelerator Facility: CEBAF at the Jefferson Laboratory", Ann. Rev. Nucl. Part. Sci. **51**, 413 (2001); http://www.jlab.org/accelerator-science, http://www.jlab.org/brochures.

[71] http://www.jlab.org/photos.

[72] M. Drury *et al.* "CEBAF cryomodule commissioning", JLab Progress Report PR-93-66 (1993).

[73] D.I. Sober *et al.*, "The bremsstrahlung tagged photon beam in Hall B at JLab", NIM A **440**, 263 (2000).

[74] H. Olsen and L. C. Maximon, "Photon and Electron Polarization in High-Energy Bremsstrahlung and Pair Production with Screening", Phys. Rev. **114**, 887 (1957).

[75] B. Mukherjee and A.J.F. Boyle, "On the Debye Characteristic Temperature of Diamond", Phys. Stat. Solidi **22**, K131 (1967).

[76] F.H. Dyson and H. Überall, "Anisotropy of Bremsstrahlung and Pair Production in Single Crystals", Phys. Rev. **99**, 604 (1955); U. Timm, "Coherent Bremsstrahlung of Electrons in Crystals", Fortschr. Phys. **17**, 765 (1969).

[77] F.J. Klein *et al.*, "The Coherent Bremsstrahlung Facility in Hall B at Jefferson Lab", Nucl. Instr. Meth. **A** (submitted, 2005), available online: http://www2.cose.isu.edu/ cole/g8/papers/cbf_nim_v1.8a.pdf.

[78] B.A. Mecking *et al.*, "The CEBAF Large Acceptance Spectrometer", Nucl. Instr. Meth. A **503**, 513 (2003).

[79] J. O'Meara *et al.*, "A Superconducting Toroidal Magnet for the CEBAF Large Acceptance Spectrometer", IEEE Trans. Mag. 25, 1902 (1989).

[80] S. Taylor *et al.*, "The CLAS Start Counter", Nucl. Instr. Meth. A **462**, 484 (2001).

[81] M.D. Mestayer *et al.*, "The CLAS Drift Chamber System", Nucl. Instr. Meth. A **449**, 81 (2000).

[82] E.S. Smith *et al.*, "The time-of-flight system for CLAS", Nucl. Instr. Meth. A **432**, 265 (1999).

[83] See https://clasweb.jlab.org/rungroups/g9/wiki/index.php/Shift_Procedures_for_g9b.

[84] J. Ball and E. Pasyuk, "Photon Flux Determination Through Sampling of 'out-of-time' Hits with the Hall B Photon Tagger" CLAS Internal Report: CLAS-Note 2005-002 (2005).

[85] C. Keith, "Freezing the Spin of the Proton", Talk at the JLab Graduate Student Seminar Series, June 9, 2004 (http://clasweb.jlab.org/frost/Files/talks/2004/Keith_2004_06_09.pdf)

[86] C. Keith *et al.*, "The Jefferson Lab frozen spin target", Nucl. Instr. Meth A **684**, 27 (2012).

[87] C. Keith, FROST website at https://userweb.jlab.org/ ckeith/Frozen/Frozen.html

[88] D. Cords, L. Dennis, D. Heddle, and B.B. Niczyporuk, "CLAS Event Format with BOS", CLAS Internal Report: CLAS-Note 94-012 (1994).

[89] S. Stepanyan, "Proposal for the Production of the DST's to Distribute CLAS Data", CLAS Internal Report: CLAS-Note 99-002 (1999).

[90] B.B. Niczyporuk, "Track Fitting in an Inhomogeneous Magnetic Field", CLAS Internal Report: CLAS-Note 91-001 (1991).

[91] E. Pasyuk, "Brief User Guide to GPID", CLAS Internal Report: CLAS-Note 2007-008 (2007).

[92] R. Brun *et al.*, "ROOT. Data Analysis Framework", Available at http://root.cern.ch/drupal/ .

[93] J. Li, "The New Tagger Calibration Program", CLAS Internal Report: CLAS-Note 2003-004 (2003).

[94] J. Salamanca, J. Langheinrich, P. Cole, E. Pasyuk, "New Start Counter Calibration Procedures", CLAS Internal Report: CLAS-Note 2007-005 (2007).

[95] O. Cortes, "Start Counter Calibration for g9b". Available at clasweb.jlab.org/ rungroups/g13/wiki_secure/index.php/Pass0_v7_ST_Paddle_to_Paddle.

[96] D. Lawrence, M. Mestayer, "CLAS Drift Chamber Calibration: Software and Procedures", CLAS Internal Report: CLAS-Note 99-018 (1999).

[97] S. Park, "DC calibration for g9b". Available at https://clasweb.jlab.org/rungroups/g9/wiki/index.php/DC_Calibration

[98] A. Sabinstev, "Time-of-Flight Calibration for Photoproduction Experiments", CLAS Internal Report: CLAS-Note 2010-013 (2010).

[99] http://www.jlab.org/Hall-B/secure/g9/yuqing/

[100] R. Tucker's analysis webpage at https://clasweb.jlab.org/rungroups/g9/wiki/index.php/Ross's_analysis_page

[101] FROST wiki. Available at https://clasweb.jlab.org/rungroups/g9/wiki/

[102] https://clasweb.jlab.org/rungroups/g9/wiki/index.php/Circular_Beam_Polarization

[103] D. Sober, H. Crannell, F. J. Klein, "The Tagged Energy Scale: Interpreting the CMU Kinematic Fit Results", CLAS Internal Report: CLAS-Note 2004-019 (2004).

[104] A. Netz, TOF study. Available at http://www.jlab.org/Hall-B/secure/g9/anetanet/g9b_TOF_study_Frost_022014.pdf

[105] https://clasweb.jlab.org/rungroups/g9/wiki/index.php/TSCtimeCorr

[106] https://clasweb.jlab.org/rungroups/g9/wiki/index.php/G9b_TOF_problems

[107] H. Bethe and J. Ashkin in "Experimental Nuclear Physics", ed. E. Segré, J. Wiley, New York, 1953, p. 253.

[108] E. Pasyuk, "Energy loss corrections for charged particles in CLAS", CLAS Internal Report: CLAS-Note 2007-016 (2007).

[109] M. Dugger, P. Roy and N. Walford, "Momentum corrections for pi+ and protons in g9b data", CLAS Internal Report: CLAS-Note 2013-011 (2013).

[110] L. Casey, "The Search for Missing Resonances in $\gamma p \to K^+\Lambda$ Using Circularly Polarized Photons on a Longitudinally Polarized Frozen Spin Target", Ph.D. thesis, Catholic Univ. of America, May 2011.

[111] S. Fegan, "Polarization Observables from Strangeness Photoproduction on a Frozen Spin Target with CLAS at Jefferson Lab", Ph.D. thesis, Glasgow University, October 2011.

[112] Quasi-free kaon production reduced due to Fermi motion and strong $\Lambda - N$ final state interaction, cf. H. Yamazaki, "The $^{12}C(\gamma, K^+)$ reaction in the threshold region", Phy. Rev. C **52**, R1157 (1995); T.A. Rijken, V.G.J. Stoks, and Y. Yamamoto, "Soft-core hyperon nucleon potentials", Phys. Rev. C **59**, 21 (1999); J. Haidenbauer and U.-G. Meissner, "The Jülich hyperon-nucleon model revisited", Phys. Rev C **72** , 044005 (2005).

[113] N. Zachariou and Y. Ilieva, "Determination of the Beam-Spin Asymmetry Using the phi-bin Method", CLAS Internal Report: CLAS-Note 2012-011 (2012).

[114] M. Dugger, B.G. Ritchie, P. Collins, E. A. Pasyuk, "Beam asymmetry extraction technique for g8b", CLAS Internal Report: CLAS-Note 2008-05 (2008).

[115] M. Dugger, B. G. Ritchie, M. A. Garcia, E. A. Pasyuk, P. Collins, B. Morrison, "Extraction technique for Σ and G for pseudoscalar meson photoproduction", CLAS Internal Report: CLAS-Note 2009-026 (2009).

[116] M. Dugger, "Preliminary target asymmetry for pi+ n (version 2)", available at https://clasweb.jlab.org/rungroups/g9/wiki/index.php/Mike's_analysis_page

[117] T. Vrancx, personal communication.